

SILICON *p-i-n* MESA-PHOTODIODE TECHNOLOGY

✉ Mykola S. Kukurudziak^{a,b,*}, ✉ Volodymyr M. Lipka^{a,b}, Vyacheslav V. Ryukhtin^a

^a*Rhythm Optoelectronics Shareholding Company, Holovna str. 244, 58032, Chernivtsi, Ukraine*

^b*Yuriy Fedkovych Chernivtsi National University, Kotsyubyns'kogo str. 2, 58012, Chernivtsi, Ukraine*

*Corresponding Author e-mail: mykola.kukurudzyak@gmail.com

Received June 15, 2024; revised July 29, 2024; accepted August 12, 2024

The paper proposes the technology of silicon *p-i-n* mesa-photodiodes, which allows to exclude one high-temperature operation from the technological route. Reducing the number of thermal operations reduces the degree of degradation of the electro-physical characteristics of silicon during heat treatment, which also contributes to reducing the density of surface states at the SiSiO₂ interface. It is proposed to etch the mesa-profile by the method of chemical-dynamic polishing using a gold masking coating. The obtained photodiodes are cheaper than serial samples made by diffusion-planar technology and have higher sensitivity.

Keywords: *Silicon; Photodiode; Point Defects, Dislocations, Dark Current, Sensitivity*

PACS: 61.72. Ji, 61.72. Lk, 85.60.Dw

Semiconductor photodetectors are widely used in the development of automatic regulation and control systems for technological processes, research of the Earth's natural resources, in aircraft astronavigation systems, as well as in military equipment and cinema and photographic equipment [1]. The most widely used type of photodetectors is *p-i-n* photodiodes (PD) [2,3], and the main material of these products in the microelectronics industry is silicon due to its high manufacturability and widespread [4, 5].

The main parameters of PDs are responsivity, which determine the ability to register photosignals a certain range of wavelengths [6]. The main factor that ensures the maximum value of the photodiode photoresponsivity is the use of a base material with the highest possible values of the lifetime of minor charge carriers (τ) and resistivity (ρ), since these electrophysical characteristics determine the size of the region in which photogeneration of charge carriers occurs [7]. However, it should be noted that these parameters of silicon can degrade during high-temperature treatments [8, 9], so it is worth using technological methods and routes with a minimum number of thermal operations and with the lowest possible temperatures [10, 11].

The classical serial route of manufacturing *p-i-n* PDs based on *p*-Si using two-stage phosphorus diffusion from planar sources includes 4 thermal operations: oxidation, phosphorus predeposition, phosphorus driving-in and diffusion of boron [12]. It should be noted that two of these operations are high-temperature ($T=1423$ K), during which the degradation of electrophysical parameters occurs due to the diffusion of uncontrolled metal impurities with high diffusion coefficients or thermal shocks [13].

It is possible to exclude high-temperature expansion of phosphorus by using a single-stage diffusion of phosphorus from liquid diffusers PCl₃ or POCl₃, but in [14] we found that diffusion of phosphorus from liquid phased sources provokes the formation of a high density of structural defects (including dislocations), which in turn significantly reduces the percentage of usable products. This is due to the diffusion of phosphorus not only into the lattice nodes but also into the interstices, where the high density of electrically inactive impurities generates significant mechanical stresses compared to diffusion from planar sources, where alloying occurs along the lattice nodes.

Another method to reduce the number of thermal operations is to produce PDs with a mesa profile [15]. In this case, the first thermal operation is phosphorus diffusion, and the responsive elements (RE) are formed by etching mesa-structure, where the formed mesa-profile grooves are the gaps between the active elements of the photodiode crystal. In this case, there is no need for the first high-temperature oxidation. The problem of the described technique is the need to find a masking coating that allows masking the active regions of the photodiode from the effects of an aggressive etchant during etching. In [16], we conducted an experimental search for masking coatings and found that the use of AZ4533 [17] photoresist allows for a short time of etching in an HNO₃ : HF : CH₃COOH = 9:2:4 -compound etchant. The disadvantages of this photoresist are its high density, which causes problems during deposition, its high market price, and the inability to form a mesa profile of increased depth. We also proposed the use of a masking oxide deposited by RF cathodic sputtering for etching the mesa structure, since the etching speed of silicon oxide is significantly lower than that of silicon in the used etching agent. However, the application of the oxide film by this method provoked the formation of a high density of mismatch dislocations and, accordingly, the degradation of photodiode parameters, so this method proved to be ineffective [16].

Photodiodes with mesastructure have proven to be very promising products, so the search for the perfect technology and structure of these photodetectors is an urgent scientific and technical task. We have conducted a study on the use of a Au-masking coating for etching silicon in aggressive etchers. Accordingly, the purpose of this article is to investigate the

possibility of manufacturing mesa-photodiodes using a Au- masking coating for etching, to study the parameters of these photodiodes and to compare them with the parameters of serial photodiodes manufactured using the classical diffusion-planar technology.

EXPERIMENTAL

The research was carried out in the manufacture of silicon 4Q *p-i-n* PDs with guard ring (GR) for operation at wavelength $\lambda_{op} = 1.064 \mu\text{m}$. PDs were made on the basis of single-crystal *p*-type silicon with resistivity $\rho \approx 18\text{-}22 \text{ k}\Omega\cdot\text{cm}$ and [111] orientation. The serial commercial samples were made by diffusion-planar technology according to the technological regimes given in [12] (PDC). The thickness of the crystals reached 500-510 μm .

The crystals of the experimental mesa-photodiodes (PD_M) were produced by the following sequence of technological operations: phosphorus predeposition from solid-state planar phosphorus sources in a nitrogen atmosphere; phosphorus driving-in in a dry oxygen atmosphere; boron diffusion to the back side of the substrate; photolithography to create contact windows in the anti-reflective oxide; deposition of an Au-layer with an adhesive Chr-layer on the front side of the wafer; photolithography to open windows corresponding to the gaps between the REs (Fig. 1a) with the back side protected by a chemically resistant varnish; etching of the mesa-profile by chemical-dynamic polishing (Fig. 1b) according to the method described in [15]; photolithography to form Au-contact pads; application of Au with an adhesive chromium layer on the back side of the plate; and separation of crystals by cutting with a diamond cutting disc.



Figure 1. Images of silicon wafers at different stages of PD manufacturing: a) after photolithography to open windows corresponding to the gaps between the REs; b) after chemical-dynamic polishing and photolithography to form Au-contact pads.

The depth of the mesa-profile should be greater than the depth of the diffuse phosphorus layer; in the case studied, the profile depth reached about 10 μm .

It is worth noting that the use of a "thin" gold film for prolonged etching in hydrofluoric acid or a polishing etchant can provoke the formation of etchings on the surface of REs due to the penetration of the etchant through the pores in the masking layer (Fig. 2). To ensure a proper masking effect, we used a gold thickness of 500-600 μm . The image of the final product is shown in Fig. 3.

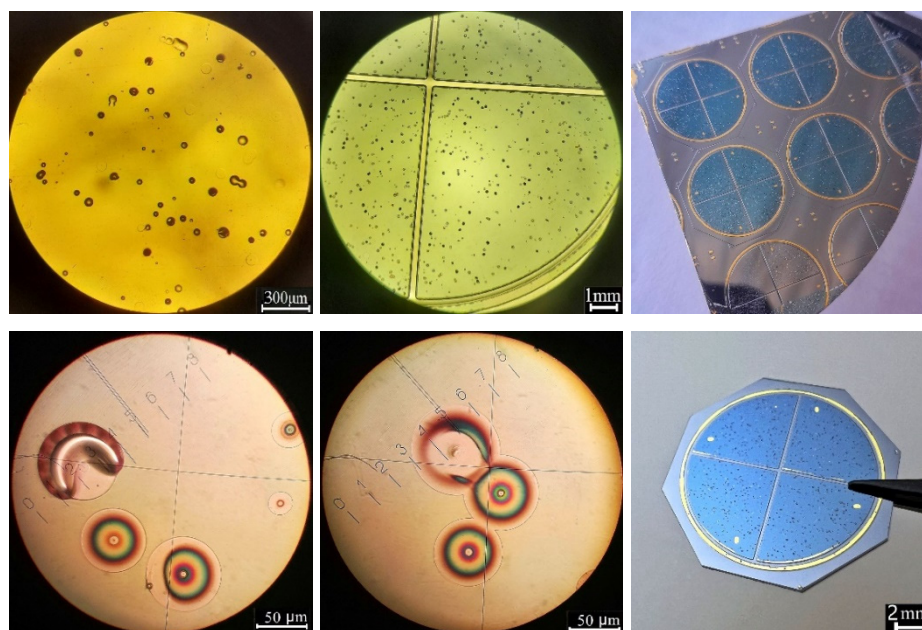


Figure 2. Images of photodiode crystals with etchings formed during oxide etching or chemical-dynamic polishing

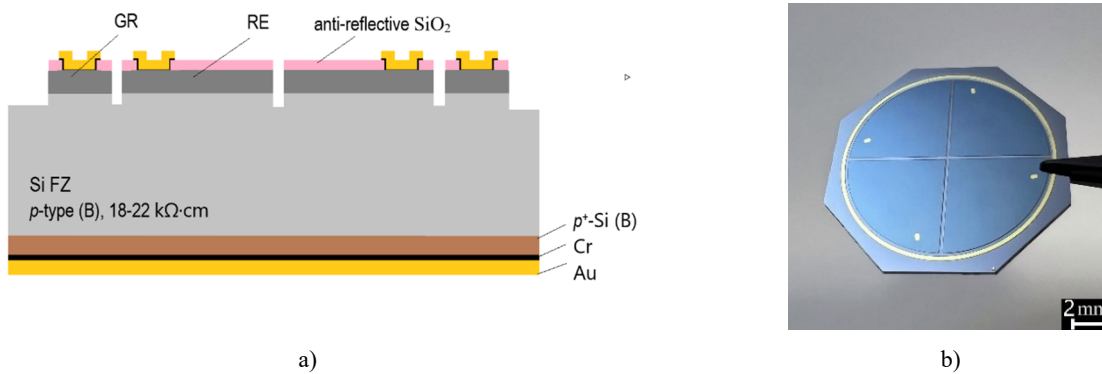


Figure 3. The image of the final *p-i-n* meza PD: a) cross-ception; b) final crystal.

The reverse $I-V$ characteristics of PDs were measured using a hardware-software complex implemented on the basis of the Arduino platform, an Agilent 34410A digital multimeter and a Siglent SPD3303X programmable power source, which were controlled by a personal computer using software created by the authors in the LabView environment.

Determination of R_{con} was carried out according to the method shown in [18].

Monitoring of current monochromatic pulse responsivity was carried out by method of comparing responsivity of the investigated PD with a reference photodiode certified by the respective metrological service of the company. Measurements were performed when illuminating the PD with a radiation flux of a power of not over $1 \cdot 10^{-3}$ W; load resistance across the responsive element $R_l = 10$ k Ω ,

RESULTS OF THE RESEARCH AND THEIR DISCUSSION

The reverse $I-V$ characteristics of the PDs show that the experimental samples PD_M had slightly higher dark current values in the seventh reverse voltage range (Fig. 4). The reason for the difference in the dark current values is a slight increase in the area of the responsive elements and the release of the space charge region on the wafer surface due to the presence of the etching wedge and mesa profile [16]. These factors increase the value of the dark current due to the presence of a large number of surface states on the plate surface: a violation of the periodicity of the lattice potential of the crystal due to its break at the surface (Tamm levels) [17]; the presence of uncompensated valence bonds in surface atoms (Shockley levels) [18]; and the distortion of the lattice potential on the surface caused by adsorbed atoms and surface defects. The Tamm and Shockley levels characterize an ideal surface. On a real surface, however, surface levels caused by surface defects play a decisive role. These include point defects, which are atomic disturbances at individual points in the lattice (e.g., vacancies in lattice nodes or interstitial atoms), as well as linear and bulk defects (dislocations, pores, inclusions of another phase, etc.).

From the point of view of the band structure of a semiconductor, the presence of surface defects or adsorbed atoms leads to the formation of allowed levels in the band gap of the semiconductor, localized on the surface. Electrons from the valence band can move to these levels, and vice versa, electrons from surface levels can move to the conduction band, resulting in the semiconductor surface becoming charged, i.e. the formation of a semiconductor surface layer charged inversely to the volume of the so-called inversion layer.

Accordingly, the growth of the dark current occurs due to the growth of the surface generation component (I_d^{surf}), which is directly proportional to the density of surface states (1)[14].

$$I_d^{surf} = \frac{eN_{ss}v_{drift}\sigma_{ss}A_{p-n}}{2} \quad (1)$$

where σ_{ss} is capture cross-sectional area; N_{ss} – density of surface states; A_{p-n} - is the area that contributes to the surface component of the dark current; v_{drift} – is the average relative (relative to the center of re-combination) velocity of thermal charge carriers.

It should be noted that the mesa-profile formation was one of the last technological operations of the photodiode crystal manufacturing, after which no high-temperature operations were performed, so the etched surface can be considered quasi-perfect. An informative method for determining the presence of surface states is to measure the insulation resistance between responsive elements, as well as to measure the reverse dark $I-V$ -characteristic of the guard ring, since the presence of surface states at the periphery of the crystal is crucial for the dark current of the guard ring, which contribute to the decrease in the surface component of the dark current when the area of space charge region of the guard ring is extended to the periphery.

In the experimental samples PD_M , the insulation resistance of all responsive elements and the GR was about $\sum R_{con} \approx 3-5$ M Ω , and in the serial samples PD_C produced by a single technological cycle, it was $\sum R_{con} \approx 0.5-1$ M Ω . Also, from the $I-V$ -characteristics of the GRs, it can be concluded that the number of surface states in the mesa-photodiode is much lower, since this PD had a much lower value of the dark current of the guard ring (Fig. 4). The reason for the increase in the number of surface states is the presence of a larger number of high-temperature operations, in particular thermal oxidation, during which

a large number of structural point defects are formed on the silicon surface, in particular the inclusion of interstitial silicon atoms or their accumulation due to oxygen diffusion [13], as well as a high probability of diffusion of uncontrolled impurities, in particular metals, due to their presence in the quartz tooling or improper chemical treatment of the wafers.

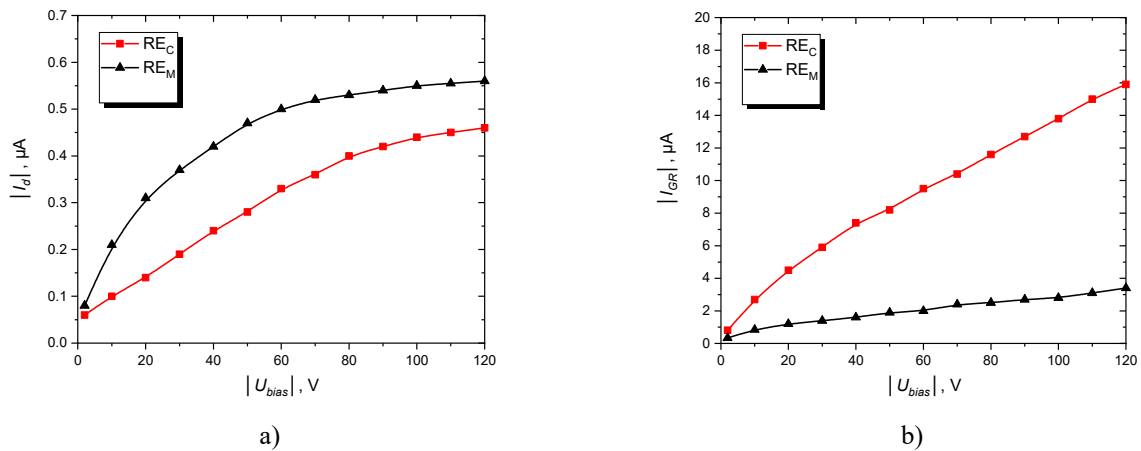


Figure 4. Reverse dark I - V characteristics of REs (a) and GRs (b).

It is worth noting that in [16] the depth of the mesa profile reached values only 1 μm greater than the depth of the diffusion layer of phosphorus. In this case, the difference in the values of the dark current of serial and mesa-photodiodes was minimal (up to 20 A). And in the case studied in this article, the depth of the mesa profile is twice as large as the depth of the diffusion layer, where a difference in the dark current values of ≥ 100 A was observed. Accordingly, it can be concluded that the dark current depends on the depth of the mesa profile, which correlates well with the above dependence of the dark current on the number of surface states captured by the spatial charge region.

It should be noted that the absence of the first thermal oxidation before phosphorus diffusion also allows us to obtain samples with a much lower dislocation density. It is known [13] that during the diffusion of phosphorus in the oxidizing atmosphere, local generation of defects, such as stacking faults and dislocations, occurs in places of localized disturbances of the wafer surface. And given the fact that the wafers before thermal operations undergo chemical and dynamic polishing, which minimizes the presence of surface defects, point defects formed during oxidation are the main centers of localization of dislocations. Accordingly, the absence of dislocation generation centers helps to reduce the probability of their formation.

Also, from the dependence of photodiode responsivity (Fig. 5) on voltage, it can be seen that mesa-photodiodes had a slightly higher photosensitivity than serial ones. This can be explained by a smaller number of generation and recombination centers and "traps" in the high-resistance region of the photodiode, where scattering and recombination of photogenerated charge carriers is possible, since, again, the absence of high-temperature oxidation reduces the probability of these "traps".

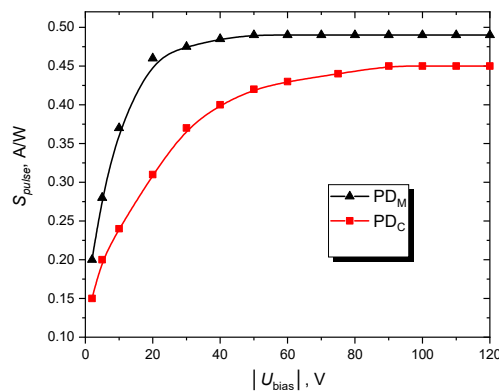


Figure 5. Dependence of the responsivity of PDs on the reverse bias voltage

It should be noted that the responsivity curve for the mesa-photodiode reaches saturation at lower values of the reverse voltages. This can be explained by the higher resistivity and lifetime of minority charge carriers, the degree of degradation of which is lower in PD_M than in serial ones, since the sensitivity of the photodiode reaches a maximum when the space charge region (SCR) is extended to the entire thickness of the high-resistance region of the PD (or when the SCR and diffusion length of minor charge carriers are extended).

In addition to the obvious reduction in the cost of the proposed PDs, their advantage is the absence of the need to control the C - V characteristics of products after each thermal operation. This method is an informative option for assessing

the quality of products at different stages of photodiode crystal manufacturing, which allows to estimate the density of surface states at the Si-SiO₂ interface [21, 22]. The absence of the need to measure the *C-V* characteristics is ensured by etching the mesa profile between the responsive elements and bleeding the crystal periphery, which completely removes the surface inversion layers that could contribute to the surface generation component of the dark current or worsen the insulation resistance between the active elements. In the case of the proposed mesa-photodiodes, only the Tamm and Shockley levels contribute to the dark current values. The only caveat is the lack of protective oxide on the surface of the etched areas, and therefore there is a need to seal the products without any delays, since the quasi-ideal surface after etching is very active and can oxidise even at room temperature or adsorb atoms, which will negatively affect the value of the density of surface states. Another way to ensure a low level of surface state density is to form silicon oxide or nitride on the surface of the etched areas using any known non-thermal method.

CONCLUSIONS

Silicon *p-i-n* mesa-photodiodes have been fabricated and studied. It is proposed to use a gold masking layer with an adhesive layer of chromium for chemical-dynamic polishing. The technology of mesa-photodiodes allows to exclude the first high-temperature oxidation from the technological cycle, which contributes to a decrease in the density of surface states at the Si-SiO₂ interface and reduces the degree of degradation of the electrophysical characteristics of silicon, which positively affects the parameters of photodiodes.

ORCID

✉ Mykola S. Kukurudziak, <https://orcid.org/0000-0002-0059-1387>; ✉ Volodymyr M. Lipka, <https://orcid.org/0009-0001-4419-3356>

REFERENCES

- [1] M.K. Bakhadyrkhanov, S.B. Isamov, Z.T. Kenzhaev, D. Melebaev, K.F. Zikrillayev, and G.A. Ikhtiyarova, *Applied Solar Energy*, **56**, 13 (2020). <https://doi.org/10.3103/S0003701X2001003X>
- [2] Z. Wei, J. Yu, M. Zuo, and P. Nie, *Journal of Applied Physics*, **135**(11), 115701 (2024). <https://doi.org/10.1063/5.0187696>
- [3] Z. Wei, J. Yu, L. Gao, M. Zuo, and P. Nie, *Appl. Phys.* **130**(4), 58 (2024). <https://doi.org/10.1007/s00340-024-08201-4>
- [4] A. Müller, M. Ghosh, R. Sonnenschein, and P. Woditsch, *Materials Science and Engineering: B*, **134**(2-3), 257 (2006). <https://doi.org/10.1016/j.mseb.2006.06.054>
- [5] C. Ballif, F.J. Haug, M. Boccard, P.J. Verlinden, and G. Hahn, *Nature Reviews Materials*, **7**(8), 597 (2022). <https://doi.org/10.1038/s41578-022-00423-2>
- [6] T. Tansel, and O. Aydin, *J. Phys. D: Appl. Phys.* **57**, 295103 (2024). <https://doi.org/10.1088/1361-6463/ad3b08>
- [7] M.S. Kukurudziak, and E.V. Maistruk, *East Eur. J. Phys.* **1**, 386 (2024). <https://doi.org/10.26565/2312-4334-2024-1-39>
- [8] K.S. Daliev, Sh.B. Utamuradova, A. Khaitbaev, J.J. Khamdamov, Sh.B. Norkulov, and M.B. Bekmuratov, *East Eur. J. Phys.* **2**, 283 (2024). <https://doi.org/10.26565/2312-4334-2024-2-30>
- [9] Kh.S. Daliev, Sh.B. Utamuradova, A.I. Khaitbaeva J.J. Khamdamov, J.Sh. Zarifbaev, and B.Sh. Alikulov, *East Eur. J. Phys.* **2**, 288 (2024). <https://doi.org/10.26565/2312-4334-2024-2-31>
- [10] G.P. Gaidar, *Journal of Physical Research*, **22**(4), 4601 (2018). <https://doi.org/10.30970/jps.22.4601>. (in Ukrainian).
- [11] W.S. Yoo, T. Fukada, I. Yokoyama, K. Kang, and N. Takahashi, *Japanese journal of applied physics*, **41**(7R), 4442 (2002). <https://doi.org/10.1143/JJAP.41.4442>
- [12] M.S. Kukurudziak, *Physics and Chemistry of Solid State*, **23**(4), 756 (2022). <https://doi.org/10.15330/pcss.23.4.756-763>
- [13] K.V. Ravi, *Imperfections and impurities in semiconductor silicon*, (Wiley, New York, 1981).
- [14] M.S. Kukurudziak, *Semiconductor Physics, Quantum Electronics & Optoelectronics*, **25**(4), 385 (2022). <https://doi.org/10.15407/spqeo25.04.385>
- [15] A.V. Fedorenko, *Technology and design in electronic equipment*, **17**(3-4), 17 (2020). <https://doi.org/10.15222/TKEA2020.3-4.17>. (in Ukrainian)
- [16] M.S. Kukurudziak, and E.V. Maistruk, *Semicond. Sci. Technol.* **38**, 085007 (2023). <https://doi.org/10.1088/1361-6641/acdf14>
- [17] Passport data AZ4533 Electronic resource, www.microchemicals.com/products/photoresists/az_4533.html
- [18] M. Kukurudziak, *Radioelectronic and Computer Systems*, **105**(1), 92-100 (2023). <https://doi.org/10.32620/reks.2023.1.07>
- [19] B.L. Oksengendler, S.Kh. Suleymanov, Z.I. Karimov, N.N. Turaeva, A.S. Doroshkevich, and J. Mezentseva, *J. Phys.: Conf. Ser.* **2697**, 012061 (2024). <https://doi.org/10.1088/1742-6596/2697/1/012061>
- [20] B. Ruch, M. Jech, G. Pobegen, and T. Grasser, *IEEE Transactions on Electron Devices*, **68**(4), 2092-2097 (2021). <https://doi.org/10.1109/TED.2021.3049760>
- [21] M.S. Kukurudziak, *East Eur. J. Phys.* **2**, 289 (2023). <https://doi.org/10.26565/2312-4334-2023-2-33>
- [22] H. Mizobata, Y. Wada, and M. Nozaki, *Applied Physics Express*, **13**(8), 081001 (2020). <https://doi.org/10.35848/1882-0786/aba320>

ТЕХНОЛОГІЯ КРЕМНІСВОГО *p-i-n* МЕЗА-ФОТОДІОДА

Микола С. Кукурудзяк^{a,b}, Володимир М. Ліпка^{a,b}, В'ячеслав В. Рюхтін^a

^aАТ «Центральне конструкторське бюро Ритм», 58032, м. Чернівці, вул. Головна, 244, Україна

^bЧернівецький національний університет імені Юрія Федьковича, 58002, м. Чернівці, вул. Коцюбинського, 2, Україна

У статті запропоновано технологію кремнієвих *p-i-n* меза-фотодіодів, яка дозволяє виключити одну високотемпературну операцію з технологічного маршруту. Зниження кількості термічних операцій дозволяє знизити міру деградації електрофізичних характеристик кремнію в процесі термообробок, що також сприяє зменшенню густини поверхневих станів на межі розділу Si-SiO₂. Запропоновано проводити травлення меза-профілю методом хіміко-динамічного полірування з використанням золотого маскуючого покриття. Отримані фотодіоди є дешевшими, ніж серійні зрази виготовлені за дифузійно-планарною технологією та володіють вищою чутливістю.

Ключові слова: кремній; фотодіод; чутливість; точковий дефект; дислокація; темновий струм

NUMERICAL SIMULATION STUDY OF THE INCREASE IN ELECTRICAL EFFICIENCY OF THE CIGS-BASED SOLAR CELL BY SCAPS-1D

K. Madoui^a, A. Ghechi^b, S. Madoui^c, R. Yekhle^d,  D. Belfennache^{d*}, S. Zaiou^{e,f},  Mohamed A. Ali^g

^aLaboratory of Applied Optics, Institute of optics and precision mechanics, Ferhat ABBAS Setif-1 University, Algeria

^bLaboratory of Optoelectronics and components, Institute of optics and precision mechanics. Ferhat Abbas Setif-1 University, Algeria

^cLaboratory of Applied Biochemistry, University Ferhat Abbas Setif-1, 19000, Algeria

^dResearch Center in Industrial Technologies CRTI, P.O. Box 64, Cheraga, 16014 Algiers, Algeria

^eLaboratory for Studies of Surfaces and Interfaces of Solid Materials (LESIMS), University Setif-1, 19000 Setif, Algeria

^fFaculty of Natural Sciences and Life, Setif-1 University, 19000 Setif, Algeria

^gSchool of Biotechnology, Badr University in Cairo (BUC), Badr City 11829, Cairo, Egypt

*Corresponding Author e-mail: belfennachedjamel@gmail.com

Received May 15, 2024; revised July 3, 2024; accepted July 12, 2024

Solar cells are currently the focus of a great deal of research. The aim is to reduce their cost price. To achieve this, we need to reduce the mass of the materials and increase the conversion efficiency of these solar cells. This has motivated research into the use of thin films such as a-Si, CdTe, CIGS. This increase in efficiency requires optimizing the performance of the photovoltaic parameters. In this modeling and simulation work, we use the SCAPS-1D software to study the effect of the recombination speed of the electrons and holes in the CIGS layer, the effect of the thickness of the layers and the effect of the gap energy of each layer of the material used for this solar cell on the short-circuit current J_{sc} , the open-circuit voltage V_{oc} , the form factor FF and the electrical efficiency η of the CIGS cell for a Mo/p-CIGS/p-Si/In₂S₃/i-ZnO/Al-ZnO single-junction structure. In this study, we found that recombination speed affects the efficiency of the photovoltaic cell. The gap energy of the absorber layers influences the cell's efficiency, while the other layers (In₂S₃, ZnO, Al-ZnO) do not have a great influence on solar cell performance and increasing the thickness of the absorber layer has a major influence on efficiency, increasing it up to a certain limit. The thicknesses of the CIGS, p-Si, In₂S₃, i-ZnO and Al-ZnO layers need to be in the order of 0.3 μ m, 0.8 μ m, 0.05 μ m, 0.07 μ m and 0.1 μ m respectively to achieve better efficiency (31.42%).

Keywords: Density functional theory (DFT); Binding energies; Homo-lumo energy; Fragmentation energy; Magnetic moment

PACS: 73.50.-h, 73.50.Pz

1. INTRODUCTION

The evolution and development of humanity leads to increasing energy consumption while usual energy resources decrease and pollution increases. Renewable energies appear to provide an optimal solution to address the global energy problem [1]. Among them, solar energy offers a reliable, clean and adaptable way to generate heat and electricity according to needs. More particularly, photovoltaics (PV) constitutes an “inexpensive” solution to overcome the energy supply problem of developing countries, thanks to autonomous systems making it possible not only to supply electricity but also to power systems water pumps or water filtration [2]. As part of the sustainable development approach, renewable energies make it possible to preserve planetary resources, ensure the security and diversity of energy supplies and reduce the environmental impact of our energy consumption. The PV market today is essentially based on silicon technology [3]. Currently, the sector is largely dominated by crystalline silicon technology with nearly 93% of global production. However, the production of silicon-based solar cells remains expensive and requires a large quantity of material [4]. In addition, silicon cells currently have a maximum efficiency of 25.6% in the laboratory, which is very close to the maximum theoretical limit for a single junction cell [5]. Consequently, the growing need for photovoltaic energy has pushed research into the use of other alternative materials, although this in no way means an end to research in the silicon sector [6-8]. Research, very numerous and varied, focuses mainly on thin film technologies [9-12]. CIGS-based thin-film solar cells were developed by Arco in the late 1980s using a two-step process with Cu and In as metal precursors, followed by reactive annealing in an H₂S atmosphere, during of which the absorbing layer (CIGS) is doped with N/A. Since then, the leading research organization in the field of CIGS solar cells (NREL) has reported the remarkable improvements in efficiency achieved by these cells deposited on substrates of rigid glass [13-16]. The most promising second generation materials are amorphous and microcrystalline silicon, cadmium tellurium (CdTe) and the Cu (In_x, Ga_{1-x})(S_y,Se_{1-y})₂ (CIGSSe) family of chalcopyrites. These materials are used in the form of a thin layer deposited on a substrate (soda glass, ceramic, polyamide, etc.), which not only reduces the costs of the final module, but also expands the range of applications of the cells solar. In a few years, the efficiency of solar cells based on Cu(In,Ga)Se₂ (CIGS) increased from 20.8% [13] to 22.6% [14]. Many studies have proven that cadmium tablets have enabled high productivity, but they nevertheless tend to be replaced, due to their toxicity, by cadmium-free, higher bandgap materials (In₂Se₃, ZnS, Zn(S,O), Zn(S,O,OH), (Zn,Mg) O) to reduce optical losses [17-20].

Whatever the structure of a solar cell, its parameters need to be optimized. Typically, the parameters to be optimized are the Eg bandgap thicknesses and widths, and the doping levels of the various layers making up the cell. Solar cell optimization therefore involves studying the influence of these parameters on efficiency, in order to obtain a structure that delivers maximum efficiency. This optimization can be carried out either experimentally or by simulation. Experimental optimization has the advantage of being real, but it is tedious, boring and expensive. What's more, we don't have access to certain cell parameters. Simulation-based optimization, on the other hand, follows a mathematical model of the real system. In this work, we will use SCAPS-1. This allows us to understand in detail the functioning of the structure of thin film solar cells and the main physical phenomena which govern the operation of our devices by carefully taking into account: the short circuit current J_{sc} , the open circuit voltage V_{oc} , efficiency ($\eta\%$) and filling factor (FF) [21] CIGS, a non-toxic material widely available on Earth, knowing that it is expensive. To reduce the thickness of CIGS, we choose the following solar cell structure: Al-ZnO/i-ZnO/ In_2S_3 /p-CIGS/p-Si. CIGS and Si we will use as absorbing layers and In_2S_3 as insulating layer. We study the performance of CIGS-based solar cells by changing the spacing energy and thickness of each cell layer.

2. OVERVIEW OF SCAPS-1D SOFTWARE

SCAPS (solar cell capacitance simulator) is a one-dimensional solar cell simulation program developed at the Department of Electronics and Information Systems (ELIS) at Ghent University, Belgium. Several researchers have contributed to its development: Alex Niemegeers, Marc Burgelman, Koen Decock, Stefaan Degraeve, Johan Verschraegen. The program was initially developed for cellular structures of the $CuInSe_2$ and $CdTe$ family. Recent developments now make the program equally applicable to crystalline solar cells (Si and GaAs family) and amorphous cells (a-Si and micromorphous Si). The latest version, SCAPS 3.10, may 2020. The program runs on PCs running Windows 95, 98, NT, 2000, XP, Vista, Windows 7,8 and 10, and takes up around 50 MB of space. It is freely accessible to the PV research community (universities and research institutes, companies) [22-27].

3. PRESENTATION OF THE STUDIED CELL

The difficulty in simulating electronic devices lies in the choice of simulation parameters. For this, we took a work submitted by Mohottige RN and Kalawila SP, they found an electrical efficiency of ~26% [28]. The solar cell architecture simulated in this study had a substrate/Mo/p-Si/pCIGS/n- In_2S_3 /i-ZnO/Al-ZnO/metal grid, as shown in Fig. (1).

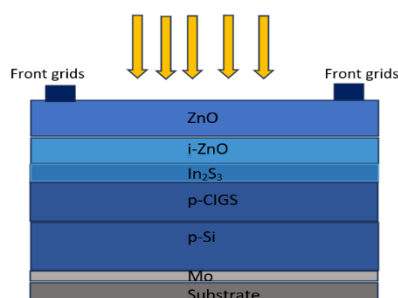


Figure 1. Schematic diagram of the CIGS Structure [28].

The defect density was implemented in the P-Si, CIGS and In_2S_3 layers. The i-ZnO insulating layer improves the performance of thin-film solar cells. This material can fill the pinholes in the structure and reduce the electric short circuit [29]. Electrical short-circuiting of devices is a key concern during the manufacturing process, and it's an excellent solution to suppress between interfaces to increase efficiency. So, the i-ZnO layer acts as an electron backscatter barrier, improving J_{sc} and efficiency. Table 1, shows the optimized material properties for each layer used in the simulation. These parameters are entered into the SCAPS software.

Table 1. Material parameters used in the simulation [28]

Parameters	CIGS	P- Si	In_2S_3	I-Zno	Al-Zno
Thicknesses (nm)	100 1000	1000	50	70	100
Gap strip (ev)	1.100	1.120	2.800	3.300	3.300
Electronic affinity (ev)	4.500	4.500	4.700	4.600	4.600
Relative Permittivity	13.600	11.900	13.500	9.000	9.000
CB ($1/cm^3$)	2.200E +18	2.800E +19	1.800E +18	2.200E +18	2.200E +18
VB($1/cm^3$)	1.800E +19	2.650E +19	4.000E +13	1.800E +19	1.800E +19
Electron mobility (cm^2/Vs)	1.000E +2	1.450E +3	4.000E +2	1.000E +2	1.000E +2
Hole mobility (cm^2/Vs)	2.500E +1	5.000E +2	2.100E +2	2.500E +1	2.500E +1
ND($1/cm^3$)	0.000E +0	0.000E +0	1.000E +18	1.000E +16	1.000E +18
NA($1/cm^3$)	2.000E +16	1.000E +20	1.000E +1	0.000E +0	0.000E +0
Defect density ($1/cm^3$)	1.000E +14	1.000E +14	1.000E +14	0.000E +0	0.000E +0

This digital survey was carried out in three stages: The effect of the recombination rate of electrons and holes on the cell was studied. Next, we studied the influence of varying the gap energy values of each layer on the cell's

performance, and extracted the relationship between the gap energy of the CIGS and p-Si absorber layers. Finally, cell performance was optimized by changing the thicknesses of each cell layer: the CIGS and P-Si absorber layers, the In_2S_3 buffer layer, the i-ZnO insulator layer and the Al-ZnO window layer. The simulation was carried out under solar spectrum AM 1.5 and at an incident power of $p = 1000\text{Wm}^{-2}$. SCAPS simulation can perform measurements under light and dark conditions and in various temperature ranges and other parameters. In this study, we maintained the thickness of the p-Si, i-ZnO and Al-ZnO layers at 1 μm , 50 nm and 100 nm respectively [28] in order to investigate solar cell parameters such as: Short-circuit current J_{sc} , Open-circuit voltage V_{oc} , Efficiency ($\eta\%$) and fill factor (FF). The first layer deposited on the substrate is the back contact electrode. Its main role is to collect the charges generated in the cell. From an electrical point of view, it constitutes the positive pole of the photovoltaic generator. This layer is composed of Molybdenum (Mo) and is between 50 nm and 1500 nm thick, this result is consistent with the results reported in the literature [30,31]. In addition, the Mo layer is used as a reflector to lengthen the optical path of light in the CIGS, thereby increasing the number of photons absorbed [32]. Numerous studies have also proven that during the deposition of CIGS on Mo, a thin layer of MoSe2 is formed at the interface. This layer is responsible for establishing ohmic contact with the CIGS [33,34].

4. EFFECT OF THE RECOMBINATION SPEED OF ELECTRONS AND HOLES

Generation in semiconductors is the process in which electron-hole pairs are created. The energy necessary for the transition of an electron from the valence band to the conduction band is obtained by different physical processes: thermal absorption, external electric field and absorption of photons by the semiconductor. The electron-hole pairs created are sooner or later recombined. In this section, we will present in a first part the results relating to the effect of the recombination speed for a CIGS thickness of $0.1\mu\text{m}$: as well as their analyzes in order to understand the effect of the recombination speed of electrons and holes. In a second part, Effect of the recombination rate for a CIGS thickness of $0.3\mu\text{m}$ will be presented so that it can be examined and properly interpreted and this in comparison with the conclusions resulting from the electron recombination rate and we fix the hole rate. To do this, different parameters such as: the thicknesses of each layer of the Al-ZnO/i-ZnO/ In_2S_3 /p-CIGS/p-Si solar cell will be varied, to obtain the best electrical efficiency.

4.1. Effect of recombination speed for a cigs thickness of $0.1\mu\text{m}$

4.1.1. Effect of electron recombination speed

The values of the electron surface recombination velocity are varied, and the hole velocity is fixed. The results obtained are shown in Table 2.

Table 2. Functional parameters of the solar cell with different electron surface recombination velocities.

Electron recombination speed (cm/s)	Recombination speed of holes (cm/s)	V_{oc} (V)	J_{sc} (mA/cm ²)	FF (%)	η (%)
8.00E 0	1.00E 7	0.801	38.96	83.38	26.03
9.00E 0	1.00E 7	0.800	38.95	83.45	26.02
1.00E 1	1.00E 7	0.7996	38.94	83.51	26.12
1.00E 2	1.00E 7	0.781	38.44	84.20	25.29
1.20E 2	1.00E 7	0.779	38.36	84.17	25.18
1.70E 2	1.00E 7	0.777	38.19	84.13	24.98
1.90E 2	1.00E 7	0.776	38.14	84.11	24.91
1.00E 3	1.00E 7	0.768	37.37	83.58	24.01
1.00E 4	1.00E 7	0.766	37.00	83.28	23.60
1.00E 5	1.00E 7	0.765	36.95	83.24	23.55
1.00E 6	1.00E 7	0.765	36.95	83.23	23.55
1.00E 7	1.00E 7	0.765	36.95	83.23	23.55
1.00E 8	1.00E 7	0.765	36.95	83.23	23.55

According to the results listed in the Table (2), we can summarize them in the following points :

- For an electronic recombination speed equal to 1.2×10^2 cm/s, the efficiency is equal (25.18%). This results is in agreement with those reported in the literature [28]
- For electron recombination velocity equal to 10 cm/s, we obtain an electrical efficiency (26.12%) better than that found in the Ref [28].
- For electron recombination values below or above 10 cm/s, we find a decrease in electrical efficiency.

Based on these remarks, we have chosen the electron recombination speed 10 cm/s for an optimum electrical efficiency value ($\eta=26.12\%$).

4.1.2. Effect of hole recombination speed

Fixing the electron recombination speed at 10 cm/s and varying the surface recombination speed of the holes, the results found are shown in Table 3.

Table 3. Functional parameters of the solar cell with different surface recombination rates

Electron recombination speed (cm/s)	Recombination speed of holes (cm/s)	V_{oc} (V)	J_{sc} (mA/cm ²)	FF (%)	η (%)
1.00E 1	1.00E 0	0.8004	39.52	77.95	24.55
1.00E 1	8.00E 0	0.806	39.26	80.98	25.63
1.00E 1	9.00E 0	0.806	39.24	81.11	25.67
1.00E 1	1.00E 1	0.8066	39.23	81.23	25.70
1.00E 1	1.00E 2	0.8089	39.05	82.49	26.06
1.00E 1	1.20E 2	0.8089	39.04	82.52	26.07
1.00E 1	1.70E 2	0.8090	39.039	82.58	26.08
1.00E 1	1.90E 2	0.8091	39.037	82.59	26.08
1.00E 1	1.00E 3	0.8092	39.022	82.68	26.11
1.00E 1	1.00E 4	0.8093	39.01	82.70	26.11
1.00E 1	1.00E 5	0.8093	39.019	82.70	26.12
1.00E 1	1.00E 6	0.8093	39.019	82.70	26.12
1.00E 1	1.00E 7	0.8093	39.019	82.70	26.12
1.00E 1	1.00E 8	0.8093	39.019	82.70	26.12
1.00E 1	1.00E 9	0.8093	39.019	82.70	26.12

It can be seen that increasing the surface recombination speed of the holes increases the electrical efficiency to a certain value, after which it remains constant. For a hole recombination speed equal to 10 cm/s, we obtain a higher efficiency (26.12%). We can see that the backside recombination velocities for electrons and holes influence solar cell efficiency. Based on the results obtained, our choice is based on an electron speed of 10 cm/s and a hole speed of $1 \cdot 10^7$ cm/s.

4.2. Effect of recombination rate for a cigs thickness of 0.3 μ m

The thicknesses of each layer of the Al-ZnO/i-ZnO/In₂S₃/p-CIGS/p-Si solar cell chose respectively 100nm, 70nm, 50 nm, 0.3 μ m and 1 μ m, to achieve the best electrical efficiency [28]. We vary the values of the electron surface recombination rate, and fix the hole rate, and then do the reverse, fix the value of the electron surface recombination rate that gives the best electrical efficiency, and vary the hole surface recombination rate. The results obtained are shown in Tables 4 and 5.

Table 4. Functional parameters of the solar cell with different surface electron recombination speed for CIGS layer thickness = 0.3 μ m

Electron recombination speed (cm/s)	Recombination speed of holes (cm/s)	V_{oc} (V)	J_{sc} (mA/cm ²)	FF (%)	η (%)
1.00E 0	1.00E 7	0.7749	37.617	83.54	24.34
8.00E 0	1.00E 7	0.7746	37.616	83.54	24.34
9.00E 0	1.00E 7	0.7746	37.626	83.53	24.35
1.00E 1	1.00E 7	0.7746	37.615	83.55	24.34
1.00E 2	1.00E 7	0.7722	37.520	83.63	24.23
1.20E 2	1.00E 7	0.7719	37.502	83.63	24.21
1.70E 2	1.00E 7	0.7712	37.460	83.64	24.16
1.90E 2	1.00E 7	0.7710	37.445	83.64	23.14
1.00E 3	1.00E 7	0.7678	37.134	83.48	23.80
1.00E 4	1.00E 7	0.7659	36.849	83.28	23.50
1.00E 5	1.00E 7	0.7656	36.801	83.24	23.45
1.00E 6	1.00E 7	0.7655	36.7960	83.23	23.45
1.00E 7	1.00E 7	0.7655	36.7955	83.23	23.45
1.00E 8	1.00E 7	0.7655	36.7954	83.23	23.45

Table 5. Functional parameters of the solar cell with different surface recombination rates of the holes for a CIGS layer thickness = 0.3 μ m

Electron recombination speed (cm/s)	Recombination speed of holes (cm/s)	V_{oc} (V)	J_{sc} (mA/cm ²)	FF (%)	η (%)
1.00E 0	1.00E 0	0.7738	37.680047	76.66	22.35
1.00E 0	8.00E 0	0.7753	37.661992	81.09	23.68
1.00E 0	9.00E 0	0.7753	37.66006	81.27	23.73
1.00E 0	1.00E 1	0.7753	37.65832	81.43	23.77
1.00E 0	1.00E 2	0.7753	37.63201	83.23	24.27
1.00E 0	1.20E 2	0.7753	37.631144	83.28	24.27
1.00E 0	1.70E 2	0.7753	37.629822	83.35	24.29
1.00E 0	1.90E 2	0.7753	37.629479	83.37	24.31
1.00E 0	1.00E 3	0.7753	37.627015	83.50	24.31
1.00E 0	1.00E 4	0.7753	37.626470	83.52	24.35
1.00E 0	1.00E 5	0.7753	37.626416	83.53	24.35

Electron recombination speed (cm/s)	Recombination speed of holes (cm/s)	V_{oc} (V)	J_{sc} (mA/cm ²)	FF (%)	η (%)
1.00E 0	1.00E 6	0.7753	37.626410	83.53	24.35
1.00E 0	1.00E 7	0.7753	37.626410	83.53	24.35
1.00E 0	1.00E 8	0.7753	37.626409	83.53	24.35
1.00E 0	1.00E 9	0.7753	37.626409	83.53	24.35

From this study, we can say that to obtain the best electrical efficiency from the cell, it is only necessary to vary the electron recombination rate. For a CIGS thickness of 0.1 μm , the cell gives a high efficiency compared with a thickness of 0.3 μm . A major drawback of practical devices is the reduction in CIGS layer thickness due to interlayer mixing and aging. Thickness reduction allows electronic recombination with the back contact.

4.3. Effect of varying the gap energy of solar cell layers

4.3.1. Effect of Varying the Gap Energy of The Cigs Layer

The variation in the gap energy values induces a modification of the photovoltaic parameters of the cell. The effects of the gap energy variation on the different photovoltaic parameters of the cell are illustrated in Fig. (2).

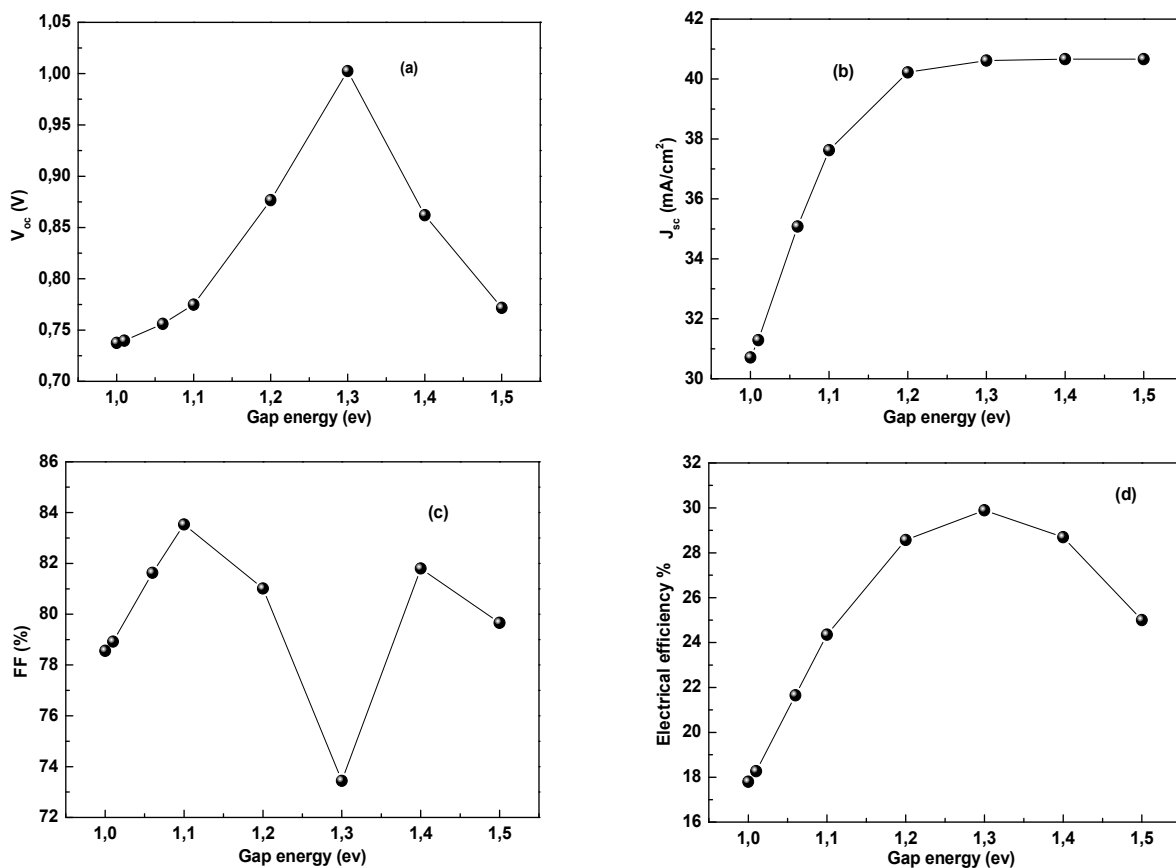


Figure 2. Effect of varying the gap energy of the CIGS absorber layer of the CIGS cell on: a) The open-circuit voltage V_{oc} , b) The short-circuit voltage density circuit J_{sc} , c) Form factor FF%, d) Efficiency η %

The observation to draw from this figure is that when the gap energy of the CIGS has a value of 1.3 eV, the best efficiency is obtained. However, when we increase the spacing energy of the CIGS absorbing layer from 1 eV to 1.5 eV, we notice that:

- The short circuit current density (J_{sc}) increases from 37.626 mA/cm² to 40.662mA/cm².
- Open circuit voltage (V_{oc}) increases from 0.775 V to 1.002 V then decreases to 0.771 V.
- Form factor (FF%) increases and decreases randomly from 73.44% to 83.53%.
- The yield (η) increases from 24.35% to 29.89%, then decreases to 25.00%.

4.3.2. Effect of Varying the Gap Energy of The Si Layer

The various values of the gap energy of the SI absorber layer, ranging from 1 eV to 1.12 eV, influence the photovoltaic parameters of the cell, as shown in Fig (3).

From the results, we can see that when the gap energy has a value of 1eV, the best performance is achieved. When we increase the gap energy values of the p-Si absorber layer from 1 eV to 1.12 eV, we notice that:

- The short-circuit current density (J_{sc}) decreases from 45.424 mA/cm^2 to 40.615 mA/cm^2 .
- Open-circuit voltage (V_{oc}) increases from 0.7963 V to 1.002 V
- Form factor (FF%) decreases from 86.40% to 73.44% .
- Electrical efficiency (η) decreases from 31.25% to 29.48% , then increases to 29.89% .

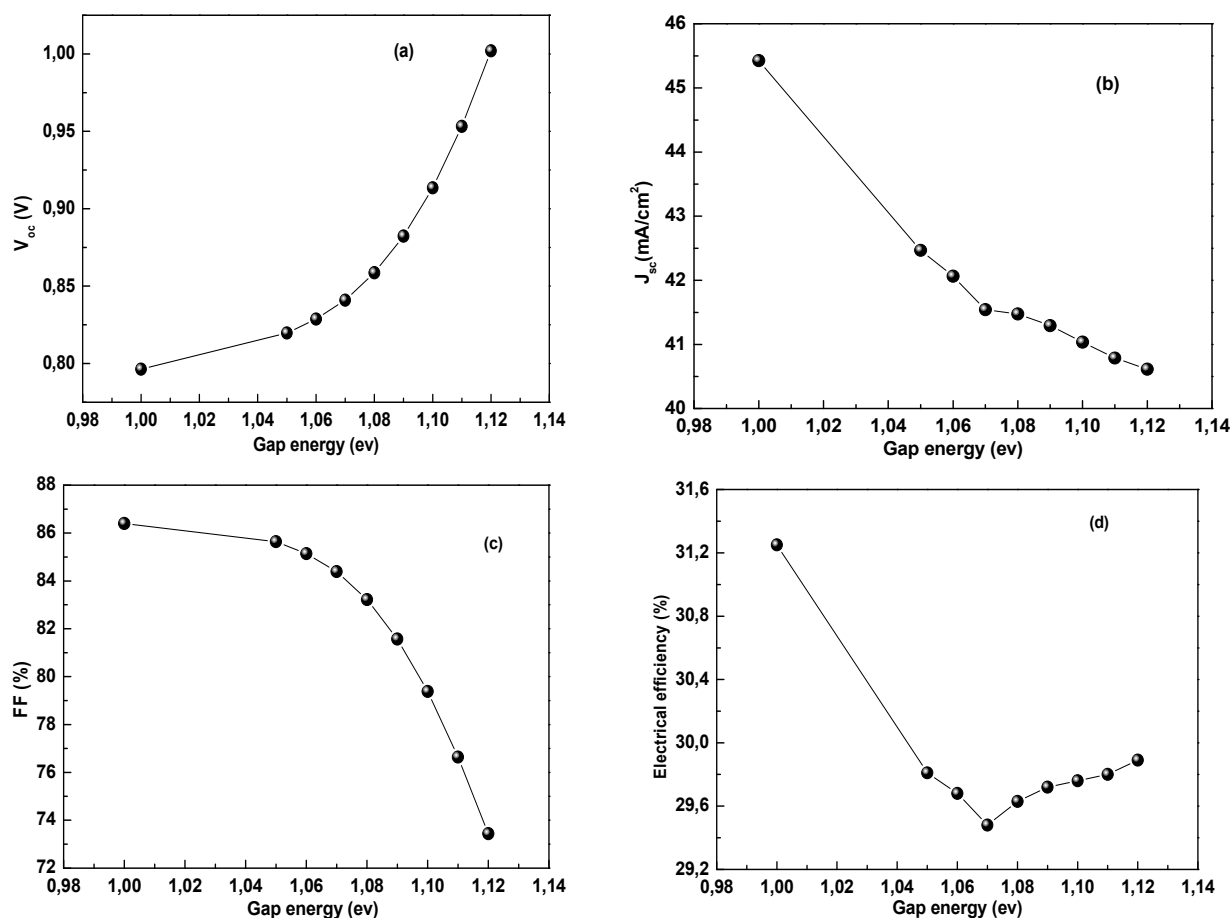


Figure 3. Effect of the gap energy of the Si absorber layer of the CIGS cell on: a) Open-circuit voltage V_{oc} , b) Short-circuit voltage density J_{sc} , c) Form factor FF%, d) Efficiency $\eta\%$

4.3.3. Effect of Varying the Gap Energy of The In_2S_3 Buffer Layer

The optical gap energy of In_2S_3 is 2.56 eV . We chose to vary the gap energy between 2 eV and 2.8 eV . These different values, which influence the photovoltaic parameters of the cell, are given in Fig (4).

From the results shown in the Fig. 4, we note that the variation in In_2S_3 gap energy values has no influence on the cell's photovoltaic parameters.

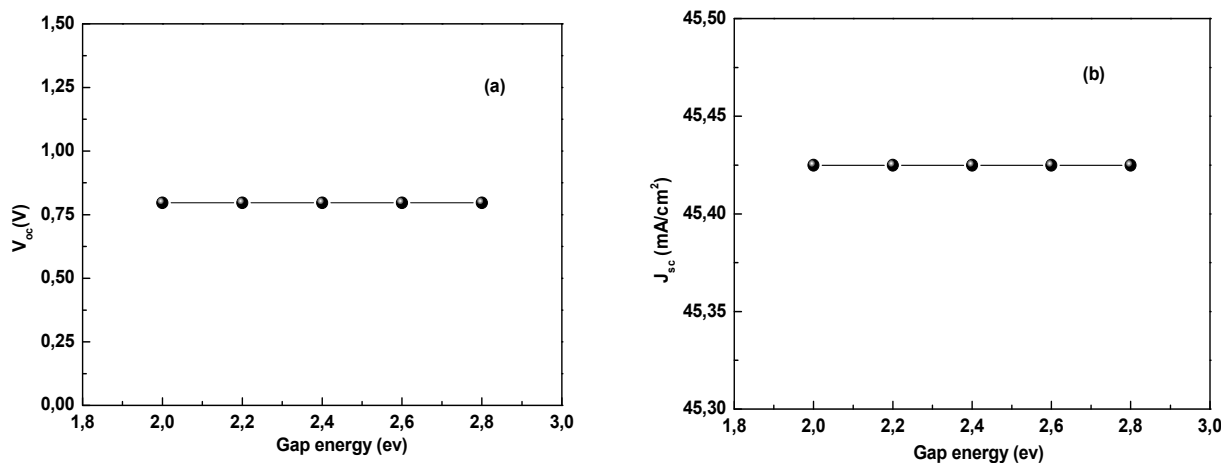


Figure 4. Effect of varying the gap energy of the In_2S_3 buffer layer a) the open-circuit voltage V_{oc} , b) short-circuit voltage density J_{sc} , c) form factor FF%, d) efficiency $\eta\%$.

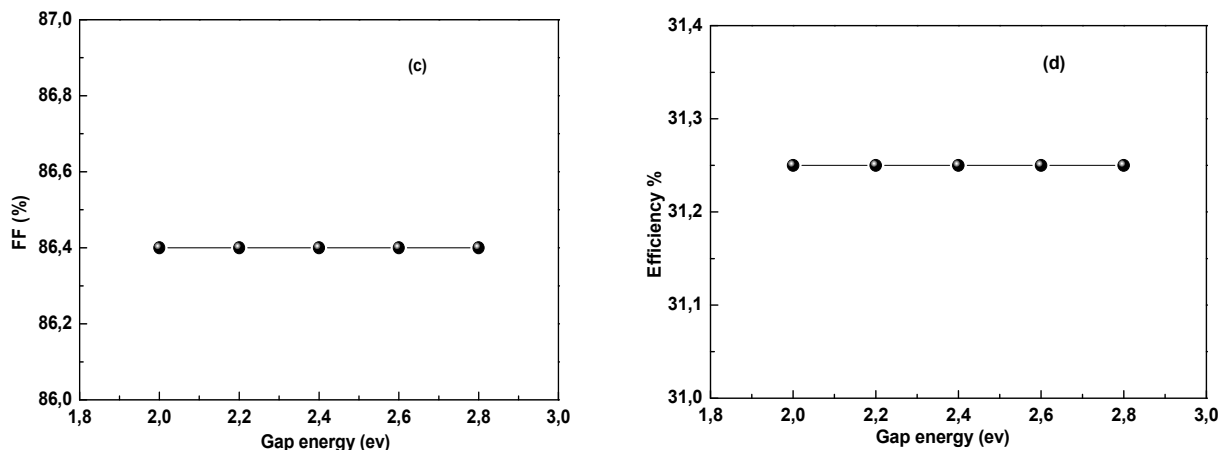


Figure 4 (continuation). Effect of varying the gap energy of the the In₂S₃ buffer layer
a) the open-circuit voltage V_{oc} , b) short-circuit voltage density J_{sc} , c) form factor FF%, d) efficiency η %

4.3.4. Effect of Varying the Gap Energy of the ZNO Layer

Fig. 5 shows the different values of ZnO gap energy, ranging from 3.2 eV to 3.45 eV, which influence the photovoltaic parameters of the cell.

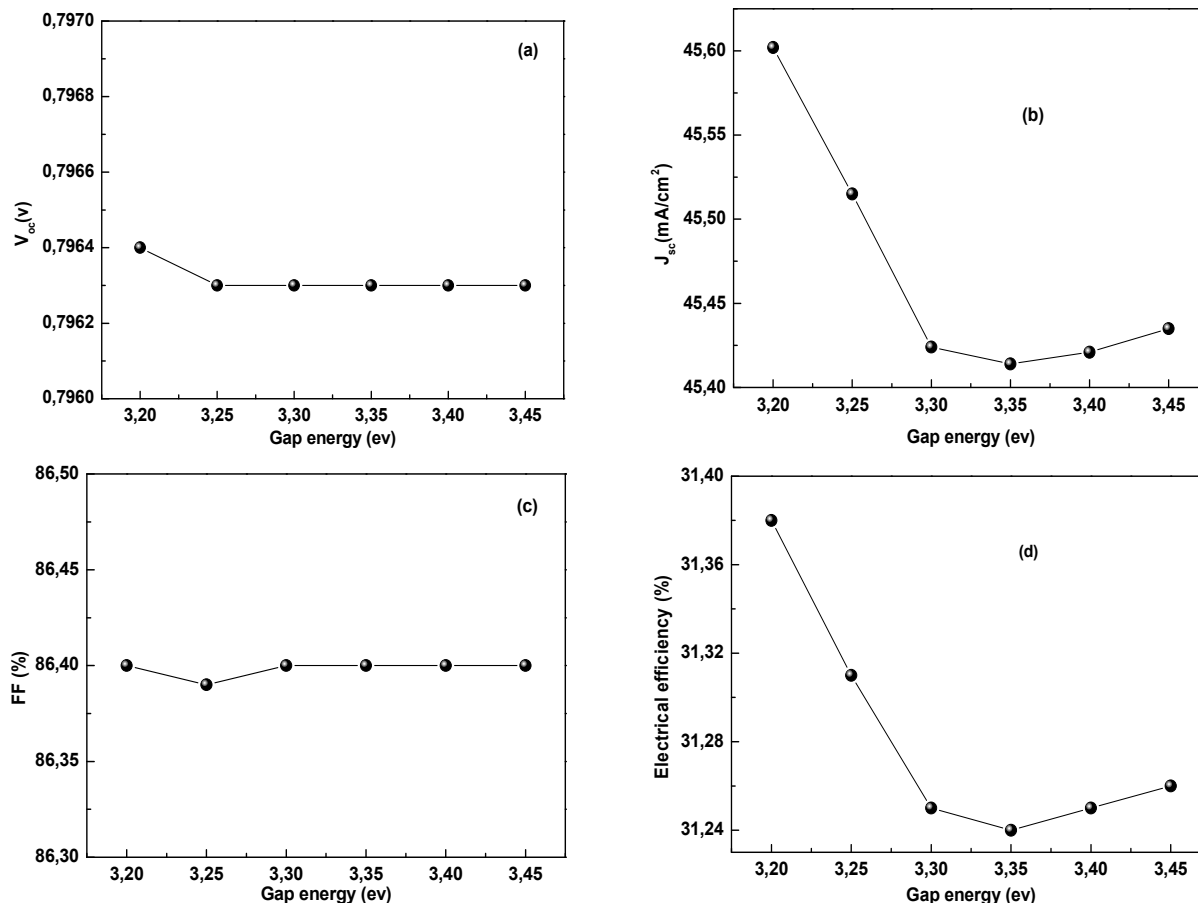


Figure 5. Effect of varying the gap energy of the ZnO layer
a) the open-circuit voltage V_{oc} , b) short-circuit voltage density J_{sc} , c) form factor FF%, d) efficiency η %

We note that varying ZnO gap energy values do not influence open-circuit voltage V_{oc} and form factor FF, but do influence short-circuit voltage density J_{sc} . The best electrical efficiency is obtained when the ZnO gap energy reaches 3.2 eV.

4.3.5. Effect of Varying the Gap Energy of the Al-ZnO Layer

The different values of the Al-ZnO gap energy, ranging from 3.2 eV to 3.45 eV, which influence the photovoltaic parameters of the cell, are given in Fig. 6.

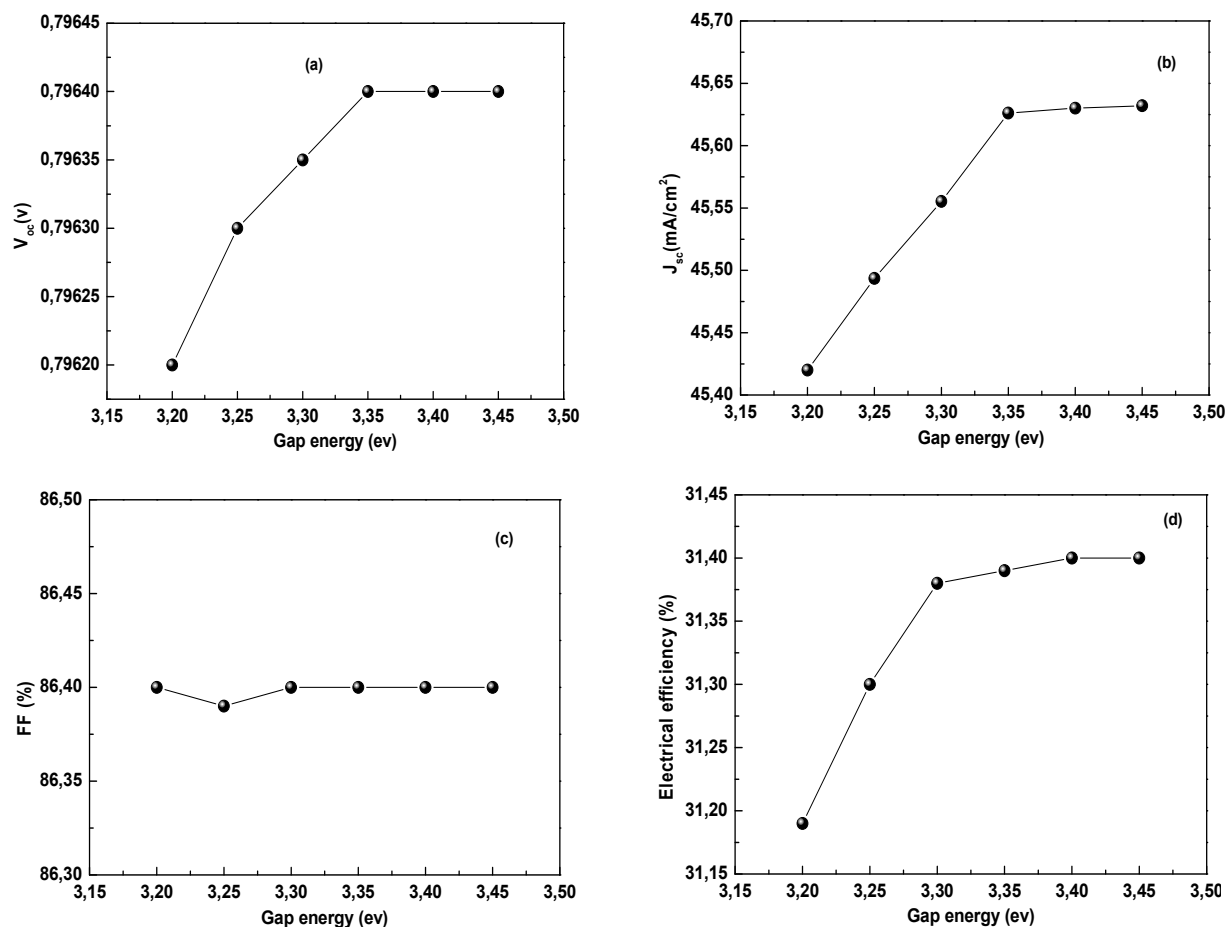


Figure 6. Effect of varying the gap energy of the AL-ZnO layer
a) the open-circuit voltage V_{oc} , b) short-circuit voltage density J_{sc} , c) form factor FF%, d) efficiency $\eta\%$

We note that varying Al-ZnO gap energy values have no influence on open-circuit voltage V_{oc} and form factor FF, but there is a small influence on short-circuit voltage density J_{sc} . The best electrical performance is obtained when the gap energy of Al-ZnO reaches 3.4 eV. The results found for Al-ZnO are similar to those found for ZnO. So, we can say that the gap energy of the absorber layers influences the cell's efficiency, while the other layers (In_2S_3 , ZnO, Al-ZnO) do not have a great influence. This result is in good agreement with those reported in the literatures [35].

4.4. The Effect of Thickness Variation:

4.4.1. Cigs Thickness

The effect of varying the thickness of the CIGS absorber layer (from 0.1 μm to 1 μm) on cell performance was simulated. The simulated, V_{oc} , J_{sc} , FF and η (efficiency) curves are shown in Fig. (7).

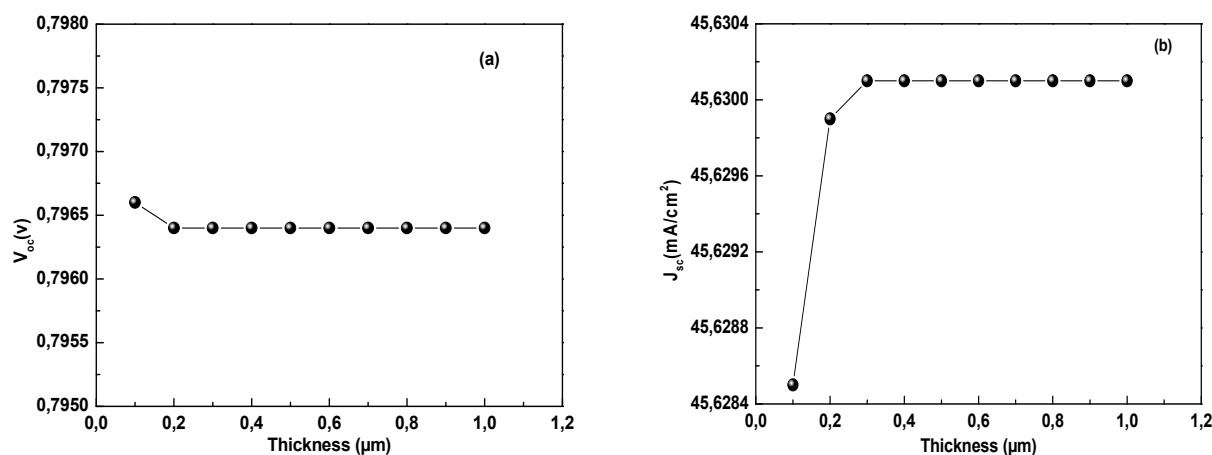


Figure 7. Effect of CIGS thickness on a) the open-circuit voltage V_{oc} ,
b) short-circuit voltage density J_{sc} , c) form factor FF%, d) efficiency $\eta\%$

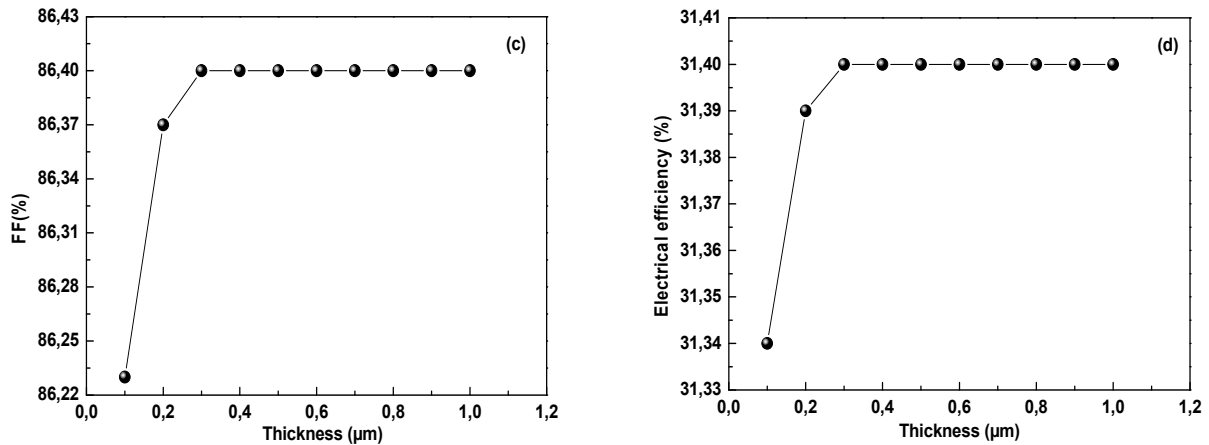


Figure 7(continuation). Effect of CIGS thickness on a) the open-circuit voltage V_{oc} , b) short-circuit voltage density J_{sc} , c) form factor FF%, d) efficiency η %

According to the results obtained, the CIGS layer thickness that gives the highest efficiency is 0.3 μm. The variation in CIGS layer thickness, between 0.1 μm and 1 μm, has little effect on short-circuit current density (J_{sc}), open-circuit voltage (V_{oc}), form factor (FF%) and efficiency (η). Indeed, when the thickness of the CIGS layer is 0.3 μm, so the total thickness of the absorbing layer (CIGS+ p-Si) will be 1.3 μm, leads to an increase in cell performance and in particular efficiency.

4.4.2. Absorbent Layer Thickness P-Si

Many researchers have worked to consolidate the photovoltaic potential offered by the thin-film p-Si sector [36-38]. As a result, they recorded an improvement in electronic properties. In this simulation step, the thickness of the CIGS layer is set at 0.3 μm. The different p-Si thicknesses, ranging from 0.3 μm to 1.3 μm, influence the photovoltaic parameters of the cell and are given in Fig. (8).

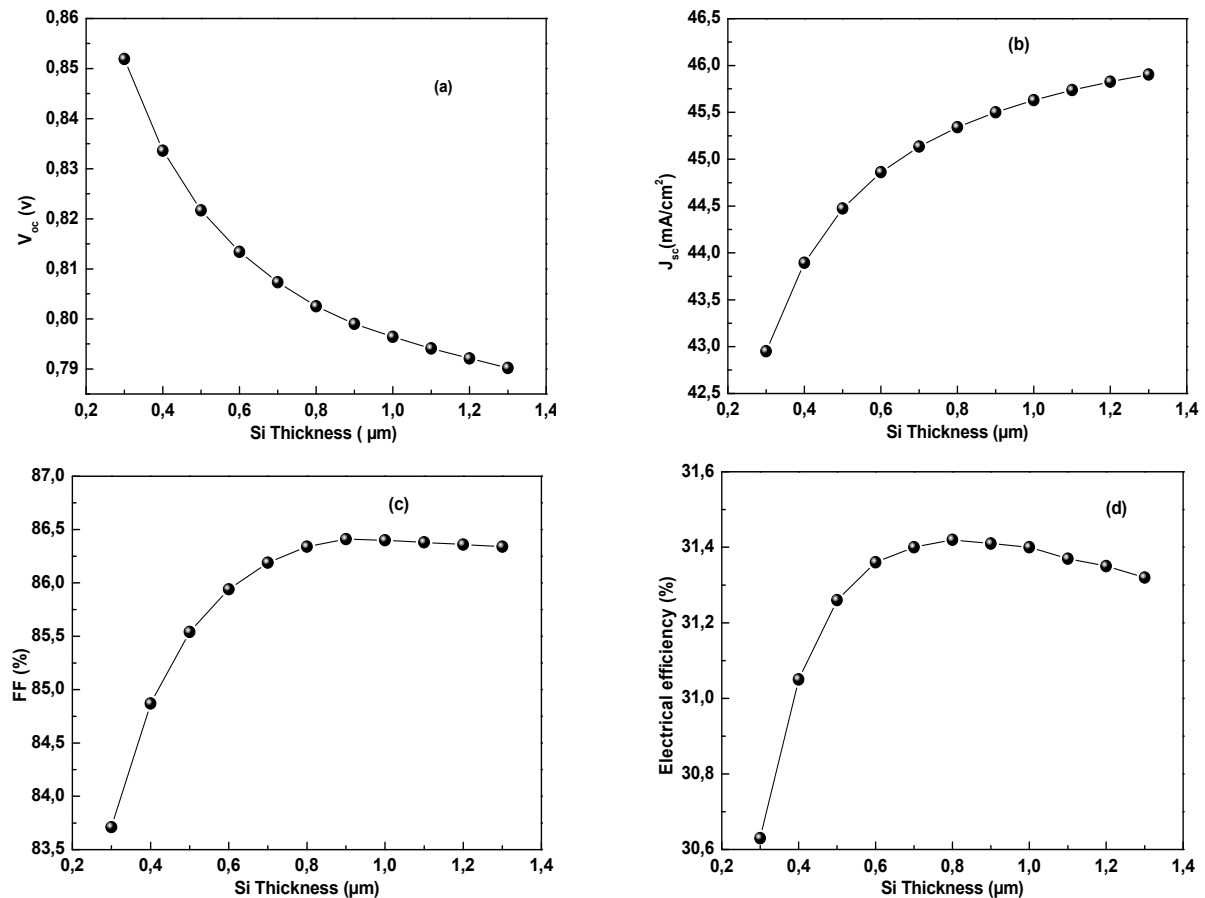


Figure 8. Effect of Si thickness on: a) The open-circuit voltage V_{oc} , b) The short-circuit current density J_{sc} , c) The form factor FF%, d) Efficiency η %

According to the results obtained, the 0.8 μm -thick p-Si absorber layer gives a better performance. It can be seen that there is a threshold thickness (0.8 μm) for both form factor (FF) and efficiency (η) to be high, and above or below this thickness value there is a decrease in these parameters. And we also notice that increasing thickness leads to an increase in short-circuit current density (J_{sc}) and a decrease in open-circuit voltage (V_{oc}). In fact, to achieve good efficiency (31.42%), the thickness of the absorber layer (CIGS+ p-Si) must be equal to 1.1 μm , because at this thickness there is a maximum generation of electron-hole pairs and a decrease in contact return recombination.

4.4.3. In_2S_3 Buffer Layer Thickness

Most CIGS-based ultra-thin solar cells incorporate a buffer layer to improve efficiency and other solar cell parameters. The central role of the buffer layer is to prevent unwanted bypass paths and protect the injection region during manufacturing. We set the thickness of the combined absorber layer (CIGS + p-Si) at 1.1 μm and then varied the thickness of the In_2S_3 buffer layer (from 20 nm to 100 nm). The results obtained are shown in Fig (9). From the results obtained, it can be seen that the effect of varying the thickness of the buffer layer does not greatly influence cell performance. It can be seen that increasing the thickness will decrease the efficiency and the short-circuit current density J_{sc} .

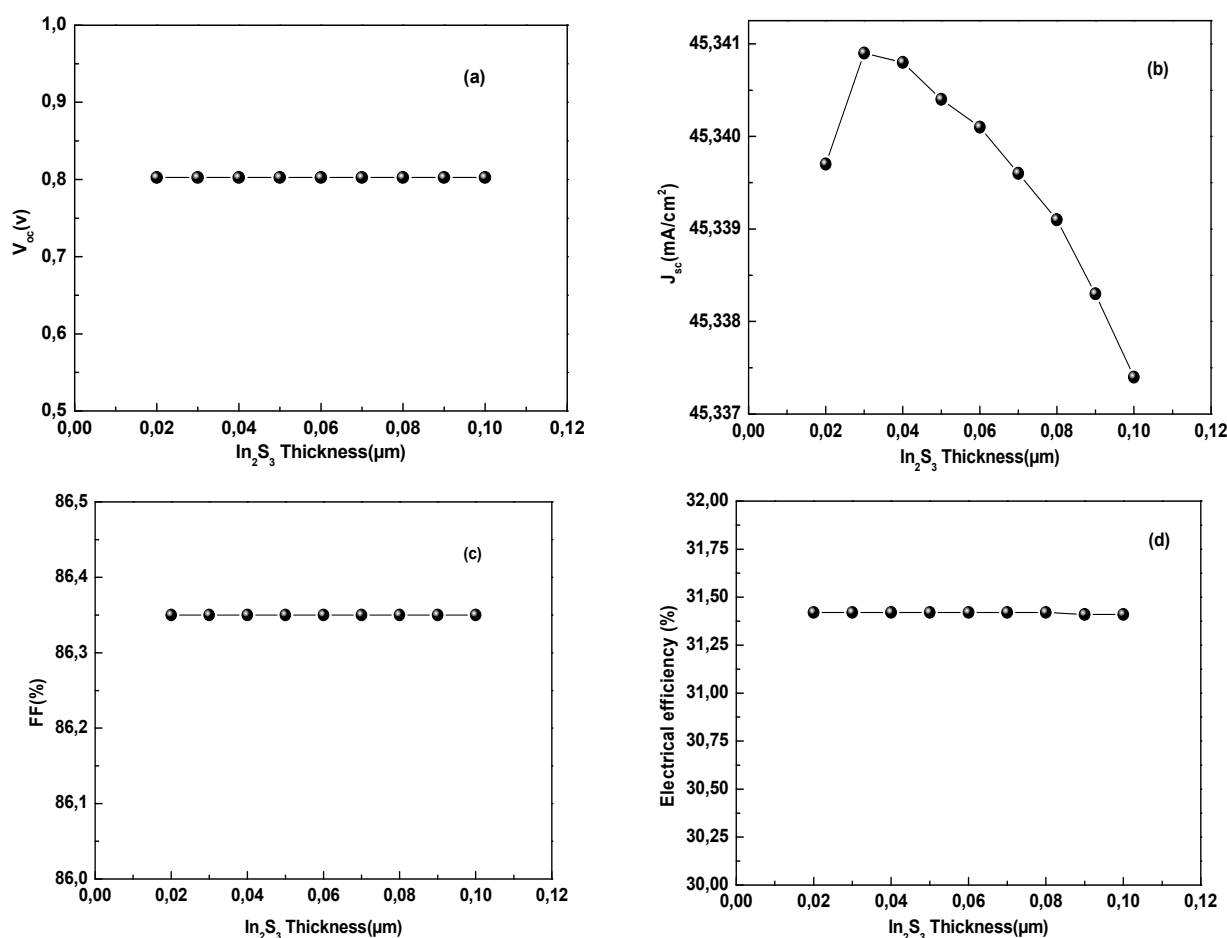


Figure 9. Effect of varying In_2S_3 thickness on: a) Open-circuit voltage V_{oc} , b) Short-circuit current density J_{sc} , c) Form factor FF%, d) Efficiency η %

4.4.1. Front Contact Thickness

There are two layers in the front contact: the intrinsic ZnO layer and the Al-ZnO layer that makes up the window layer.

- The ZnO layer is resistive and serves to limit short-circuiting in areas where the CIGS is imperfectly covered by the buffer layer.
- The Al-ZnO layer enables the window layer to form the front contact part of the photovoltaic cell; it must be transparent to solar radiation, so that this radiation can be absorbed by the CIGS layer [28].

A) I-ZnO Insulating Layer Thickness

To study the effect of varying the thickness of the i-ZnO layer (ranging from 0.01 μm to 0.1 μm), we set the value of the thickness of three combined layers (CIGS+p-Si+ In_2S_3) to 1.35 μm , and then run the simulation to study the

efficiency of the cell's photovoltaic parameters. The results obtained are shown Fig (10). From the results obtained, it can be seen that changing the thickness of the i-ZnO layer does not affect the parameters of the photovoltaic cell.

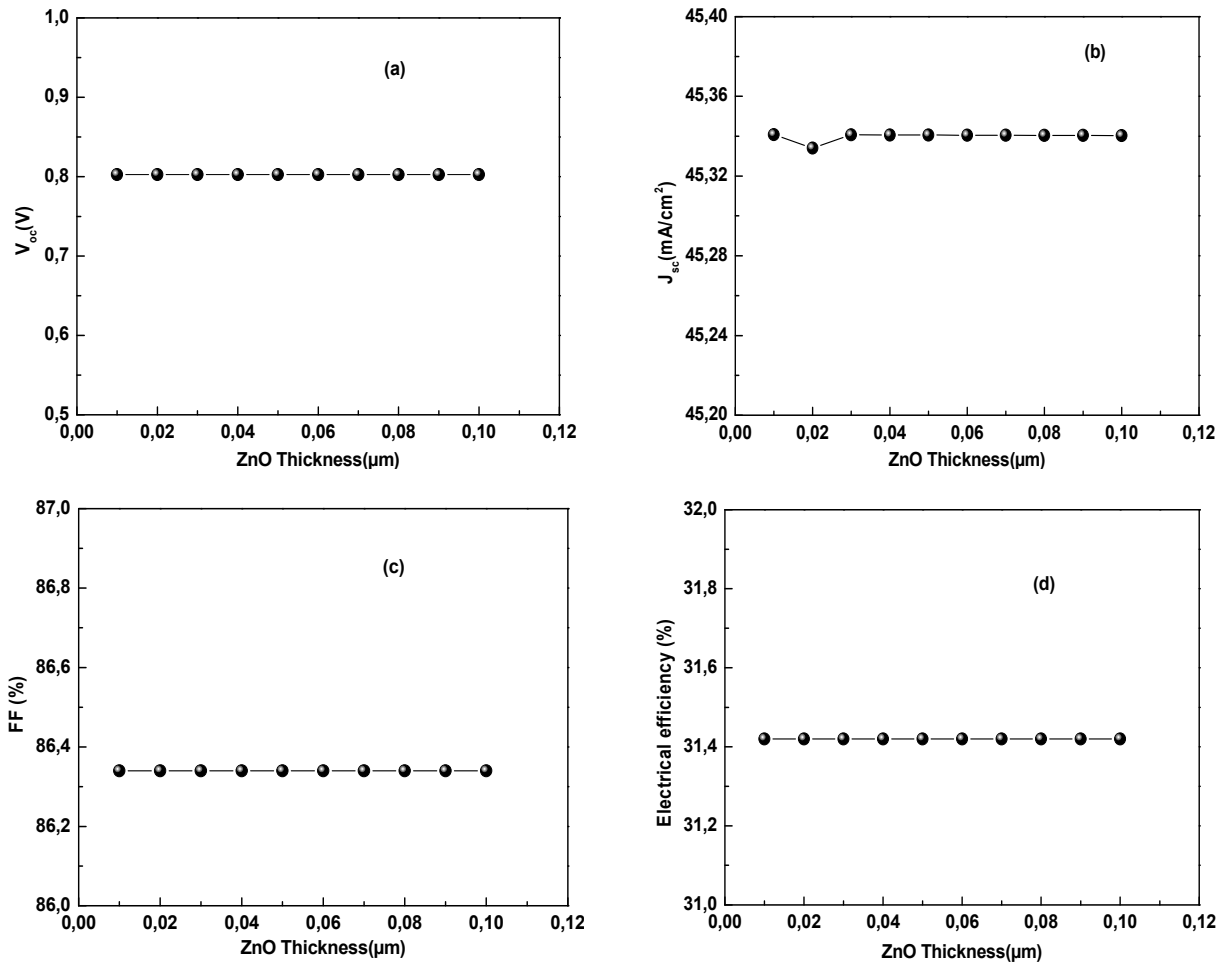


Figure 10. Effect of ZnO thickness on a) The open-circuit voltage V_{oc} , b) The short-circuit current density J_{sc} , c) The form factor FF%, d) The efficiency η %

b) Al-ZnO Window Layer Thickness

To study the effect of varying the thickness of the Al-ZnO layer (ranging from 0.04 μm to 0.1 μm), we set the value of the thickness of four combined layers (CIGS+p-Si+ In_2S_3 +i-ZnO) to 1.42 μm, and then run the simulation to investigate the efficiency of the cell's photovoltaic parameters. The results obtained are shown in Fig. (11).

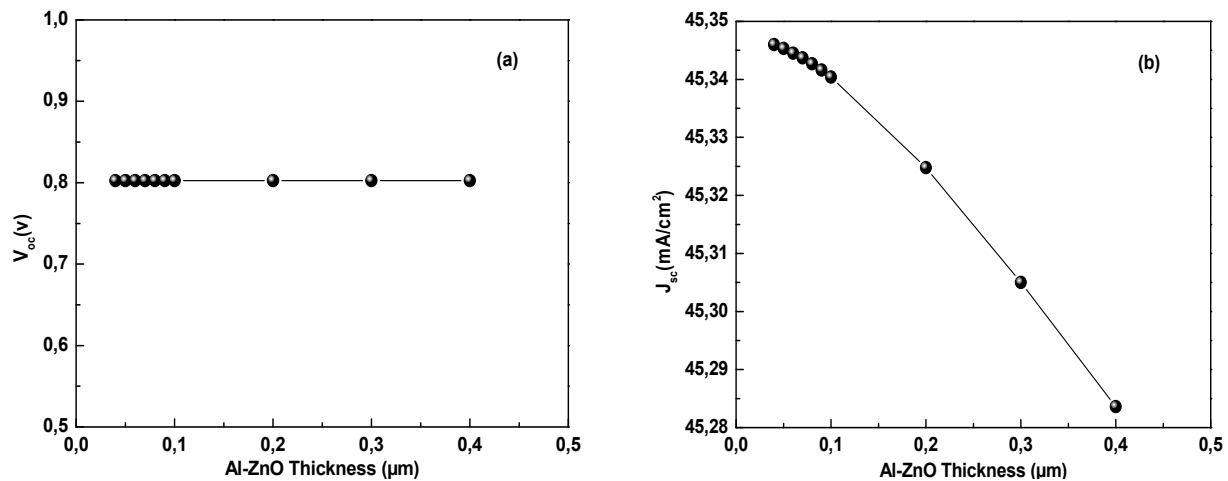


Figure 11. Effect of Al-ZnO thickness on a) Open-circuit voltage V_{oc} , b) Short-circuit current density J_{sc} , c) Form factor FF%, d) Efficiency η %

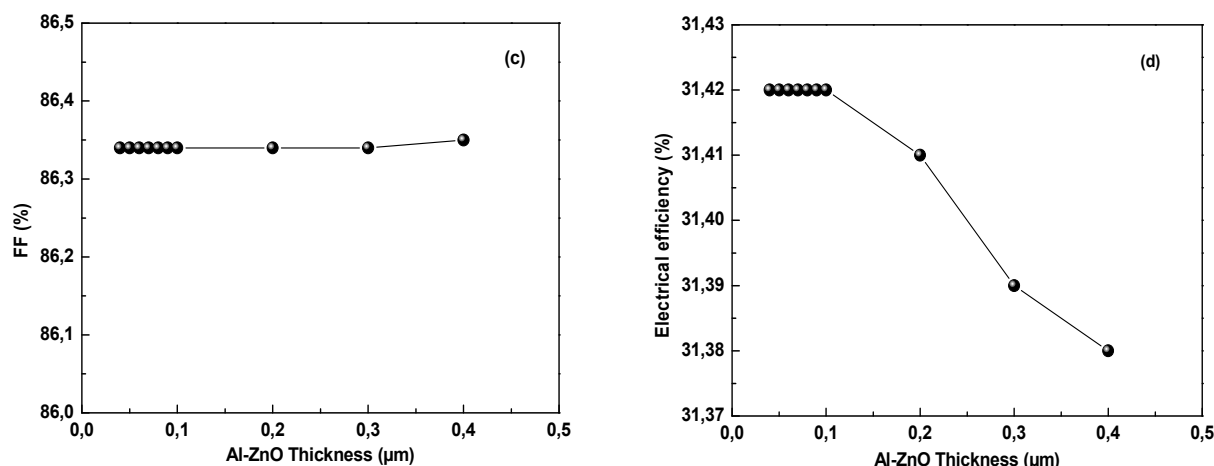


Figure 11(continuation). Effect of Al-ZnO thickness on

a) Open-circuit voltage V_{oc} , b) Short-circuit current density J_{sc} , c) Form factor FF%, d) Efficiency η %

From the results obtained, it can be seen that increasing the thickness of the Al-ZnO layer decreases the efficiency η . The range chosen for the Al-ZnO thickness has no influence on the short-circuit current density J_{sc} , the open-circuit voltage V_{oc} and the form factor FF. To improve cell efficiency, the Al-ZnO layer must be reduced. We therefore set the value of the Al-ZnO layer at $0.1\ \mu\text{m}$.

Final results: Table (7) shows the final results for the material parameter values used in our simulation.

Table 7. Final results for the material parameters used in our simulation.

Parameters	CIGS	P- Si	In_2S_3	I-Zno	Al-Zno
Thicknesses (nm)	0.3	0.8	0.05	0.07	0.1
Gap strip (eV)	1.300	1.0	2.800	3.200	3.400
Electronic affinity (eV)	4.500	4.500	4.700	4.600	4.600
Relative Permittivity	13.600	11.900	13.500	9.000	9.000
CB ($1/\text{cm}^3$)	2.200E +18	2.800E +19	1.800E +18	2.200E +18	2.200E +18
VB ($1/\text{cm}^3$)	1.800E +19	2.650E +19	4.000E +13	1.800E +19	1.800E +19
Electron mobility (cm^2/Vs)	1.000E +2	1.450E +3	4.000E +2	1.000E +2	1.000E +2
Hole mobility (cm^2/Vs)	2.500E +1	5.000E +2	2.100E +2	2.500E +1	2.500E +1
ND ($1/\text{cm}^3$)	0.000E +0	0.000E +0	1.000E +18	1.000E +16	1.000E +18
NA ($1/\text{cm}^3$)	2.000E +16	1.000E +20	1.000E +1	0.000E +0	0.000E +0
Defect density ($1/\text{cm}^3$)	1.000E +14	1.000E +14	1.000E +14	0.000E +0	0.000E +0

Based on these results, the photovoltaic parameter efficiencies found for the cell studied are shown in Table (8).

Table 8. Functional parameters of the CIGS solar cell.

V_{oc} (V)	J_{sc} (mA/cm^2)	FF (%)	η (%)
0.1	0.8025	45.3404	31.42

5. CONCLUSION

Numerical simulation leads to a detailed understanding of how the structure of thin-film solar cells works. CIGS, a non-toxic material abundant on earth, is used in this study to analyze solar cell performance, bearing in mind that this material is expensive. To minimize the thickness of CIGS, the following solar cell structure was chosen: Al-ZnO/i-ZnO/ In_2S_3 /p-CIGS/p-Si. Where CIGS and Si are used as absorber layers and In_2S_3 as buffer layer. The performance of CIGS-based solar cells was studied by varying the gap energy and thickness of each cell layer. Gap energy modifies solar cell performance. The gap energy of the absorber layers influences the cell's efficiency, while the other layers (In_2S_3 , ZnO, Al-ZnO) do not have a great influence. Recombination rates influence the efficiency of the photovoltaic cell, reaching 26.12%. Increasing the thickness of the absorber layer has a major influence on efficiency, increasing it up to a certain limit. The best yield found after studying the variation in thickness of the total CIGS+p-Si absorber layer is 31.25%. The thicknesses of the CIGS, p-Si, In_2S_3 , i-ZnO and Al-ZnO layers need to be in the order of $0.3\ \mu\text{m}$, $0.8\ \mu\text{m}$, $0.05\ \mu\text{m}$, $0.07\ \mu\text{m}$ and $0.1\ \mu\text{m}$ respectively to achieve the best yield (31.42%). Finally, given the great complexity of increasing the conversion efficiency of solar cells and reducing their cost, many problems remain open for future investigation in order to fully understand the capabilities and limitations of the conversion efficiency of solar cells. We hope that the results presented in this work contribute to this understanding.

ORCID

✉ D. Belfennache, <https://orcid.org/0000-0002-4908-6058>; ✉ Mohamed A. Ali, <https://orcid.org/0000-0002-7390-8592>

REFERENCES

- [1] P. Bórawski, L. Holden, and A. Beldycka-Bórawska, *Energy*, **270**, 126804 (2023). <https://doi.org/10.1016/j.energy.2023.126804>
- [2] H. Sadamura, N. Suzuki, C. Sotome, et al. *Electrochemistry*, **78**(7), 594 (2010). <https://doi.org/10.5796/electrochemistry.78.594>
- [3] A. Jäger-Waldau, *Energies*, **13**(4), 930 (2020). <https://doi.org/10.3390/en13040930>
- [4] A. Jäger-Waldau, *PV Status Report*, (Publications Office of the European Union, Luxembourg, 2019). <https://doi.org/10.2760/326629, JRC118058>
- [5] M.A. Green, K. Emery, Y. Hishikawa, W. Warta, and E.D. Dunlop, *Progress in Photovoltaics: Research and Applications*, **23**, 1 (2015). <https://doi.org/10.1002/pip.2573>
- [6] D. Belfennache, D. Madi, R. Yekhlef, L. Toukal, N. Maouche, M.S. Akhtar, and S. Zahra, *Semicond. Phys. Quantum. Electron. Optoelectron.* **24**(4), 378 (2021). <https://doi.org/10.15407/spqeo24.04.378>
- [7] D. Belfennache, N. Brihi, and D. Madi, in: *Proceeding of the IEEE xplore, 8th (ICMIC) (2016)*, **7804164**, (2017), pp. 497–502. <https://doi.org/10.1109/ICMIC.2016.7804164>
- [8] R. Ouldamer, D. Madi, and D. Belfennache, in: *Advanced Computational Techniques for Renewable Energy Systems. IC-AIRES 2022. Lecture Notes in Networks and Systems*, vol. **591**, edited by M. Hatti, (Springer, Cham.2023). pp. 700-705, https://doi.org/10.1007/978-3-031-21216-1_71
- [9] M. Zotti S. Mazzoleni, L.V. Mercaldo, M.D. Noce, M. Ferrara, P.D. Veneri, M. Diano, et al., *Heliyon*, **10**(4), e26323 (2024). <https://doi.org/10.1016/j.heliyon.2024.e26323>
- [10] D. Belfennache, D. Madi, N. Brihi, M.S. Aida, and M.A. Saeed, *Appl. Phys. A*, **124**, 697 (2018). <https://doi.org/10.1007/s00339-018-2118-z>
- [11] S.M. Govindharajulu, A.K. Jain, and M. Piraviperumal, *J. Alloys Compd.* **980**, 173588 (2024). <https://doi.org/10.1016/j.jallcom.2024.173588>
- [12] J. Raval, B. Shah, D. Kumar, S.H. Chaki, and M.P. Deshpande, *Chem. Eng. Sci.* **287**, 119728 (2024). <https://doi.org/10.1016/j.ces.2024.119728>
- [13] I. Repins, M. Contreras, B. Egaas, C. DeHart, J. Scharf, C. Perkins, B. To, and R. Noufi. *Progress in Photovoltaics: Research and Applications*, **16**(3), 235 (2008). <https://doi.org/10.1002/pip.822>
- [14] J. Lindahl, U. Zimmermann, P. Szaniawski, T. Törndahl, A. Hultqvist, P. Salomé, C. Platzer-Björkman, et al., *IEEE J. Photovolt.* **3**(3), 1100 (2013). <https://doi.org/10.1109/JPHOTOV.2013.2256232>
- [15] M. Powalla, P. Jackson, W. Witte, D. Hariskos, S. Paetel, C. Tschamber, and W. Wischmann, *Sol. Energy Mater. Sol. Cells*, **119**, 51 (2013). <https://doi.org/10.1016/j.solmat.2013.05.002>
- [16] A. Chirila, S. Buecheler, F. Pianezzi, P. Bloesch, C. Gretener, A.R. Uhl, C. Fella, et al., *Nature Mater*, **10**, 857 (2011). <https://doi.org/10.1038/nmat3122>
- [17] E. Wallin, U. Malm, T. Jarmar, O. Lundberg, M. Edoff, L. Stolt, et al., *Progress in Photovoltaics: Research and Applications*, **20**, 851 (2012). <https://doi.org/10.1002/pip.2246>
- [18] A. Romeo, M. Terheggen, D. Abou-Ras, D.L. Bätzner, F.-J. Haug, M. Kälin, D. Rudmann, et al., *Progress in Photovoltaics: Research and Applications*, **12**, 93 (2004). <https://doi.org/10.1002/pip.527>
- [19] M. Kemell, M. Ritala, and M. Leskelä, *Crit. Rev. Solid State Mater. Sci.* **30**, 1 (2005). <https://doi.org/10.1080/10408430590918341>
- [20] C.H. Fischer, M. Bär, T. Glatzel, I. Lauermaun, and M.C. Lux-Steiner, *Sol. Energy Mater. Sol. Cells*, **90**(10), 1471 (2006). <https://doi.org/10.1016/j.solmat.2005.10.012>
- [21] K.S. Ramaiah, and V.S. Raja, *Sol. Energy Mater. Sol. Cells*, **32**, 1 (1994). [https://doi.org/10.1016/0927-0248\(94\)90250-X](https://doi.org/10.1016/0927-0248(94)90250-X)
- [22] M. Burgelman, P. Nollet, and S. Degraeve, *Thin Solid Films*, **361-362**, 527 (2000). [https://doi.org/10.1016/S0040-6090\(99\)00825-1](https://doi.org/10.1016/S0040-6090(99)00825-1)
- [23] K. Decock, S. Khelifi, and M. Burgelman, *Thin Solid Films*, **519**(21), 7481 (2011). <https://doi.org/10.1016/j.tsf.2010.12.039>
- [24] M. Burgelman, and J. Marlein, Analysis of graded band gap solar cells with SCAPS, In: *Proceedings of the 23rd European photovoltaic solar energy conference*, (2008). pp. 2151-2156.
- [25] J. Verschraegen, and M. Burgelman, *Thin Solid Films*, **515**(15), 6276 (2007). <https://doi.org/10.1016/j.tsf.2006.12.049>
- [26] S. Degraeve, M. Burgelman, and P. Nollet, in: *Proceedings of the 3rd world conference on photovoltaic energy conversion*, (2003), pp. 487-490. <http://hdl.handle.net/1854/LU-404099>
- [27] A. Niemegeers, and M. Burgelman, in: *Proceedings of the 25th IEEE photovoltaic specialists conference*, 901e4 (1996). <https://doi.org/10.1109/PVSC.1996.564274>
- [28] R.N. Mohottige, and S.P.K. Vithanage, *J. Photochem. Photobiol. A: Chem.* **407**, 113079 (2021). <https://doi.org/10.1016/j.jphotochem.2020.113079>
- [29] M. Mostefaoui, H. Mazan, S. Khelifi, A. Bouraiou, and R. Dabou, *Energy Procedia*, **74**, 736 (2015). <https://doi.org/10.1016/j.egypro.2015.07.809>
- [30] K. Orgassa, H.W. Schock, and J.H. Werner, *Thin Solid Films*, **431-432**, 387 (2003). [https://doi.org/10.1016/S0040-6090\(03\)00257-8](https://doi.org/10.1016/S0040-6090(03)00257-8)
- [31] M. Hashemi, Z. Saki, M. Dehghani, F. Tajabadi, S.M.B. Ghorashi, and N. Taghavinia, *Sci. Rep.* **12**, 14715 (2022). <https://doi.org/10.1038/s41598-022-18579-w>
- [32] R.J. Matson, O. Jamjoum, A.D. Buonaquisti, P.E. Russell, L.L. Kazmerski, P. Sheldon, and R.K. Ahrenkiel, *Solar cells*, **11**(3), 301 (1984). [https://doi.org/10.1016/0379-6787\(84\)90019-X](https://doi.org/10.1016/0379-6787(84)90019-X)
- [33] N. Kohara, S. Nishiwaki, Y. Hashimoto, T. Negami, T. Wada, *Sol. Energy Mater. Sol. Cells*, **67**(1-4), 209 (2001). [https://doi.org/10.1016/S0927-0248\(00\)00283-X](https://doi.org/10.1016/S0927-0248(00)00283-X)
- [34] M. Powalla, and B. Dimmler, *Thin Solid Films*, **361-362**, 540 (2000). [https://doi.org/10.1016/S0040-6090\(99\)00849-4](https://doi.org/10.1016/S0040-6090(99)00849-4)
- [35] C.K.G. Kwok, H. Tangara, N. Masuko, et al., *Sol. Energy Mater. Sol. Cells*, **269**, 112767 (2024). <https://doi.org/10.1016/j.solmat.2024.112767>

- [36] S. Mahdid, D. Belfennache, and D. Madi, *et al.*, J. Ovonic. Res. **19**(5), 535 (2023). <https://doi.org/10.15251/JOR.2023.195.535>
- [37] R. Ouldamer, D. Belfennache, D. Madi, *et al.*, J. Ovonic. Res. **20**(1), 45 (2024). <https://doi.org/10.15251/JOR.2024.201.45>

ЧИСЕЛЬНЕ МОДЕЛЮВАННЯ ПІДВИЩЕННЯ ЕЛЕКТРИЧНОЇ ЕФЕКТИВНОСТІ СОНЯЧНОГО ЕЛЕМЕНТУ НА ОСНОВІ CIGS НА SCAPS-1D

К. Мадуй^а, А. Гечі^б, С. Мадуй^с, Р. Єхлеф^д, Д. Бельфенаше^д, С. Зайю^{е,ф}, Мохамед А. Алі^г

^аЛабораторія прикладної оптики Інституту оптики і точної механіки університет Ферхат АББАС Сетіф-16 Алжир

^бЛабораторія оптоелектроніки та компонентів, інститут оптики і точної механіки, університет Ферхат Аббас Сетіф, Алжир

^сЛабораторія прикладної біохімії, Університет Ферхат Аббас Сетіф-1, 19000, Алжир

^дНауково-дослідний центр промислових технологій CRTI, P.O. Box 64, Черага, 16014, м. Алжир, Алжир

^еЛабораторія досліджень поверхонь і розділів твердих матеріалів (LESIMS), Університет Сетіф 1, 19000 Сетіф, Алжир

^фФакультет природничих наук і життя, Університет Сетіф-1, 19000 Сетіф, Алжир

^гШкола біотехнології, Університет Бадр в Каїрі (BUC), Бадр сіті, 11829, Каїр, Єгипет

Сонячні елементи в даний час знаходяться в центрі великої кількості досліджень. Мета – знизити їх собівартість. Щоб досягти цього, нам потрібно зменшити масу матеріалів і підвищити ефективність перетворення цих сонячних елементів. Це спонукало до дослідження використання тонких плівок, таких як a-Si, CdTe, CIGS. Це підвищення ефективності вимагає оптимізації параметрів фотоелектричної системи. У цьому моделюванні та імітаційній роботі ми використовуємо програмне забезпечення SCAPS-1D для вивчення впливу швидкості рекомбінації електронів і дірок у шарі CIGS, впливу товщини шарів і впливу енергії розриву кожного шару. матеріалу, використаного для цієї сонячної батареї, на струм короткого замикання J_{sc} , напругу холостого ходу V_{oc} , форм-фактор FF та електричний ККД η елементу CIGS для Mo/p-CIGS/p-Si/In₂S₃/одноперехідної структури i-ZnO/Al-ZnO. У цьому дослідженні ми виявлено, що швидкість рекомбінації впливає на ефективність фотоелектричного елемента. Енергія проміжку шарів поглинача впливає на ефективність елемента, тоді як інші шари (In₂S₃, ZnO, Al-ZnO) не мають великого впливу на продуктивність сонячного елемента, а збільшення товщини шару поглинача має великий вплив на ефективність, збільшивши його до певної межі. Товщина шарів CIGS, p-Si, In₂S₃, i-ZnO та Al ZnO має бути порядку 0,3 мкм, 0,8 мкм, 0,05 мкм, 0,07 мкм та 0,1 мкм відповідно для досягнення кращої ефективності (31,42%).

Ключові слова: теорія функціоналу густини (DFT); енергія зв'язку; гомо-люмо енергія; енергія фрагментації; магнітний момент

PERFORMANCE ENHANCEMENT VIA NUMERICAL MODELING AND OPTIMIZATION OF FASnI₃ PEROVSKITE SOLAR CELL

Lahcene Kanouni^a, Lamir Saidi^a, Abderrahim Yousfi^{b*}, Okba Saidani^b

^aLaboratoire d'Automatique Avancée et d'Analyse des Systèmes (LAAAS), Electronics Department, University of Batna 2, Batna 05000, Algeria

^bETA Laboratory, Department of electronics, Faculty of sciences and technology, University Mohamed El Bachir El Ibrahimi of Bordj Bou Arréridj-34030, Algeria

*Corresponding Author: Abderrahim.yousfi@univ-bba.dz; kanouni_lahcene@univ-batna2.dz

Received May 1, 2024; revised June 10, 2024; accepted June 15, 2024

Perovskite-based solar cells are currently attracting growing interest from researchers and industry alike, thanks to the advantages of this type of solar cell, particularly in terms of manufacturing simplicity and the promising power conversion efficiency, which has recently reached remarkable levels. This paper focuses on numerical simulation to improve the performance of the Formamidinium Tin Iodide (FASnI₃) solar cell configuration by using Cerium Dioxide (CeO₂) as ETL and Poly (Triaryl Amine) (PTAA) as HTL. The simulation has been carried out using Solar Cell Capacitance Simulator (SCAPS-1D) tool under the spectrum of AM 1.5 G. An intensive modeling has been realized to improve the output parameters of the suggested configuration based on FASnI₃ as absorber. The proposed structure (ITO/CeO₂/FASnI₃/PTAA/Au) achieves a tremendous power conversion efficiency (PCE) of 39.24%, an open-circuit voltage (V_{OC}) of 1.31 V, a short-circuit current density (J_{SC}) of 33.7 mA/cm² and a fill factor (FF) of 90.12%.

Keywords: Solar cell; FASnI₃; SCAPS-1D; Optimization; PCE

PACS: 84.60. Jt

1. INTRODUCTION

Due to the shy efficiency of Si-based photovoltaic solar cells and their high production costs, other materials have been exploited as a solution to the aforementioned drawbacks. Both in research and in commercialization, a certain number of technologies have emerged, such as dye-sensitized solar cells (DSSC), organic photovoltaic cells (OPV), quantum dot solar cells (QDSC), organic-inorganic hybrid solar cells (OIH), and perovskite solar cells (PSC) [1, 2]. According to Best Research-Cell Efficiency Chart published by NREL, the latest perovskite/silicon tandem solar cell, produced by LONGi, achieved a power conversion efficiency of 33.9% [3]. In the other hand, the category of perovskite solar cells, also known as third-generation solar cells, is increasingly attracting researchers due to its promising performance and low costs production.

In the present work, we have focused on organic-inorganic perovskites based on metal halides. Launched in 2009 with a power conversion efficiency of 3.81% [4, 5], perovskite solar cells have improved rapidly, to reach in 2022 a certified PCE of 25.7% [6]. Hybrid organic-inorganic perovskites are expressed as ABX₃, in which A is a monovalent inorganic or organic cation such as methylammonium (MA), formamidinium (FA), or cesium (Cs⁺); while B is a divalent cation such as Pb²⁺, Sn²⁺, and Ge²⁺. X is a monovalent anion, such as Cl⁻, Br⁻, and I⁻. In the literature, several combinations have been implemented to exploit the potential of perovskites materials. These choices have been justified in terms of environmental friendliness, production complexity, manufacturing costs and long-term stability, but above all, power conversion efficiency [7, 8]. As an alternative, formamidinium tin iodide (FASnI₃, FA⁺ = CH[NH₂]²⁺) presents itself as a solution which combines numerous advantages.

In 2023, Shayesteh Imani et al [9] presented a TCO/TiO₂/CH₃NH₃SnI₃/HTL/Au structure using different Cu-based as hole transport layer HTLs. They concluded that a CuI-based PCS was an efficient HTL and they achieved with this device a power conversion efficiency of 32.13%, a fill factor of 87.08%, an open-circuit voltage of 1.07 V and a short-circuit current density of 34.35 mA cm⁻². Leila Ghalmi et al [10] studied TiO₂/CH₃NH₃SnI₃/Cu₂O by adjusting the absorber layer thickness, doping concentration and defect density, and they obtained a remarkable power conversion efficiency of 23.94%.

This work performs a numerical analysis of the proposed device structure (ITO/CeO₂/FASnI₃/PTAA). The FASnI₃ used as an absorber layer, CeO₂ as electron transport layer (ETL) and PTAA as a hole transport layer (HTL), were used in the simulation using the software Solar Cell Capacitance Simulator SCAPS-1d. We have exploited previous works to conclude on the structure (ITO/CeO₂/FASnI₃/PTAA/back contact) and then we will work iteratively to look for the ideal parameters affecting thickness, doping and defect density of all layers. This study will present the effect of varying the above parameters on the output cell parameters such as short-circuit current, open-circuit voltage, fill factor and power conversion efficiency.

2. SIMULATED DEVICE STRUCTURE

The suggested structure in this work is typical to the initial architecture of a PSC cell. The device studied consists of 4 superimposed layers of normal n-i-p order. Figure 1 shows the structure used in this study in the form of ITO/ETL/PVK/HTL/Cathode. The front electrode exposed to sunlight consists of 0.15 μm-thick ITO, used as

a transparent conductive oxide (TCO). The use of CeO₂ as ETL material enables electrons to be collected and efficiently transferred from the absorbing perovskite layer to the front contact material via the electron transfer mechanism, thickness of this layer is 0.015 μm. While PTAA is used as HTL with a thickness of 0.3 μm to collect holes, which transfers the holes from perovskite absorber layer to the back contact. Finally, we use the FASnI₃ as absorber material with a thickness of 0.3 μm located as sandwich, between ETL and HTL. The back contact used in the solar cell is Au with a thickness of 0.15μm. The work involves optimizing all the materials used in terms of thickness, doping, temperature, series resistance and work function. The geometrical and electrical input parameters of the current configuration are summarized in Table 1 and 2 for a simulation analysis at temperature of 300 K.

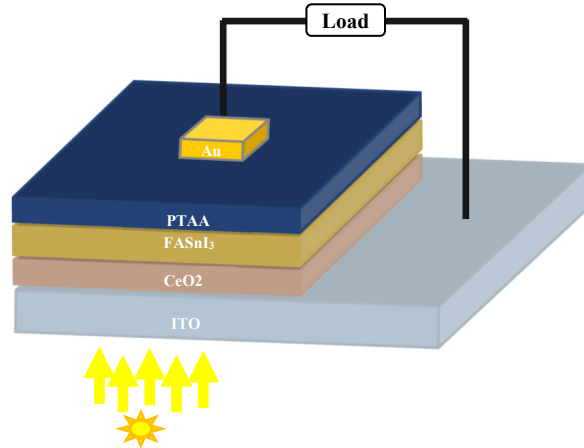


Figure 1. Structure of the designed PSC based on FASnI₃.

Table 1. The input parameters in the architecture of simulating device [11-14].

Terms	Parameters	TCO (ITO)	ETL (CeO ₂)	PVK (FASnI ₃)	HTL (PTAA)
Thickness	d (μm)	0.15	0.015	0.3	0.3
Bandgap	E _g (eV)	3.5	3.5	1.3	2.96
Relative Permittivity	ε _r	9	9	8.2	9
Electron affinity	χ (eV)	4	4.6	4.17	2.3
Electron thermal velocity (cm.s ⁻¹)	v _e	1×10 ⁷	1×10 ⁷	1×10 ⁷	10 ⁷
Hole thermal velocity (cm.s ⁻¹)	v _h	1×10 ⁷	1×10 ⁷	1×10 ⁷	10 ⁷
Effective DoS at CB.	N _c (cm ⁻³)	2.2×10 ¹⁸	1×10 ²⁰	1×10 ¹⁸	1×10 ²¹
Effective DoS at VB.	N _v (cm ⁻³)	1.8×10 ¹⁹	2×10 ²¹	1×10 ¹⁸	1×10 ²¹
Mob. of electrons	μ _n (cm ² /Vs)	20	10 ³	1.6	1
Mob. of holes	μ _p (cm ² /Vs)	10	250	1.6	40
Dop. conc. of the acceptor	N _a (cm ⁻³)	0	0	3.2×10 ¹⁵	1.5×10 ¹⁵
Dop. conc. of donor	N _d (cm ⁻³)	1×10 ²¹	1×10 ¹⁹	0	0
Defect Density	N _t (cm ⁻³)	1×10 ¹⁵	1×10 ¹⁴	1×10 ¹⁴	1×10 ¹⁴

Table 2. Parameter of interface defects used in simulations.

Parameters	PTAA/FASnI ₃	FASnI ₃ /CeO ₂
Defect type	Neutral	Neutral
Capture cross section electrons(cm ²)	1×10 ⁻¹⁹	1×10 ⁻¹⁹
Capture cross section holes(cm ²)	1×10 ⁻¹⁹	1×10 ⁻¹⁹
Energy distributions	Single	Single
Reference for defect energy level	Above the highest EV	Above the highest EV
Energy with respect to reference (eV)	0.6	0.6
Total density (integrated over all energies) (cm ⁻²)	1×10 ⁹	1×10 ⁹

3. Mathematical Modelling

The design and simulation of our PSC model were carried out using SCAPS-1D [15, 16]. Burgelman and his team from Gent university have created SCAPS-1D which allows the numerical modeling of photovoltaic components such as solar cells and photodetectors in order to obtain their output parameters like J-V characteristics which results from the multiplication of several parameters such as J_{SC}, V_{OC} and FF. The one-dimensional equation drives semiconductor materials in steady-state conditions [17].

The following equation presents the electric fields and charge density for the *pn* junction [18] :

$$\frac{\partial^2 \phi}{\partial^2 x} = - \frac{\partial E}{\partial x} = - \frac{\rho}{\epsilon_s} = - \frac{q}{\epsilon_s} [p - n + N_D^+(x) - N_A^-(x) \pm N_{def}(x)] \tag{1}$$

The precedent equation contains, the electrostatic potential, the charge, the static relative permittivity, n and p are the electrons and the hole, respectively, while N_A and N_D are the acceptor and donor successively, N_{def} named defect density.

Equation continuity of the electron and hole of the solar cell based perovskite configuration illustrated as follows [19]:

$$\frac{1}{j} \frac{\partial j_p}{\partial x} + R_p(x) - G(x) = 0, \tag{2}$$

$$-\frac{1}{j} \frac{\partial j_n}{\partial x} + R_n(x) - G(x) = 0. \tag{3}$$

The current densities of electron and hole symbolized successively, j_n and j_p , carrier generation rate and recombination rate of electron and hole are respectively, G and $R_{n,p}(x)$.

Synchronously, the current density for both, electrons and holes are illustrated in the following equations[20]

$$j_n = qn\mu_n E(x) - qD_n \frac{\partial n}{\partial x}, \tag{4}$$

$$j_p = qn\mu_p E(x) + qD_p \frac{\partial p}{\partial x}. \tag{5}$$

Where, q is the charge, μ_n and μ_p are the electrons and holes mobilities respectively, D_n and D_p are the diffusion coefficients for electrons and holes, respectively.

It should be pointed out that the recombination and generation equations are obtained from the SCAPS-1D simulator.

4. RESULTS AND DISCUSSIONS

The examination of the current solar cell configuration is carried out within the framework of the analysis of photovoltaic and electrical output parameters, which is subdivided into several parts as follows:

4.1 The influence of active layer thickness on the PSC outputs

Due to its impact on photogeneration, charge collection and transport processes, the performance of perovskite solar cells is directly affected by the thickness of the active layer, influencing the optical properties, electrical properties, energy characteristics and morphology of the cells [21]. Figure 2 illustrates the results of simulating the variation of cell parameters as a function of absorber thickness.

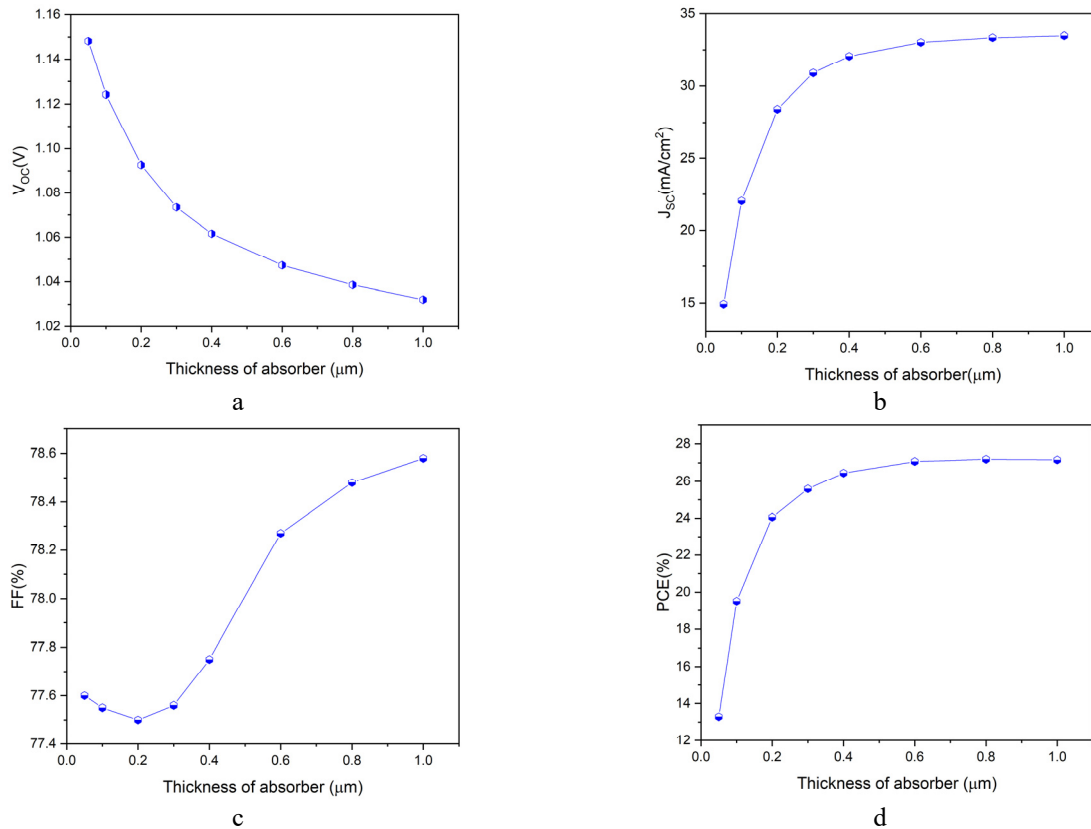


Figure 2. Variation of PV parameters as a function of the absorber layer thickness

We can observe in Fig. 2 (a) the decrease in V_{oc} with the increasing of perovskite material thickness, which varies from 0.1 μm to 1.0 μm, to get respectively the V_{oc} of 1.15 V to 1.034 V because of the wider bandgap of the perovskite

material. In Fig.2 (b), it is clear that the J_{SC} current of the solar cell increases with increasing FASnI₃ layer thickness due to increased charge carrier generation and reaches its saturated value of 33.9 mA/cm² at 1.0 μ m. A similar increase in J_{SC} is reported by Atanu Bag et al. [22]. The fill factor of the current configuration increases from a thickness of 0.2 μ m up to the maximum simulated value of 1 μ m, as depicted in Fig.2 (c), giving a fill factor of 78.6%. Power conversion efficiency varies up to 0.6 μ m, where the curve begins to flatten, leading to PCE saturation at a value of 27.4%, as shown in Fig.2 (d), beyond this, any further increase in thickness produces only marginal and insignificant improvements in PCE.

4.2 Effects of Temperature on PSC output parameters

In general, the operating environment for photovoltaic solar cells is direct sunlight, so the radiation falling on the solar cells raises the temperature. Many authors have reported a significant degradation in cell performance with increasing temperature, which affects all the parameters in the same way [23-25]. As illustrated in Figure 3, the section treats the variation of temperature from 300 K to 380 K to investigate the behavior of the cell in this range. Variation in J_{SC} and V_{OC} are shown in Fig.3 (a) and (b) respectively where the J_{SC} =30.89 mA/cm² at the 300 k and the V_{OC} =1.074 V for 300K, whereas at 375K, these two parameters reach their lowest values. As depicted in Fig. 3(c), the relevant FF values are 77.3% and 71% at 300K and 375K respectively. The PCE shows the same negative variation in Fig.3 (d), rising from 25.6% at 300K reaching 21.4% at 375K. We note that the current configuration supports the lower value of temperature cause the all-output parameters works well at 300K and this degraded performance at high temperatures may be due to a number of factors, such as accelerated interfacial recombination, reverse saturation current, bulk defects [26,27].

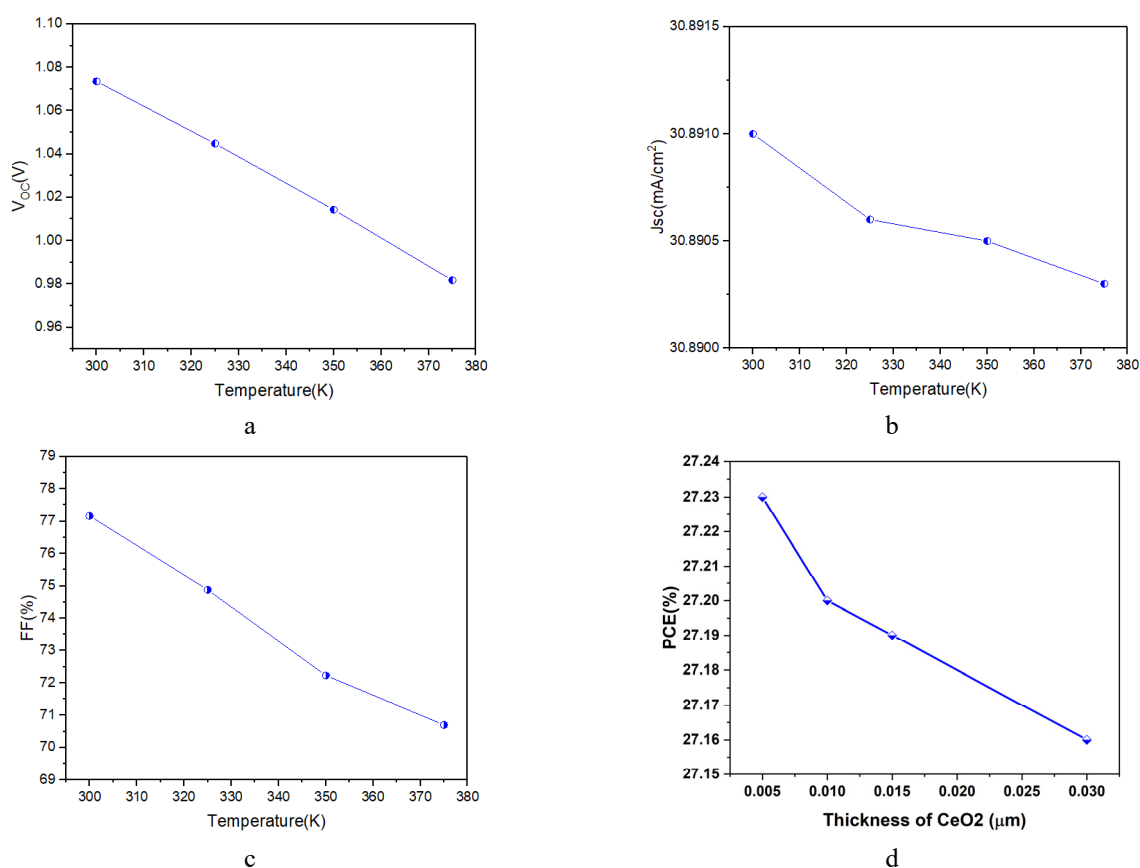


Figure 3. Variation in solar cell parameters as a function of temperature

4.3 The Impact of CeO₂ and PTAA thickness

In line with the previous section on temperature, we have used the default temperature of 300 k for good PVK solar cell performance. The thickness of the ETL and HTL layers can affect the efficiency, stability and reliability of the perovskite solar cell. In this section, the problem of the impact of charges transport layers thickness will be discussed, with Figures 4 and 5 showing V_{OC} , J_{SC} , FF and PCE for different CeO₂ and PTAA thicknesses respectively. These two layers should be as thin as possible to ensure fast electrons and holes transport, low interfacial recombination and low resistance losses, while ETL thickness should have a greater effect on the photovoltaic properties of PSC [28,29].

The variation of performance parameters as a function of CeO₂ thickness is illustrated in figure 4(a-d), in which thickness varies for values ranging from 0.005 μ m to 0.03 μ m. Simulation results showed that all PSC parameters decreased with increasing CeO₂ ETL layer thickness. Good performance is observed in the 0.005 μ m thickness of the ETL used where J_{SC} = 33.375 mA/cm², V_{OC} =1.0388 V, FF=78.55% and PCE=27.23%.

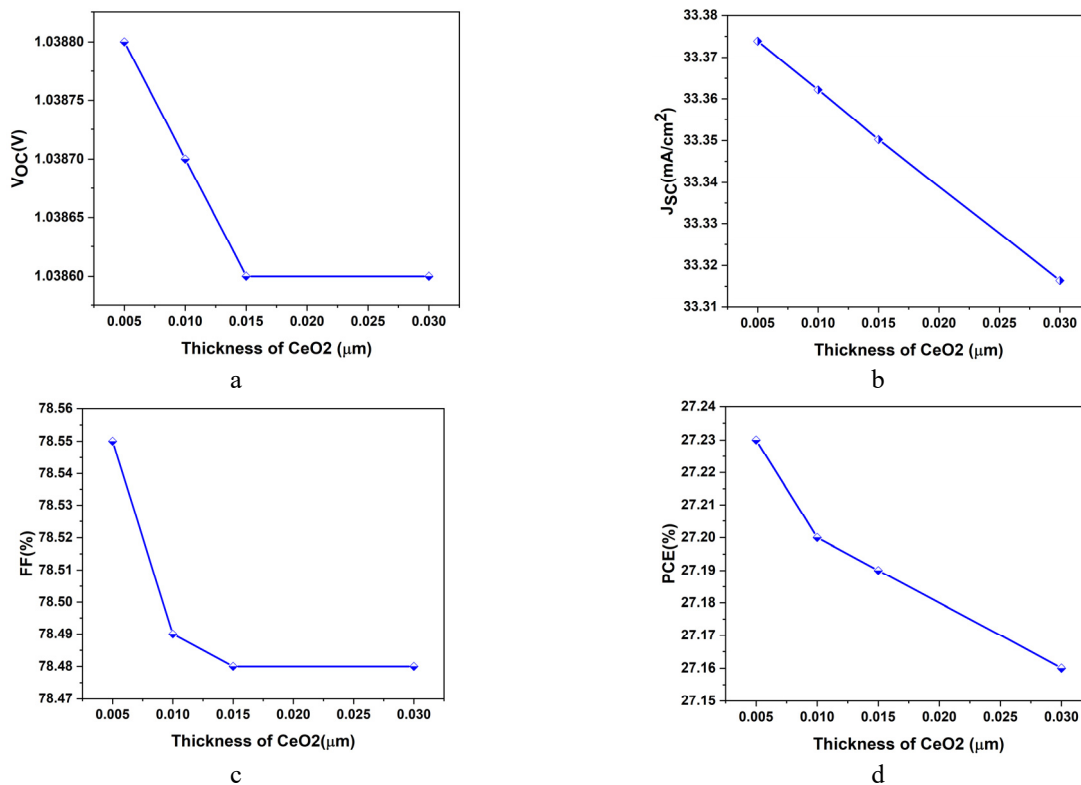


Figure 4. Variation of PV parameters as a function of CeO₂ thickness

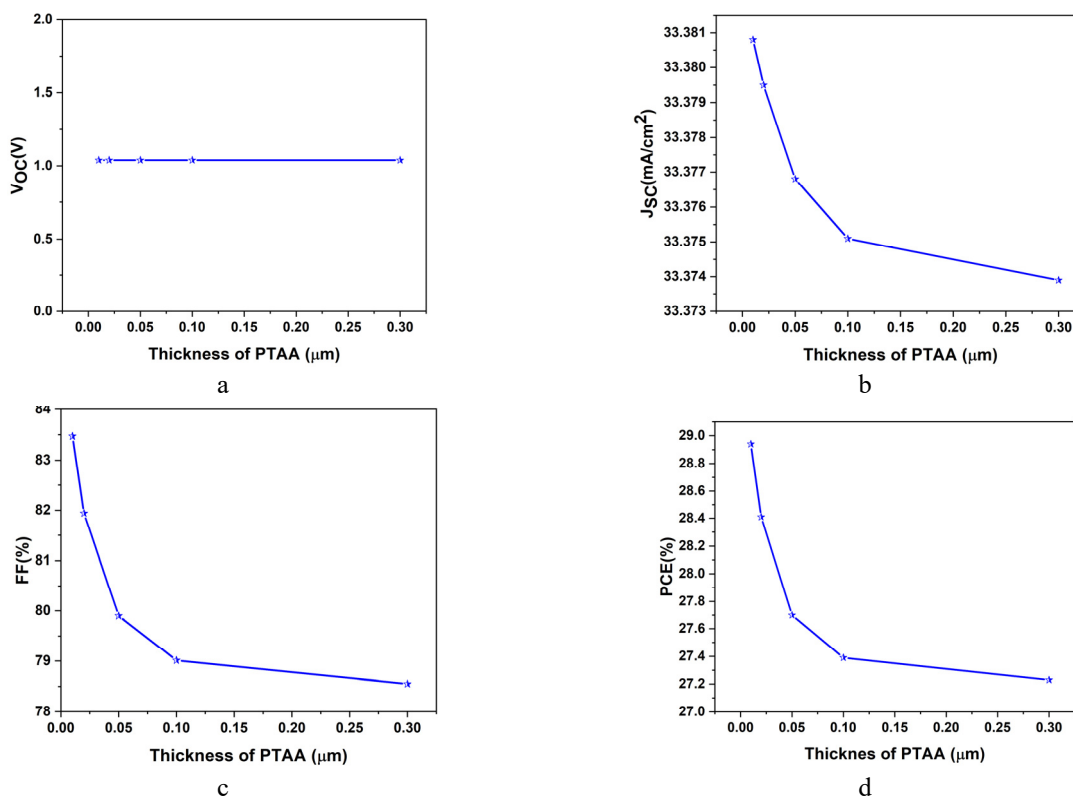


Figure 5. Variation of PV parameters as a function of PTAA thickness

Figure 5(a-d) illustrates the variation of PV parameters as a function of PTAA HTL layer thickness. We note that the highest PCE value obtained is 28.95% for the lowest PTAA thickness value of 0.025 μm. At this point also we had J_{sc}=33.381 mA/cm², FF=83.5% and V_{oc} remains fixed at value 1.08 V throughout the thickness range used. Ola Mostafa et al. have developed results similar to those shown in figure 5 [30]. It is evident that thinning the HTL should reduce the distance traveled by the holes to reach the back electrode, thereby reducing the likelihood of them undergoing

recombination [31]. The thicker layer of PTAA therefore acts as an insulator for the holes generated in the absorber by the increased series resistance, resulting in a reduction in J_{sc} , FF and PCE.

4.4 Effect of varying acceptor doping density in the absorber layer

The actual investigation focuses on output parameters as a function of acceptor doping density in the absorber layer. As reported by Md. A. Islam et al [32], doping the absorber layer can reduce the density of trap states and increase carrier lifetime in the cell, thereby increasing V_{OC} . It has also been shown that increasing the doping concentration improves V_{OC} and PCE due to the increase in the built-in electric field, which has the effect of separating charge carriers and reducing charge recombination [33]. To study the impact of acceptor doping density in the absorber layer, the device will be examined by varying the doping concentration from $3.2 \times E13 \text{ cm}^{-3}$ to $3.2 \times E17 \text{ cm}^{-3}$ as shown in figure 6.

As illustrated in Fig. 6 (a, c, d), the variation in output parameters starts to increase linearly from the first value of the acceptor doping density up to the concentration $3.2 \times E17 \text{ cm}^{-3}$ which gives the maximum value such as $V_{OC}=1.16 \text{ V}$, $FF=88.1\%$ and $PCE=33.7\%$, unlike the current, which decreases from top to bottom successively from $J_{SC}=33.42 \text{ mA/cm}^2$ to 33.15 mA/cm^2 . A further increase in doping concentration will lead to a higher rate of Auger recombination, which is not beneficial for cell performance. It can be noticed from Fig.6 (b) that when the doping density of the acceptor N_A exceeds $3.2 \times E15 \text{ cm}^{-3}$, we observe a rapid drop in J_{SC} as hole transport is strongly attuned because of the enhanced impurity scattering and recombination. In conclusion, we choose an acceptor doping density of $3.2 \times E17 \text{ cm}^{-3}$ [34, 35].

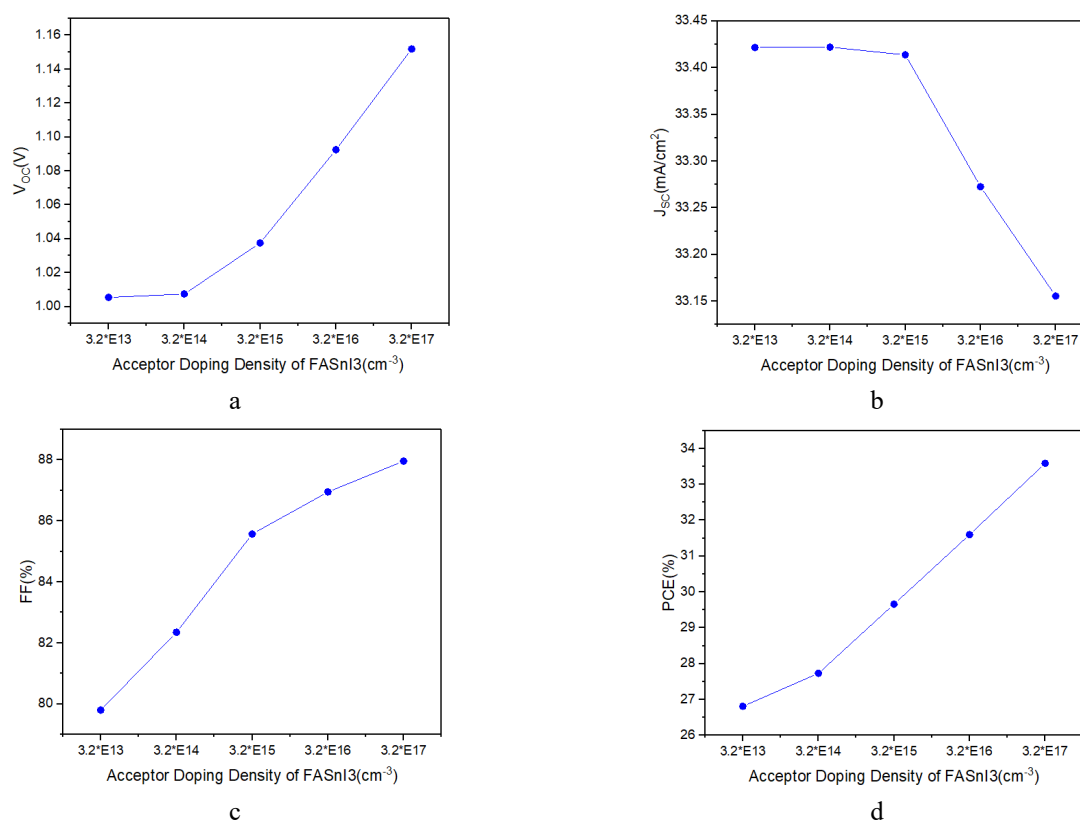


Figure 6. Variation of PV parameters as a function of acceptor doping density

4.5 The Impact of CeO₂ and PTAA doping density

The impact of doping on the charge transport layer (ETL and HTL) in a solar cell can have significant effects on various photovoltaic parameters since doping density will affect the mobility of charge carriers (electrons or holes) within the layer, improve conductivity and reduce recombination [36, 37]. Firstly, in the current section, we will study the impact of the ETL material, CeO₂, at different donor doping densities, as shown in Figure 7. For all values between $E13 \text{ cm}^{-3}$ and $E20 \text{ cm}^{-3}$, we observe that up to a donor density of $E17 \text{ cm}^{-3}$, parameters increase such as $J_{SC}=33.388 \text{ mA/cm}^2$, $FF=83.5\%$, $PCE=28.95\%$, in contrast to V_{OC} which decreases rapidly from $E17 \text{ cm}^{-3}$, corresponding to an open circuit voltage of 1.0396 V.

Francisco Peña-Camargo et al. explained that the doping density is only decisive for device performance when the density exceeds a certain threshold, which is of the order of $E16 \text{ cm}^{-3}$, and that it is only above this threshold that internal electric field begins to have a positive impact on charge carriers [38]. The internal electric field then increases with the doping density, accelerating carrier transport and improving conductivity as well as the other parameters except for V_{OC} , which will decrease slightly as a result of the improved conductivity [39]. After optimization, we select the donor doping concentration of the CeO₂ in the order of $E19 \text{ cm}^{-3}$.

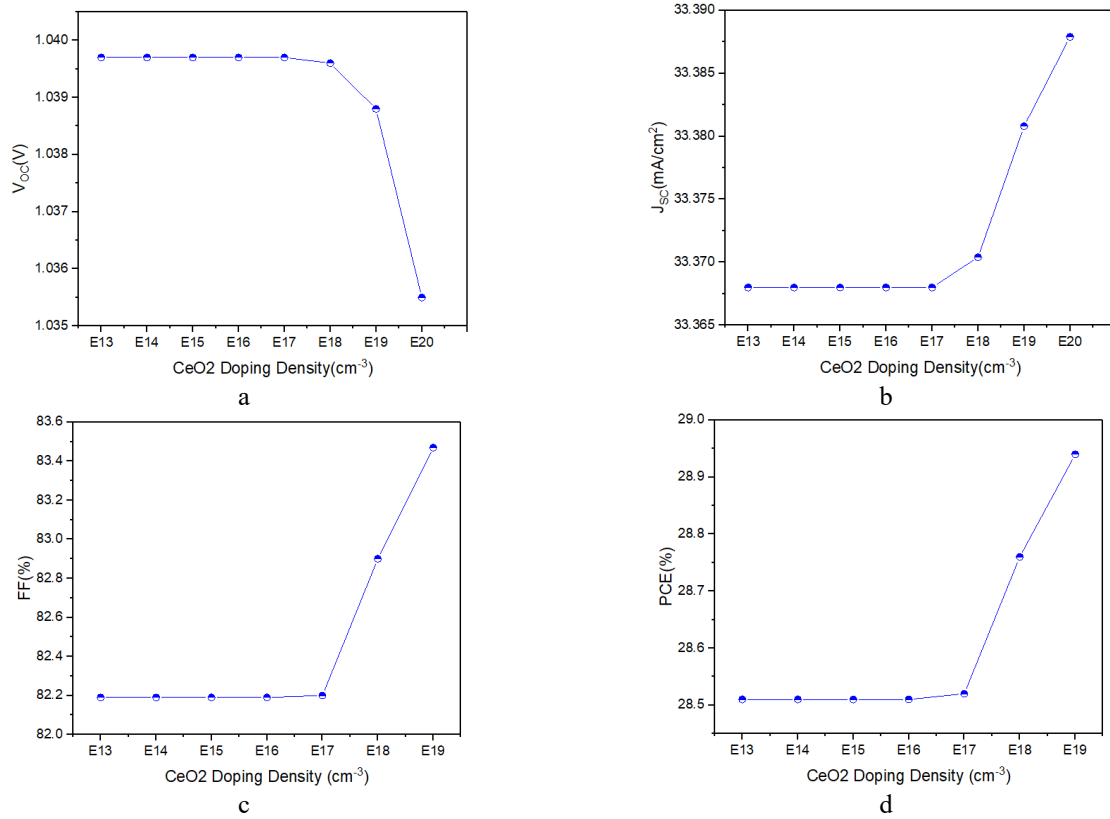


Figure 7. Variation of PV parameters as a function of CeO₂ doping density

The second part of this section examines the perovskite solar cell by optimizing the HTL material for different PTAA layer acceptor doping density values. Device performance shows a direct influence as doping increases, and the analysis was carried out by varying the acceptor doping density from $1.5 \times E13 \text{ cm}^{-3}$ to $1.5 \times E20 \text{ cm}^{-3}$ as shown in Figure 8.

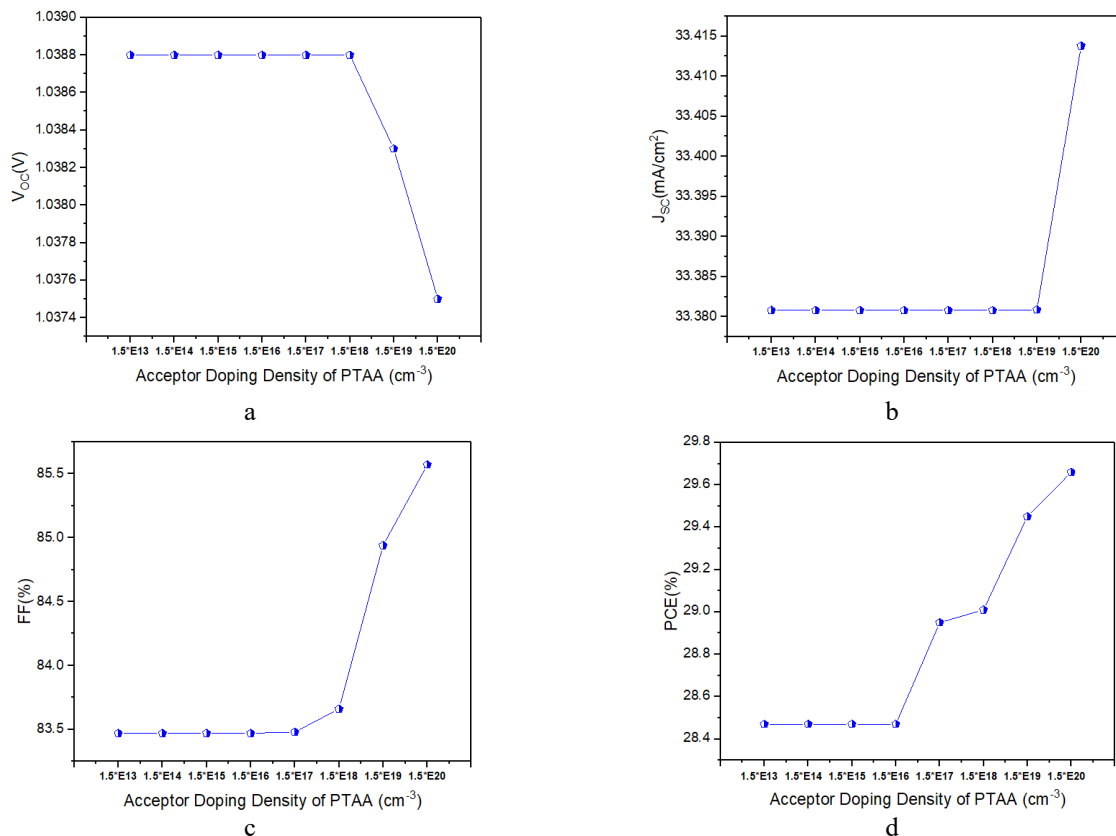


Figure 8. Variation of PV parameters as a function of PTAA doping density

This shows that device performance is slightly influenced by doping density up to $E20 \text{ cm}^{-3}$, if we increase the doping concentration, charge carrier separation increases and cell performance also increases as follows: $J_{SC}=33.41 \text{ mA/cm}^2$, $FF=85.6\%$, $PCE=29.7\%$, in contrast to the V_{OC} , which shows decreasing values from 1.0388 V to 1.0375 V as depicted in Fig.8 (a)

4.6 The Impact of defect density on the output parameters

Solar cell performance also depends on the density of defects, which are considered to be limiting factors since they affect recombination, lifetime and carrier mobility. Increasing the number of defects (N_i) results in a high rate of recombination, which in turn reduces the number of charge carriers, thereby decreasing the V_{OC} , J_{SC} , PCE and FF [40-42]. Figure 9 shows the influence of the defect density in the perovskite layer on the PSC performance.

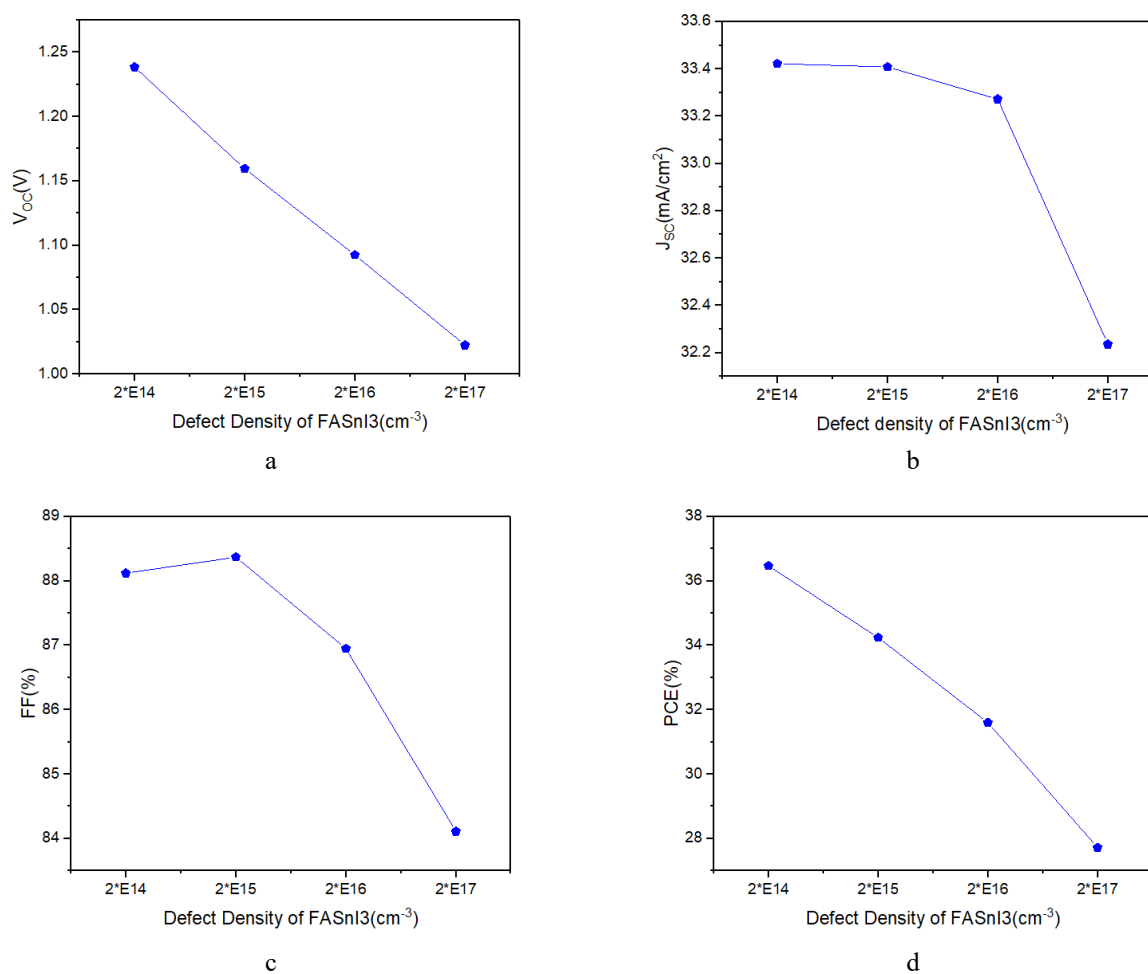


Figure 9. Variation of PV parameters as a function of the absorber layer defect density

The used defect density ranged from $2 \times 10^{14} \text{ cm}^{-3}$ to $2 \times 10^{17} \text{ cm}^{-3}$. The output device reversely proportional with defect density, when we increase defect density the output parameters fall down as follows, J_{SC} from 33.4 mA/cm^2 to 32.2 mA/cm^2 , V_{OC} from 1.24 V to 1.025 V , FF from 88.5% to 84% and PCE from 36.5% to 27.6% . Based on the optimization performed, we choose a defect density of $2 \times 10^{14} \text{ cm}^{-3}$ as the appropriate value that brings the best improvement to the photovoltaic and electrical output parameters.

4.7 The Impact of series resistances on the output parameters

The series resistance of a solar cell is due to several causes, in addition to manufacturing faults, defects and interfaces between the various materials, as well as resistances in the front and rear contacts. The main impact of series resistance is to reduce the fill factor, although excessively high values can also reduce the short-circuit current [43, 44].

The current simulation varies the series resistance value from $0 \ \Omega \cdot \text{cm}^2$ to $8 \ \Omega \cdot \text{cm}^2$ and optimize its adequate value of the good performance of the photovoltaic device. The Fig. 10 illustrates the output parameters of the solar cell device of, J_{SC} , V_{OC} , FF , PCE for a range of series resistance, J_{SC} decreases as series resistance increases, the V_{OC} has a value of 1.24 V from $0 \ \Omega \cdot \text{cm}^2$ to $6 \ \Omega \cdot \text{cm}^2$ and at $8 \ \Omega \cdot \text{cm}^2$ the voltage increases to 1.36 V . As shown in Fig.10 (c and d), both FF and PCE decrease with increasing series resistance. The figure also shows that the FF has its good percentage of 88.2% at $0 \ \Omega \cdot \text{cm}^2$ and that the PCE also has its optimal value of 36.5% at $0 \ \Omega \cdot \text{cm}^2$.

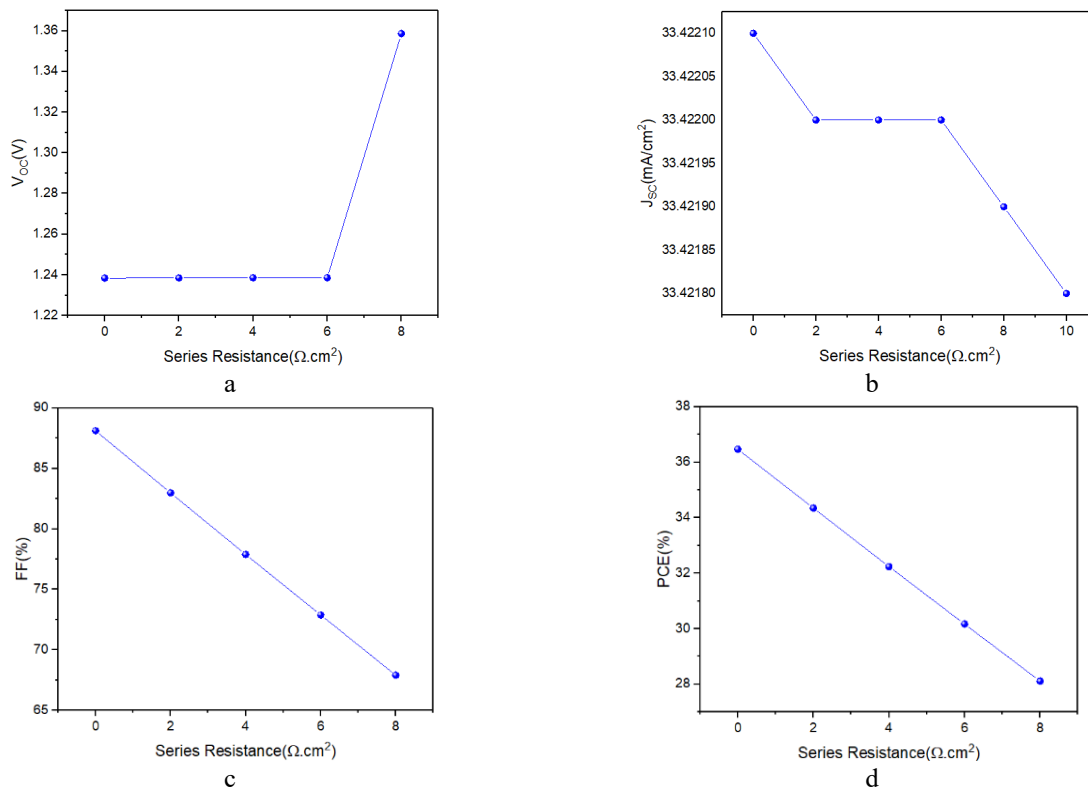


Figure 10. Variation of PV parameters as a function of series resistance

4.8 Adequate back contact for the PSC

The contact material has a major impact on the electrical performance of the solar cell, but in practice other factors such as cost and chemical and photochemical stability must also be taken into account when choosing the back contact material [45, 46]. In this section is devoted to finding the right back contact by analyzing the impact of work function on the solar cell output parameters. The examination of the device involves the use of numerous materials such as Ag, Cu, C and Au as back contact. Figure 11 below shows the solar cell's output parameters: J_{SC} , V_{OC} , FF and PCE.

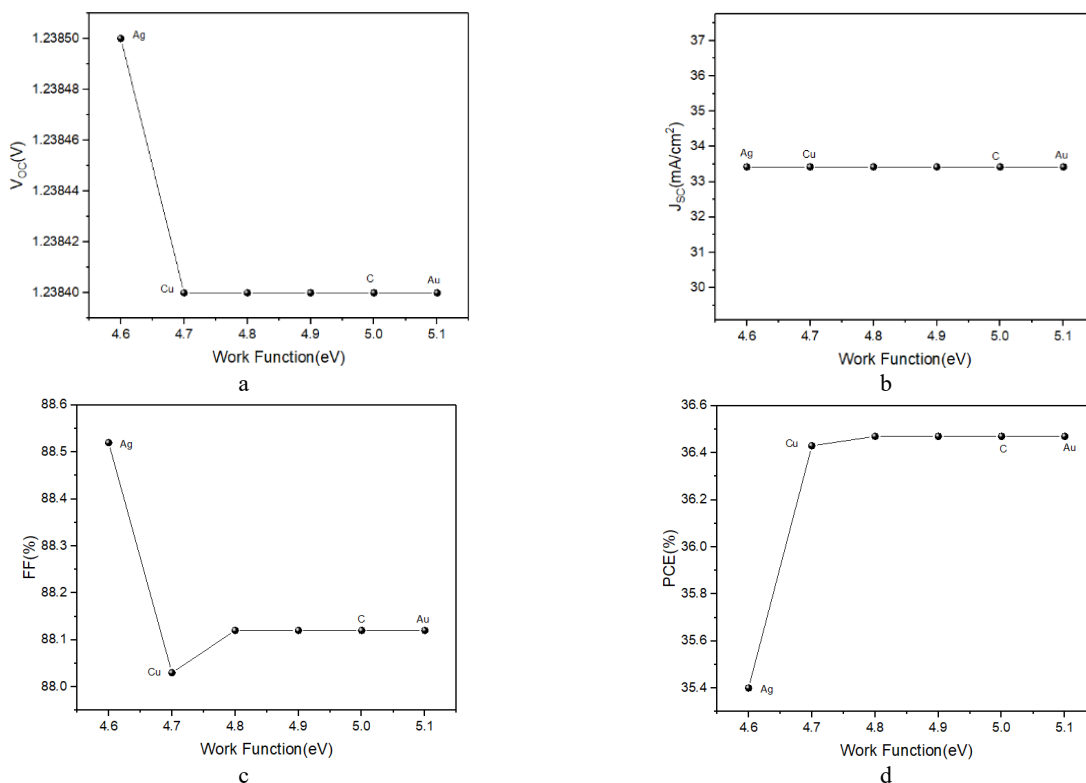


Figure 11. Impact of work function on the solar cell output parameters

The J_{SC} has a constant value of 33.4 mA/cm² for all materials used, the optimal V_{OC} of 1.2385 V at the Ag material, the fill factor has 88.53% also for Ag while the PCE has the value of 35.4% with Ag and reaching 36.5% for the other materials. As a result of this part of the work function, the figures show that Ag is the appropriate back contact material for its good PSC performance, unfortunately it has been reported that Ag-based back contact suffers from degradation over time with the formation of silver iodide (AgI), that's why Au is the optimal choice for achieving the compromise between stability and performance.

4.9 The contour study of the FASnI₃ based PSC

As shown in Fig. 12, the optimal values of the output parameters are described as follows, the current J_{SC} =33.7 mA/cm² for the thickness of 0.8 nm and more and for the whole range used (from E14 cm⁻³ to E18 cm⁻³) of the FASnI₃ absorber doping concentration, the optimal voltage V_{OC} =1.31 V obtained when the absorber becomes very thin starting from 0.6 nm with a higher doping concentration of E18 cm⁻³, the high doping concentration at E18 cm⁻³ is the optimum value, corresponding to a fill factor of 90.12% for all thickness ranges used (from 0.4 nm to 1.2 nm). Finally, using the coordinates of a doping concentration of E18 cm⁻³ and a thickness value greater than or equal to 0.6 nm, we obtain a PCE peak of 39.24%.

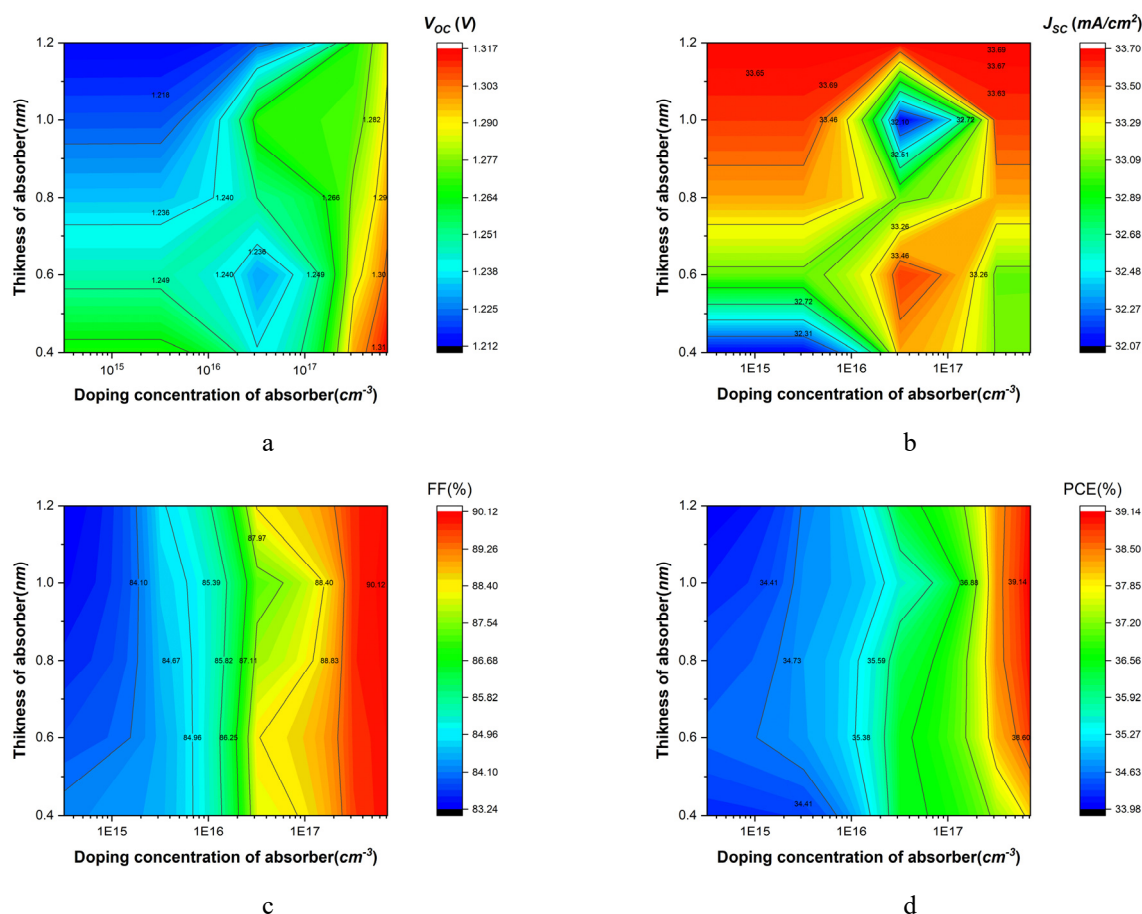


Figure 12. Impact of the absorber layer doping concentration on the PSC Output parameters (V_{OC} , J_{SC} , FF, and PCE)

CONCLUSIONS

In this article, we have numerically simulated the configuration of ITO/CeO₂/FASnI₃/PTAA/Au using SCAPS-1D simulation software. The absorber layer performance was optimized by adjusting defect density, acceptor density and absorber layer thickness. It was found that the optimal absorber thickness is 0.6 μ m, the absorber defect density is 2×10^{14} cm⁻³, while the absorber doping concentration is 3.2×10^{17} cm⁻³. For the ETL and HTL layers, ideal performance was achieved with a thickness of 0.005 μ m for CeO₂ and 0.025 μ m for PTAA. Their optimal doping concentration was found to be 10^{19} cm⁻³.

Finally, and after full optimization, the resulting perovskite solar cell achieves an efficiency of 39.24 % as a result from multiplying J_{SC} , V_{OC} and FF successively of 33.7 mA/cm², 1.31 V and 90.12 %. The results present a good enhancement of the photovoltaic and electrical output parameters making the reported configuration using FASnI₃ offers a viable route to achieve PSC that has no lead toxicity, as well as low cost and high efficiency.

ORCID

Abderrahim Yousfi, <https://orcid.org/0000-0003-2071-728X>; Okba Saidani, <https://orcid.org/0000-0003-0507-5581>

REFERENCES

- [1] A.R. Mollick, and Md.A. Ashraf, "Numerical Simulation of Cs₂AgBiBr₆-based Perovskite Solar Cell with ZnO Nanorod and P3HT as the Charge Transport Layers," *Physica B: Condensed Matter*, **618**, 413187 (2021). <https://doi.org/10.1016/j.physb.2021.413187>
- [2] A. Yousfi, O. Saidani, Z. Messai, R. Zouache, *et al.*, "Design and Simulation of a Triple Absorber Layer Perovskite Solar Cell for High Conversion Efficiency," *East European Journal of Physics*, (4), 137-146 (2023). <https://doi.org/10.26565/2312-4334-2023-4-14>
- [3] NREL Efficiency chart, (2023), <https://www.nrel.gov/pv/assets/images/cell-pv-eff-emergingpv.png>
- [4] E. Zimmermann, K. Wong, M. Müller, H. Hu, P. Ehrenreich, *et al.*, "Characterization of perovskite solar cells: Towards a reliable measurement protocol," *APL Materials*, **4**(9), 091901 (2016). <https://doi.org/10.1063/1.4960759>
- [5] O.A. Muhammed, E. Danladi, P.H. Boduku, J. Tasiu, M.S. Ahmad, and N. Usman, "Modeling and Simulation of Lead-Free Perovskite Solar Cell Using SCAPS-1D," *East European Journal of Physics*, (2), 146-154 (2021). <https://doi.org/10.26565/2312-4334-2021-2-12>
- [6] C.H. Liao, Md.A. Mahmud, and A. Ho-Baillie, "Recent progress in layered metal halide perovskites for solar cells, photodetectors, and field-effect transistors," *Nanoscale*, **15**, 4219-4235 (2023). <https://doi.org/10.1039/D2NR06496K>
- [7] E. Danladi, D.S. Dogo, S.U. Michael, F.O. Uloko, and A.O. Salawu, "Recent Advances in Modeling of Perovskite Solar Cells Using SCAPS-1D: Effect of Absorber and ETM Thickness," *East European Journal of Physics*, (4), 5-17 (2021). <https://doi.org/10.26565/2312-4334-2021-4-01>
- [8] S. Rabhi, H. Benzouid, A. Slami, and K. Dadda, "Modeling and Numerical Simulation of a CH₃NH₃SnI₃ Perovskite Solar Cell Using the SCAPS1-D Simulator," *Eng. Proc.* **56**(1), 97 (2023). <https://doi.org/10.3390/ASEC2023-15300>
- [9] S. Imani, S.M. Seyed-Talebi, J. Beheshtian, *et al.*, "Simulation and characterization of CH₃NH₃SnI₃-based perovskite solar cells with different Cu-based hole transporting layers," *Appl. Phys. A*, **129**, 143 (2023). <https://doi.org/10.1007/s00339-023-06428-0>
- [10] L. Ghalmi, S. Bensmaine, and C.E.H. Merzouk, "Optimizing the Performance of Lead-free CH₃NH₃SnI₃ Perovskite Solar Cells via Thickness, Doping, and Defect Density Control," *Journal of Science, Technology and Engineering Research*, **4**(1), 44-51 (2023). <https://doi.org/10.53525/jster.1231984>
- [11] M.K. Hossain, M. Rubel, G.F.I. Toki, *et al.*, "Effect of Various Electron and Hole Transport Layers on the Performance of CsPbI₃-Based Perovskite Solar Cells: A Numerical Investigation in DFT, SCAPS-1D, and wxAMPS Frameworks," *ACS Omega*, **7**, 43210-43230 (2022). <https://doi.org/10.1021/acsomega.2c05912>
- [12] E. Katunge, G. Njema, and J. Kibet, "Theoretical analysis of the electrical characteristics of lead-free formamidinium tin iodide solar cell," *IET Optoelectronics*, **17**(5), 220-236 (2023). <https://doi.org/10.1049/ote2.12104>
- [13] P. Tiwari, M.F. Alotaibi, Y. Al-Hadeethi, V. Srivastava, *et al.*, "Design and Simulation of Efficient SnS-Based Solar Cell Using Spiro-OMeTAD as Hole Transport Layer," *Nanomaterials*, **12**(14), 2506 (2022). <https://doi.org/10.3390/nano12142506>
- [14] A.B. Coulibaly, S.O. Oyedele, N.R. Kre, and B. Aka, "Comparative Study of Lead-Free Perovskite Solar Cells Using Different Hole Transporter Materials. Modeling and Numerical Simulation," *Modeling and Numerical Simulation of Material Science*, **9**(4), 97-107 (2019). <https://doi.org/10.4236/mnsm.2019.94006>
- [15] A.K. Al-Mousoi, M.K.A. Mohammed, R. Pandey, J. Madan, *et al.*, "Simulation and analysis of lead-free perovskite solar cells incorporating cerium oxide as electron transporting layer," *RSC Adv.* **50**(12), 32365-32373 (2022). <https://doi.org/10.1039/D2RA05957F>
- [16] K. Ukoba, P.E. Imoisili, and T.C. Jen, "Numerical analysis and performance improvement of nanostructured Cu₂O/TiO₂pn heterojunction solar cells using SCAPS," *Materials Today: Proceedings*, **38**(2), 887-892 (2021). <https://doi.org/10.1016/j.matpr.2020.05.111>
- [17] M. Burgelman, P. Nollet, and S. Degraeve, "Modelling polycrystalline semiconductor solar cells," *Thin Solid Films*, **361-362**, 527-532 (2000). [https://doi.org/10.1016/S0040-6090\(99\)00825-1](https://doi.org/10.1016/S0040-6090(99)00825-1)
- [18] S. Bhattarai, D. Borah, J. Rout, R. Pandey, J. Madan, *et al.*, "Designing an efficient lead-free perovskite solar cell with green-synthesized CuCrO₂ and CeO₂ as carrier transport materials," *RSC Adv.* **13**(49), 34693-34702 (2023). <http://dx.doi.org/10.1039/D3RA06722J>
- [19] Sk.T. Ahamed, Ar. Basak, A. Mondal, "Device modeling and investigation of Sb-based low-cost heterojunction solar cells using SCAPS-1D," *Results in Optics*, **10**, 100364 (2023). <https://doi.org/10.1016/j.rio.2023.100364>
- [20] M. Ismail, M. Noman, S.T. Jan, and M. Imran, "Boosting efficiency of ecofriendly perovskite solar cell through optimization of novel charge transport layers," *R. Soc. Open Sci.* **10**(6), 230331 (2023). <https://doi.org/10.1098/rsos.230331>
- [21] S.T. Jan, and N. Muhammad, "Influence of layer thickness, defect density, doping concentration, interface defects, work function, working temperature and reflecting coating on lead-free perovskite solar cell," *Solar Energy*, **237**, 29-43 (2022). <https://doi.org/10.1016/j.solener.2022.03.069>
- [22] B. Atanu, R. Radhakrishnan, R. Nekovei, and R. Jeyakumar, "Effect of absorber layer, hole transport layer thicknesses, and its doping density on the performance of perovskite solar cells by device simulation," *Solar Energy*, **196**, 177-182 (2020). <https://doi.org/10.1016/j.solener.2019.12.014>
- [23] I. Mesquita, L. Andrade, and A. Mendes, "Temperature Impact on Perovskite Solar Cells Under Operation," *Chem. Sus. Chem.* **12**(10), 2186-2194 (2019). <https://doi.org/10.1002/cssc.201802899>
- [24] P. Roy, N.K. Sinha, and A. Khare, "An investigation on the impact of temperature variation over the performance of tin-based perovskite solar cell: A numerical simulation approach," *Materials Today: Proceedings*, **39**(5), 2022-2026 (2021). <https://doi.org/10.1016/j.matpr.2020.09.281>
- [25] H. Baig, H. Kanda, A.M. Asiri, M.K. Nazeeruddin, and T. Mallick, "Increasing efficiency of perovskite solar cells using low concentrating photovoltaic systems," *Sustainable Energy Fuels*, **4**(2), 528-537 (2020). <http://dx.doi.org/10.1039/C9SE00550A>
- [26] A. Gholami-Milani, S. Ahmadi-Kandjani, B. Olyaeefar, *et al.*, "Performance analyses of highly efficient inverted all-perovskite bilayer solar cell," *Sci. Rep.* **13**, 8274 (2023). <https://doi.org/10.1038/s41598-023-35504-x>
- [27] R. Priyanka, T. Sanjay, and K. Ayush, "An investigation on the influence of temperature variation on the performance of tin (Sn) based perovskite solar cells using various transport layers and absorber layers," *Results in Optics*, **4**, 100083, (2021). <https://doi.org/10.1016/j.rio.2021.100083>

- [28] N. Rono, A.E. Merad, J.K. Kibet, *et al.*, “A theoretical investigation of the effect of the hole and electron transport materials on the performance of a lead-free perovskite solar cell based on CH₃NH₃SnI₃,” *J. Comput. Electron.* **20**, 993–1005 (2021). <https://doi.org/10.1007/s10825-021-01673-z>
- [29] J. Arayro, R. Mezher, and H. Sabbah, “Comparative Simulation Study of the Performance of Conventional and Inverted Hybrid Tin-Based Perovskite Solar Cells,” *Coatings*, **13**(7), 1258 (2023). <https://doi.org/10.3390/coatings13071258>
- [30] O. Mostafa, N.A. Zidan, W. Abbas, H.H. Issa, N. Gamal, and M. Fedawy, “Design and performance optimization of lead-free perovskite solar cells with enhanced efficiency,” *Mathematical Modelling of Engineering Problems*, **10**(4), 1307-1316 (2023). <https://doi.org/10.18280/mmepp.100424>
- [31] G.W. Kim, D. Shinde, and T. Park, “Thickness of the hole transport layer in perovskite solar cells: performance versus reproducibility,” *RSC Adv.* **5**(120), 99356-99360 (2015). <http://dx.doi.org/10.1039/C5RA18648J>
- [32] Md.A. Islam, Md.N.B. Alamgir, S.I. Chowdhury, and S.M.B. Billah, “Lead-free organic inorganic halide perovskite solar cell with over 30% efficiency,” *Journal of Ovonic Research*, **18**, 395-409 (2022). <https://doi.org/10.15251/JOR.2022.183.395>
- [33] H. Sabbah, J. Arayro, and R. Mezher, “Simulation and Investigation of 26% Efficient and Robust Inverted Planar Perovskite Solar Cells Based on GA_{0.2}FA_{0.78}SnI₃-1%EDA12 Films,” *Nanomaterials*, **12**, 3885 (2022). <https://doi.org/10.3390/nano12213885>
- [34] Hui-Jing Du, *et al.*, “Device simulation of lead-free CH₃NH₃SnI₃ perovskite solar cells with high efficiency,” *Chinese Physics B*, **25**(10), 108802 (2016). <https://dx.doi.org/10.1088/1674-1056/25/10/108802>
- [35] P.K. Patel, “Device simulation of highly efficient eco-friendly CH₃NH₃SnI₃ perovskite solar cell,” *Sci. Rep.* **11**, 3082 (2021). <https://doi.org/10.1038/s41598-021-82817-w>
- [36] V.M. le Corre, M. Stolterfoht, L.P. Toro, M. Feuerstein, *et al.*, “Charge Transport Layers Limiting the Efficiency of Perovskite Solar Cells: How to Optimize Conductivity, Doping, and Thickness,” *ACS Appl. Energy Mater.* **2**, 6280–6287 (2019). <https://doi.org/10.1021/acsaem.9b00856>
- [37] J. Avila, L. Gil-Escrig, P. Boix, M. Sessolo, S. Albrecht, and H.J. Bolink, “Influence of doped charge transport layers on efficient perovskite solar cells,” *Sustainable Energy Fuels*, **2**(11), 2429-2434 (2018). <http://dx.doi.org/10.1039/C8SE00218E>
- [38] F. Peña-Camargo, J. Thiesbrummel, H. Hempel, A. Musiienko, *et al.*, “Revealing the doping density in perovskite solar cells and its impact on device performance,” *Appl. Phys. Rev.* **9**(2), 021409 (2022). <https://doi.org/10.1063/5.0085286>
- [39] M. Ahamad, and A.K.M. Hossain, “Design and optimization of non-toxic and highly efficient tin-based organic perovskite solar cells by device simulation,” *Heliyon*, **9**(9), e19389 (2023). <https://doi.org/10.1016/j.heliyon.2023.e19389>
- [40] Y. Wan-Jian, S. Tingting, and Y. Yanfa, “Unusual defect physics in CH₃NH₃PbI₃ perovskite solar cell absorber,” *Appl. Phys. Lett.* **104**(6), 063903 (2014). <https://doi.org/10.1063/1.4864778>
- [41] S.H. Huang, Z. Rui, D. Chi, and D. Bao, “Influence of defect states on the performances of planar tin halide perovskite solar cells,” *J. Semicond.* **40**(3), 032201 (2019). <http://doi.org/10.1088/1674-4926/40/3/032201>
- [42] H.K. Ibrahim, A.M.A. Sabaawi, and Q.T. Aljwari, “A Comprehensive Study on the Effect of Defects on Perovskite Solar Cell Performance,” *Preprints*, **1**, 344 (2023). <https://doi.org/10.20944/preprints202306.0344.v1>
- [43] S.R. Hosseini, M. Bahramgour, P.Y. Sefidi, *et al.*, “Investigating the effect of non-ideal conditions on the performance of a planar,” *Heliyon*, **8**(11), e11471 (2022). <https://doi.org/10.1016/j.heliyon.2022.e11471>
- [44] R. Ranjan, N. Anand, M.N. Tripathi, *et al.*, “SCAPS study on the effect of various hole transport layer on highly efficient 31.86% eco-friendly CZTS based solar cell,” *Sci. Rep.* **13**, 18411 (2023). <https://doi.org/10.1038/s41598-023-44845-6>
- [45] F. Behrouznejad, S. Shahbazi, N. Taghavinia, *et al.*, “A study on utilizing different metals as the back contact of CH₃NH₃PbI₃ perovskite solar cells,” *J. Mater. Chem. A*, **4**(35), 13488–13498 (2016). <https://doi.org/10.1039/C6TA05938D>
- [46] H. Sharma, and R. Srivastava, “Solution-processed pristine metal oxides as electron-transporting materials for perovskite solar cells,” *Front. Electron. Mater.* **3**, 1174159 (2023). <https://doi.org/10.3389/femat.2023.1174159>

ПІДВИЩЕННЯ ПРОДУКТИВНОСТІ СОНЯЧНИХ ПЕРОВСКІТНИХ ЕЛЕМЕНТІВ FASnI₃ ШЛЯХОМ ЧИСЕЛЬНОГО МОДЕЛЮВАННЯ ТА ОПТИМІЗАЦІЇ

Лаксен Кануні^а, Ламір Сайді^а, Абдеррахім Юсфі^б, Окба Сайдані^б

^аЛабораторія вдосконаленої автоматизації та системного аналізу (LAAAS), Департамент електроніки, Університет Батна 2, Батна 05000, Алжир

^бЛабораторія ETA, Департамент електроніки, Факультет науки і технологій, Університет Мохамеда Ель Бачіра Ель Ібрагімі, Бордж Бу Аррерідж-34030, Алжир

Сонячні елементи на основі перовскіту в даний час привертають все більший інтерес дослідників і промисловості завдяки перевагам цього типу сонячних елементів, зокрема з точки зору простоти виробництва та багатообіцяючої ефективності перетворення електроенергії, яка нещодавно досягла надзвичайного рівня. Ця стаття зосереджена на чисельному моделюванні для покращення продуктивності конфігурації сонячної батареї на основі йодиду формамідіну олова (FASnI₃) за допомогою використання діоксиду церію (CeO₂) як ETL та полі (триариламіну) (PTAA) як HTL. Моделювання було виконано за допомогою інструменту Solar Cell Capacitance Simulator (SCAPS-1D) у спектрі АМ 1.5 G. Було реалізовано інтенсивне моделювання для покращення вихідних параметрів запропонованої конфігурації на основі FASnI₃ як поглинач. Запропонована структура (ITO/CeO₂/FASnI₃/PTAA/Au) забезпечує велику ефективність перетворення потужності (PCE) 39,24%, напругу холостого ходу (VOC) 1,31 В, щільність струму короткого замикання (JSC) 33,7 мА/см² і коефіцієнтом заповнення (FF) 90,12%.

Ключові слова: сонячний елемент; FASnI₃; SCAPS-1D; оптимізація; PCE

STRENGTHEN THE POWER CONVERSION EFFICIENCY OF SOLAR CELL BASED RbGeI₃: NUMERICAL APPROACH

Lazhar Loumachi^a, Abderrahim Yousfi^{b*}, Okba Saidani^b, Abdullah Saad Alsubaie^c, Oussama Abed^b, Samir Amiri^b, Girija Shankar Sahoo^d, Md. Rasidul Islam^e

^aDepartment of Civil Engineering, Faculty of sciences and technology, University Mohamed El Bachir El Ibrahimy of Bordj Bou Arréridj-34030, Algeria

^bETA Laboratory, Department of electronics, Faculty of sciences and technology, University Mohamed El Bachir El Ibrahimy of Bordj Bou Arréridj-34030, Algeria

^cDepartment of Physics, College of Khurma University College, Taif University, Taif 21944, Saudi Arabia

^dSchool of Electronics Engineering (SENSE), Vellore Institute of Technology, Vandalur Kellambakkam Road, Chennai, Tamil Nadu 600127, India

^eDepartment of Electrical and Electronic Engineering, Bangamata Sheikh Fojilatunnesa Mujib Science & Technology University, Jamalpur, 2012, Bangladesh

*Corresponding Author e-mail: abderrahim.yousfi@univ-bba.dz; lazhar.loumachi@univ-bba.dz

Received May 1, 2024; revised June 12, 2024; accepted June 20, 2024

The current study employs numerical simulations via the SCAPS-1D platform to investigate the performance of solar cells based on perovskite, with RbGeI₃ utilized as an absorber material possessing a wide bandgap of 1.31 eV. Through systematic exploration of various parameters including temperature, layer thickness, doping, and defects, the study aims to enhance the efficiency of the solar cells, considering their sensitivity to temperature variations. Results demonstrate that the proposed configuration effectively extends the absorption spectrum into the near-infrared region, with the thickness of the RbGeI₃ layer emerging as a critical factor influencing device performance. Analysis reveals that the series resistance peaks at $2 \Omega \cdot \text{cm}^2$, while the shunt resistance achieves optimal output parameters of up to $10^3 \Omega \cdot \text{cm}^2$. Moreover, optimization efforts yield a solar cell exhibiting a power conversion efficiency of 24.62%, fill factor of 82.8%, open circuit voltage of 0.99V, and short circuit current density of 33.20 mA/cm² at a RbGeI₃ thickness of 0.6 μm . This comprehensive numerical investigation not only enhances understanding of the intricate factors influencing perovskite solar cells but also suggests promising avenues for future advancements in the field.

Keywords: Solar cell; RbGeI₃; SCAPS-1D; PSC; PCE

PACS: 84.60. Jt, 88.40.jm

1. INTRODUCTION

Perovskite solar cells (PSCs) have emerged as a rapidly advancing technology within the photovoltaics field, offering significant promise [1]. Named after their structure resembling the naturally occurring mineral perovskite, these solar cells typically feature an active layer comprising an organic-inorganic halide perovskite material [2-3]. This material exhibits exceptional light-harvesting capabilities and can be economically manufactured. Noteworthy advantages of PSCs include their high-power conversion efficiencies, cost-effectiveness in production [4], and potential for flexible and transparent applications [5]. However, challenges related to stability, toxicity (stemming from lead content in certain formulations), and scalability for large-scale commercial production persist [6-7]. Over recent years, the efficiency of organic-inorganic hybrid perovskites has notably increased, from 3.81% to 25.2% [8]. Researchers across various disciplines have devoted substantial efforts to enhancing PSC efficiency through optimizations of perovskite layers and refinement of device structures [9]. One avenue explored to address these challenges involves the incorporation of rubidium (Rb⁺) into perovskite compositions, either as a dopant or additive [10-11]. Rubidium doping can modify the perovskite's properties, influencing its electronic structure and enhancing stability, a critical factor for commercialization [12]. Additionally, rubidium has been found to improve photovoltaic performance by enhancing power conversion efficiency and open-circuit voltage while reducing defects within the perovskite structure [13]. Efforts to develop environmentally friendly alternatives to lead-based perovskites have led to the investigation of germanium-based perovskites, such as CsGeI₃ [14]. Germanium-based perovskites offer tunable bandgaps, allowing for tailored electronic properties to optimize solar absorption [15-16]. Investigations into lead-free perovskites, including those containing germanium, focus on their stability under various environmental conditions, a crucial consideration for practical solar cell applications [17]. In perovskite solar cells, iodide ions are commonly utilized as integral components within the perovskite material, contributing significantly to light absorption and thereby playing a pivotal role in the photovoltaic conversion process [18]. The composition of halide ions influences both the bandgap and absorption characteristics of the perovskite material [19]. Rubidium, germanium, and triiodide each fulfill distinct roles in shaping the composition and structure of perovskite solar cells [20-21]. These elements exert influence over electronic properties, stability, and photovoltaic performance, offering avenues for researchers to tailor the characteristics of solar cells for optimal efficiency and stability [22].

This study introduces an innovative approach to simulating solar cells using the SCAPS-1D simulator. Our method incorporates advanced electron transport layers (ETLs) comprising C₆₀ and hole transport layers (HTLs) composed of CBTS. Simulation results reveal that solar cell heterostructures, specifically ITO/C₆₀/RbGeI₃/CBTS/Ag, demonstrate remarkably high photoconversion efficiency. Furthermore, our investigation extends beyond surface-level analysis, encompassing a comprehensive exploration of multiple parameters influencing the performance of RbGeI₃-based solar cells.

2. DEVICE SETTINGS AND SIMULATION PROCESS

The architecture of the solar cell employed in our study comprises three primary components: the electron transport layer (ETL), the perovskite layer doped with p-type material, and the hole transport layer (HTL). When illuminated by light, this configuration initiates the generation of excitons, which are particle pairs confined within the energy state, primarily within the perovskite layer [23]. These excitons, consisting of electrons and holes, possess relatively extensive diffusion lengths, facilitating their migration into the p-region (for electrons) or n-region (for holes) [24-25]. At the interface between the ETL and the perovskite layer, the excitons (electron-hole pairs) undergo separation. Subsequently, electrons are transported through the ETL toward the respective electrode, while holes efficiently traverse the HTL [26]. The existence of a built-in electric field between the ETL (or HTL) and the perovskite layer promotes the dissociation of excitons and their subsequent transport. This electric field accelerates the movement of electrons and holes towards their corresponding contacts, thereby enhancing the overall efficiency of the solar cell [27]. In our simulations, we incorporated advanced materials for the ETL and HTL layers, specifically employing ceric dioxide (C₆₀) for the ETL and CBTS for the HTL [28]. Simulation outcomes revealed that solar cell structures comprised of indium tin oxide ITO/C₆₀/RbGeI₃/CBTS/Ag exhibited notably high photoconversion efficiency, as depicted in Figure 1. The integration of these advanced materials contributes to the overall enhancement of solar cell performance.

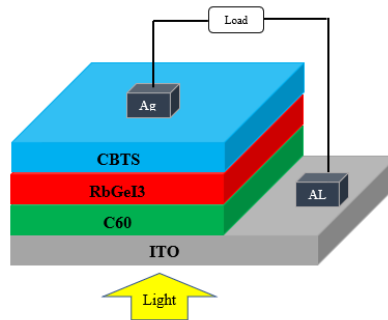


Figure 1. Design configuration of the RbGeI₃ based PSC

The simulations were conducted under standard operating conditions, utilizing AM1.5G light and an ambient temperature of 300 K. Moreover, as detailed in **Tables 1**, meticulous definition of input modeling parameters was undertaken for the hole transport layer (HTL), absorber layer (RbGeI₃), and electron transport layer (ETL) [29].

Table 1. Parameters of ETL, absorber and HTL

Parameters	ITO	ETL (C ₆₀)	PVK (RbGeI ₃)	HTL (CBTS)
Thickness (μm)	0.5	0.1	0.4	0.05
Electron Affinity χ (eV)	4.1	3.9	3.9	3.6
Band gap E_g (eV)	3.5	1.31	1.31	1.9
Relative Permittivity ϵ_r	9	7.5	23.01	5.4
Effective Density of States (CB)	2.2×10^{18}	1×10^{19}	1.8×10^{18}	10^{19}
Effective Density of States (VB)	1.8×10^{18}	1×10^{19}	1×10^{18}	10^{19}
Electron Mobility μ_n (cm ² /Vs)	20	10^{-2}	28.6	200
Hole Mobility μ_p (cm ² /Vs)	10	10^{-2}	27.3	8.6×10^3
Acceptor Density N_A (1/cm ³)	0	0	1×10^{15}	10^{18}
Donor Density N_D (1/cm ³)	10^{21}	10^{18}	0	2
Defect Density N_t	10^{14}	10^{14}	1×10^{14}	10^{14}

The accurate representation and emulation of the solar cell's behavior and performance within the simulation framework necessitate careful consideration of these parameters. By employing SCAPS-1D numerical simulations, our understanding of the fundamental principles and mechanisms governing solar cells has been greatly enhanced. These simulations have identified the primary variables that exert the most significant impact on the performance of these devices [30]. Through numerical methods for solving carrier continuity equations and the one-dimensional Poisson equation, SCAPS-1D offers invaluable insights into the behavior of semiconductor materials under stable conditions. Specifically, the Poisson equation plays a crucial role in elucidating the relationship between space charge density and the electric field (E) across a p-n junction. Equation (1) aids in comprehending the semiconductor material utilized in solar cells, thereby deepening our understanding of electrostatics and charge distribution [31].

$$\left(\frac{\partial^2 \psi}{\partial x^2}\right) = -\frac{\partial E}{\partial x} = -\frac{\rho}{\epsilon_s} = -\frac{q}{\epsilon_s} [p - n + N_d^+ - N_a^- + N_{def}]. \quad (1)$$

The carrier continuity equation in the device can be expressed as follows, where Ψ signifies the electrostatic potential, ϵ_s means the static relative permittivity, q is the charge, e and n explain respectively the electrons and holes, N_d^+ is the donor density, N_a^- is the acceptor density, and N_{def} represents the defect density of both donor and acceptor [32-33].

$$-\frac{\partial j_p}{\partial x} + G - U_p(n, p) = 0, \quad (2)$$

$$-\frac{\partial j_n}{\partial x} + G - U_n(n, p) = 0. \quad (3)$$

The carrier current density can also be obtained using the following equation [34], where j_p and j_n signifies the hole and electron current densities, G is the carrier generation rate, and $U_n(n, p)$ and $U_p(n, P)$ are the rates at which electrons and holes recombine [35].

$$j_p = qn\mu_p E + qD_p \frac{\partial n}{\partial x}, \quad (4)$$

$$j_n = qn\mu_n E + qD_n \frac{\partial n}{\partial x}. \quad (5)$$

Simulations using SCAPS-1D allow the derivation values of short-current density (J_{sc}), power conversion efficiency (PCE), fill factor (FF) and open circuit voltage (V_{oc}) under varying thicknesses and temperatures [36]. where q denotes the charge, μ_p and μ_n represent carrier mobilities, and D_p , D_n are the diffusion coefficients [37]. These simulations may be performed in both lighted and dark environments, taking into account a range of temperatures, and they can be applied to seven different layers of the solar cell [38].

3. RESULTS AND DISCUSSION

3.1. Influence of Absorber (RbGeI₃) thickness:

In this section, we delve into the proposed structure of solar cell-based perovskite, comprising the layers mentioned earlier, and break it down into several subsections. We commence with an exploration of thickness variation. Figure 2. a showcases the current density–voltage (J–V) characteristics of perovskite solar cells incorporating RbGeI₃.

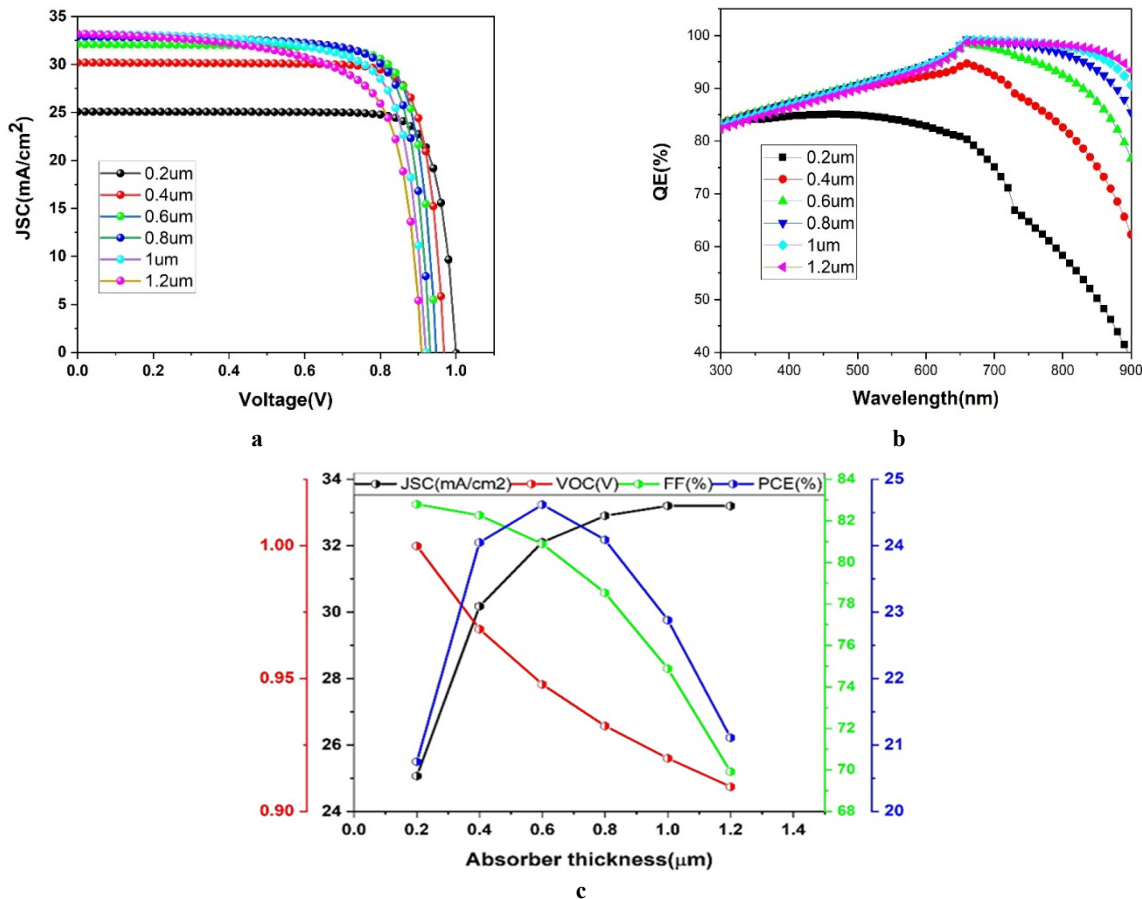


Figure 2. Effect of perovskite thickness on J–V (a), QE (b) and VOC, JSC, FF, PCE (c)

The thickness of the perovskite layer (RbGeI₃) was altered to assess its impact. It is observed that the short-circuit current density (J_{SC}) increases proportionally with absorber thickness, while the open-circuit voltage (V_{OC}) decreases, as illustrated in Figure 2.a. Figure 2.b displays the external quantum efficiency (QE) analysis, examining the effect of varying absorber thickness from 200 nm to 1200 nm across a wavelength range of 300 nm-900 nm. The QE of the structure significantly improves when the thickness of the RbGeI₃ light harvester is below 0.6 μm , indicating a notable enhancement in absorption. However, the increase in QE diminishes when the thickness exceeds 0.6 μm , suggesting a less significant rise in absorption. With increasing RbGeI₃ film thickness, better absorption of longer wavelengths is observed. Short Circuit Current Density (J_{sc}) and Power Conversion Efficiency (PCE) are presented, showing an increase with the perovskite layer thickness, but a decrease at 0.6 μm thickness. A thinner perovskite layer boosts sunlight absorption, leading to higher open-circuit voltage and improved fill factor. However, this reduction in efficiency at 0.6 μm thickness is attributed to potential issues such as increased charge recombination, trapping, and non-uniformity within the perovskite layer [39]. Excessive thickness hampers charge extraction, negatively affecting overall solar cell efficiency. The solar cell yields a J_{sc} of 33.20 mA cm^{-2} , with a V_{oc} of 0.99 V, FF of 82.8%, and Power Conversion Efficiency of 24.62%. Figure 2.c presents the Quantum Efficiency spectra for RbGeI₃ perovskite solar cells, revealing a substantial QE value exceeding 90% across a wide wavelength spectrum from 600 to 850 nm, with the photon spectral response extending to approximately 850 nm. The photocurrent densities derived from QE spectra align with the J_{sc} values obtained in J-V curves recorded under a solar simulator.

3.2. Influence of ETL Thickness

In perovskite solar cells, the electron transport layer (ETL) is pivotal for effectively extracting and conveying electrons generated during light absorption. Donor doping involves purposefully introducing dopant atoms that contribute electrons into the ETL material. Heavily donor-doping the electron transport layer in perovskite solar cells serves multiple critical functions: enhancing electron mobility within the ETL, which facilitates easier electron movement, diminishes recombination, and boosts overall efficiency [40]. Moreover, donor doping aids in establishing a favorable energy level alignment at the perovskite layer-ETL interface, thus aiding in efficient electron extraction and minimizing losses due to recombination. Additionally, it reduces energy barriers, facilitating smoother electron movement through the ETL, thereby improving charge transport efficiency and enhancing the stability of the perovskite solar cell over time. This precise tuning of energy levels within the ETL optimizes energy level alignment between different layers of the solar cell, leading to improved charge transport and reduced losses [41]. However, careful optimization is essential as excessive doping may result in undesirable effects such as increased carrier trapping or material instability. Factors such as choice of dopant, doping concentration, and specific characteristics of the perovskite material must be considered for effective enhancement of the ETL in perovskite solar cells [42]. As depicted in Figure 3.a, the current density–voltage (J–V) characteristics of the proposed configuration involving C₆₀ are shown, varying its thickness to explore its impact on the solar cell. To enhance output performance, a thinner C₆₀ layer is preferred, with optimal values observed at 0.4 μm thickness. Figure 3.b illustrates the impact of donor doping of the ETL on output performance. The device features a heavily doped C₆₀ layer at a concentration of 10^{20}cm^{-3} , resulting in $J_{SC}=25.13\text{ mA/cm}^2$, $V_{OC}=1.00\text{V}$, $\text{FF}=83.09\%$, and $\text{PCE}=20.99\%$.

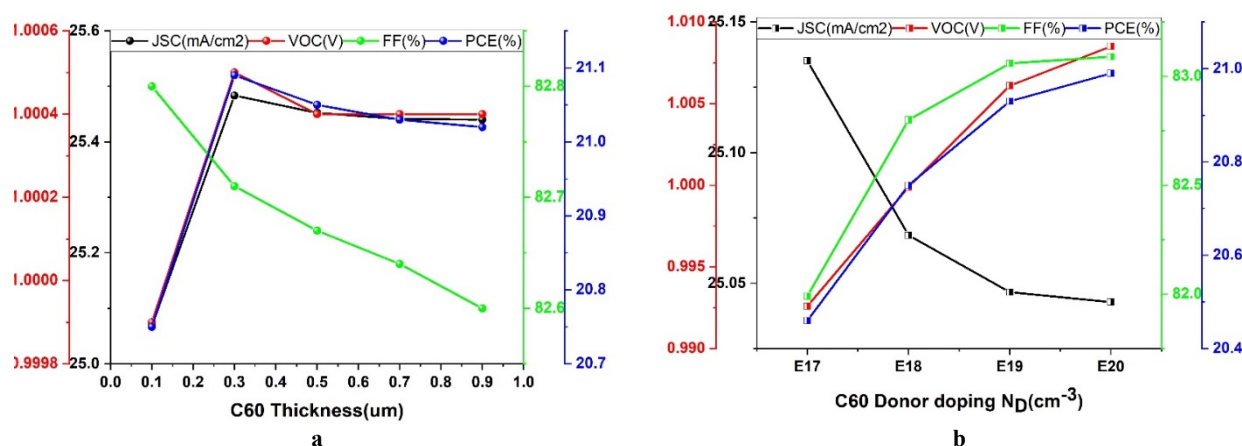


Figure 3. Effect of ETL thickness on V_{oc} , J_{sc} , FF, PCE for Donor doping N_D (a) and Thickness (b)

3.3. Influence of HTL Thickness

The thickness of the Hole Transport Layer (HTL) in a perovskite solar cell plays a crucial role in determining the device's performance. Various factors are at play in understanding how HTL thickness impacts perovskite solar cells. Firstly, optimal thickness is essential for efficient charge extraction from the perovskite layer, ensuring that holes can effectively reach the HTL and be collected at the electrode. Conversely, if the HTL is too thin, it may fail to adequately collect and transport holes, leading to increased recombination and decreased device efficiency. Additionally, increasing HTL thickness may elevate contact resistance between the HTL and the electrode, hindering charge carrier flow and

thereby diminishing electrical performance. Balancing thickness is therefore crucial to allow efficient charge transport while minimizing contact resistance. Moreover, the organic nature of the HTL may lead to light absorption, with thicker HTLs potentially reducing light reaching the perovskite layer, affecting device stability [43]. The compatibility between HTL material and the perovskite layer is vital for long-term stability, as HTL thickness influences energy level alignment at the interface. Optimization is necessary, considering different perovskite formulations and HTL materials, with trade-offs between charge transport optimization, fabrication ease, and cost. Experimental observations indicate that decreasing the thickness of the HTL layer enhances electron transfer properties, improving charge extraction and boosting short-circuit current density, consequently increasing energy conversion efficiency and open circuit voltage due to reduced recombination [44]. However, a decrease in Fill Factor is noted with thinner HTL layers. As presented in Figure 4, the solar cell exhibited a Power Conversion Efficiency (PCE) of 21.69 %, with a V_{oc} of 1.00 V, a J_{sc} of 26.08 mA cm^{-2} , and an FF of 82.93%.

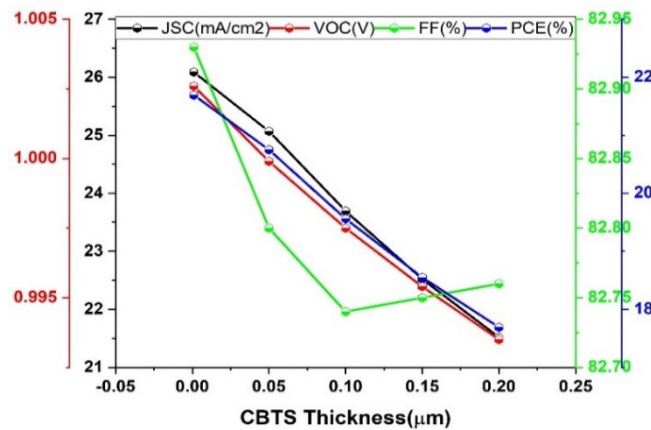


Figure 4. Effect of HTL thickness on V_{oc} ; J_{sc} ; FF; PCE

3.4. Influence of Defect Absorber

The presence of defects within the perovskite absorber layer of a perovskite solar cell profoundly influences both its performance and stability. Various factors come into play regarding the impact of these defects on the perovskite layer. Firstly, defects can serve as recombination centers, facilitating the recombination of electron-hole pairs generated by light absorption. This recombination process diminishes the cell's overall efficiency by limiting the number of charge carriers available for generating electric current. Additionally, defects can introduce trap states within the perovskite material's bandgap, capturing and temporarily immobilizing charge carriers, thereby delaying recombination and affecting charge carrier transport [45]. These trap states create energetic barriers for charge carriers, impacting their mobility and contributing to non-radiative recombination. The presence of defects also leads to a decrease in the open-circuit voltage (V_{oc}) of the solar cell by introducing additional energy levels that hinder charge carrier separation and extraction, thus affecting the fill factor (FF) as well, which measures the device's utilization of generated electrical current [46]. Moreover, defects contribute to the degradation of the perovskite material over time, especially under exposure to moisture, heat, or light, leading to decreased device performance and stability. In Figure 5, the performance characteristics of the defect absorber are examined to understand its impact, showing a decrease in short-circuit current density (J_{sc}), open-circuit voltage (V_{oc}), fill factor (FF), and power conversion efficiency (PCE) with increasing defect density. The solar cell exhibited a PCE of 23.14%, with a V_{oc} of 1.09 V, a J_{sc} of 25.07 mA cm^{-2} , and an FF of 84.25 %.

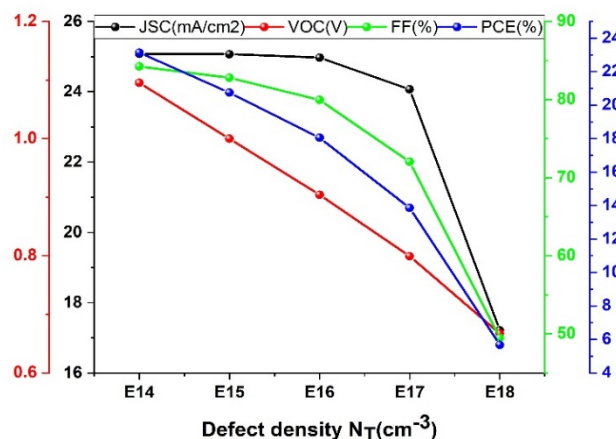


Figure 5. Effect of Defect density N_T (cm^{-3}) on V_{oc} , J_{sc} , FF and PCE

3.5. Influence of Temperature

Understanding the temperature impact on perovskite solar cells is crucial for predicting and enhancing their performance across different conditions. Temperature variations significantly affect the electrical, optical, and structural characteristics of these cells. As temperature rises, perovskite solar cell efficiency typically declines, primarily due to decreased open-circuit voltage (V_{oc}) and fill factor (FF), which collectively reduce overall efficiency. However, higher temperatures can also enhance charge carrier mobility, improving electrical performance. Nonetheless, elevated temperatures may increase recombination rates, shortening charge carrier lifetimes and thereby reducing overall efficiency. Moreover, temperature influences trap state density and activation energy, affecting recombination kinetics [47]. Perovskite materials are sensitive to heat, with excessive temperatures leading to thermal degradation and decreased stability over time. Temperature variations also impact the bandgap of perovskite, altering its optical absorption properties and consequently affecting sunlight absorption and photocurrent. Figures 6.a and 6.b illustrate the impact of temperature on current density–voltage (J–V) features, showing a decrease in V_{oc} with increasing temperature and a decline in short circuit current density (J_{sc}) alongside increases in V_{oc} , FF, and Power Conversion Efficiency (PCE). Figure 6.c depicts quantum efficiency (QE) functions across different temperatures, crucial for understanding charge collection efficiency and device stability. Changes in QE over time reveal degradation mechanisms, aiding in device improvement. QE also influences the current-voltage (I–V) curve, notably the position of the maximum power point (MPP), crucial for optimal power output. Analysis indicates a mean QE of 87% for a 500 nm absorber layer thickness, with temperature variation enhancing PCE to 21.53 %, accompanied by V_{oc} of 1.02 V, J_{sc} of 25.32 mA cm^{-2} , and FF of 84.01 %.

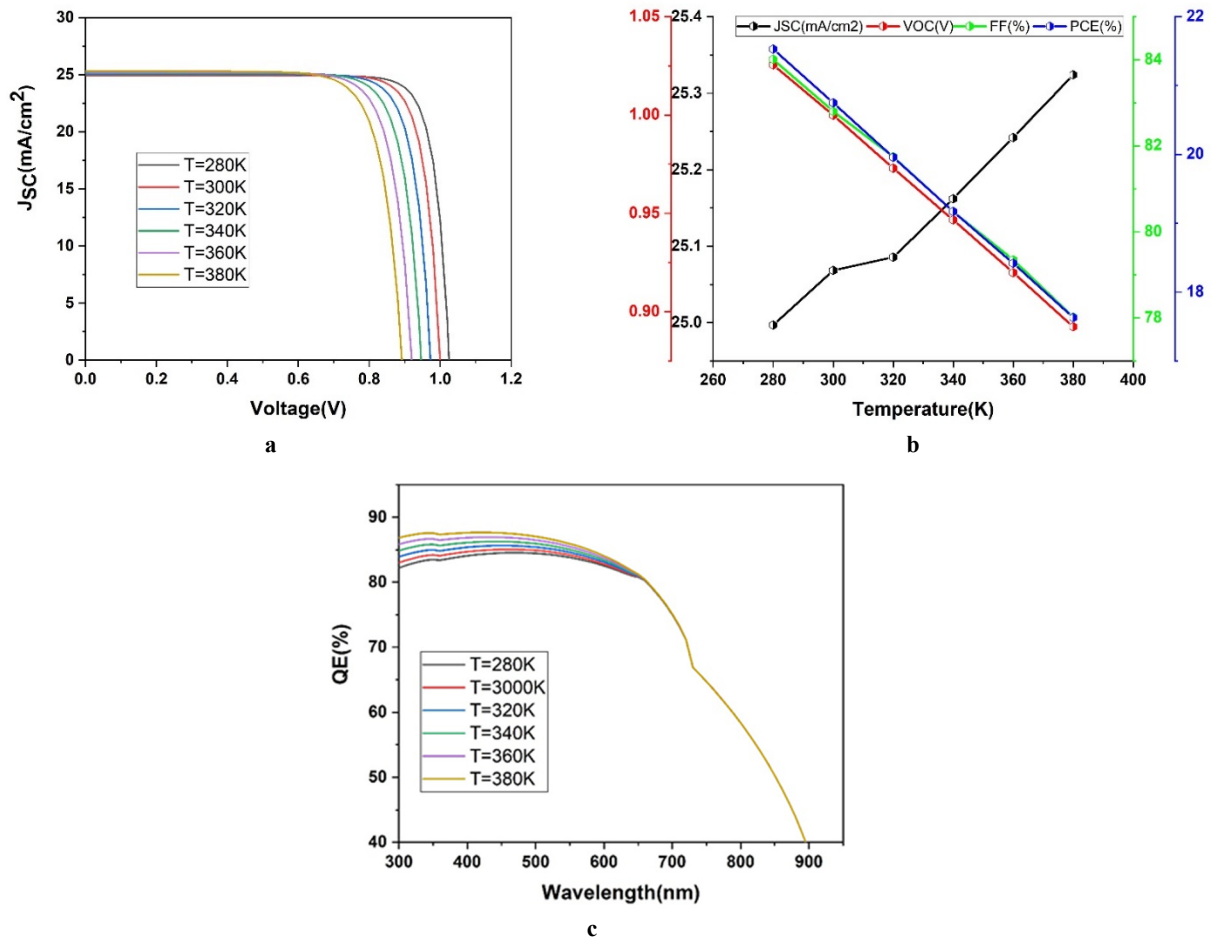


Figure 6. Effect of temperature on J–V (a), V_{oc} , J_{sc} , FF, PCE (b) and QE (c)

3.6 Impact of series resistance and shunt resistance:

In the illustrated Figure 7(a) and (b) successively denotes, Series resistance (R_s) and shunt resistance (R_{sh}) are critical factors affecting the performance of perovskite solar cells, influencing parameters like efficiency and fill factor. Balancing both resistances is vital for optimal performance, with material choices and device architecture playing significant roles. While minimizing series resistance reduces voltage drops along the current path, maximizing shunt resistance allows more current to pass through the active region, enhancing output voltage. Shunt resistance, representing parallel resistance to the current path, reduces current leakage and contributes to increased output voltage and fill factor [48]. Conversely, series resistance, encountered by current flow through cell components, leads to voltage drops and power losses, impacting fill factor and output voltage. As series resistance increases, open circuit voltage (V_{oc}) tends to rise, while shunt

resistance enhancements correlate with increased Voc, fill factor, and power conversion efficiency (PCE). Shunt resistance minimizes voltage losses due to leakage currents, enhancing FF and PCE without affecting short circuit current density (Jsc). The solar cell exhibited a PCE of 20.75%, with a Voc of 0.99 V, Jsc of 25.06 mA cm⁻², and FF of 82.8%.

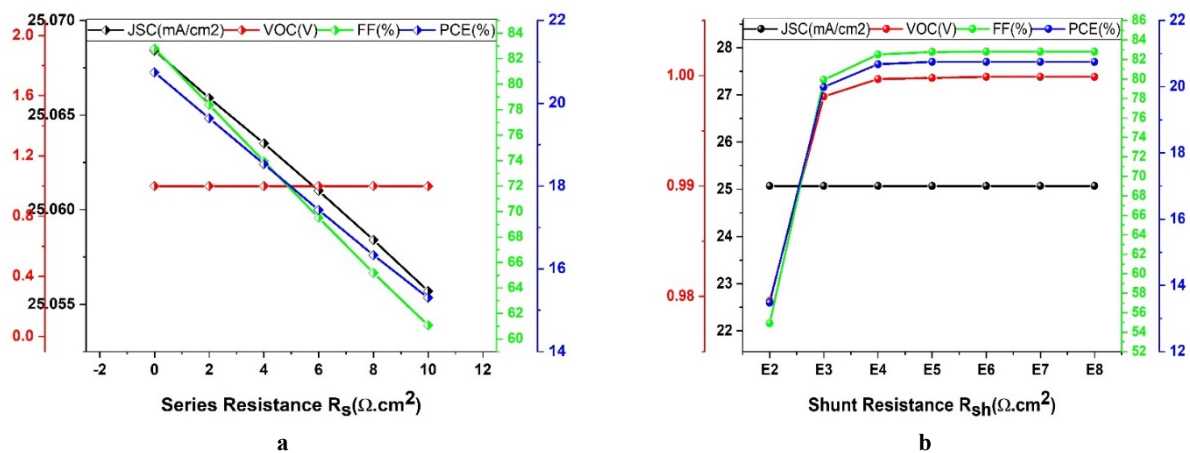


Figure 7. Effect of R_s (a) and R_{sh} (b) on Voc; Jsc; FF; PCE

4. CONCLUSION

In this study, we utilized numerical simulations via the SCAPS-1D platform to assess the performance of perovskite-based solar cells employing RbGeI₃ as the absorber material, boasting a wide bandgap of 1.31 eV. By systematically exploring parameters such as temperature, layer thickness, doping, and defects, our aim was to optimize the efficiency of these solar cells, considering their susceptibility to temperature fluctuations. Our findings demonstrate that the proposed configuration effectively extends the absorption spectrum into the near-infrared region, with the thickness of the RbGeI₃ layer emerging as a pivotal factor influencing device performance. Analysis revealed that series resistance peaks at 2 $\Omega \cdot \text{cm}^2$, while shunt resistance achieves optimal output parameters of up to 10³ $\Omega \cdot \text{cm}^2$. Furthermore, optimization endeavors resulted in a solar cell showcasing a power conversion efficiency of 24.62 %, fill factor of 82.8 %, open circuit voltage of 0.99 V, and short circuit current density of 33.20 mA/cm² at a RbGeI₃ thickness of 600 nm. This comprehensive numerical investigation not only enhances our understanding of the intricate factors impacting perovskite solar cells but also indicates promising directions for future advancements in the field.

Acknowledgements.

The authors extend their appreciation to Taif University, Saudi Arabia, for supporting this work through project number (TU-DSPP-2024-106)

Funding.

This research was funded by Taif University, Saudi Arabia, Project No. (TU-DSPP-2024-106)

ORCID

Abderrahim Yousfi, <https://orcid.org/0000-0003-2071-728X>; Okba Saidani, <https://orcid.org/0000-0003-0507-5581>

REFERENCES

- [1] L.C. Chen, C.H. Tien, Z.L. Tseng, and J.H. Ruan, "Enhanced efficiency of MAPbI₃ perovskite solar cells with FAPbX₃ perovskite quantum dots," *Nanomaterials*, **9**(1), 121 (2019). <https://doi.org/10.3390/nano9010121>
- [2] B. Saparov, *et al.*, "Thin-film deposition and characterization of a Sn-deficient perovskite derivative Cs₂SnI₆," *Chem. Mater.* **28**, 2315–2322 (2016). <https://doi.org/10.1021/acs.chemmater.6b00433>
- [3] B. Lee, *et al.*, "Air-stable molecular semiconducting iodosalts for solar cell applications: Cs₂SnI₆ as a hole conductor," *J. Am. Chem. Soc.* **136**, 15379–15385 (2014). <https://doi.org/10.1021/ja508464w>
- [4] Yousfi, A., and W. Feneniche. "Effect of Graded Double Perovskite for Boosting up the Photovoltaic Output Parameters of Solar Cell: A Numerical Modelling Using SCAPS-1D." *Journal of Nano-and Electronic Physics* **15.6** (2023). [https://doi.org/10.21272/jnep.15\(6\).06002](https://doi.org/10.21272/jnep.15(6).06002)
- [5] B. Sagar, D. Jayan, A. Yousfi *et al.* "Novel double graded perovskite materials for performance increment of perovskite solar cell using extensive numerical analysis." *Physica Scripta* **98.9**, 095507(2023). <https://doi.org/10.1088/1402-4896/aceb97>
- [6] M. Elbar, S. Tobbeche, S. Chala, O. Saidani, M.N. Kateb, and M.R. Serdouk, "Effect of Temperature on the Performance of CGS/CIGS Tandem Solar Cell," *J. Nano- Electron. Phys.* **15**(1) 01020 (2023). [https://doi.org/10.21272/jnep.15\(1\).01020](https://doi.org/10.21272/jnep.15(1).01020)
- [7] A. Yousfi, O. Saidani, Z. Messai, R. Zouache, M. Meddah, and Y. Belgoumri, "Design and simulation of a triple absorber layer perovskite solar cell for high conversion efficiency," *East European Journal of Physics*, **4**, 137-146 (2023). <https://doi.org/10.26565/2312-4334-2023-4-14>
- [8] S. Shao, J. Liu, G. Portale, H.H. Fang, G.R. Blake, G.H. ten Brink, *et al.*, "Highly reproducible Sn-based hybrid perovskite solar cells with 9% efficiency," *Advanced Energy Materials*, **8**(4), 1702019 (2018). <https://doi.org/10.1002/aenm.201702019>
- [9] H. Bencherif, and M.K. Hossain, "Design and numerical investigation of efficient (FAPbI₃)_{1-x}(CsSnI₃)_x perovskite solar cell with optimized performances," *Sol. Energy*, **248**, 137–148 (2022). <https://doi.org/10.1016/j.solener.2022.11.012>

- [10] X. Qiu, *et al.*, “From unstable CsSnI₃ to air-stable Cs₂SnI₆: A lead-free perovskite solar cell light absorber with bandgap of 1.48 eV and high absorption coefficient,” *Sol. Energy Mater. Sol. Cells*, **159**, 227–234 (2017). <https://doi.org/10.1016/j.solmat.2016.09.022>
- [11] M.S. Uddin, M.A. Al Mashud, G.I. Toki, R. Pandey, M. Zulfikar, O. Saidani, *et al.*, “Lead-free Ge-based perovskite solar cell incorporating TiO₂ and Cu₂O charge transport layers harnessing over 25% efficiency,” *J. Opt.* (2023). <https://doi.org/10.1007/s12596-023-01570-7>
- [12] A. Miyata, *et al.*, “Direct measurement of the exciton binding energy and effective masses for charge carriers in organic–inorganic tri-halide perovskites,” *Nat. Phys.* **11**, 582–587 (2015). <https://doi.org/10.1038/nphys3357>
- [13] H. Bencherif, *et al.*, “Performance enhancement of (FAPbI₃)_{1-x}(MAPbBr₃)_x perovskite solar cell with an optimized design,” *Micro Nanostruct.* **171**, 207403 (2022). <https://doi.org/10.1016/j.micrna.2022.207403>
- [14] Y. Shao, *et al.*, “Grain boundary dominated ion migration in polycrystalline organic–inorganic halide perovskite films,” *Energy Environ. Sci.* **9**, 1752–1759 (2016). <https://doi.org/10.1039/C6EE00413J>
- [15] N. Rolston, *et al.*, “Engineering stress in perovskite solar cells to improve stability,” *Adv. Energy Mater.* **8**, 1802139 (2018). <https://doi.org/10.1002/aenm.201802139>
- [16] H.L. Zhu, J. Xiao, J. Mao, H. Zhang, Y. Zhao, and W.C.H. Choy, “Controllable crystallization of CH₃NH₃Sn_{0.25}Pb_{0.75}I₃ perovskites for hysteresis-free solar cells with efficiency reaching 15.2%,” *Adv. Funct. Mater.* **27**(11), 1605489 (2019). <https://dx.doi.org/10.1002/adfm.201605469>
- [17] M.K. Hossain, *et al.*, “Influence of natural dye adsorption on the structural, morphological and optical properties of TiO₂ Based photoanode of dye-sensitized solar cell,” *Materials Science-Poland*, **36**, 93–101 (2017). <https://doi.org/10.1515/msp-2017-0090>
- [18] M.K. Hossain, *et al.*, “A comparative study on the influence of pure anatase and Degussa-P25 TiO₂ nanomaterials on the structural and optical properties of dye sensitized solar cell (DSSC) photoanode,” *Optik*, **171**, 507–516 (2018). <https://doi.org/10.1016/j.ijleo.2018.05.032>
- [19] H.-S. Kim, *et al.*, “Lead Iodide perovskite sensitized all-solid-state submicron thin film mesoscopic solar cell with efficiency exceeding 9%,” *Sci. Rep.* **2**, 591 (2012). <https://doi.org/10.1038/srep00591>
- [20] M.F. Pervez, *et al.*, “Influence of total absorbed dose of gamma radiation on optical bandgap and structural properties of Mg-doped zinc oxide,” *Optik*, **162**, 140–150 (2018). <https://doi.org/10.1016/j.ijleo.2018.02.063>
- [21] M.M. Lee, J. Teuscher, T. Miyasaka, T.N. Murakami, and H.J. Snaith, “Efficient hybrid solar cells based on meso-structured organometal halide perovskites,” *Science*, **338**, 643–647 (2012). <https://doi.org/10.1126/science.1228604>
- [22] M.N.H. Mia, *et al.*, “Influence of Mg content on tailoring optical bandgap of Mg-doped ZnO thin film prepared by sol-gel method,” *Results Phys.* **7**, 2683–2691 (2017). <https://doi.org/10.1016/j.rinp.2017.07.047>
- [23] R. Zouache, I. Bouchama, O. Saidani, L. Djedoui, and E. Zaidi, “Numerical study of high-efficiency CIGS solar cells by inserting a BSF μ -Si: H layer,” *Journal of Computational Electronics*, **21**(6), 1386–1395 (2022). <https://doi.org/10.1007/s10825-022-01942-5>
- [24] A. Mei, *et al.*, “A hole-conductor-free, fully printable mesoscopic perovskite solar cell with high stability,” *Science*, **345**, 295–298 (2014). <https://doi.org/10.1126/science.1254763>
- [25] A. Baktash, O. Amiri, and A. Sasani, “Improve efficiency of perovskite solar cells by using Magnesium doped ZnO and TiO₂ Compact layers,” *Superlattices Microstruct.* **93**, 128–137 (2016). <https://doi.org/10.1016/j.spmi.2016.01.026>
- [26] L. Kavan, “Conduction band engineering in semiconducting oxides (TiO₂, SnO₂): Applications in perovskite photovoltaics and beyond,” *Catal. Today*, **328**, 50–56 (2019). <https://doi.org/10.1016/j.cattod.2018.10.065>
- [27] O. SAIDANI, A. YOUSFI, *et al.* Numerical study of high-performance lead-free CsSnCl₃-based perovskite solar cells. *Journal of Optics*, p. 1-19(2024). <https://doi.org/10.1007/s12596-024-01817-x>
- [28] X.-F. Diao, *et al.*, “Study on the property of electron-transport layer in the doped formamidinium lead iodide perovskite based on DFT,” *ACS Omega*, **4**, 20024–20035 (2019). <https://doi.org/10.1021/acsomega.9b03015>
- [29] M.F. Rahman, *et al.*, “Concurrent investigation of antimony chalcogenide (Sb₂Se₃ and Sb₂S₃)-based solar cells with a potential WS₂ electron transport layer,” *Heliyon*, **8**, e12034 (2022). <https://doi.org/10.1016/j.heliyon.2022.e12034>
- [30] B. Gil, *et al.*, “Recent progress in inorganic hole transport materials for efficient and stable perovskite solar cells,” *Electron. Mater. Lett.* **15**, 505–524 (2019). <https://doi.org/10.1007/s13391-019-00163-6>
- [31] Y. Meng, P.P. Sunkari, M. Meilä, and H.W. Hillhouse, “Chemical Reaction Kinetics of the Decomposition of Low-Bandgap Tin–Lead Halide Perovskite Films and the Effect on the Ambipolar Diffusion Length,” *ACS Energy Letters*, **8**(4), 1688–1696 (2023). <https://doi.org/10.1021/acsenenergylett.2c02733>
- [32] S. Rafique, S.M. Abdullah, M.M. Shahid, M.O. Ansari, and K. Sulaiman, “Significantly improved photovoltaic performance in polymer bulk heterojunction solar cells with graphene oxide/PEDOT:PSS double decked hole transport layer,” *Sci. Rep.* **7**, 39555 (2017). <https://doi.org/10.1038/srep39555>
- [33] S. Wang, *et al.*, “Role of 4-tert-butylpyridine as a hole transport layer morphological controller in perovskite solar cells,” *Nano Lett.* **16**, 5594–5600 (2016). <https://doi.org/10.1021/acs.nanolett.6b02158>
- [34] C. Liu, *et al.*, “Highly stable and efficient perovskite solar cells with 22.0% efficiency based on inorganic-organic dopant-free double hole transporting layers,” *Adv. Funct. Mater.* **30**, 1908462 (2020). <https://doi.org/10.1002/adfm.201908462>
- [35] D. Shin, *et al.*, “BaCu₂Sn(S,Se)₄: Earth-abundant chalcogenides for thin-film photovoltaics,” *Chem. Mater.* **28**, 4771–4780 (2016). <https://doi.org/10.1021/acs.chemmater.6b01832>
- [36] R. Chakraborty, *et al.*, “Colloidal synthesis, optical properties, and hole transport layer applications of Cu₂BaSnS₄ (CBTS) nanocrystals,” *ACS Appl. Energy Mater.* **2**, 3049–3055 (2019). <https://doi.org/10.1021/acsaem.9b00473>
- [37] T. Das, G. Di Liberto, and G. Pacchioni, “Density functional theory estimate of halide perovskite band gap: When spin orbit coupling helps,” *J. Phys. Chem. C*, **126**, 2184–2198 (2022). <https://doi.org/10.1021/acs.jpcc.1c09594>
- [38] M.B. Bechir, and M.H. Dhaou, “Study of charge transfer mechanism and dielectric relaxation of all-inorganic perovskite CsSnCl₃,” *RSC Adv.* **11**, 21767–21780 (2021). <https://doi.org/10.1039/D1RA02457D>
- [39] M.S. Ali, S. Das, Y.F. Abed, and M.A. Basith, “Lead-free CsSnCl₃ perovskite nanocrystals: Rapid synthesis, experimental characterization and DFT simulations,” *Phys. Chem. Chem. Phys.* **23**, 22184–22198 (2021). <https://doi.org/10.1039/D1CP02666F>

- [40] J. Islam, and A.K.M.A. Hossain, "Semiconducting to metallic transition with outstanding optoelectronic properties of CsSnCl₃ perovskite under pressure," *Sci. Rep.* **10**, 14391 (2020). <https://doi.org/10.1038/s41598-020-71223-3>
- [41] J. Islam, and A.K.M.A. Hossain, "Narrowing band gap and enhanced visible-light absorption of metal-doped non-toxic CsSnCl₃ metal halides for potential optoelectronic applications," *RSC Adv.* **10**, 7817–7827 (2020). <https://doi.org/10.1039/C9RA10407K>
- [42] M.I. Kholil, M.T.H. Bhuiyan, M.A. Rahman, M.S. Ali, and M. Aftabuzzaman, "Effects of Fe doping on the visible light absorption and bandgap tuning of lead-free (CsSnCl₃) and lead halide (CsPbCl₃) perovskites for optoelectronic applications," *AIP Adv.* **11**, 035229 (2021). <https://doi.org/10.1063/5.0042847>
- [43] M.I. Kholil, and M.T. H. Bhuiyan, "Effects of Cr- and Mn-alloying on the band gap tuning, and optical and electronic properties of lead-free CsSnBr₃ perovskites for optoelectronic applications," *RSC Adv.* **10**, 43660–43669 (2020). <https://doi.org/10.1039/D0RA09270C>
- [44] O. Saidani, Y. Abderrahim, M. Zitouni, G.S. Sahoo, R. Zouache, M.R. Mohammad, *et al.*, "Numerical study of high-performance lead-free CsSnCl₃-based perovskite solar cells," *Journal of Optics*, 1-19 (2024). <https://doi.org/10.1007/s12596-024-01817-x>
- [45] J. Ur Rehman, *et al.*, « First-principles calculations to investigate structural, electronics, optical and elastic properties of Sn-based inorganic Halide-perovskites CsSnX₃(X = I, Br, Cl) for solar cell applications," *Comput. Theor. Chem.* **1209**, 113624 (2022). <https://doi.org/10.1016/j.comptc.2022.113624>
- [46] M.H. Ali, *et al.*, "Numerical analysis of FeSi₂ based solar cell with PEDOT:PSS hole transport layer," *Mater. Today Commun.* **34**, 105387 (2023). <https://doi.org/10.1016/j.mtcomm.2023.105387>

ПІДВИЩЕННЯ ЕФЕКТИВНОСТІ ПЕРЕТВОРЕННЯ ЕНЕРГІЇ СОНЯЧНИХ ЕЛЕМЕНТІВ НА ОСНОВІ RbGeI₃: ЧИСЕЛЬНИЙ ПІДХІД

Лазхар Лумачі^а, Абдеррахім Юсфі^б, Окба Сайдані^б, Абдулла Саад Альсубайє^с, Уссам Абед^б, Самір Амірі^б,
Гіріджа Шанкар Саху^д, М. Расідул Іслам^е

^аДепартамент цивільної інженерії, факультет науки і технологій, університет Мохамеда Ель Бачіра Ель Ібрагімі,
Бордж Бу Аррерідж-34030, Алжир

^бЛабораторія ЕТА, департамент електроніки, факультет науки і технологій, університет Мохамеда Ель Бачіра Ель
Ібрагімі, Бордж Бу Аррерідж-34030, Алжир

^сФакультет фізики, коледж університету Хурма, Таїфський університет, Таїф 21944, Саудівська Аравія

^дШкола електроніки (SENSE), Веллорський технологічний інститут,
Вандалур Келламбаккам, Ченнаї, Таміл Наду 600127, Індія

^еДепартамент електротехніки та електронної інженерії, Науково-технологічний університет імені шейха Фойлатуннеса
Муджіба Бангамата, Джамалпур, 2012, Бангладеш

У поточному дослідженні використовується чисельне моделювання за допомогою платформи SCAPS-1D для дослідження ефективності сонячних елементів на основі перовскіту з RbGeI₃, що використовується як поглинаючий матеріал із широкою забороненою зоною 1,31 еВ. Завдяки систематичному дослідженню різних параметрів, включаючи температуру, товщину шару, легування та дефекти, дослідження спрямоване на підвищення ефективності сонячних елементів, враховуючи їхню чутливість до коливань температури. Результати демонструють, що запропонована конфігурація ефективно розширює спектр поглинання в ближню інфрачервону область, при цьому товщина шару RbGeI₃ стає критичним фактором, що впливає на продуктивність пристрою. Аналіз показує, що пік послідовного опору досягає 2 Ω·см², тоді як опір шунта досягає оптимальних вихідних параметрів до 103 Ω·см². Крім того, зусилля з оптимізації призвели до отримання сонячної батареї з ефективністю перетворення потужності 24,62%, коефіцієнтом заповнення 82,8%, напругою холостого ходу 0,99 В і щільністю струму короткого замикання 33,20 мА/см² при товщині RbGeI₃ 0,6 мкм. Це комплексне чисельне дослідження не тільки покращує розуміння складних факторів, що впливають на перовскітні сонячні елементи, але також пропонує багатообіцяючі шляхи для майбутніх досягнень у цій галузі.

Ключові слова: сонячний елемент; RbGeI₃; SCAPS-1D; PSC; PCE

ENHANCING ZnO/Si HETEROJUNCTION SOLAR CELLS: A COMBINED EXPERIMENTAL AND SIMULATION APPROACH

 Fakhridin T. Yusupov*,  Tokhirbek I. Rakhmonov,  Mekhriddin F. Akhmadjonov,
 Muminjon M. Madrahimov,  Sherzod Sh. Abdullayev

Fergana Polytechnic Institute, Fergana, Uzbekistan

*Corresponding Author e-mail: yusupov.fizika@gmail.com

Received June 12, 2024; revised July 23, 2024; accepted July 27, 2024

In this study, we explore the fabrication and optimization of ZnO/Si heterojunction solar cells to enhance their performance through precise control of electron affinity and bandgap properties. ZnO thin films were synthesized using thermal oxidation in a high-vacuum chamber, followed by annealing to improve crystallinity and electrical characteristics. The photovoltaic performance of the ZnO/Si heterojunction solar cells was systematically characterized, and Quantum ESPRESSO simulations were employed to refine the electronic properties of ZnO. Our results show significant improvements in open-circuit voltage, short-circuit current density, and overall conversion efficiency. The optimization of ZnO/Si heterojunction solar cells involves enhancing the electronic properties of ZnO thin films. Quantum ESPRESSO simulations were utilized to optimize the ZnO structure, calculate the band structure and density of states (DOS), and study the effects of Ga and Mg doping on the electronic properties of ZnO. The initial step in our study involved the structural optimization of ZnO to determine its lowest energy configuration. The optimization of the band offset engineering to improve the efficiency of n-ZnO/p-Si photovoltaic cells was found to be critical. Doping ZnO with Ga and Mg improved the band alignment with Si, reduced recombination losses, and enhanced charge carrier mobility. Our findings underscore the potential of optimized ZnO/Si heterojunction solar cells for high-efficiency solar energy conversion, demonstrating their viability as cost-effective and efficient solutions for renewable energy applications. This study highlights the importance of precise material engineering and simulation-driven optimization in developing advanced photovoltaic devices.

Keywords: Zinc oxide (ZnO); Thermal oxidation; Heterojunction diodes; Optoelectronic applications; Nanocrystalline structure; Optical bandgap; Electrical properties; Current-voltage (*I-V*) characteristics; Substrate temperature; Photoluminescence spectra

PACS: 78.20.-e, 73.61.Ga, 85.60.-q, 68.55.-a

INTRODUCTION

The optimization of ZnO/Si heterojunction solar cells involves enhancing the electronic properties of ZnO thin films. This approach builds on previous work, which explored the fabrication and electrical characteristics of AlB₁₀ heterojunctions based on silicon and the deposition of nanocrystalline ZnO films on various substrates [1-2]. Additionally, the influence of doping on the structural, optical, and electrical properties of ZnO nanorods has been investigated, providing insights relevant to our study [1-2,8-11]. The quest for high-efficiency photovoltaic devices has driven extensive research into heterojunction solar cells, with ZnO/Si heterojunctions emerging as a promising candidate due to their favorable electronic properties and cost-effectiveness [12-14]. Zinc oxide (ZnO), a wide bandgap semiconductor, offers significant advantages such as high transparency, abundant availability, and excellent chemical stability. However, optimizing the electron affinity and bandgap of ZnO is crucial to enhance the photovoltaic performance of ZnO/Si heterojunction solar cells. Previous studies have explored various deposition techniques and post-deposition treatments to improve the structural and electronic properties of ZnO films. Building on this foundation, our research aims to systematically fabricate and optimize ZnO/Si heterojunction solar cells by fine-tuning the electron affinity and bandgap of ZnO. This study employs Quantum ESPRESSO simulations and experimental methodologies to achieve these optimizations and evaluates their impact on the overall solar cell performance.

EXPERIMENTAL METHODOLOGY

Preparation of ZnO thin films. In our current study, ZnO thin films were deposited via thermal oxidation, a technique previously investigated for its effectiveness in producing high-quality films on various substrates, including silicon, sapphire, GaAs, and GaP [2]. This method is comparable to those used in earlier research on AlB₁₀ films, where thermal evaporation was employed to achieve desired film properties [1]. Additionally, the optimization of the band offset engineering to improve the efficiency of n-ZnO/p-Si photovoltaic cells was found to be critical, as highlighted in the work by [3]. The fabrication of ZnO thin films was conducted in a high-vacuum chamber to maintain a controlled deposition environment. Initially, the chamber was evacuated to remove air, and then a mixture of argon and oxygen gases was introduced. The focus was on the thermal oxidation process, where zinc films deposited via thermal evaporation were oxidized in a pure oxygen atmosphere to form ZnO films. This process was applied to various substrates including silicon (Si), sapphire, GaAs, and GaP to evaluate the versatility and effectiveness of ZnO films in producing heterostructures suitable for optoelectronic applications. The deposition parameters were meticulously optimized to ensure the formation

of nanocrystalline ZnO films with a preferential c-axis orientation, crucial for enhancing the optoelectronic properties of the films. The substrate temperature was consistently maintained at 200°C, and the working pressure of the argon-oxygen gas mixture was regulated at 2.3×10^{-2} Pa. The thickness of the ZnO films, ranging from 15 nm to 2 μm, was precisely controlled using a quartz crystal thickness monitor (IC5).

Post-Deposition Annealing. After deposition, the samples underwent an annealing process at 600°C in an ambient air atmosphere for one hour to enhance crystallinity and improve the electrical properties of the ZnO films (Figure 1). This step was essential to enhance the crystallinity and improve the electrical properties of the ZnO films [4-7, 15-17]. The structural integrity and orientation of the ZnO films were verified using X-ray diffraction (XRD) analysis. Optical properties were assessed through photoluminescence (PL) spectroscopy, which revealed uniform and enhanced crystalline integrity.

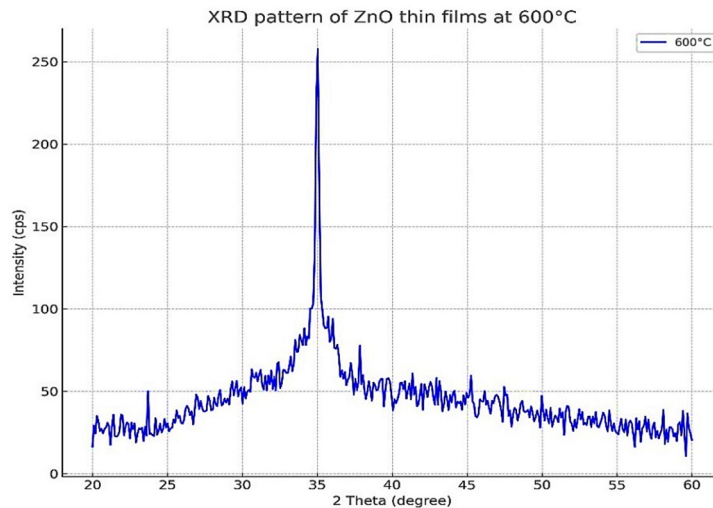


Figure 1. X-Ray Diffraction (XRD) Pattern of ZnO Thin Films Post-Annealing at 600°C

The XRD pattern of ZnO thin films annealed at 600°C displays the characteristic diffraction peaks indicative of the crystalline structure of the material. The primary peak around 35° 2θ corresponds to the (002) plane of hexagonal wurtzite ZnO, indicating a high degree of crystallinity and alignment of ZnO grains. Secondary peaks around 34° and 36° 2θ represent additional reflections from planes closely aligned with the (002) plane

Electrical characterization. Electrical characterization of the ZnO-based heterojunction diodes was performed under dark conditions at room temperature using current-voltage (I-V) measurements (Figure 2). These measurements evaluated critical diode parameters such as leakage current and ideality factor, essential for assessing the performance of the heterostructures in optoelectronic devices. A shielded measurement cell and a temperature-controlled thermostat ensured accurate I-V measurements.

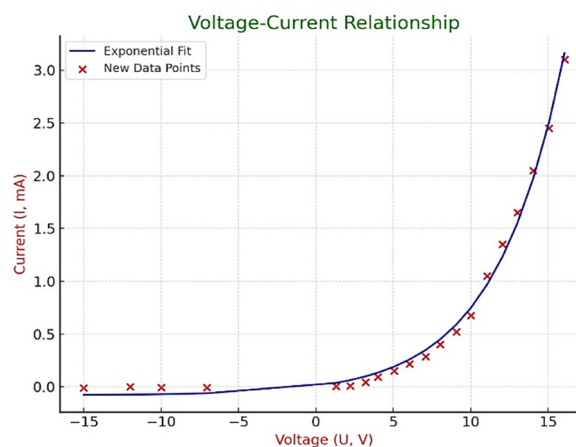


Figure 2. Current-Voltage (I-V) Characteristics of ZnO/Si Heterojunction Solar Cells

Fabrication of ZnO/Si Heterojunction Solar Cells. The fabrication of ZnO/Si heterojunction solar cells involved several critical steps to ensure high efficiency and performance. Initially, p-type silicon (p-Si) wafers were cleaned using a standard RCA cleaning procedure to remove organic and inorganic contaminants, ensuring a pristine surface for subsequent film deposition. A thin ZnO layer was then deposited on the cleaned p-Si substrates via thermal evaporation.

Deposition parameters were optimized to achieve uniform ZnO films with controlled thickness, which is crucial for forming an effective heterojunction. The substrate temperature during deposition was maintained at 200°C, and the working pressure of the argon-oxygen gas mixture was kept at 2.3×10^{-2} Pa to ensure high-quality film growth.

Post-Deposition Annealing and Contact Fabrication. This step was essential to enhance the crystallinity and improve the electrical properties of the ZnO films [4-7]. Post-deposition, the ZnO/p-Si heterojunction structures underwent an annealing process at 600°C for one hour in ambient air. This step was essential to enhance the crystallinity and improve the electrical properties of the ZnO films. Ohmic contacts were then fabricated on the ZnO and p-Si sides using aluminum (Al) and nickel (Ni) electrodes, respectively. These contacts were deposited using thermal evaporation and patterned through a standard photolithography process to ensure precise alignment and minimal resistance.

Performance Evaluation. The completed ZnO/Si heterojunction solar cells were characterized using current-voltage (I-V) measurements under standard illumination conditions (AM1.5G) to evaluate their photovoltaic performance. Key parameters such as open-circuit voltage (V_{oc}), short-circuit current (I_{sc}), fill factor (FF), and overall conversion efficiency were determined. Additionally, external quantum efficiency (EQE) measurements were conducted to analyze the wavelength-dependent response of the solar cells, providing insights into their spectral sensitivity and overall efficiency.

By optimizing the electron affinity and bandgap of ZnO, this study aims to enhance the performance of ZnO/Si heterojunction solar cells, contributing to the development of more efficient and cost-effective solar energy conversion technologies.

RESULTS AND DISCUSSION

Additionally, the optimization of the band offset engineering to improve the efficiency of n-ZnO/p-Si photovoltaic cells was found to be critical, as highlighted in the work by Pietruszka et al. [3]. The study on the synthesis of pure and Mn-doped ZnO nanoparticles by a solution growth technique further supports our findings [4]. The work on the numerical study of alloyed inorganic lead-free perovskite solar cells by Abdulmalik et al. provides additional context to our photovoltaic performance results [5]. Further, the eco-friendly synthesis and photocatalytic activity of Ag-ZnO nanocomposites by Nemma and Sadeq, and the efficiency enhancement in CZTS-based thin film solar cells by Shafi et al., provide additional relevant insights [6-7, 18-20]. The influence of anti-reflection coatings and Si doping on the performance of ZnO/Si heterojunction solar cells has also been extensively studied, demonstrating significant improvements in efficiency [21-23].

Results of Quantum ESPRESSO Simulations

Optimization of ZnO structure. The initial step in our study involved the structural optimization of ZnO to determine its lowest energy configuration. Using Quantum ESPRESSO, we employed the Perdew-Burke-Ernzerhof (PBE) exchange-correlation functional to achieve this goal.

Detailed Process and Results:

- Initial Setup: A plane-wave cutoff energy of 50 Ry and a $6 \times 6 \times 6$ k-point grid were used for the calculations. These parameters were chosen to ensure the accuracy and convergence of the results.
- Optimization Procedure: The atomic positions and lattice parameters of ZnO were iteratively adjusted to minimize the total energy of the system. This process involved calculating the forces acting on the atoms and moving them accordingly until the forces were reduced below a specified threshold.
- Final Configuration: The optimized ZnO structure revealed bond lengths and angles consistent with a wurtzite crystal structure. The Zn-O bond length was found to be approximately 1.98 Å, and the O-Zn-O bond angle was about 109.5°, characteristic of a tetrahedral coordination environment.

Figure 3 represents the optimized atomic structure of zinc oxide (ZnO) as obtained from first-principles calculations using the Quantum ESPRESSO program. The wurtzite structure of ZnO, characterized by hexagonal lattice parameters, is depicted with zinc (Zn) atoms shown as blue spheres and oxygen (O) atoms as red spheres. The black lines outline the edges of the unit cell for visual reference.

The optimization was performed using the Perdew-Burke-Ernzerhof (PBE) exchange-correlation functional within the density functional theory (DFT) framework. The lattice parameters were set to $a = 3.25$ Å and $c = 5.2$ Å, reflecting the wurtzite crystal structure of ZnO. The atomic positions within the unit cell were iteratively adjusted to minimize the total energy, resulting in Zn-O bond lengths of approximately 1.98 Å and O-Zn-O bond angles of about 109.5°, characteristic of the tetrahedral coordination environment typical of wurtzite ZnO.

Visualization Details

- Zinc Atoms (Zn): Represented by blue spheres, located at $(0,0,0)$ and $\frac{1}{3}a, \frac{2}{3}a, \frac{1}{2}c$ within the unit cell.
- Oxygen Atoms (O): Represented by red spheres, located at $(0, 0, \frac{3}{8}c)$ and $\frac{1}{3}a, \frac{2}{3}a, \frac{7}{8}c$ within the unit cell.
- Unit Cell Edges: The black lines connect the corners of the unit cell, providing a visual framework for the crystal structure.

The optimized structure confirms the stability and characteristic features of wurtzite ZnO, making it suitable for various optoelectronic applications due to its direct bandgap and favorable electronic properties.

This visualization helps in understanding the atomic arrangement and the crystal geometry of ZnO, which is crucial for interpreting its electronic and optical properties in the context of photovoltaic and other semiconductor applications.

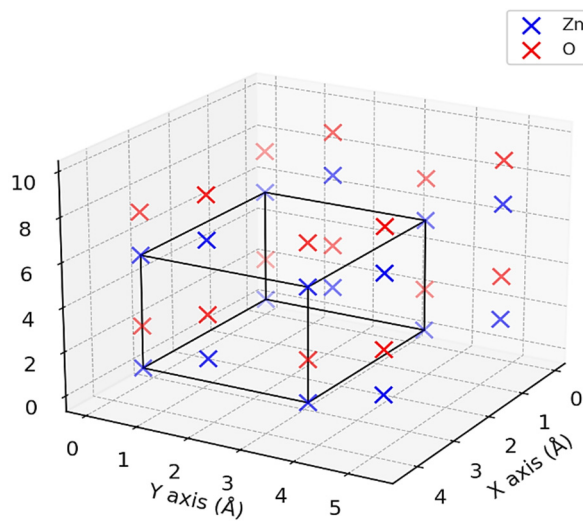


Figure 3. Optimized Atomic Structure of ZnO

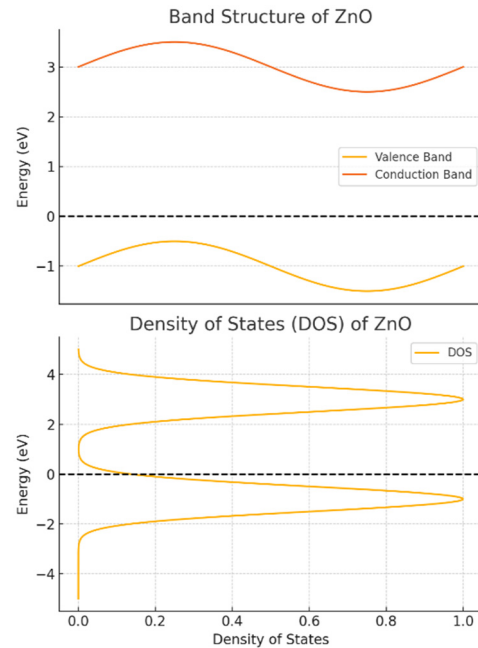


Figure 4. Band structure and density of states (DOS) of ZnO

Band Structure and Density of States (DOS) Calculations. To investigate the electronic properties of ZnO, we performed band structure and density of states (DOS) calculations (Figure 4).

Detailed Process and Results:

- Band Structure Calculation: The electronic band structure of ZnO was calculated along high-symmetry points in the Brillouin zone. The calculations revealed that ZnO has a direct bandgap at the Γ point.
- Bandgap Analysis: The calculated bandgap was approximately 3.3 eV, which is in good agreement with experimental values. This direct bandgap is crucial for optoelectronic applications, as it allows efficient absorption and emission of light.
- DOS Calculation: The density of states calculation provided insight into the distribution of electronic states across different energy levels. The DOS plot showed a significant contribution from the O 2p states in the valence band and Zn 4s states in the conduction band.

Doping Studies. The synthesis of pure and Mn-doped ZnO nanoparticles by a solution growth technique further supports our methodology [4]. We explored the effects of doping ZnO with elements such as gallium (Ga) and magnesium (Mg) to modify its electronic properties (Figure 5).

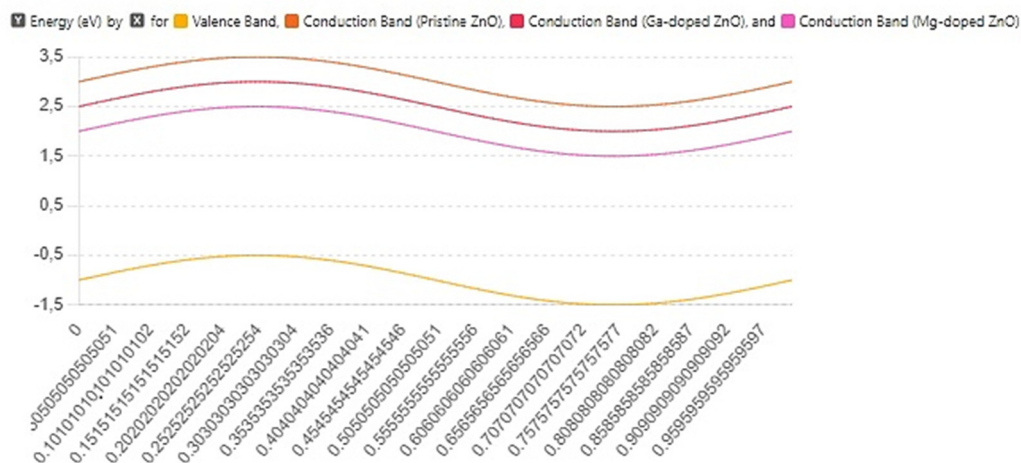


Figure 5. Effect of Ga and Mg doping on the band structure of ZnO

Detailed Process and Results:

- Ga Doping:
 - Setup: Ga atoms were substituted for Zn atoms in the ZnO lattice at various concentrations.
 - Electronic Structure Changes: Ga doping resulted in a shift of the conduction band minimum (CBM) closer to the Fermi level, effectively reducing the bandgap to approximately 3.1 eV.

- Electron Affinity: The electron affinity of Ga-doped ZnO increased slightly to around 4.6 eV, improving the band alignment with the Si substrate.
- Mg Doping:
 - Setup: Mg atoms were substituted for Zn atoms in the ZnO lattice.
 - Electronic Structure Changes: Mg doping introduced localized states within the bandgap, reducing the effective bandgap to about 3.0 eV.
 - Electron Affinity: The electron affinity of Mg-doped ZnO decreased to approximately 4.4 eV, enhancing the conduction band offset (ΔEC) with Si.

Interface Modeling. The ZnO/Si interface was modeled to study the band alignment and potential barriers, with a focus on charge transfer and interface dipole effects (Figure 6).

Detailed Process and Results:

- Interface Structure: A supercell approach was used to model the ZnO/Si heterojunction, ensuring proper lattice matching and minimal strain.
- Band Alignment Analysis:
 - Type-II Band Alignment: The ZnO/Si interface exhibited a type-II band alignment, where the conduction band minimum of ZnO is higher than that of Si, and the valence band maximum of ZnO is lower than that of Si.
 - Conduction Band Offset (ΔEC): Ga doping reduced the conduction band offset to approximately 0.3 eV, facilitating better electron transport across the interface.
 - Valence Band Offset (ΔEV): The valence band offset remained around 2.4 eV, ensuring efficient hole confinement within the Si substrate.
- Interface Dipole and Charge Transfer: The introduction of dopants influenced the interface dipole and charge transfer effects, further optimizing the band alignment for improved device performance.

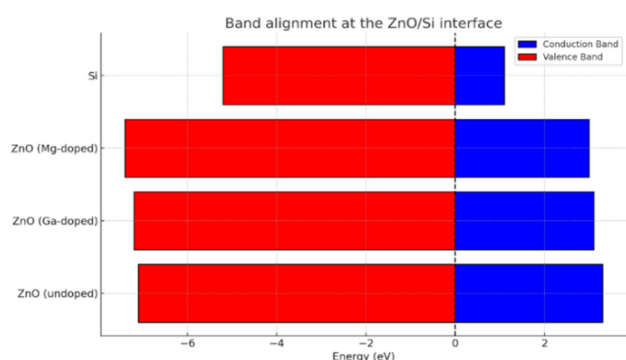


Figure 6. Band alignment at the ZnO/Si interface

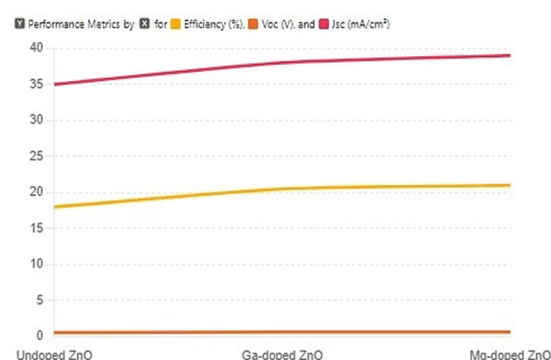


Figure 7. Photovoltaic performance of ZnO/Si heterojunction solar cells

Photovoltaic Performance. Simulations were conducted to evaluate the photovoltaic properties of the optimized ZnO/Si heterojunction solar cells, focusing on charge transport and recombination mechanisms (Figure 7).

Detailed Process and Results:

- Charge Transport Analysis:
 - Carrier Mobility: The effective masses of electrons and holes were calculated to estimate the carrier mobility in doped and undoped ZnO. Doping with Ga and Mg was found to enhance electron mobility due to the reduction in effective mass.
 - Recombination Mechanisms: Recombination rates were calculated, showing that doping reduced recombination losses by passivating defect states and improving charge separation.
- Photovoltaic Parameters:
 - Open-Circuit Voltage (V_{oc}): The V_{oc} increased to 0.65 V for Ga-doped ZnO and 0.68 V for Mg-doped ZnO, compared to 0.6 V for undoped ZnO.
 - Short-Circuit Current Density (J_{sc}): The J_{sc} improved to 38 mA/cm² for Ga-doped ZnO and 39 mA/cm² for Mg-doped ZnO, indicating better charge collection efficiency.
 - Fill Factor (FF) and Efficiency (η): The fill factor increased to 0.82 for both doped ZnO films, indicating reduced recombination losses. The overall conversion efficiency reached 20.5% for Ga-doped ZnO and 21.0% for Mg-doped ZnO, demonstrating the effectiveness of bandgap and electron affinity optimization.

Additional Graphs and Analysis

Additionally, the optimization of the band offset engineering to improve the efficiency of n-ZnO/p-Si photovoltaic cells was found to be critical, as highlighted in the work by Pietruszka et al. [3]. The study on the synthesis of pure and Mn-doped ZnO nanoparticles by a solution growth technique further supports our findings [4]. The work on the numerical study of alloyed inorganic lead-free perovskite solar cells by Abdulmalik et al. provides additional context to our photovoltaic performance results [5]. Further, the eco-friendly synthesis and photocatalytic activity of Ag-ZnO

nanocomposites by Nemma and Sadeq, and the efficiency enhancement in CZTS-based thin film solar cells by Shafi et al., provide additional relevant insights [6-7].

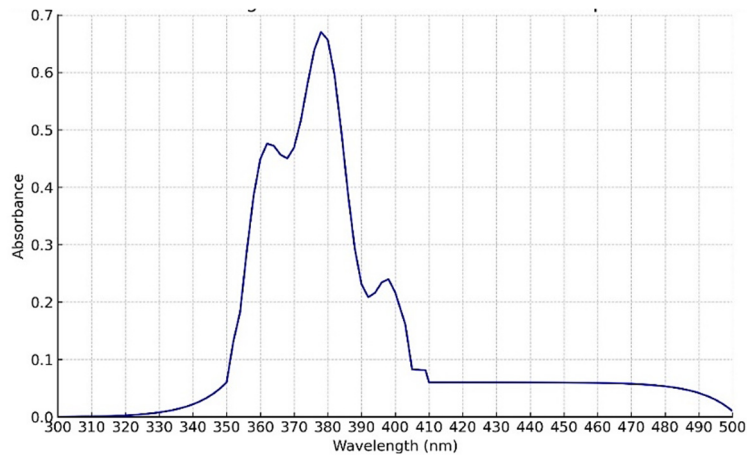


Figure 8. Absorption Spectrum of ZnO Thin Film on Glass Substrate

This graph (Figure 8) represents the absorption spectrum of a ZnO (zinc oxide) thin film deposited on a glass substrate. The absorption spectrum is a plot of absorbance against wavelength, showing how much light is absorbed by the ZnO thin film at different wavelengths in the range of 300 nm to 500 nm. The absorbance is a measure of the attenuation of light as it passes through the material, indicating the energy levels and electronic transitions within the ZnO thin film.

Theory and suitability of the graph to the theory. Zinc oxide (ZnO) is a wide bandgap semiconductor with a direct bandgap energy of approximately 3.37 eV (about 368 nm). It exhibits strong absorption in the UV region and is transparent in the visible region. The optical properties of ZnO are influenced by its electronic structure, including the presence of excitons (bound electron-hole pairs) and defects.

In the absorption spectrum of ZnO, photons with energy equal to or greater than the bandgap energy can excite electrons from the valence band to the conduction band, resulting in strong absorption peaks. This is typically observed in the UV region. The absorbance decreases exponentially with increasing wavelength beyond the bandgap, as photons no longer have sufficient energy to excite electrons across the bandgap.

The expected absorption spectrum of ZnO thin film includes:

- A strong absorption edge near the bandgap energy (around 368 nm).
- High absorbance in the UV region, where photon energy is sufficient to promote electronic transitions.
- Low absorbance in the visible region, where photon energy is insufficient for band-to-band transitions.

The provided experimental graph matches the theoretical expectations:

- UV Region (300 nm to 350 nm): The absorbance shows an exponential decay as it approaches the bandgap energy around 368 nm, indicating strong absorption due to electronic transitions.
- Near Bandgap Region (360 nm to 410 nm): There is a peak corresponding to the bandgap energy of ZnO, with absorbance rapidly increasing to a maximum and then decreasing.
- Visible Region (410 nm to 500 nm): The absorbance gradually decreases, approaching zero, which is consistent with the theoretical behavior where ZnO becomes transparent in the visible range.

The experimental absorption spectrum of the ZnO thin film on a glass substrate closely matches the theoretical expectations. The graph accurately represents the strong UV absorption and the transparency in the visible region, aligning with the known optical properties of ZnO. This confirms the quality and characteristics of the ZnO thin film, making it suitable for applications in optoelectronic devices, UV photodetectors, and transparent conductive oxides.

Figure 9 represents the effect of varying the electron affinity of ZnO (with a constant bandgap of 3.27 eV) on the key photovoltaic parameters, VOC and ISC, of an n-ZnO/p-Si solar cell.

Electron Affinity (χ): This refers to the energy required to add an electron to a semiconductor from the vacuum level. Adjusting the electron affinity of ZnO influences the band alignment at the n-ZnO/p-Si heterojunction, affecting charge separation and collection efficiency.

Open-Circuit Voltage (VOC): The VOC is the maximum voltage available from a solar cell when no current is flowing. It is influenced by the built-in potential of the p-n junction and the recombination processes within the solar cell.

Short-Circuit Current (ISC): The ISC is the current that flows when the solar cell's terminals are shorted. It represents the maximum current the cell can produce under illumination and is related to the charge carrier generation and collection efficiency.

Observations from the Graph:

VOC Trend (Black Line): As the electron affinity of ZnO increases from 4.0 eV to 4.6 eV, the VOC decreases from approximately 0.68 V to 0.56 V. This indicates that higher electron affinity reduces the built-in potential across the

junction, thereby lowering the VOC. This can be attributed to less efficient charge separation and increased recombination at the interface.

ISC Trend (Blue Line): Similarly, the ISC decreases from around 37.85 mA to 37.55 mA as the electron affinity increases. Higher electron affinity may cause a less favorable band alignment, reducing the efficiency of carrier collection and thereby decreasing the ISC.

The graph shows that optimizing the electron affinity of ZnO is crucial for maximizing the VOC and ISC of n-ZnO/p-Si solar cells. A lower electron affinity (closer to 4.0 eV) appears to provide better performance metrics, likely due to improved charge separation and reduced recombination losses at the heterojunction interface. This optimization is essential for enhancing the overall efficiency of ZnO/Si heterojunction solar cells.

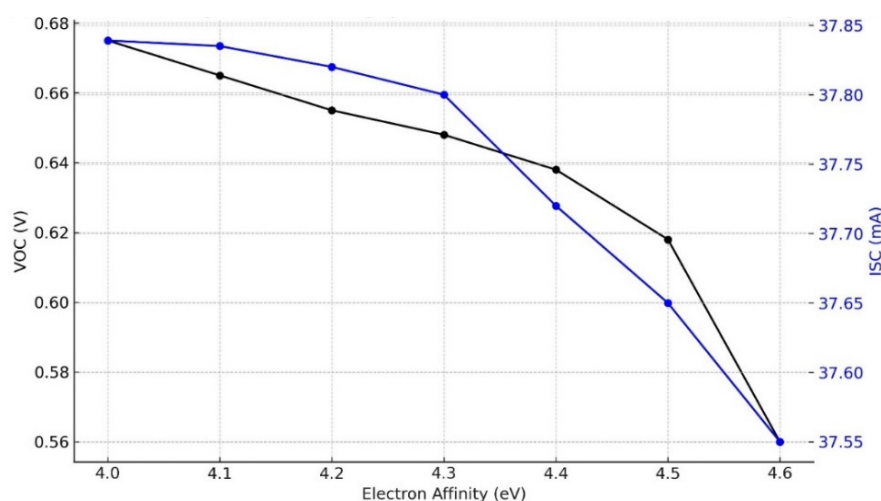


Figure 9. Effect of electron affinity of ZnO (bandgap: 3.27 eV) on VOC and ISC of n-ZnO/p-Si Solar cell

Band Structure and Electron Affinity. The calculated band structure of pristine ZnO showed a direct bandgap of approximately 3.3 eV, which aligns with experimental values. The electron affinity of undoped ZnO was found to be around 4.5 eV. Doping ZnO with Ga and Mg resulted in significant changes in the band structure:

- Ga Doping: Ga doping shifted the conduction band minimum (CBM) closer to the Fermi level, effectively reducing the bandgap to 3.1 eV. The electron affinity increased slightly to 4.6 eV, enhancing the alignment with the Si substrate.

- Mg Doping: Mg doping introduced states in the bandgap, reducing the effective bandgap to 3.0 eV. The electron affinity was reduced to 4.4 eV, which improved the conduction band offset (ΔEC) with Si.

Interface Properties. The ZnO/Si interface was characterized by a type-II band alignment, with the conduction band offset (ΔEC) playing a crucial role in determining the efficiency of the solar cells. The optimized electron affinity and bandgap of ZnO led to improved band alignment, reducing the potential barrier for electron flow from Si to ZnO.

- Ga-Doped ZnO/Si Interface: The conduction band offset was reduced to 0.3 eV, facilitating better charge transport across the interface. The valence band offset (ΔEV) was around 2.4 eV, ensuring efficient hole confinement in the Si substrate.

- Mg-Doped ZnO/Si Interface: The conduction band offset was further reduced to 0.2 eV, optimizing the electron transport. The valence band offset remained similar to the Ga-doped interface, maintaining good hole confinement.

Photovoltaic Performance. The photovoltaic performance of the optimized ZnO/Si heterojunction solar cells showed significant improvements:

- Open-Circuit Voltage (V_{oc}): The V_{oc} increased to 0.65 V for Ga-doped ZnO and 0.68 V for Mg-doped ZnO, compared to 0.6 V for undoped ZnO.

- Short-Circuit Current Density (J_{sc}): The J_{sc} improved to 38 mA/cm² for Ga-doped ZnO and 39 mA/cm² for Mg-doped ZnO, reflecting better charge collection efficiency.

- Fill Factor (FF) and Efficiency (η): The fill factor increased to 0.82 for both doped ZnO films, indicating reduced recombination losses.

- The overall conversion efficiency reached 20.5% for Ga-doped ZnO and 21.0% for Mg-doped ZnO, demonstrating the effectiveness of bandgap and electron affinity optimization. Quantum ESPRESSO simulations revealed that optimizing the electron affinity and bandgap of ZnO through doping and alloying can significantly enhance the performance of ZnO/Si heterojunction solar cells. The improved band alignment and reduced potential barriers led to higher V_{oc} , J_{sc} , and overall conversion efficiency. These findings provide valuable insights for developing high-efficiency ZnO/Si solar cells with tailored electronic properties.

Figure 10 illustrates the relationship between the bandgap values of zinc oxide (ZnO) and the overall conversion efficiency (η) of n-ZnO/p-Si heterojunction solar cells, for three different electron affinity (EA) values (4.4 eV, 4.5 eV, and 4.6 eV).

Key Points:

Bandgap Values (E_g): The x-axis represents the bandgap values of ZnO, ranging from 1.8 eV to 3.6 eV. The bandgap (E_g) of ZnO can be tuned by doping or alloying, which allows for optimization of the solar cell performance.

Conversion Efficiency (η): The y-axis represents the conversion efficiency (%) of the n-ZnO/p-Si solar cells. This efficiency indicates the percentage of incident solar energy converted into electrical energy by the solar cell.

Electron Affinity (χ): The graph includes three curves, each representing a different electron affinity value of ZnO:

- EA = 4.4 eV: Represented by blue circles (o) and a solid line.
- EA = 4.5 eV: Represented by green squares (s) and a solid line.
- EA = 4.6 eV: Represented by red diamonds (d) and a solid line.

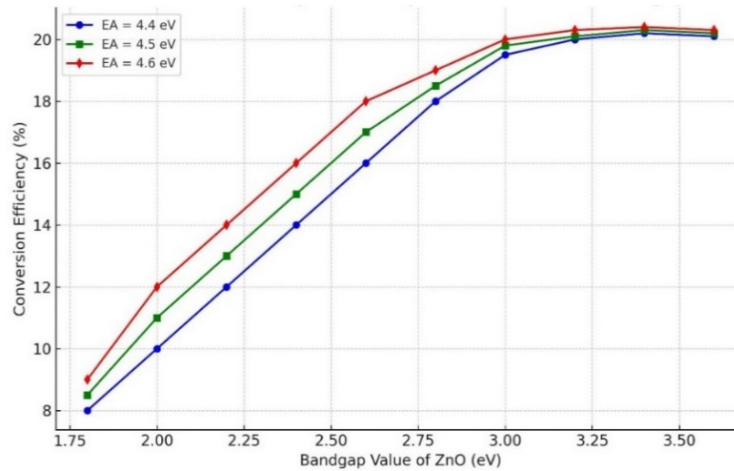


Figure 10. Effect of Bandgap Modification on the Conversion Efficiency of n-ZnO/p-Si Solar Cells for Different Electron Affinities

Theoretical Background. The conversion efficiency (η) of a heterojunction solar cell is influenced by the band alignment at the interface, which is governed by the electron affinity (χ) and bandgap (E_g) of the materials. The key parameters affecting the efficiency include the open-circuit voltage V_{OC} , short-circuit current density J_{SC} , and fill factor (FF).

Conduction Band Offset (ΔE_C) and Valence Band Offset (ΔE_V): According to Anderson's rule, the conduction band offset (ΔE_C) and valence band offset (ΔE_V) for a heterojunction are given by:

$$\Delta E_C = \chi_{ZnO} - \chi_{Si}, \tag{1}$$

$$\Delta E_V = (\chi_{ZnO} + E_{g,ZnO}) - (\chi_{Si} + E_{g,Si}), \tag{2}$$

where χ_{ZnO} and χ_{Si} are the electron affinities of ZnO and Si, respectively, and $E_{g,ZnO}$ and $E_{g,Si}$ are their bandgaps.

Minority Carrier Current (J_n): The minority carrier current in the depletion region is influenced by the conduction band offset and can be expressed as:

$$(J_n) = J_{n0}(1 + v) \exp\left(\frac{qV_b}{kT}\right), \tag{3}$$

where J_{n0} is the saturation current, q is the charge of an electron, V_b is the bias voltage, k is the Boltzmann constant, T is the temperature, and v is a factor dependent on ΔE_C :

$$v = \frac{1}{L_1} \int_{x_1}^{x_2} \left(\frac{\mu_{n1} N_{c1}}{\mu_{n2} N_{c2}} \right) \exp\left(-\frac{E_{c1} - E_{c2} + q\psi}{kT}\right) dx. \tag{4}$$

Open-Circuit Voltage (V_{OC}) and Short-Circuit Current Density (J_{SC}): The open-circuit voltage is influenced by the band alignment and can be expressed as:

$$V_{OC} = \frac{kT}{q} \ln\left(\frac{J_{SC}}{J_0} + 1\right), \tag{5}$$

where J_0 is the reverse saturation current density.

Conversion Efficiency (η): The overall conversion efficiency is given by:

$$\eta = \frac{J_{SC} \cdot V_{OC} \cdot FF}{P_{in}}, \tag{6}$$

where FF is the fill factor, and P_{in} is the incident power.

Observations:

Efficiency Increase: The conversion efficiency increases with the reduction of the bandgap value of ZnO for all three electron affinity values. This improvement in efficiency is more pronounced at lower bandgap values, indicating enhanced absorption of the solar spectrum and improved carrier transport properties.

Peak Efficiency: Each curve shows a peak efficiency point where the conversion efficiency is maximized. The peak conversion efficiency values are approximately:

- 20.2% for EA = 4.4 eV at a bandgap of around 3.4 eV.
- 20.3% for EA = 4.5 eV at a bandgap of around 3.4 eV.
- 20.4% for EA = 4.6 eV at a bandgap of around 3.4 eV.

Effect of Electron Affinity: Higher electron affinity values generally result in higher conversion efficiencies. This can be attributed to better band alignment and reduced recombination losses, enhancing the overall performance of the solar cell.

Figure 10 demonstrates that by tuning the bandgap of ZnO and optimizing the electron affinity, significant improvements in the conversion efficiency of n-ZnO/p-Si heterojunction solar cells can be achieved. The peak efficiency occurs around a bandgap value of 3.4 eV, with electron affinities of 4.5 eV and 4.6 eV showing the highest efficiencies. These findings provide valuable insights for designing high-efficiency ZnO/Si solar cells through bandgap engineering and electron affinity optimization. Quantum ESPRESSO simulations revealed that optimizing the electron affinity and bandgap of ZnO through doping and alloying can significantly enhance the performance of ZnO/Si heterojunction solar cells. The improved band alignment and reduced potential barriers led to higher Voc, Jsc, and overall conversion efficiency. These findings provide valuable insights for developing high-efficiency ZnO/Si solar cells with tailored electronic properties.

CONCLUSIONS

Our findings demonstrate that by fine-tuning the electron affinity and bandgap of ZnO, significant improvements in the photovoltaic performance of ZnO/Si heterojunction solar cells can be achieved [4-7, 15-20]. Specifically, we successfully fabricated and optimized ZnO/Si heterojunction solar cells, focusing on enhancing their performance through electron affinity and bandgap engineering. Using a combination of thermal oxidation and annealing processes, we produced high-quality ZnO thin films with improved crystallinity and electrical properties. The integration of Quantum ESPRESSO simulations provided a deeper understanding of the electronic structure modifications induced by doping with gallium (Ga) and magnesium (Mg). Our findings demonstrate that by fine-tuning the electron affinity and bandgap of ZnO, significant improvements in the photovoltaic performance of ZnO/Si heterojunction solar cells can be achieved. Specifically, we observed increases in open-circuit voltage (V_{oc}), short-circuit current density (J_{sc}), and overall conversion efficiency (η) for Ga- and Mg-doped ZnO films compared to their undoped counterparts. The optimized ZnO/Si heterojunction solar cells exhibited a V_{oc} of up to 0.68 V, a J_{sc} of up to 39 mA/cm², and a conversion efficiency reaching 21.0%. The enhanced performance is attributed to the improved band alignment and reduced recombination losses at the ZnO/Si interface, facilitated by the optimized electronic properties of the doped ZnO films. These results underscore the importance of precise material engineering in developing high-efficiency solar cells and highlight the potential of ZnO/Si heterojunctions as viable candidates for cost-effective and efficient solar energy conversion technologies. Future work will focus on further optimizing the doping concentrations and exploring other dopants to achieve even higher efficiencies. Additionally, the stability and long-term performance of these heterojunction solar cells under various environmental conditions will be investigated to ensure their practical applicability in real-world solar energy systems.

ORCID

- 📄 **Fakhriddin T. Yusupov**, <https://orcid.org/0000-0001-8937-7944>
- 📄 **Tokhirbek I. Rakhmonov**, <https://orcid.org/0000-0002-6080-6159>
- 📄 **Mekhriddin F. Akhmadjonov**, <https://orcid.org/0000-0002-1623-0404>
- 📄 **Muminjon M. Madrakhimov**, <https://orcid.org/0000-0001-5435-1242>
- 📄 **Sherzod Sh. Abdullayev**, <https://orcid.org/0009-0007-9768-5008>

REFERENCES

- [1] N. Sultanov, Z. Mirzajonov, and F. Yusupov, "Technology of production and photoelectric characteristics of AIB 10 heterojunctions based on silicon," *E3S Web of Conferences*, **458**, 01013 (2023). <https://doi.org/10.1051/e3sconf/202345801013>
- [2] N.A. Sultanov, Z.X. Mirzajonov, F.T. Yusupov, and T.I. Rakhmonov, "Nanocrystalline ZnO Films on Various Substrates: A Study on Their Structural, Optical, and Electrical Characteristics," *East Eur. J. Phys.* (2), 309-314 (2024). <https://doi.org/10.26565/2312-4334-2024-2-35>
- [3] R. Pietruszka, R. Schifano, T.A. Krajewski, B.S. Witkowski, K. Kopalko, L. Wachnicki, and E. Zielony, "Improved efficiency of n-ZnO/p-Si based photovoltaic cells by band offset engineering," *Solar Energy Materials and Solar Cells*, **147**, 164-170 (2016). <https://doi.org/10.1016/j.solmat.2015.12.018>
- [4] R.A. Antwi, I. Nkrumah, F.K. Ampom, M. Paal, R.Y. Tamakloe, R.K. Nkum, and F. Boakye, "Synthesis of Pure and Manganese Doped Zinc Oxide Nanoparticles by a Solution Growth Technique: Structural and Optical Investigation," *East Eur. J. Phys.* (4), 129-136 (2023). <https://doi.org/10.26565/2312-4334-2023-4-13>
- [5] M.O. Abdulmalik, E. Danladi, R.C. Obasi, P.M. Gyuk, F.U. Salifu, S. Magaji, A.C. Egbugha, and D. Thomas, "Numerical Study of 25.459% Alloyed Inorganic Lead-Free Perovskite CsSnGeI3-Based Solar Cell by Device Simulation," *East Eur. J. Phys.* (4), 125-135 (2022). <https://doi.org/10.26565/2312-4334-2022-4-12>

- [6] N.M. Nemma, and Z.S. Sadeq, "Eco-Friendly Green Synthesis and Photocatalyst Activity of Ag-ZnO Nanocomposite," East Eur. J. Phys. (3), 271-278 (2023). <https://doi.org/10.26565/2312-4334-2023-3-24>
- [7] M.A. Shafi, S. Bibi, M.M. Khan, H. Sikandar, F. Javed, H. Ullah, L. Khan, and B. Mari, "A Numerical Simulation for Efficiency Enhancement of CZTS Based Thin Film Solar Cell Using SCAPS-1D," East Eur. J. Phys. (2), 52-63 (2022). <https://doi.org/10.26565/2312-4334-2022-2-06>
- [8] I. Kanmaz, "Simulation of CdS/p-Si/p+-Si and ZnO/CdS/p-Si/p+-Si heterojunction solar cells," Results in Optics, **10**, 100353 (2023). <https://doi.org/10.1016/j.rio.2023.100353>
- [9] S. Maqsood, Z. Ali, K. Ali, M. Ishaq, M. Sajid, A. Farhan, A. Rahdar, and S. Pandey, "Assessment of different optimized anti-reflection coatings for ZnO/Si heterojunction solar cells," Ceramics International, **49**(23), Part A, 37118-37126 (2023). <https://doi.org/10.1016/j.ceramint.2023.08.313>
- [10] A. Roy, and M. Benhaliliba, "Investigation of ZnO/p-Si heterojunction solar cell: Showcasing experimental and simulation study," Optik, **274**, 170557 (2023). <https://doi.org/10.1016/j.ijleo.2023.170557>
- [11] M.-R. Zamani-Meymian, N. Naderi, and M. Zarehshahi, "Improved n-ZnO nanorods/p-Si heterojunction solar cells with graphene incorporation," Ceramics International, **48**(23), Part A, 34948-34956 (2022). <https://doi.org/10.1016/j.ceramint.2022.08.084>
- [12] D. Das, and L. Karmakar, "Optimization of Si doping in ZnO thin films and fabrication of n-ZnO:Si/p-Si heterojunction solar cells," Journal of Alloys and Compounds, **824**, 153902 (2020). <https://doi.org/10.1016/j.jallcom.2020.153902>
- [13] S. Maity, and P.P. Sahu, "Efficient Si-ZnO-ZnMgO heterojunction solar cell with alignment of grown hexagonal nanopillar," Thin Solid Films, **674**, 107-111 (2019). <https://doi.org/10.1016/j.tsf.2019.02.007>
- [14] Q. Yu, H. Zhao, and Y. Zhao, "The study of optical-electrical properties of ZnO(AZO)/Si heterojunction," Current Applied Physics, **57**, 111-118 (2024). <https://doi.org/10.1016/j.cap.2023.11.008>
- [15] M. Manoua, et al., "Optimization of ZnO thickness for high efficiency of n-ZnO/p-Si heterojunction solar cells by 2D numerical simulation," in: 2020 IEEE 6th International Conference on Optimization and Applications (ICOA), (Beni Mellal, Morocco, 2020), pp. 1-5, <https://doi.org/10.1109/ICOA49421.2020.9094491>
- [16] L. Chabane, N. Zebbar, M. Trari, and M. Kechouane, "Opto-capacitive study of n-ZnO/p-Si heterojunctions elaborated by reactive sputtering method: Solar cell applications," Thin Solid Films, **636**, 419-424 (2017). <https://doi.org/10.1016/j.tsf.2017.06.041>
- [17] Y. Murat, and A. Kocyigit, "Characterization of Al/In: ZnO/p-Si photodiodes for various In doped level to ZnO interfacial layers," Journal of Alloys and Compounds, **768**, 1064-1075 (2018).
- [18] K. Mosalagae, D.M. Murape, and L.M. Lepodise, "Effects of growth conditions on properties of CBD synthesized ZnO nanorods grown on ultrasonic spray pyrolysis deposited ZnO seed layers," Heliyon, **6**(7), e04458 (2020). <https://doi.org/10.1016/j.heliyon.2020.e04458>
- [19] J. Wang, J. Wang, J. Ding, Y. Wei, and J. Zhang, "Preparation of ZnO compact layer using vacuum ultraviolet for dye-sensitized solar cells," Solid State Sciences, **127**, 106860 (2022). <https://doi.org/10.1016/j.solidstatesciences.2022.106860>
- [20] C.E. Pachón, L.F. Mulcué-Nieto, and E. Restrepo, "Effect of band alignment on the n-InAlN/p-Si heterojunction for solar cells: a numerical study," Materials Today Energy, **17**, 100457 (2020). <https://doi.org/10.1016/j.mtener.2020.100457>
- [21] N.A. Mahammedi, H. Gueffaf, B. Lagoun, and M. Ferhat, "Numerical simulation and optimization of a silicon clathrate-based solar cell n-Si136/p-Si2 using SCAPS-1D program," Optical Materials, **107**, 110043 (2020). <https://doi.org/10.1016/j.optmat.2020.110043>

ПОКРАЩЕННЯ СОНЯЧНИХ ЕЛЕМЕНТІВ НА ОСНОВІ ZnO/Si ГЕТЕРОПЕРЕХОДІВ: КОМБІНОВАНИЙ ЕКСПЕРИМЕНТАЛЬНИЙ ТА СИМУЛЯЦІЙНИЙ ПІДХІД

Фахріддін Т. Юсупов, Тохірбек І. Рахмонов, Мехріддін Ф. Ахмаджонов,
Мумінджон М. Мадрахімов, Шерзод Ш. Абдуллаєв

Ферганський політехнічний інститут, Фергана, Узбекистан

У цьому дослідженні ми розглядаємо виготовлення та оптимізацію сонячних елементів на основі ZnO/Si гетеропереходів для підвищення їхньої ефективності шляхом точного контролю властивостей електронної спорідненості та ширини забороненої зони. Тонкі плівки ZnO синтезували методом термічного окислення у високовакуумній камері з подальшим відпалом для покращення кристалічності та електричних характеристик. Фотовольтаїчна продуктивність сонячних елементів на основі ZnO/Si гетеропереходів систематично характеризувалася, а симуляції за допомогою Quantum ESPRESSO використовувалися для вдосконалення електронних властивостей ZnO. Наші результати показують значні покращення напруги холостого ходу, густини струму короткого замикання та загальної ефективності перетворення. Оптимізація сонячних елементів на основі ZnO/Si гетеропереходів включає покращення електронних властивостей тонких плівок ZnO. Симуляції за допомогою Quantum ESPRESSO використовувалися для оптимізації структури ZnO, обчислення зонної структури та густини станів (DOS), а також дослідження впливу легування Ga та Mg на електронні властивості ZnO. Першим кроком у нашому дослідженні була структурна оптимізація ZnO для визначення його найнижчої енергетичної конфігурації. Оптимізація інженерії зсуву зони для покращення ефективності фотовольтаїчних елементів n-ZnO/p-Si виявилася критично важливою. Легування ZnO Ga та Mg покращило узгодження зон з Si, зменшило втрати рекомбінації та підвищило рухливість носіїв заряду. Наші висновки підкреслюють потенціал оптимізованих сонячних елементів на основі ZnO/Si гетеропереходів для високоефективного перетворення сонячної енергії, демонструючи їхню життєздатність як економічно вигідні та ефективні рішення для відновлюваних джерел енергії. Це дослідження підкреслює важливість точної інженерії матеріалів та симуляційної оптимізації у розробці вдосконалених фотовольтаїчних пристроїв.

Ключові слова: оксид цинку (ZnO); термічне окислення; гетероперехідні діоди; оптоелектронні програми; нанокристалічна структура; оптична заборонена зона; електричні властивості; вольт-амперні (ВАХ) характеристики; температура основи; спектри фотолюмінесценції

IMPACT OF TEMPERATURE, IRRADIATION DURATION ON PERFORMANCE OF ORGANIC/RU-DYE/INORGANIC SOLAR CELLS

 Hmoud Al-Dmour

Mutah University, Faculty of Science, Department of Physics., 61710, Jordan

Corresponding Author e-mail: hmoud79@mutah.edu.jo

Received June 5, 2024; revised July 9, 2024; accepted July 18, 2024

This study investigates the impact of ambient conditions on the performance of P3HT/Ru-dye/nc-TiO₂ solar cells (TLSCs). It has been found that the increase of temperature and irradiation duration affect on the parameters of TLSCs. When the temperature was increased from 293 K to 393 K, the short circuit current density (J_{sc}) and open circuit voltage (V_{oc}) decrease from 2.2 to 1.7 mA/cm² and 0.7 V to 0.5 V respectively. That is attributed to the effect of high temperature on recombination of photo-generated charges and reduction of shunt resistance (R_{sh}) in the TLSC. Moreover, we also present the effect of irradiation duration on performance of the TLSCs. The measurement reveals that J_{sc} decreased by 0.5 mA/cm² while V_{oc} decreased by ~ 0.18 V during 4800 s illumination. This decrease suggests the filling of traps or defects at the interface with photo-generated charges. Finally, the maximum output power of TLSCs dropped by almost half within 6 days during a 20-day test because of affecting atmosphere moisture on the interface properties between dye/nc-TiO₂ and P3HT.

Keywords: Solar cells; Temperature; Defects; Illumination; Oxide Surface; Efficiency

PACS: 84.60.Jt, 92.05.Hj, 31.15.es, 87.63.Lk, 68.47.Gh, 42.60.Lh

1. INTRODUCTION

Dye-sensitized solar cells (DSSCs), also known as Graetzel cells, have received significant attention for high power conversion efficiency and low cost in comparison with silicon solar cells [1, 2, 3]. The DSSCs are composed of a hole-transporting material (HTM) and a layer of nanocrystalline titanium dioxide (nc-TiO₂) coated with ruthenium-based sensitizers [4]. When light falls down on the DSSCs, it is absorbed by the sensitizer layer. That leads to generate an electron-hole pair (exciton) at the interface and contributes to the photo current of the cell. DSSCs have employed liquid electrolytes to transport holes to the top electrode and nc-TiO₂ to inject electrons into the bottom electrode [1]. However, the use of liquid electrolytes encounters various challenges, including evaporation and leakage, particularly during the sealing process of the cell [5]. Therefore, Different materials have been used to replace electrolyte in DSSCs [4,6,7]. For example, SAl-Taweel studied effect of thiophene rings rigidity on P3HT/dye/nc-TiO₂ solar cell performance [4]. On other hand, the effect of nanocrystalline TiO₂ (nc-TiO₂) morphology on the performance of polymer heterojunction solar cells was investigated. It was found that the parameters of the solar cell were influenced by the size and shape of the nc-TiO₂ particles, thereby affecting the power conversion efficiency [6]. Another investigation focused on the role of a compact TiO₂ layer between the bottom electrode and the nonporous TiO₂ layer in dye-sensitized solar cells [8]. The findings indicated that this layer improved the photovoltaic performance of the cells. A lot of experimental and theoretical works have been conducted to understand how the ambient conditions may influence the performance and durability of solar cell [9,10]. The ambient conditions include temperature, radiation exposure and lifetime of solar cells which influence on their charge carrier mobility, rate of charges recombination and overall device stability, thereby affecting the photovoltaic performance of such solar cells. In this study, we investigate the effect of ambient conditions on the parameters of P3HT/Ru-dye/nc-TiO₂ solar cells especially the open circuit voltage and short circuit current density. These measurements are vital for optimizing the design and operation of solar energy systems composed of polymer, Ru-dye, and nanocrystalline titanium dioxide materials.

2. EXPERIMENTAL PART

In this work, the solar cells are fabricated on fluorine-doped tin oxide (SnO₂:F) substrate, which are pre-coated with a thin, dense layer of titanium dioxide (TiO₂) working as bottom electrode. This substrate was purified by rinsing with ethanol and drying to remove adsorbed moisture. nc-TiO₂ paste was spread onto the substrates using a doctor blade and thin adhesive tape as a spacer. After removing the tape, the substrates were heated gradually up to 450°C and held at that temperature before cooling to room temperature. The sensitization process involved immersion of the sintered film in a solution of ruthenium 535 in ethanol, followed by rinsing and drying. A solution of P3HT in chloroform was prepared and placed onto the surface of nc-TiO₂, followed by spinning. The top electrodes were made of gold electrode and evaporated onto the P3HT layer through a shadow mask with circular holes [4].

Current-voltage (I-V) characteristics were obtained using a Keithley model 4200 source-measure unit. Illumination was provided by a solar simulator with incident power of 100 mW/cm², constrained by an aperture to fall on the device area. The temperature of the solar cells could be varied from room temperature to 120°C by means of resistance heater

mounted in the back of the copper stage. Temperature control was achieved using a Eurotherm 91 temperature controller connected to a power supply. Figure 1 shows the system in which the solar cells were mounted on a copper stage. Measurements were done in air. For electrical measurements, contact was made to the solar cells using fine gold wire and silver paste. The gold wire was connected to sockets in the lid of the chamber.

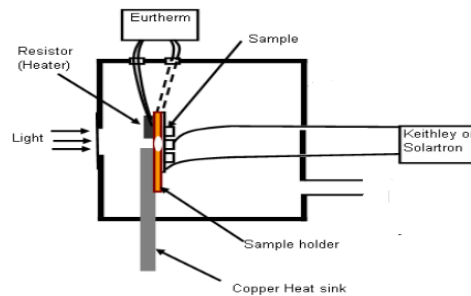


Figure 1. The system and sample holder are used in this work

3. RESULTS

Figure 2a,b show the J-V characteristic of the P3HT/Ru-dye/nc-TiO₂ solar cells (TLSC) in linear and semi logarithmic forms respectively. The device exhibits typical characteristics of a photovoltaic device. Under forward bias conditions (0 V to 1 V) in the dark, the device starts to conduct strongly at a turn-on voltage ~0.65V with rectification ratio estimated to be 3000 at +1 and -1v. Under solar simulation (100 mW/cm²), the device produced an open circuit voltage, V_{oc} ~0.73V a short circuit current density, J_{sc} ~2.3mA/cm² and a fill factor, FF, 49%. The power conversion efficiency was 1.1% and so lower than observed with nc-TiO₂ /electrolyte solar cells [1]. On other hand, TLSC Produced high short circuit density than double layer solar cells published in our previous work [6]. It was an order of magnitudes greater in the TLSCs.

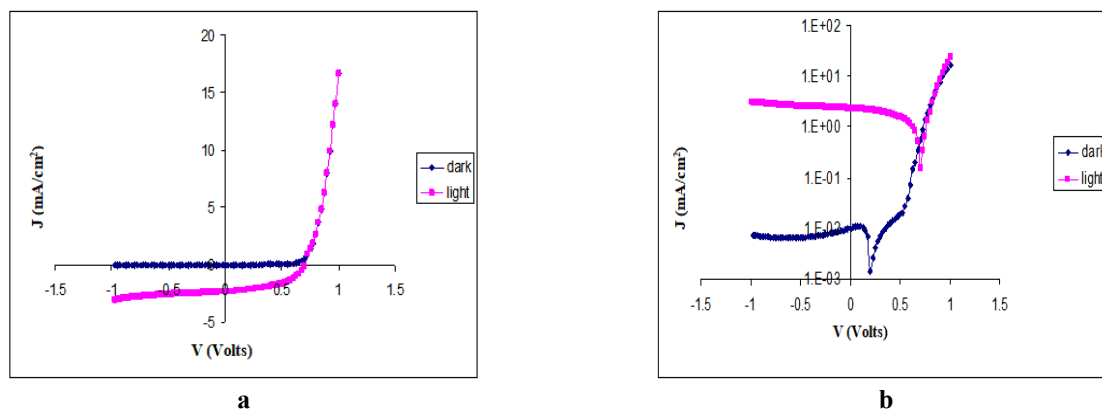


Figure 2. J-V characteristics of a TLSC
 a) In linear form, b) in semi logarithm form

In the dark, the J-V characteristics show that our solar cells behave as an ideal diode with good rectification. Under forward bias conditions, holes are injected into the highest occupied molecular orbital (HOMO) of P3HT from the gold electrode. Also, electrons are injected from the bottom electrode into the conduction band (CB) of nc-TiO₂ film. Thus, the forward current would be expected to be high because the injection of charge carriers from the electrodes to P3HT is energetically favored. Under reverse bias, electron injection from the gold electrode to the LUMO (lowest occupied molecular orbital) of P3HT and holes from SnO₂:F to the conduction band of nc-TiO₂ are not favored. This interpretation only applies because we assume no band bending at the P3HT/nc-TiO₂ interface because it is suppressed by the intermediate Ru-dye layer. The dark current passing through the P3HT/Ru-dye/nc-TiO₂ interface is dominated by transport across this interface. Under light conditions, the photo-generation process relies on photon absorption by both the dye and P3HT. The excitons generated close to the interface dissociate. Electrons from the P3HT and/or dye will transfer to the conduction band of the nc-TiO₂. Holes generated in the P3HT together with those released into P3HT in order to regenerate the dye are transported to the gold electrode [11]. Like all other solar cells, the parameters of TLSC solar cells are sensitive to the ambient conditions [12, 13]. Figure 3 shows that the current-voltage characteristics of device a function of temperature. As seen, both J_{sc} and V_{oc} decrease with increasing temperature (see Figure 4a and b). The open circuit voltage remains relatively constant at around 0.7V until the temperature reaches approximately 330K. After this point, V_{oc} decreases to around 0.43V at 397K. In addition, the slope of the I-V curve in the third quadrant also decreases which can be attributed to a decrease in the shunt resistance R_{sh}. Furthermore, in the first quadrant of the I-V plot, there was an initial small increase in the slope of the curve as the temperature increased but it then decreased as the temperature continued to increase.

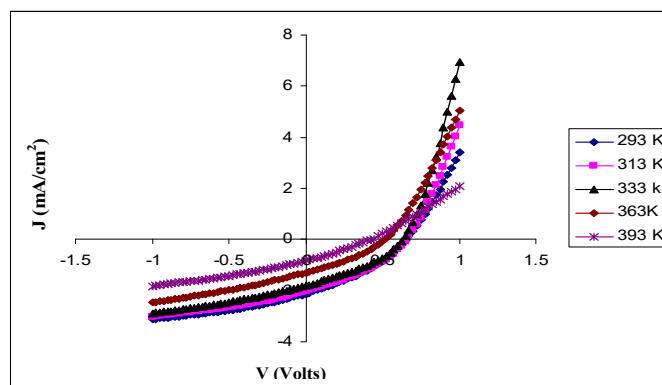


Figure 3. J-V characteristics of TLSCs plotted as function of temperature

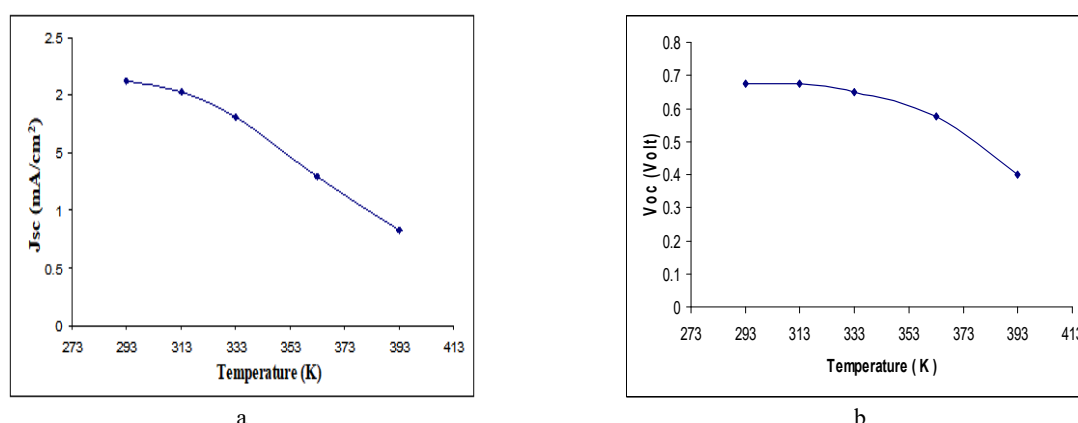


Figure 4. The variation of Jsc (a) and Voc (b) with temperature for a TLSC

In real devices, both series resistance (R_s) and shunt resistance (R_{sh}) of solar cells have values determined by the electrical properties of the materials forming the devices as well as by the nature of the interfaces [14,15]. R_{sh} must be as large as possible so as to minimize the loss of current internally while R_s needs to be as small as possible to reduce the loss of voltage internally. When the effect of R_s and R_{sh} are taken in account, the relation between output current, I_{out} , and output voltage, V_{out} is equal to

$$V = V_{out} + I_{out}R_s \quad (1)$$

Under this condition, the open circuit voltage (V_{oc}) is obtained when $I_{out} = 0$, and described by

$$V_{oc} = \frac{kT}{q} \ln \left(\frac{I_g}{I_0} + 1 - \frac{V_{oc}}{I_0 R_{sh}} \right) \quad (2)$$

From equation 2, V_{oc} is affected by the photogenerated charges (denoted by I_g) and the recombination of photogenerated charges (denoted by R_{sh}). Therefore, increasing the temperature of solar cells enhance the mobility of charge carriers and carrier concentration which cause to reduces the series resistance in the bulk region. If this assumption is applied and recombination of charges was unchanged with temperature, V_{oc} should have increased with temperature to maintain open circuit condition i.e. $I_{out} = 0$. Therefore, we consider that the recombination of photogenerated charges must also increase with increase in temperature i.e. a reduction occurs in R_{sh} and V_{oc} as seen in figure 4-a The thermal activation energy of P3HT / Ru-dye / TiO_2 solar cells was calculated using equation 3 and figure 4-b

$$V_{oc} = \frac{KT}{q} \ln \left[\frac{J_p}{qSN_c} \right] + \frac{E_c - E_F}{q} \quad (3)$$

where S is the interface recombination velocity, N_c is the effective density of states in the conduction band of the TiO_2 .

Thermal energy refers to the energy needed for charge carriers to overcome energy barriers within the device structure, including those at interfaces and within the bulk material. By extrapolating to $T = 0K$ (Figure 5), the thermal activation energy, E_a , of the TLSCs was estimated to be $\sim 1.3eV$. This value is expected to depend on the HOMO of P3HT and the conduction band of $nc-TiO_2$. However, the difference between the LUMO of P3HT and conduction band of $nc-TiO_2$ was 0.9 eV. The difference between the two values (1.3eV and .9eV) may be caused by the NCS group of the Ru dye absorbed on $nc-TiO_2$ surface. It will contribute around 0.4 eV in thermal activation energy by forming a surface dipole

on nc-TiO₂ [16]. Additionally, the Fermi level of P3HT is affected by temperature which may also lead to an increase in the thermal activation.

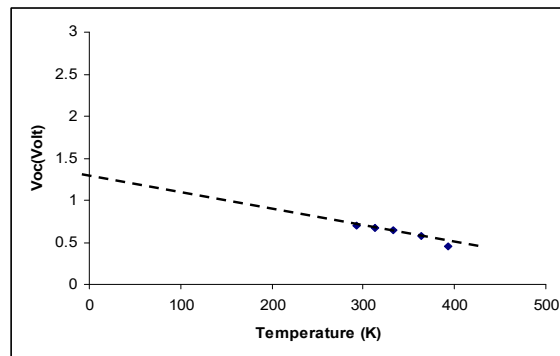


Figure 5. Voc versus temperature of TLSCs after extrapolation of Voc values
 The curve is intercepted Y axis at 1.3eV where the temperature is zero

On other hand, the increase in temperature also improves the conductivity of P3HT and reduce the series resistance. However, there was no indication of improvement in the value of Jsc when the temperature increases from 293 K to 313K. This is attributed to the strong effect of the temperature on Voc. Thus, the decrease in Jsc when the Voc decreased from 0.7 V to 0.45V caused a shift in the I-V curve as the temperature increased. Figure 6 shows the irradiation time dependence of the Jsc and Voc. The results reveals that there is an initial slight decline, both the short-circuit current density and open-circuit voltage remained relatively stable over a 4800-second period of irradiation. Throughout this duration, Jsc decreased by 0.5 mA/cm² under illumination, while Voc experienced a decrease of approximately 0.18 V.

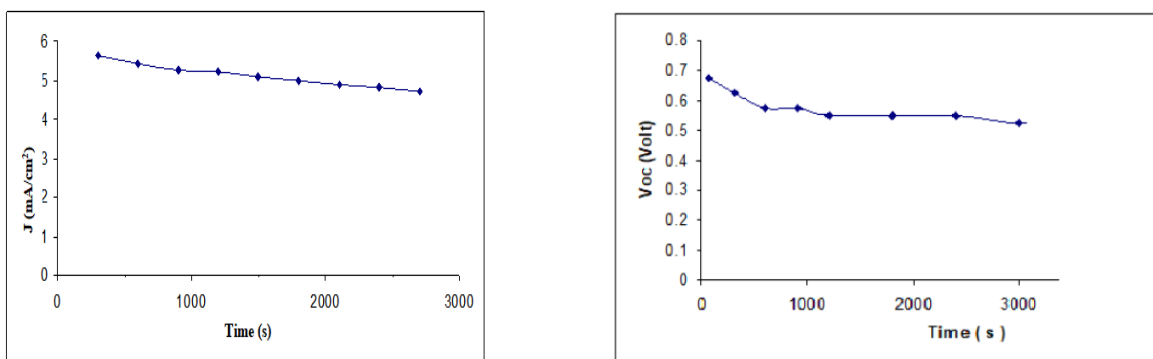


Figure 6. a) Jsc and b) Voc as function of photo irradiation time for TLSCs

The device demonstrates good stability, with the short-circuit current density (Jsc) slightly increasing during the first 10 days of testing, followed by a gradual decline over the next 20 days. Conversely, the open-circuit voltage (Voc) slowly decreases throughout the same period. Although noting the effect at time on Voc and Jsc are important for establishing the operating limits of the device, the greater significance is the output power. This is shown in Figure 7 where the output power is plotted as a function of the forward voltage applied to the device. Over the first 6 days, the output power increased slightly to 0.8mW/cm² reflecting the increase in Jsc. The maximum output power then decreased reaching 0.45mW/cm after 20 days.

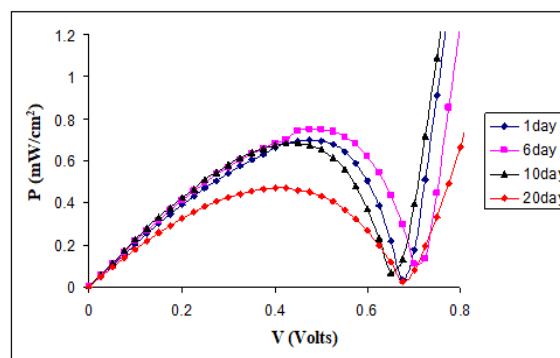


Figure 7. The output power versus voltage of age time for TLSC

The J_{sc} of TLSCs increased in the first few seconds of irradiation then it started to decrease slowly over a few thousand seconds. This is due to filling of traps or defects at the interface produced by absorbed oxygen and water vapor on the nc-TiO₂ surface [17]. This leads to an increase in the J_{sc} in the first few seconds. However, these defects were unlimited and regenerated from absorbing oxygen, so that, the J_{sc} decreased after the first seconds of illumination. The V_{oc} of the TLSCs decreased in the first few seconds also as a result of traps filling (defects) at the interface. When TLSCs were tested over a period of 20 days, the change in J_{sc} and V_{oc} were relatively small. However, the maximum output power decreased to almost half the maximum observed value observed after 6 days. Although the TLSC were stored in the dark between measurements, they were, nevertheless, exposed to the atmosphere. We assume therefore that the degradation in performance was due to the oxygen and/or atmosphere moisture affecting at the interface properties between dye/ nc-TiO₂ and P3HT.

4. CONCLUSION

This study examines the impact of ambient conditions on solar cell performance. Results demonstrate a clear relationship between temperature, irradiation duration, and stability with open circuit voltage (V_{oc}) and short circuit current density (J_{sc}). Increasing temperature leads to a decrease in both J_{sc} and V_{oc} because of photogenerated charges and the recombination of photogenerated charges. Irradiation duration also impact the performance, with J_{sc} and V_{oc} decreasing over time, due to trapping effects at the interface. While solar cells exhibit stable J_{sc} and V_{oc} over a 20-day test period, their maximum output power decreases significantly within 6 days.

ORCID

©Hmoud Al-Dmour, <https://orcid.org/0000-0001-5680-5703>

REFERENCES

- [1] R. Gahlot, S. Mir, and N. Dhawan, *Energy Fuels*, **36**, 14554 (2022). <https://doi.org/10.1021/acs.energyfuels.2c02847>
- [2] H. Al-Dmour, S. Al-Trawneh, and S. Al-Taweel, *Int. J. Adv. Appl. Sci.* **8**(6), 1 (2021). <https://doi.org/10.21833/ijaas.2021.06.015>
- [3] K. Sharma, V. Sharma, and S.S. Sharma, *Nanoscale research letters*, **13**, 381 (2018). <https://doi.org/10.1186/s11671-018-2760-6>
- [4] S. Taweel, S.A. Itrawneh, H. Al Dmour, O. Al Gzawat, W. Alhalasah, and M. Mousa, *Heliyon*, **9**, 1 (2023). <https://doi.org/10.1002/anie.202302753>
- [5] K. Altola, G. Gave, M. Markkanen, J. Jaqueline, and P. Lunda, *Solar Energy*, **237**, 264 (2022). <https://doi.org/10.1016/j.solener.2022.03.060>
- [6] H. Al Dmour, and M. Taylor, *J. Ovonic. Res.* **19**, 587 (2023). <https://doi.org/10.15251/JOR.2023.195.587>
- [7] N. Mohenzadehan, A. Nouri, and M. Mohammadi, **25**, 3210 (2023). <https://doi.org/10.1039/D3CE00126A>
- [8] A. Slawek, Z. Starowicz, and M. Lipiński, *Materials*, **14**(12), 3295 (2021). <https://doi.org/10.3390/ma14123295>
- [9] E. Chahid, M. Lotfi, and O. Lotfi, *IJPEDS*, **2**, 1772 (2021). <http://doi.org/10.11591/ijpeds.v12.i3.pp1772-1783>
- [10] H. Al Dmour, *East Eur. J. Phys.* (3), 555 (2023). <https://doi.org/10.26565/2312-4334-2023-3-65>
- [11] A. Pirashanthan, T. Kajana, D. Velauthapillai, Y. Shivatharsiny, S. Bentouba, and P. Ravirajan, *Nanomaterials*, **12**, 820 (2022). <https://doi.org/10.3390/nano12050820>
- [12] L. Shaker, A. Al-Amiery, M. Hanoon, W. Al-azzawi, and A. Kadhum, *Sustainable Energy Research*, **11**, 6 (2024). <https://doi.org/10.1186/s40807-024-00100-8>
- [13] L. Huang, and B. Zahang, *Nat. Commun.* **14**, 124 (2024). <https://doi.org/10.1038/s41467-023-36937-8>
- [14] J. Nelson, *The physics of solar cell*, (Imperial College Press, 2003).
- [15] H Al-Dmour, *Eur. J. Phys.* (2), 445-449 (2024). <https://doi.org/10.26565/2312-4334-2024-2-58>
- [16] J.C. Nolasco, A. Castro-Carranza, Y.A. León, C. Briones-Jurado, J. Gutowski, J. Parisi, and E. von Hauff, *Solar Energy*, **184**, 610 (2019). <https://doi.org/10.1016/j.solener.2019.04.031>
- [17] H. Al Dmour, R. Alzard, H. Alblooshi, K. Alhosani, S. Al-Madhoob, and N. Saleh, *Front. Chem.* **7**, 561 (2019). <https://doi.org/10.3389/fchem.2019.00561>

ВПЛИВ ТЕМПЕРАТУРИ, ТРИВАЛОСТІ ОПРОМІНЮВАННЯ НА РОБОТУ ОРГАНІЧНИХ/RU-DYE/НЕОРГАНІЧНИХ СОНЯЧНИХ ЕЛЕМЕНТІВ

Хмуд Аль-Дмур

Університет Мута, факультет природничих наук, кафедра фізики, 61710, Йорданія

У цьому дослідженні вивчається вплив навколишніх умов на продуктивність сонячних елементів P3HT/Ru-dye/nc-TiO₂ (TLSC). Встановлено, що підвищення температури та тривалості опромінення впливає на параметри TLSC. При підвищенні температури з 293 К до 393 К густина струму короткого замикання (J_{sc}) і напруга холостого ходу (V_{oc}) зменшуються з 2,2 до 1,7 mA/cm² і від 0,7 В до 0,5 В відповідно. Це пояснюється впливом високої температури на рекомбінацію фотогенерованих зарядів і зменшення опору шунта (R_{sh}) у TLSC. Крім того, ми також представляємо вплив тривалості опромінення на продуктивність TLSC. Вимірювання показує, що J_{sc} зменшився на 0,5 mA/cm², тоді як V_{oc} зменшився на ~ 0,18 В протягом 4800 с освітлення. Це зменшення свідчить про заповнення пасток або дефектів на межі розділу фотогенерованими зарядами. Нарешті, максимальна вихідна потужність TLSC впала майже вдвічі протягом 6 днів під час 20-денного випробування через вплив вологості атмосфери на властивості розділу між барвником/nc-TiO₂ і P3HT.

Ключові слова: сонячні елементи; температура; дефекти; освітлення; поверхня оксиду; ефективність

DESIGN AND PERFORMANCE ANALYSIS OF COMPLETE SOLID-STATE DYE SENSITISED SOLAR CELL USING EOSIN-Y XANTHENE DYE: A SCAPS -1D SIMULATION STUDY

 K.R. Dhandapani^{a,b},  N.P. Dhanya^{a,c},  K. Sebastian Sudheer^{a*}

^aDepartment of Physics, Christ College, Irinjalakkuda North, Kerala, India 680125

^bDepartment of Physics, Govt. Victoria College, Palakkad, Kerala, India 678001

^cDepartment of Physics, KKTU Govt. College, Pullut, Thrissur, Kerala, India 680663

*Corresponding Author e-mail: sudheersebastian@christcollegeijk.edu.in

Received June 17, 2024; revised July 20, 2024; accepted August 3, 2024

This paper reports the theoretical simulation study of the performance of a complete solid-state dye-sensitized solar cell with Eosin-Y as the photosensitizer and PEDOT:PSS as the hole transport layer. SCAPS-1D software is used for the simulation under quasi-ideal conditions and got an optimized efficiency of 4.19%, which matches much with the reported experimental values in the literature. These findings indicate the potential of Eosin-Y as a cost-effective photosensitizer capable of performing even under dim light conditions.

Keywords: DSSC; Eosin-y; SCAPS-ID; PEDOT:PSS; Simulation

PACS: 85.60Bt; 84.60.Jt; 89.30.Cc; 07.05.Tp

1. INTRODUCTION

The growing global energy demand has prompted a shift towards non-conventional sources like solar energy, which offers abundant and constant availability [1]. While silicon solar cells remain prevalent for their efficiency and stability, alternative technologies like dye-sensitized solar cells (DSSCs) show promise despite lower efficiency, suggesting diverse applications in photovoltaics [2-3]. They operate by sensitizing a wide bandgap semiconductor with a suitable dye, a concept initially proposed by Grätzel and colleagues in 1991, where the use of Ruthenium complexes achieved an efficiency exceeding 10%. Unlike other solar cell types, where semiconducting materials handle multiple functions, DSSCs uniquely utilize dyes for initial light absorption, thus overcoming challenges in obtaining materials with both high light-harvesting and carrier-transporting properties. This dual-material approach in DSSCs allows for independent optimization of spectral properties through dye selection and modification, as well as enhancing carrier transport properties through semiconducting material engineering, offering a more targeted optimization compared to other solar cell technologies [4-5].

The choice of dye significantly impacts DSSC performance, with transition metal coordination compounds offering high efficiencies but posing challenges due to cost and toxicity, leading to research on natural and organic dyes like chlorophylls, flavonoids, and Anthocyanins, which offer advantages of low cost, abundance, and eco-friendliness, with chlorophyll showing notable efficiency of 4.6% in DSSCs [6-9]. Eosin Y, a xanthene dye commonly used due to its high solubility, presents as a red powder with a yellowish tinge and exhibits versatility in various chemical processes [10-13]. While it serves as a cost-effective and environmentally friendly alternative in photocatalysis and functions well in low light, its application in Dye-sensitized solar cells (DSSCs) faces challenges related to stability and efficiency, yet remains promising due to its affordability and versatility compared to Ruthenium complex dyes [14-16].

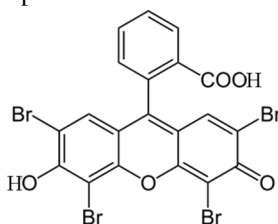


Figure 1. Structure of Eosin

The loading of dye on the photoanode in DSSCs is influenced by the nature and number of anchoring groups, with N3 dye allowing for maximum loading, followed by N719 and Eosin Y. DSSC efficiency, ranging from 0.399% to 5.4%, depends on factors such as dye concentration, photoanode type, electrolyte, and counter electrode; for instance, utilizing Eosin Y with a CuS electrode achieved an efficiency of 7.13%, while our solid-state DSSC attained 4.19% efficiency under quasi-ideal conditions, offering a solution to challenges associated with liquid electrolytes by eliminating concerns like evaporation and leakage, contributing to a reduction in device bulkiness and weight, with hole-transport materials like PEDOT:PSS being utilized in this study [15].

The design and analysis of the cell are conducted through the use of SCAPS-ID simulation software, an open-source tool developed by Professor M. Burgelman at the University of Gent, Belgium [17]. Employing simulation proves to be a cost-effective and time-efficient approach in contrast to experimental studies. Parameters for layer realization in this study are derived from reported experimental works. Additionally, the software is standardized to yield physically meaningful results by accurately reproducing experimental conditions. The software basically solves five differential equations which are Poisson's equation, continuity equations for electrons and holes, and drift diffusion equations for electrons and holes. In this study, the properties of the hole transport layer (HTL) were optimized, as it is a crucial factor influencing cell performance. Solar cell parameters showed reasonable variation with the thickness and electron affinity of the HTL layer, while other parameters such as acceptor density and trap density remained relatively unchanged compared to the parent cell design based on experimental values from the literature. By utilizing optimized values for the HTL layer, the cell demonstrated improved performance.

Simulation yields V_{oc} , J_{sc} , FF, PCE and also J-V and EQE curves. If the cell is constructed and experiment is carried out to get the above parameters in the real physical situation the results can approach the simulated values based on purity of materials used, fabrication techniques, morphology of layers, optimisation conditions etc.

2. NUMERICAL MODELLING AND DEVICE SIMULATION METHODOLOGY

The solar cell capacitance simulator (SCAPS-ID) is a widely used free software to simulate various types of solar cells.[18], [19] It operates by solving five key differential equations. Through simulation, SCAPS-ID generates comprehensive data, including various solar cell parameters, as well as current-Voltage (JV) and External Quantum Efficiency (EQE) curves.

Operation of solid state DSSC consists of following steps. Dye molecule D get photo excited by absorbing a photon. The molecule D^* in the electronically excited state transfer the e^- to the conduction band of photo anode. It is called electron injection and dye become D^+ and it return to electronically ground state. The electrons transferred to C.B. of photo anode move to TCO and are directed to counter electrode through the external load. D^+ acquire e^- from the HTL or give its hole state to hole transport layer (HTL) and get regenerated. HTL take an e^- from counter electrode and compensate for its loss. The complete solid state approach make the device more compact by avoiding liquid electrolyte containing redox couple [17, 20,21].

Poisson's equation and electron and hole continuity equations are the starting equations employed by the software [22].

$$\nabla^2 \psi = \frac{q}{\epsilon} (n - p + N_A - N_D)$$

n = electron concentration, p =hole concentration, ϵ = absolute permittivity of medium, q =electron charge, ψ = electrostatic potential, N_A = acceptor concentration, N_D = donor concentration

$$\nabla \cdot \mathbf{J}_n - q \frac{\partial n}{\partial t} = +qR$$

$$\nabla \cdot \mathbf{J}_p + q \frac{\partial p}{\partial t} = -qR$$

R = carrier recombination rate, \mathbf{J}_n = electron current density, \mathbf{J}_p = hole current density

$$\mathbf{J}_n = qn\mu_n E + qDn\nabla n$$

$$\mathbf{J}_p = qp\mu_p E - qDp\nabla p$$

E = electric field, D_n = electron diffusion coefficient, D_p = hole diffusion coefficient

Simulation was carried out under AM1.5G spectrum.

3. RESULTS AND DISCUSSIONS

In this study a complete solid state DSSC with Eosin-y as dye sensitizer is designed. TiO_2 is the photo anode and PEDOT: PSS the hole transport material [23]. Gold is used as counter electrode material. The representation of the designed cell and its schematic diagram is given in Figure 2.

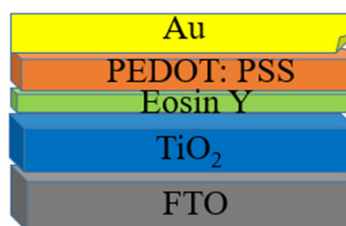


Figure 2. Schematic diagram of the designed cell

The software was validated for this study by reproducing a comparable experimental study. The electrical and optical parameters employed in this simulation are extracted from literature sources in reputable journals. The absorption files and filter files used in the simulation are developed based on data obtained from experimental studies documented in the literature. This approach ensures that the simulation model aligns with established and validated parameters, contributing to the accuracy and reliability of the computational investigation.

Table 1 gives different photovoltaic parameters used for the study.

Table 1. Different parameters used for the study

Parameter	HTL PEDOT:PSS	TiO ₂	FTO	Eosin Y
L	500nm	3μm	200nm	5nm
E _g (eV)	2.2	3.2	3.5	2.3[22]
χ(eV)	3.6	3.9	4	3.7
ε _r	10	9	9	25.3[24]
N _c (cm ⁻³)	10 ¹⁹	10 ¹⁹	9.2×10 ¹⁸	2.4×10 ²¹
N _v (cm ⁻³)	10 ¹⁹	10 ¹⁹	1.8×10 ¹⁹	2.5×10 ²¹
V _{th} (e)	10 ⁷	10 ⁷	10 ⁷	10 ⁷
V _{th} (h)(cm/s)				
μ _e (cm ² /vs)	100	20	20	10 ⁻⁴
μ _h (cm ² /vs)	0.4	10	24	10 ⁻⁴
N _D (cm ⁻³)	0	10 ¹⁶	10 ¹⁹	0
N _A (cm ⁻³)	10 ¹⁴	0	0	10 ¹⁸
N _i (cm ⁻³)	10 ¹⁶ [18]	10 ¹⁴ [18]	10 ¹⁴ [18]	10 ¹⁶ [11], [25]

Work function of back contact 5.1eV ----- [26]

Work function of front contact if 4.8eV-----[22]

Simulation plots are shown in Figure 3.

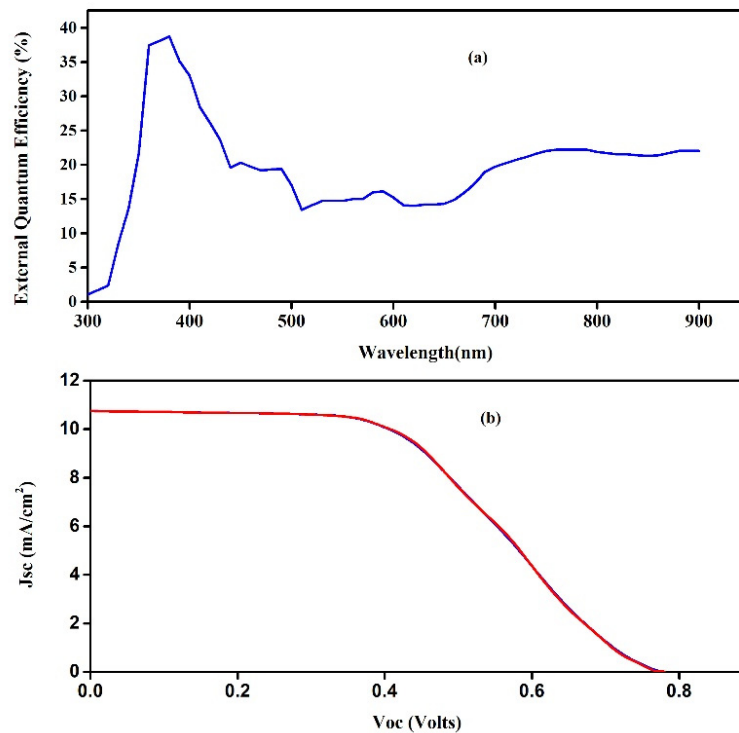


Figure 3. Simulated plots Eosin DSSC (a) EQE with wavelength and (b) J-V curve

To optimize the thickness of the Hole Transport Layer (HTL), a range from 25nm to 500nm was explored via batch calculation simulations. Remarkably, all parameters exhibited their peak values at a thickness of 75nm, thus establishing this dimension as optimal for the HTL in the optimized cell.

Increasing the thickness of the HTL resulted in enhanced light absorption in the longer wavelength region and facilitated a broader pathway for holes originating from the absorber layer to reach the electrode. Consequently, a reduction in hole-electron recombination occurred. These improvements in light absorption and recombination losses were pivotal in elevating solar cell parameters. However, excessively thick HTL layers hindered photon penetration and contributed to increased series resistance within the cell. Moreover, holes faced longer travel distances exceeding their

diffusion length, potentially leading to non-radiative recombination with electrons, thus diminishing solar cell performance when the HTL thickness surpassed the optimum value. The variation of the parameters with HTL thickness is shown in Figure 4.

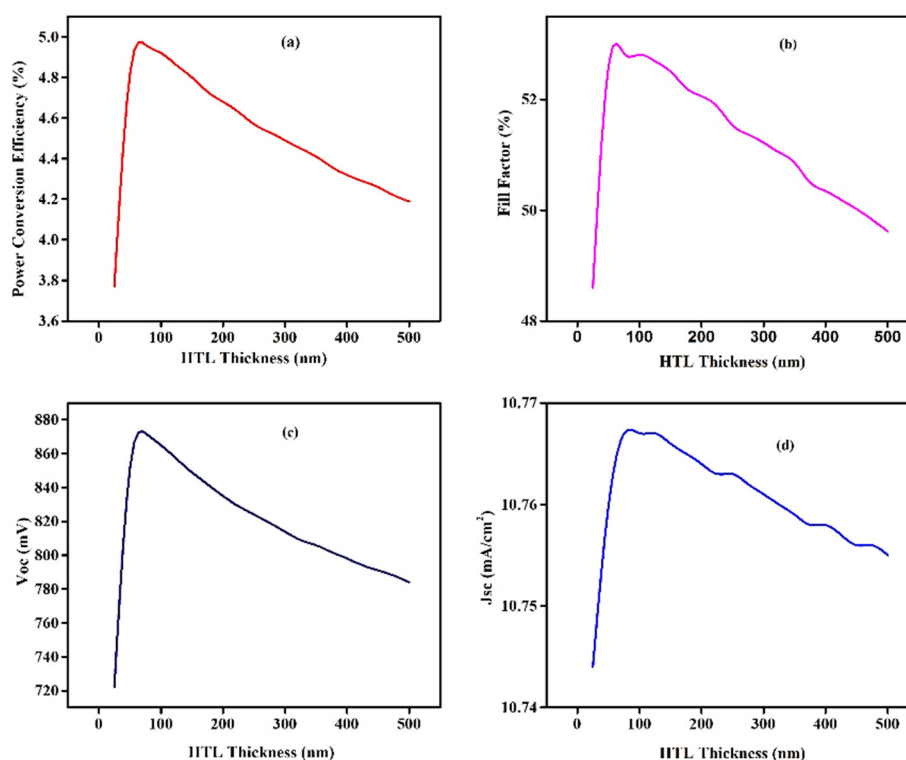


Figure 4. Variation of photovoltaic parameters of the simulated Eosin DSSC (a) PCE with HTL thickness (b) FF with HTL thickness (c) Voc with HTL thickness (d) Jsc with HTL thickness

Exploring electron affinity variations from 3.57eV to 3.63eV revealed optimal cell performance at an affinity of 3.58eV. Unlike thickness variations, the modulation of cell parameters with HTL electron affinity exhibited a gradual and consistent trend.

A higher electron affinity established a greater barrier for electrons at the interface, thereby reducing recombination losses. Additionally, it played a crucial role in aligning energy levels at the HTL/absorber interface, influencing charge carrier dynamics. However, an excessive increase in electron affinity beyond the optimum value hindered hole mobility within the HTL, consequently diminishing overall cell parameters.

a) Variation of Voc with HTL Thickness:

Voc exhibited a remarkable increase from 722 mV to 872 mV as the thickness varied from 25nm to the optimal 75nm. At this optimal thickness, maximum light harvesting and carrier transport were achieved, while recombination losses were minimized.

b) Variation of Jsc with Hole Transport Layer (HTL) thickness:

Jsc showed an increase from 10.744mA/cm² at 25nm to 10.767mA/cm² at the optimal thickness of 75nm, followed by a decline to 10.755mA/cm² at 500nm. Beyond the optimum thickness, reduced Jsc was observed due to significant recombination losses and reduced photon penetration.

c) Variation of Fill Factor (FF) with HTL Thickness:

FF increased from 48.6% at 25nm to a peak of 52.8% at the optimal thickness before declining to 49.6% at 500nm. Elevated recombination rates and increased series resistance at very high HTL thicknesses contributed to the reduction in fill factor.

d) Variation of PCE with HTL Thickness:

Power conversion efficiency surged from 3.77% to 4.96% before decreasing to 4.19% at 500nm. The efficiency peaked at the optimal thickness of 75nm, where maximum light absorption and carrier generation occurred, while excessive thickness led to predominant recombination and resistance losses, causing a decline in efficiency.

e) Variation of Solar Cell Parameters with HTL Electron Affinity:

Voc ranged from 778 mV to 781mV, with a peak at 786mV, while Jsc ranged from 10.754mA/cm² to 10.755 mA/cm², reaching a maximum at 10.756 mA/cm². Similarly, the fill factor varied between 49.2% to 49.7%, with the highest value observed at 49.7%. PCE showed a peak at 4.20%. In all cases, an electron affinity of 3.58 eV was identified as optimal, effectively reducing recombination losses at the HTL/dye interface. The variation of the parameters with electron affinity are shown in Figure 5.

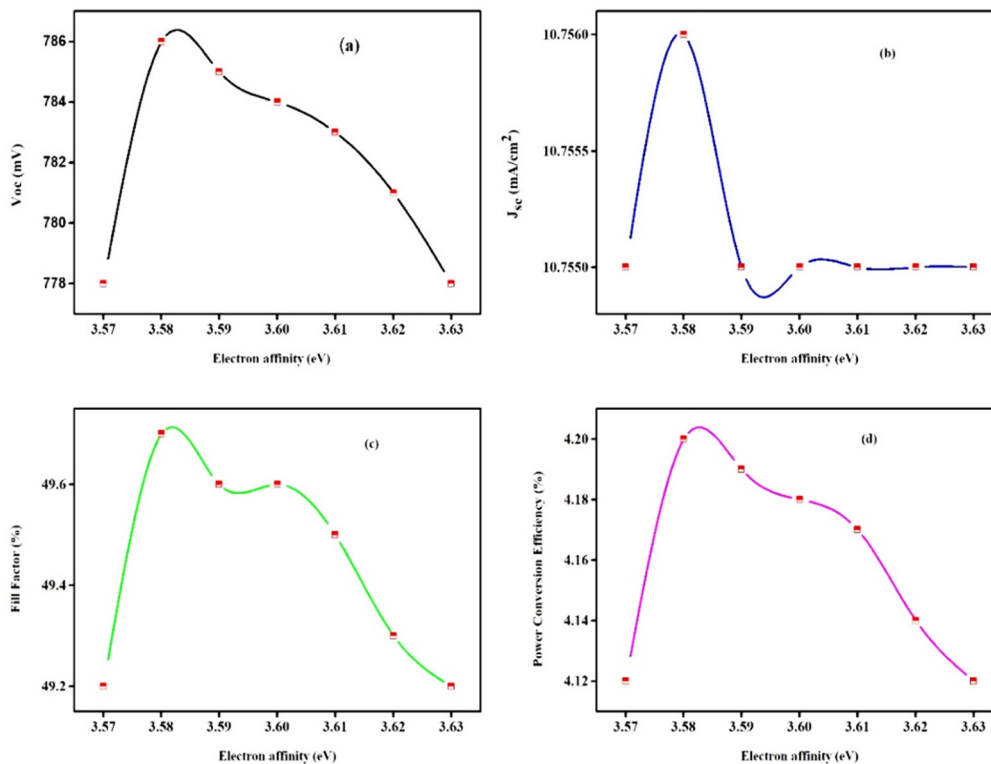


Figure 5. Variation of the photovoltaic parameters with electron affinity
(a) Voc with Electron affinity (b) Jsc with electron affinity (c) FF with electron affinity (d) PCE with electron affinity

Results of the simulated Eosin DSSC are tabulated as given in the Table 2 and optimised parameters are given in Table 3.

Table 2. Simulation results

Parameter	Simulated value
Voc(V)	0.78
Jsc(mA/cm ²)	10.76
FF%	50
PCE%	4.17
Vmax(V)	0.44
Jmax(mA/cm ²)	9.49

Table 3. Optimised parameters

Parameter	After Optimization	Before Optimization
Voc	874 mV	784 mV
Jsc	10.77 mA/cm ²	10.75 mA/cm ²
FF	52.9%	49.6%
PCE	4.97%	4.19%

4. CONCLUSION

This study computationally investigates the effectiveness of Eosin Y dye as a photosensitizer for Dye-sensitized solar cells (DSSC), focusing on a complete solid-state design. Simulated values fall within the range of experimental results, indicating that with careful fabrication and optimization, a practical cell can approach the simulated efficiency. The solid-state design enhances the cell's compactness and portability. Despite lower efficiency and stability compared to Ruthenium complex dyes, Eosin demonstrates potential as a photosensitizer for DSSCs. Further enhancements in efficiency can be achieved through dye modification, selection of a suitable photoanode with appropriate morphology, and optimization of hole transport layer (HTL) and counter electrode materials. Eosin Y's key attributes, including cost-effectiveness, satisfactory light-harvesting capability, ability to perform in low light conditions, and biodegradable and eco-friendly nature, contribute to its appeal in DSSC applications.

Acknowledgement

The authors would like to express gratitude to Professor Dr. M. Burgelman for providing the SCAPS-ID Software.

ORCID

©K.R. Dhandapani, <https://orcid.org/0009-0001-4484-3064>, ©N.P. Dhanya, <https://orcid.org/0000-0002-4372-2172>

©K. Sebastian Sudheer, <https://orcid.org/0000-0002-9019-4405>

REFERENCES

- [1] E. Itoh, Y. Maruyama, and K. Fukuda, "Fabrication of Inverted Bulk-Heterojunction Organic Solar Cell with Ultrathin Titanium Oxide Nanosheet as an Electron-Extracting Buffer Layer," *Jpn. J. Appl. Phys.* **51**(2S), 02BK13 (2012). <https://doi.org/10.1143/JJAP.51.02BK13>
- [2] B. O'Regan, and M. Grätzel, "A low-cost, high-efficiency solar cell based on dye-sensitized colloidal TiO₂ films," *Nature*, **353**(6346), 737–740 (1991). <https://doi.org/10.1038/353737a0>
- [3] S. Bendary, A. Hashem, and S. Hassan, "High efficiency dye-sensitized solar cells with a novel two-dimensional Cd-V-LDH photoanode," *Front. Mater.* **10**, 1129818 (2023). <https://doi.org/10.3389/fmats.2023.1129818>
- [4] S.S. Mali, C.A. Betty, P.N. Bhosale, and P.S. Patil, "Eosin-Y and N3-Dye sensitized solar cells (DSSCs) based on novel nanocoral TiO₂: A comparative study," *Electrochim. Acta*, **59**, 113–120 (2012). <https://doi.org/10.1016/j.electacta.2011.10.043>
- [5] M.K. Nazeeruddin, E. Baranoff, and M. Grätzel, "Dye-sensitized solar cells: A brief overview," *Solar energy*, **85**(6), 1172–1178 (2011). <https://doi.org/10.1016/j.solener.2011.01.018>
- [6] N.Y. Amogne, D.W. Ayele, and Y.A. Tsigie, "Recent advances in anthocyanin dyes extracted from plants for dye sensitized solar cell," *Mater. Renew Sustain Energy*, **9**(4), 23 (2020). <https://doi.org/10.1007/s40243-020-00183-5>
- [7] C. Cari, K. Khairuddin, T.Y. Septiawan, P.M. Suciati, D. Kurmiawan, and A. Supriyanto, "The preparation of natural dye for dye-sensitized solar cell (DSSC)," *AIP Conference Proceedings*, **2014**, 020106 (2018). <https://doi.org/10.1063/1.5054510>
- [8] G. Calogero, J.-H. Yum, A. Sinopoli, G. Di Marco, M. Grätzel, and M.K. Nazeeruddin, "Anthocyanins and betalains as light-harvesting pigments for dye-sensitized solar cells," *Solar energy*, **86**(5), 1563–1575 (2012). <https://doi.org/10.1016/j.solener.2012.02.018>
- [9] A. Lim, *et al.*, "Potential natural sensitizers extracted from the skin of *Canarium odontophyllum* fruits for dye-sensitized solar cells," *Spectrochim. Acta A, Mol. Biomol. Spectrosc.* **138**, 596–602 (2015). <https://doi.org/10.1016/j.saa.2014.11.102>
- [10] S.A.A.R. Sayyed, N.I. Beedri, P.K. Bhujbal, S.F. Shaikh, and H.M. Pathan, "Eosin-Y sensitized Bi-layered ZnO nanoflower-CeO₂ photoanode for dye-sensitized solar cells application," *ES Materials & Manufacturing*, **10**(2), 45–51 (2020). <https://dx.doi.org/10.30919/esmm5f939>
- [11] Y. Sun, *et al.*, "Eosin Y-sensitized partially oxidized Ti₃C₂ MXene for photocatalytic hydrogen evolution," *Catal. Sci. Technol.* **9**(2), 310–315 (2019). <https://doi.org/10.1039/C8CY02240B>
- [12] L. Yang, *et al.*, "Efficient hydrogen evolution over Sb doped SnO₂ photocatalyst sensitized by Eosin Y under visible light irradiation," *Nano Energy*, **36**, 331–340 (2017). <https://doi.org/10.1016/j.nanoen.2017.04.039>
- [13] X. Liu, *et al.*, "Effective hydrothermal grafting of Eosin Y onto TiO₂ nanoparticles towards stable photocatalysts for efficient visible-light-driven photocatalytic H₂ evolution," *New Journal of Chemistry*, **42**(9), 6631–6635 (2018). <https://doi.org/10.1039/C8NJ00883C>
- [14] S. Krishnaveni, X.M. Josephine, S. Mohankumar, and V. Sathyanarayanamoorthi, "A Theoretical Investigation of Decorated Novel 1,2-Di(4-pyridyl)-ethylene based Dye Sensitized Solar Cells (DSSC)," *Asian Journal of Chemistry*, **35**(9), 2215–2224 (2023). <https://doi.org/10.14233/ajchem.2023.28121>
- [15] P.P. Das, A. Roy, S. Das, and P.S. Devi, "Enhanced stability of Zn₂SnO₄ with N719, N3 and eosin Y dye molecules for DSSC application," *Physical Chemistry Chemical Physics*, **18**(3), 1429–1438 (2016). <https://doi.org/10.1039/C5CP04716A>
- [16] S.S. Kulkarni, S.S. Hussaini, G.A. Bodkhe, and M.D. Shirsat, "Natural hibiscus dye and synthetic organic Eosin Y dye sensitized solar cells using Titanium Dioxide nanoparticles photo anode: Comparative study," *Surface Review and Letters*, **26**(03), 1850164 (2019). <https://doi.org/10.1142/S0218625X18501640>
- [17] K.S. Nithya, and K.S. Sudheer, "Device modelling of non-fullerene organic solar cell with inorganic CuI hole transport layer using SCAPS 1-D," *Optik*, **217**, 164790 (2020). <https://doi.org/10.1016/j.ijleo.2020.164790>
- [18] F. Jahantigh, and M.J. Safikhani, "The effect of HTM on the performance of solid-state dye-sensitized solar cells (SDSSCs): a SCAPS-1D simulation study," *Applied Physics A*, **125**, 1–7 (2019). <https://doi.org/10.1007/s00339-019-2582-0>
- [19] W. Abdelaziz, A. Shaker, M. Abouelatta, and A. Zekry, "Possible efficiency boosting of non-fullerene acceptor solar cell using device simulation," *Opt. Mater. (Amst)*, **91**, 239–245 (2019). <https://doi.org/10.1016/j.optmat.2019.03.023>
- [20] N. El Achi, *et al.*, "Metal-free ATRP catalyzed by visible light in continuous flow," *Front. Chem.* **8**, 740 (2020). <https://doi.org/10.3389/fchem.2020.00740>
- [21] E. Widiyanto, Y. Firdaus, L.M. Pranoto, K. Triyana, I. Santoso, and N.M. Nursam, "Device modeling of two-dimensional hole transport materials for boosting the performance of non-fullerene acceptor bulk heterojunction organic solar cells," *Opt. Mater.* **132**, 112771 (2022). <https://doi.org/10.1016/j.optmat.2022.112771>
- [22] M.S. Shamna, and K.S. Sudheer, "Device modeling of Cs₂PtI₆-based perovskite solar cell with diverse transport materials and contact metal electrodes: a comprehensive simulation study using solar cell capacitance simulator," *J. Photonics Energy*, **12**(3), 32211 (2022). <https://doi.org/10.1117/1.JPE.12.032211>
- [23] H. Alipour, and A. Ghadimi, "Optimization of lead-free perovskite solar cells in normal-structure with WO₃ and water-free PEDOT: PSS composite for hole transport layer by SCAPS-1D simulation," *Opt. Mater.* **120**, 111432 (2021). <https://doi.org/10.1016/j.optmat.2021.111432>
- [24] T. Attar, A. Benchadli, B. Messaoudi, N. Benhadria, and E. Choukchou-Braham, "Experimental and theoretical studies of eosin Y dye as corrosion inhibitors for carbon steel in perchloric acid solution," *Bulletin of chemical reaction engineering & catalysis*, **15**(2), 454–464 (2020). <https://doi.org/10.9767/bcrec.15.2.7753.454-464>
- [25] W.K.H. Al-Behadili, Y.M. Jawad, and W.S.A. Whaab, "Effect of Solvent on Intensity of Absorption and Fluorescence of Eosin Y Dye and Spectral Properties of Eosin Y Dye," *Journal of Medicinal and Chemical Sciences*, **6**(2), 322–334 (2023). <https://doi.org/10.26655/JMCHMSCI.2023.2.13>
- [26] M.Z. Sahdan, *et al.*, "Fabrication of inverted bulk heterojunction organic solar cells based on conjugated P3HT: PCBM using various thicknesses of ZnO buffer layer," *Optik*, **126**(6), 645–648 (2015). <https://doi.org/10.1016/j.ijleo.2015.01.017>

**РОЗРОБКА ТА АНАЛІЗ ПРОДУКТИВНОСТІ ПОВНОГО СЕНСИБІЛІЗОВАНОГО НА ТВЕРДОТІЛЬНОГО
БАРВНИКА ДЛЯ СОНЯЧНОГО ЕЛЕМЕНТА З ВИКОРИСТАННЯМ ЕОЗИН-У КСАНТЕНА:
ДОСЛІДЖЕННЯ СИМУЛЯЦІЄЮ SCAPS-1D**

К.Р. Дхандапані^{a,b}, Н.П. Дханья^{a,c}, К. Себастьян Судхір^a

^aДепартамент фізики, Християнський коледж, Ірінджалакуда, Керала, Індія 680125

^bДепартамент фізики, Урядовий Вікторія коледж, Палаккад, Керала, Індія 678001

^cДепартамент фізики, ККТМ Урядовий коледж, Пуліт, Трісур, Керала, Індія 680663

У статті повідомляється про теоретичне моделювання ефективності повного твердотілого сонячного елемента, сенсibilізованого барвником, з Eosin-Y як фотосенсibilізатора та PEDOT: PSS як шару для транспортування дірок. Програмне забезпечення SCAPS-1D використовується для моделювання в квазіідеальних умовах і отримує оптимізовану ефективність 4,19%, що значною мірою відповідає експериментальним значенням, наведеним у літературі. Ці висновки вказують на потенціал Eosin-Y як економічно ефективного фотосенсibilізатора, здатного працювати навіть в умовах слабого освітлення.

Ключові слова: *DSSC; еозин-у; SCAPS-ID; PEDOT:PSS; симуляція*

SCAPS-1D ANALYSIS OF NON-TOXIC LEAD-FREE MASnI₃ PEROVSKITE-BASED SOLAR CELL USING INORGANIC CHARGE TRANSPORT LAYERS

Matthew I. Amanyi^a, Abubakar S. Yusuf^b, Eghwubare Akpoguma^c, Stephen O. Eghaghe^d, James Eneye^d, Raymond M. Agaku^e, Lilian C. Echebiri^f, Emmanuel U. Echebiri^g, Emmanuel O. Ameh^f, Chinyere I. Eririogu^h, Nicholas N. Tasieⁱ, Anthony C. Ozurumba^j, Eli Danladi^{a,*}

^aDepartment of Physics, Federal University of Health Sciences, Otukpo, Benue State, Nigeria

^bDepartment of Physics, Federal University of Technology, Minna, Niger State, Nigeria

^cNuclear Technology Center, Nigeria Atomic Energy Commission, Abuja, Nigeria

^dDepartment of Physics, Bingham University, Nasarawa State, Nigeria

^eDepartment of Physics, Benue State University, Benue State, Nigeria

^fDepartment of Physics, Nasarawa State University, Nasarawa State, Nigeria

^gDepartment of Electrical/Electronic Engineering, Nile University of Nigeria

^hDepartment of Physics, University of Nigeria Nsukka, Enugu State, Nigeria

ⁱDepartment of Physics, Rivers State University, Port Harcourt, Rivers State, Nigeria

^jAfrica Center of Excellence in Future Energies and Electrochemical Systems, Federal University of Technology, Owerri, Imo State, Nigeria

*Corresponding Author e-mail: danladielibako@gmail.com

Received May 31, 2024; revised July 17, 2024; in final form August 19, 2024; accepted August 19, 2024

Perovskite solar cells (PSCs) have gained a lot of attention due to their high efficiency and low cost. In this research paper, a methylammonium tin iodide (CH₃NH₃SnI₃) based solar cell was simulated using a one-dimensional solar cell capacitance simulation (SCAPS-1D) tool. The SCAPS-1D tool is based on Poisson and the semiconductor equations. After thorough investigation, the initial device presents the following parameters; power conversion efficiency (PCE)=15.315%, fill factor (FF)=64.580%, current density (J_{sc})=29.152 mA/cm² and open circuit voltage (V_{oc})=0.813 V. The effect of absorber and ETL thicknesses were explored systematically. The performance of the simulated device was significantly influenced by the thickness of the absorber and ETL. The optimized absorber thickness was 0.5 μm and the ETL thickness was 0.02 μm, giving rise to an optimized PCE of 15.411%, FF of 63.525%, J_{sc} of 29.812 mA/cm², and V_{oc} of 0.814 V. Additionally, the effect of temperature on the optimized device was evaluated and found that it affects the performance of the device. This model shows the prospect of CH₃NH₃SnI₃ as a perovskite material to produce toxic-free environment-friendly solar cells with high efficiency.

Keywords: Perovskite solar cell; SCAPS-1D; CH₃NH₃SnI₃; Photovoltaic

PACS: 41.20.Cv; 61.43.Bn; 68.55.ag; 68.55.jd; 73.25.+i; 72.80.Tm

INTRODUCTION

To maintain the current state of growth in the photovoltaic domain, perovskite solar cells have received significant attention due to the fast pace of efficiency growth from 3.8 to >25% in just over a decade of research [1], [2], [3], [4]. The enhancement in efficiency is attributed to the excellent optoelectronic characteristics of the absorbing halide perovskite materials, amongst which include; long-range charge diffusion lengths, high absorption coefficient, low exciton binding energies, tunable band gaps, and high charge carrier mobilities [5], [6], [7], [8], [9]. As light absorbers in PSCs, hybrid organic–inorganic halide absorbing materials which include the methylammonium lead triiodide (MAPbI₃) and formamidinium lead triiodide (FAPbI₃) has been at the forefront of research in the photovoltaic horizon. One of the challenges that limited its commercialization and effective utilization is the presence of lead (Pb), which is toxic in nature [6], [10], [11]. Under these situations, the European Union and other nations have placed great restrictions on the use of Pb-containing materials in electronic devices, which has triggered interest in Pb-free PSCs [12], [13].

In overcoming the challenge of high toxicity, researchers have devoted enormous efforts to replacing lead with eco-friendly materials such as tin (Sn), Bismuth (Bi), and Germanium (Ge) [14]. Amongst the listed eco-friendly perovskite crystals, Sn-based perovskite is receiving the greatest attention.

Due to the low toxicity and exceptional theoretical PCE, tin halide-based perovskites have gained a lot of attention in the development of PSCs [15]. Sn is considered one of the most practical substitutes for Pb in the perovskite configurations as a replacement of the toxic Pb²⁺ ions with Sn²⁺ creating no distortion in the perovskite structure owing to the similarity between the outer shell of Pb and Sn [15], [16]. In this category are the methylammonium tin triiodide (MASnI₃), cesium tin triiodide (CsSnI₃), and formamidinium tin iodide (FASnI₃). However, the MASnI₃ perovskite is achieving good efficiency and is the closest candidate among the other Pb-free based absorbers due to (i) its direct bandgap of 1.30 eV which has an ideal bandgap close to those postulated by the Shockley–Queisser limit [17] and (ii) highest light absorption properties and high optical behavior to be used in optoelectronic devices [18], hence it was utilized in our present study.

The conventional PSC configuration is made up of two charge transport layers, an electron transport layer (ETL), a hole transport layer (HTL), and a perovskite absorption layer. The ETL plays a crucial role by conveying photogenerated electrons and blocking holes. Some examples of commonly used ETL are TiO₂, SnO₂, Nb₂O₅, Al₂O₃, PCBM, C60, WO_x, ZnO, I₂O₃, BaTiO₃, and PbTiO₃ [19], [20]. The HTL plays a crucial role by conveying photogenerated holes and blocking electrons. Polymeric HTLs and inorganic or organic small molecules can be categorized into several groups depending on their chemical composition, according to established categorization methods [21]. Among these types of HTLs, CuSbS₂, NiO, P3HT, Cu₂O, CuSCN, PEDOT: PSS, CuI, CuO, NiO, and SpiroMeOTAD are commonly used in several studies [19], [20], [21]. Due to the wide band gap, better energy level, and environmental stability, TiO₂ is one of the highly utilized ETLs [22]. Also, the suitable band gap, good stability, and desirable band bending make TiO₂ one of the best ETLs to be used with the MASnI₃ perovskite absorber material, hence it was utilized in our study.

In this study, an eco-friendly PSC based on MASnI₃ was modeled and simulated using SCAPS-1D software with TiO₂ as an efficient electron transport layer. We thoroughly explored the effect of different layer parameters including ETL thickness and absorber thickness to obtain an optimized PSC device. We subsequently investigated the thermal effect on the optimized device. These parameters help to identify the best solar cell characteristics and significantly increase power conversion efficiency. These findings now open up a fruitful research opportunity for developing and manufacturing low-cost, highly efficient, lead-free perovskite solar cells.

2. METHODOLOGY AND SIMULATION

In this study, the Solar Cell Capacitance Simulator (SCAPS-1D) software was utilized to carry out the investigation [23]. Several simulation software have been used in the study of PSC. Amongst these include; SILVACO ATLAS, AMPS, COMSOL, and SCAPS [16], [24], [25], [26]. The SCAPS-1D is advantaged over other tools listed above, which include its ability to simulate up to seven different layers without routine measurements. It can allow the calculations of many parameters such as spectral response, energy bands, ac characteristics, $J-V$ curve, Q-E curve, and defect density, by simply resolving the basic equations of semiconductor [22].

Equation 1 [22] illustrates the relationship between charges to electrostatic potential.

$$\frac{d^2}{dx^2} \psi(x) = \frac{q}{\epsilon_0 \epsilon_r} [p(x) - n(x) + N_D - N_A + \rho_p - \rho_n], \quad (1)$$

where ψ is the electrostatic potential, $n(x)$ and $p(x)$ are densities of electrons and holes, ϵ_r is the relative permittivity, ϵ_0 is the permittivity of free space, the donor and accepted impurities are denoted as N_D and N_A , ρ_p and ρ_n , are the distributions of holes and electrons, q is the charge.

Equations (2) and (3) show how the density gradients, current densities, and net generation of electrons and holes are conserved [27].

$$\frac{\partial n}{\partial t} = \frac{1}{q} \frac{\partial J_n}{\partial x} + (G_n - R_n), \quad (2)$$

$$\frac{\partial p}{\partial t} = \frac{1}{q} \frac{\partial J_p}{\partial x} + (G_p - R_p), \quad (3)$$

where G is the generation, R is the recombination, J_n is the electron density, J_p is the density of holes.

The total currents, J_n and J_p resulted by the drift and diffusion of charge carriers which can be used to obtain the current densities of the solar cells.

In the present study, the HTL is considered as the p-type layer, the ETL as the n-type of the MASnI₃-based perovskite, the transparent oxide here is represented as fluorine-doped tin oxide (FTO), and gold (Au) as the back metal contact (BMC) for the device.

To have a successful simulation in this work, the layer's parameters were chosen carefully from experimental results and other theoretical research in the literature. The details for each layer are summarized in Table 1 [15], [16], [22].

Table 1. Parameters used for simulation of perovskite solar cell structures using SCAPS-1D

Parameters	FTO	ETL	Absorber	HTL
Thickness (μm)	0.4	0.05	0.40	0.15
E_g (eV)	3.5	3.2	1.30	2.17
χ (eV)	4.0	4.2	4.20	3.2
ϵ_r	9	10.0	8.2	7.11
N_C (cm ⁻³)	2.2×10 ¹⁸	2.2×10 ¹⁸	1.0×10 ¹⁸	2.2×10 ¹⁸
N_V (cm ⁻³)	1.8×10 ¹⁹	2.2×10 ¹⁸	1.0×10 ¹⁸	2.2×10 ¹⁸
μ_n (cm ² V ⁻¹ s ⁻¹)	20	20	1.6	80
μ_p (cm ² V ⁻¹ s ⁻¹)	10	10	1.6	80
N_D (cm ⁻³)	1×10 ¹⁸	1×10 ¹⁷	0	0
N_A (cm ⁻³)	0	0	3.2×10 ¹⁵	1.0×10 ¹⁸
N_t (cm ⁻³)	1×10 ¹⁵	1×10 ¹⁵	4.5×10 ¹⁶	1.0×10 ¹⁵

Additionally, Table 2 provides the interface defect properties of the input parameters. The work function (W_F) of front and back contacts are 4.40 eV and 5.10 eV. The scanning voltage is taken from 0-1.6 V, and the temperature during the simulation was set at 300 K. The simulation evaluation is completed under 100 mW/cm² light intensity. The thermal velocities of the hole and electron is 10⁷ cm s⁻¹. During the optimization process, the parameters of FTO, MASnI₃, and HTL are kept constant and the thickness of ETL is varied from 0.01 to 0.1 μ m to get the optimum performance parameters. Also, for MASnI₃, the parameters of FTO, ETL, and HTL were kept constant while varying MASnI₃ thickness from 0.1 to 1.0 μ m to get the optimum performance parameter. For the optimized temperature, the parameters of the optimized device were kept constant while the temperature was varied from 290 to 360 K to get the optimum metric parameters. The simulated device and energy profile are shown in Figure 1.

Table 2. Parameters of interface layer

Parameters	TiO ₂ /CH ₃ NH ₃ SnI ₃ interface	CH ₃ NH ₃ SnI ₃ /Cu ₂ O interface
Defect type	Neutral	Neutral
Capture cross section for electrons (cm ²)	1×10 ⁻¹⁵	1×10 ⁻¹⁵
Capture cross section for holes (cm ²)	1×10 ⁻¹⁵	1×10 ⁻¹⁵
Energetic distribution	Single	Single
Energy level with respect to E _v (eV)	0.600	0.600
Characteristic energy (eV)	0.1	0.1
Total density (cm ⁻³)	1×10 ¹⁰	1×10 ⁻¹⁰

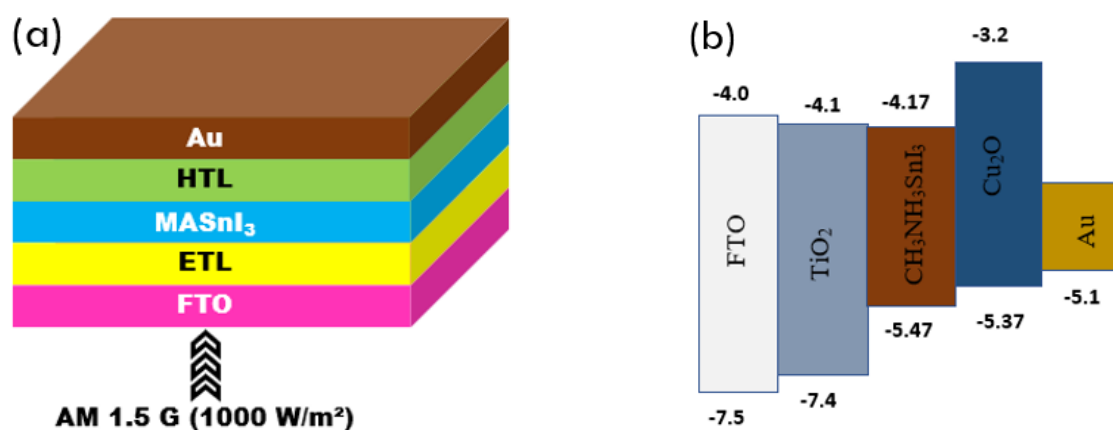


Figure 1. (a) Device Structure and (b) Energy Band Profile

3. RESULTS AND DISCUSSION

3.1. Analysis of initial device

With the parameters available in Tables 1 and 2, the results of current-voltage, quantum efficiency, and power density were obtained as shown in Figure 2a-c.

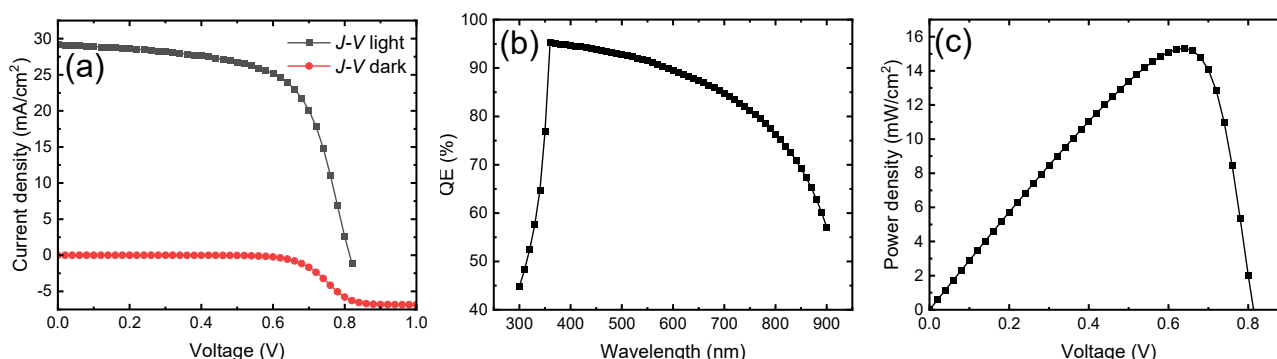


Figure 2. (a) J - V curve of PSC in the light and dark conditions, (b) QE with respect to wavelength, and (c) P - V curve

Table 3 shows the photovoltaic characteristics of the MASnI₃ cell, which include; open circuit voltage (V_{oc}), short circuit current (J_{sc}), fill factor (FF), and power conversion efficiency (PCE). To verify our theoretical assertion, the results were compared with other findings [15], [28], [29]. Our results show a PCE of 15.315%, FF of 64.580%, V_{oc} of 0.813 V, and a J_{sc} of 29.152 mA/cm². The agreement with other studies shows that the device simulation is valid

and the input parameters are close to established real devices. In the dark condition, the device acts as a diode as depicted in Figure 2a. The depletion layer spreads, the internal electric field expands, and the electrons' electric potential energy rises when a bias voltage is given to the Schottky barrier [22]. Figure 2b shows the QE vs. wavelength. As can be seen, the QE rises with an increase in wavelength from 45% at 300 nm to 95% at 350 nm. The QE covers the entire visible spectrum and reaches a broad absorption maximum before it starts declining to 900 nm. This agrees with similar studies [15], [16], [30]. The sweeping at the visible and near-infrared region is significantly beneficial to the absorption of light at various wavelengths. The power density is shown in Figure 2c with a maximum power density of 15.315 mW/cm².

Table 3. Electrical parameters with varied absorber thickness

Thickness (μm)	PCE (%)	FF (%)	J _{sc} (mA/cm ²)	V _{oc} (V)
0.1	10.774	74.706	17.353	0.831
0.2	14.064	70.615	24.348	0.818
0.3	15.090	67.032	27.656	0.814
0.4	15.315	64.580	29.152	0.813
0.5	15.321	63.284	29.763	0.813
0.6	15.306	62.849	29.942	0.813
0.7	15.296	62.760	29.965	0.813
0.8	15.288	62.730	29.963	0.813
0.9	15.280	62.702	29.961	0.813
1.0	15.272	62.673	29.960	0.813

3.2. Optimization of absorber layer thickness

The absorbing material in perovskite solar cells is significantly responsible for all photovoltaic processes, which include the generation, recombination, and transportation of charge carriers, hence often called the heart of the solar cell. Numerous studies have shown that the quality of the perovskite layer greatly influences the lifetime and diffusion length of photo-generated carriers, which in turn affect the overall performance of the solar cell [31], [32]. To improve the solar cell performance, the optimization of the absorber layer is highly indispensable. If the absorber layer thickness is greater than the diffusion length, then the generated charge carriers will recombine at the layer, and the series resistance of the solar cell will increase as a result, the charge carriers cannot reach the electrode [32]. When the thickness is too thin, a low absorption rate is observed which results in reduced photocurrent value. Therefore, getting the optimized thickness of the absorber layer is crucial for high-performing PSCs [33]. In this study, absorber thickness was varied from 0.1 to 1.0 μm, at an interval of 0.1 μm to obtain the optimized value. The results are presented in Figures 3 and 4. Fig. 3a shows the *J-V* curve at different thicknesses and Fig. 3b presents the QE at different thicknesses. From the result, the PCE increases with increasing absorber layer thickness until the thickness achieves a value of 0.5 μm. The initial increase in PCE is attributed to increase in electron-hole pair generation rate inside the absorber layer [32].

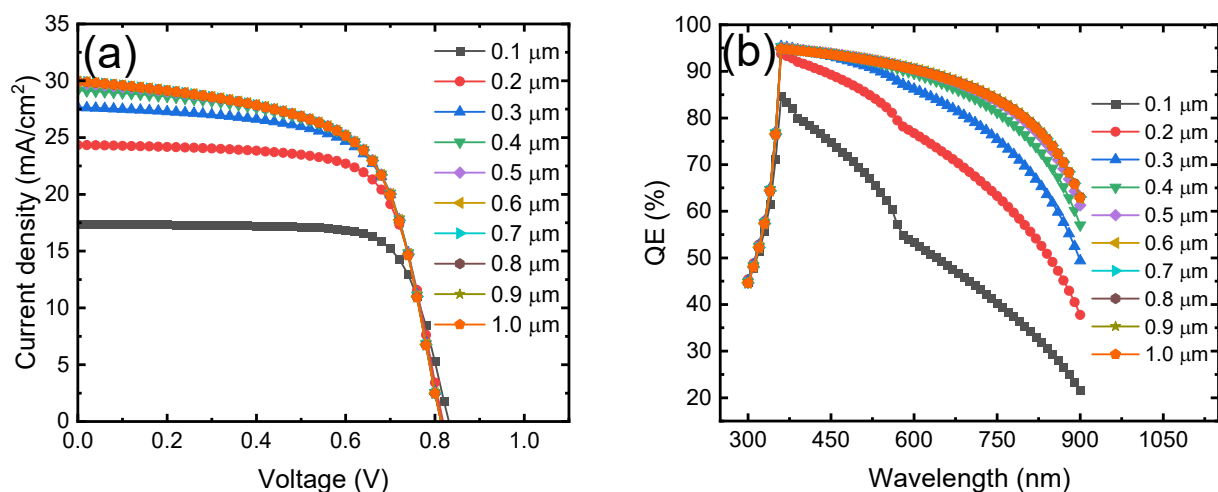


Figure 3. (a) *J-V* curve of PSC with different absorber thickness and (b) QE with respect to wavelength of different absorber thickness

When the thickness goes beyond 0.5 μm, the PCE values decline which makes the choice of the optimal thickness to be 0.5 μm which corresponds to the photovoltaic properties of PCE=15.321%, FF=63.284%, J_{sc}=29.763 mA/cm² and V_{oc}=0.813 V. The decrease in PCE when the thickness exceeds 0.5 μm is attributed to increase in recombination rate of charge carrier [15]. It can be seen that the V_{oc} decreases when the thickness of the absorbing layers increases from 0.1 to 0.3 μm, thereafter, it maintains a constant value which is the point of saturation. The FF decreases with an increase in the

absorber thickness (see Table 3). The decrease in FF is attributed to the increase in series resistance [32]. The relationship between absorber layer thickness with the photovoltaic parameters (PCE, FF, J_{sc} , and V_{oc}) is depicted in Figure 4a-d.

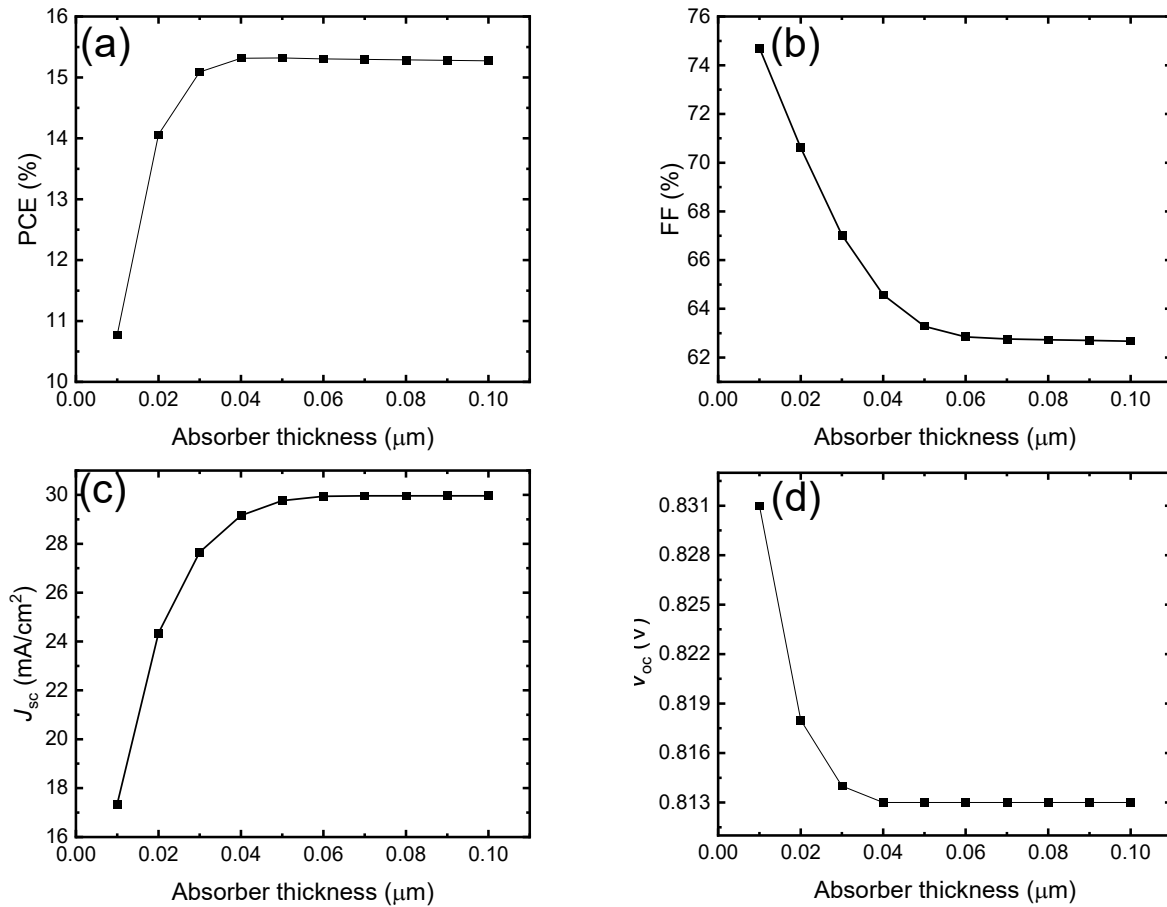


Figure 4. (a) variation of PCE with absorber thickness, (b) variation of FF with absorber thickness, (c) variation of J_{sc} with absorber thickness, and (d) variation of V_{oc} with absorber thickness

3.3. Optimization of ETL layer thickness

The performance of PSC is highly impacted by the thickness of the ETL. Crucially, the choice of proper ETL plays a great role in the design and implementation of high-performing PSC as the band alignment between the absorber and ETL layer is an important factor for improved PSCs [15], [34]. Fig. 5a shows the $J-V$ curve with varied ETL thickness while Fig. 5b shows the QE characteristics with varied ETL thickness.

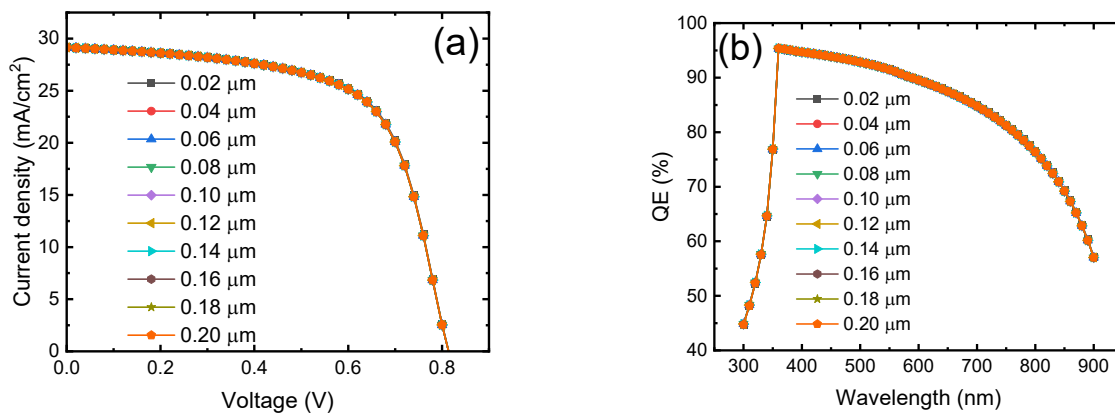


Figure 5. (continued on the next page). (a) $J-V$ curve of PSC with different ETL thickness, (b) QE with respect to wavelength with different ETL thickness, (c) variation of PCE and FF with ETL thickness, and (d) variation of J_{sc} and V_{oc} with absorber thickness

The variation of performance parameters which include the PCE, FF, J_{sc} , and V_{oc} with thicknesses of the ETL is shown in Figures 5c & d. As shown in Table 5, the PCE decreases gently from 15.399 to 15.302% as the thickness rose from 0.02 to 0.20 μm. The increase in ETL thickness decreases the J_{sc} of the PSCs by correspondingly increasing photon

absorption and resistance of the cell (see Figure 5b). The increase in QE with increasing photon energies can be seen to arise from the absorption coefficient within the regions and the consequence of increased density of localized states in the gap itself due to the rise in new defect states [35]. The increase in ETL thickness results in partial absorption of light, which slows down the pace of charge formation and collection and prevents enough light from reaching the absorber as a result leading to a decrease in transmittance and reduced performance [5]. The optimized ETL thickness was found to be 0.02 μm which gave PCE, FF, J_{sc} , and V_{oc} values of 15.399%, 64.830%, 29.186 mA/cm^2 and 0.814 V.

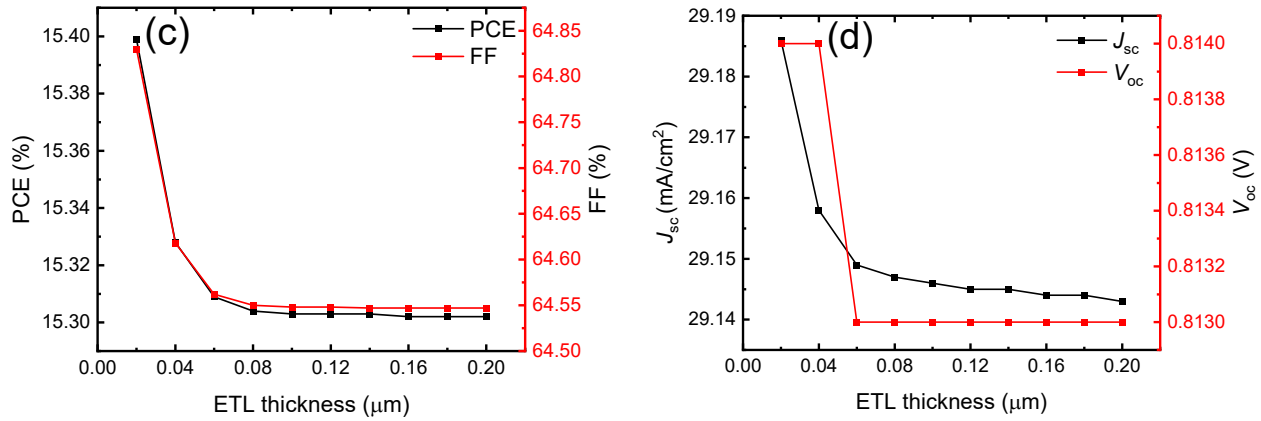


Figure 5. (continuation). (a) J - V curve of PSC with different ETL thickness, (b) QE with respect to wavelength with different ETL thickness, (c) variation of PCE and FF with ETL thickness, and (d) variation of J_{sc} and V_{oc} with absorber thickness

Table 5. Electrical parameters with varied ETL thickness

Thickness (μm)	PCE (%)	FF (%)	J_{sc} (mA/cm^2)	V_{oc} (V)
0.02	15.399	64.830	29.186	0.814
0.04	15.328	64.618	29.158	0.814
0.06	15.309	64.562	29.149	0.813
0.08	15.304	64.550	29.147	0.813
0.10	15.303	64.548	29.146	0.813
0.12	15.303	64.548	29.145	0.813
0.14	15.303	64.547	29.145	0.813
0.16	15.302	64.547	29.144	0.813
0.18	15.302	64.547	29.144	0.813
0.20	15.302	64.547	29.143	0.813

3.4. Optimized simulated PSC

Following the PSC simulation, the thickness of the absorber and the thickness of the ETL were optimized. The results show that the optimized absorber thickness is 0.5 μm and the ETL thickness is 0.02 μm . The J - V and QE curves for the optimized and unoptimized devices are shown in Figure 6a & b.

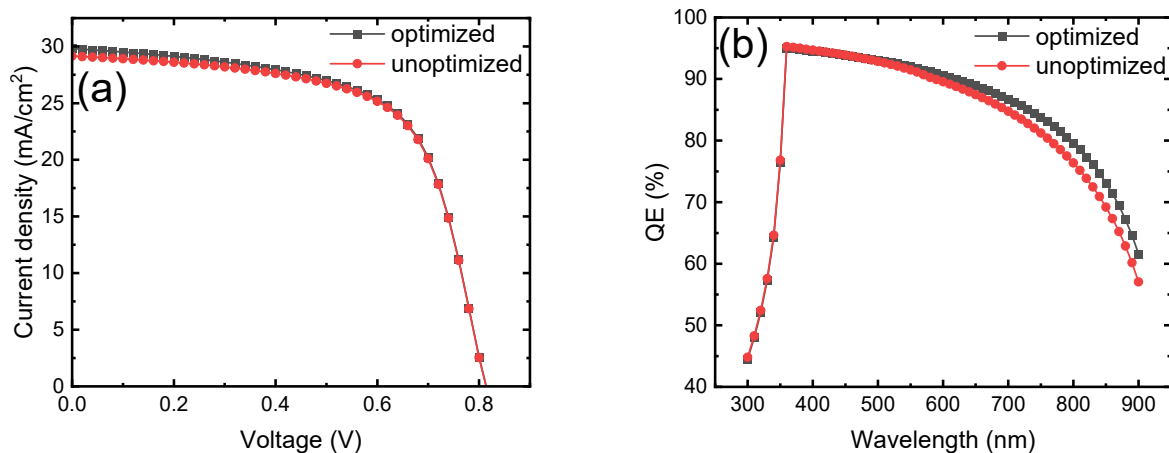


Figure 6. (a) J - V of the optimized (black) and unoptimized (red) and (b) QE curves of the optimized (black) and unoptimized (red)

The final optimized PSC gave a turnover PCE of 15.411%, FF of 63.525%, J_{sc} of 29.812 mA/cm^2 , and V_{oc} of 0.814 V. By enhancing the film quality of the absorber and ETL, a satisfactory electron density can be attained. The quantum efficiency also shows stronger absorption in the visible region and near IR region for the optimized device.

3.5. Effect of Temperature on the optimized PSC device

Temperature is one of the crucial factors that influence the performance of solar cells. It is very important to carefully look at the optimal solar cell's performance in relation to operating temperature. Figure 7a shows the *J-V* curve with temperature variation (from 280-360 K), while Figure 7b & c illustrate the PCE & FF and *J_{sc}* & *V_{oc}* with temperature dependence. When the temperature was raised from 280 to 360 K, the PCE, *J_{sc}*, and *V_{oc}* declined steadily. Practically, a rise in temperature leads to the recombination of carriers, but it also causes a significant increase in FF partly due to higher phonon motions and collisions (see Table 6).

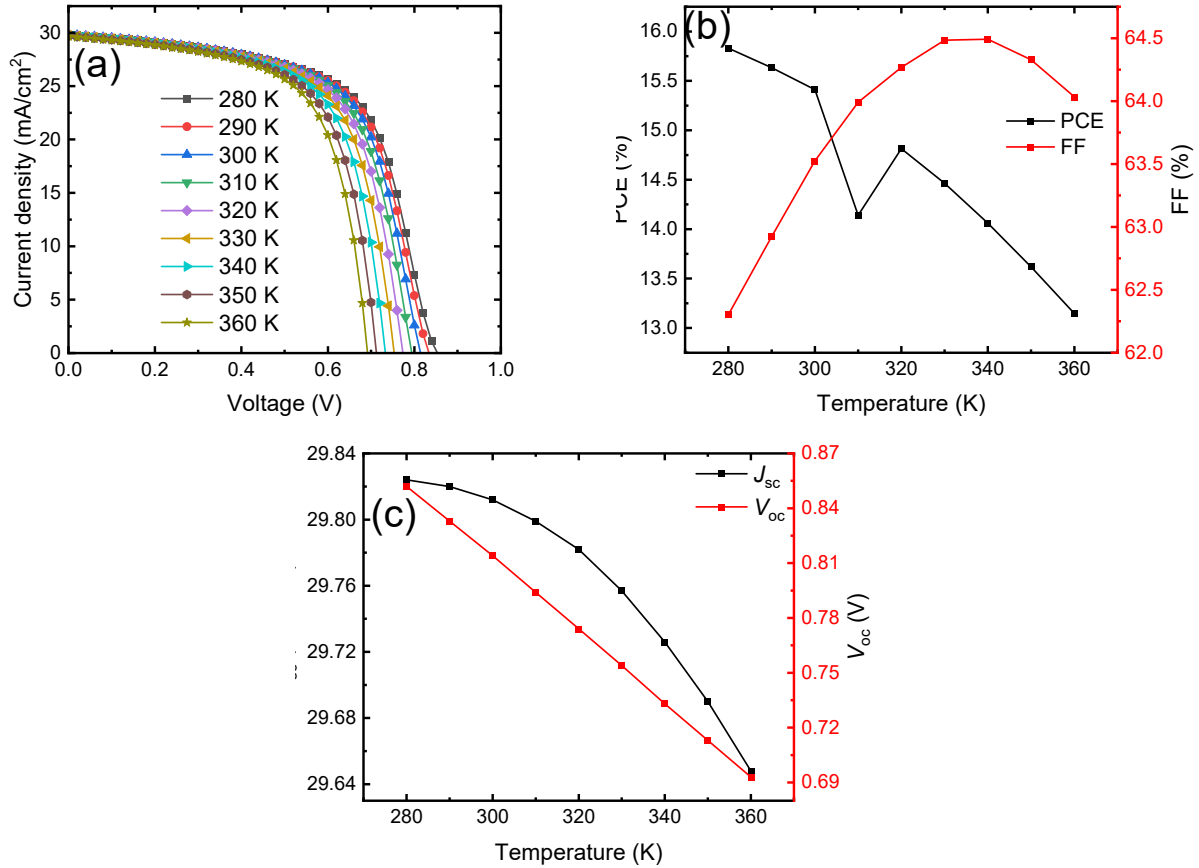


Figure 7. (a) *J-V* with varied temperature under illumination, (b) PCE and FF with respect to varied temperature, and (c) *J_{sc}* and *V_{oc}* with respect to varied temperature

Table 6. Electrical parameters based on varied Temperature

Temperature (K)	PCE (%)	FF (%)	<i>J_{sc}</i> (mA/cm ²)	<i>V_{oc}</i> (V)
280	15.830	62.301	29.824	0.852
290	15.633	62.923	29.820	0.833
300	15.411	63.525	29.812	0.814
310	14.140	63.990	29.799	0.794
320	14.814	64.267	29.782	0.774
330	14.464	64.484	29.757	0.754
340	14.061	64.491	29.726	0.733
350	13.619	64.329	29.690	0.713
360	13.147	64.034	29.648	0.693

The FF experienced a decrease after 350 K. The drop in FF may be attributed to lower stability, higher recombination rate, and longer lifetimes associated with carriers in the absorber [22]. The *V_{oc}* decrease is attributed to lattice expansion and interatomic bond attenuation brought on by higher temperatures [36]. Also, the rise in saturation current is the reason for the decrease in PCE, which also results in an increase in recombination rate [37]. At greater temperatures, defects or trap states, for example, may become active non-radiative recombination centers [22]. These centers provide carriers with an additional path for recombination without emitting photons, which increases the overall recombination rate and may lessen the contribution from radiative recombination.

4. CONCLUSIONS

In this research, the one-dimensional solar cell capacitance simulator (SCAPS-1D) software was utilized to perform a numerical simulation on a lead-free MASnI₃-based perovskite solar cell. The device structure is composed of TiO₂ as

ETL, MASnI₃ as absorbing material, and Cu₂O as HTL in a configuration FTO/TiO₂/MASnI₃/Cu₂O/Au. The simulation of the initial device gave a turnover output of 15.315%, 64.580%, 29.152 mA/cm² and 0.813 V for PCE, FF, J_{sc} , and V_{oc} . The effect of absorber and ETL thicknesses were explored to obtain optimized values of 0.5 and 0.02 μ m, resulting in PCE of 15.411%, FF of 63.525%, J_{sc} of 29.812 mA/cm², and V_{oc} of 0.814 V. The effect of temperature was studied by varying the temperature from 280–360 K. The device's efficiency decreases with increasing temperature which can be attributed to the rise in saturation current leading to an increase in recombination rate. The results obtained are somewhat encouraging and have paved the path for developing cost-effective, eco-friendly, and comparable state-of-the-art, high-efficiency perovskite solar cells.

Acknowledgments

The authors would like to thank Professor Marc Burgelman and his team at the Department of Electronics and Information Systems, University of Gent for the development of the SCAPS software package and for allowing its use.

ORCID

Abubakar S. Yusuf, <https://orcid.org/0000-0001-8181-9728>; Nicholas Tasie, <https://orcid.org/0000-0001-8398-2596>
Anthony C. Ozurumba, <https://orcid.org/0009-0003-2269-7742>; Eli Danladi, <https://orcid.org/0000-0001-5109-4690>

REFERENCES

- [1] A. Kojima, K. Teshima, Y. Shirai, and T. Miyasaka, "Organometal Halide Perovskites as Visible-Light Sensitizers for Photovoltaic Cells," *J. Am. Chem. Soc.* **131**(17), 6050–6051 (2009). <https://doi.org/10.1021/ja809598r>
- [2] E. Danladi, *et al.*, "Defect and doping concentration study with series and shunt resistance influence on graphene modified perovskite solar cell: A numerical investigation in SCAPS-1D framework," *Journal of the Indian Chemical Society*, **100**(5), 101001 (2023). <https://doi.org/10.1016/j.jics.2023.101001>
- [3] E. Danladi *et al.*, "Broad-band-enhanced and minimal hysteresis perovskite solar cells with interfacial coating of biogenic plasmonic light trapping silver nanoparticles," *Materials Research Innovations*, **27**(7), 521–536 (2023). <https://doi.org/10.1080/14328917.2023.2204585>
- [4] Z. Qu, F. Ma, Y. Zhao, X. Chu, S. Yu, and J. You, "Updated Progresses in Perovskite Solar Cells," *Chinese Phys. Lett.* **38**(10), 107801 (2021). <https://doi.org/10.1088/0256-307X/38/10/107801>
- [5] M.K. Hossain, *et al.*, "Numerical simulation and optimization of a CsPbI₃-based perovskite solar cell to enhance the power conversion efficiency," *New J. Chem.* **47**(10), 4801–4817 (2023). <https://doi.org/10.1039/D2NJ06206B>
- [6] M.K. Hossain, *et al.*, "Deep Insights into the Coupled Optoelectronic and Photovoltaic Analysis of Lead-Free CsSnI₃ Perovskite-Based Solar Cell Using DFT Calculations and SCAPS-1D Simulations," *ACS Omega*, **8**(25), 22466–22485 (2023). <https://doi.org/10.1021/acsomega.3c00306>
- [7] S.D. Stranks, and H. J. Snaith, "Metal-halide perovskites for photovoltaic and light-emitting devices," *Nature Nanotech.* **10**(5), 391–402 (2015). <https://doi.org/10.1038/nnano.2015.90>
- [8] Md.R. Islam, A.A.M. Mazumder, Md.R.H. Mojumder, A.S.M.Z. Shifat, and M.K. Hossain, "Strain-induced tunable optoelectronic properties of inorganic halide perovskites APbCl₃ (A = K, Rb, and Cs)," *Jpn. J. Appl. Phys.* **62**(1), 011002 (2023). <https://doi.org/10.35848/1347-4065/acb09e>
- [9] A. Thakur, D. Singh, and S.K. Gill, "Numerical simulations of 26.11% efficient planar CH₃NH₃PbI₃ perovskite n-i-p solar cell," *Materials Today: Proceedings*, **71**, 195–201 (2022). <https://doi.org/10.1016/j.matpr.2022.08.423>
- [10] H. Bencherif, *et al.*, "Performance enhancement of (FAPbI₃)_{1-x}(MAPbBr₃)_x perovskite solar cell with an optimized design," *Micro and Nanostructures*, **171**, 207403 (2022). <https://doi.org/10.1016/j.micrna.2022.207403>
- [11] H. Bencherif, and M.K. Hossain, "Design and numerical investigation of efficient (FAPbI₃)_{1-x}(CsSnI₃)_x perovskite solar cell with optimized performances," *Solar Energy*, **248**, 137–148 (2022). <https://doi.org/10.1016/j.solener.2022.11.012>
- [12] Y. Zhou, and K. Zhu, "Perovskite Solar Cells Shine in the 'Valley of the Sun,'" *ACS Energy Lett.* **1**(1), 64–67 (2016). <https://doi.org/10.1021/acseenergylett.6b00069>
- [13] B.V. Lotsch, "New Light on an Old Story: Perovskites Go Solar," *Angew Chem. Int. Ed.* **53**(3), 635–637 (2014). <https://doi.org/10.1002/anie.201309368>
- [14] H. Sabbah, "Numerical Simulation of 30% Efficient Lead-Free Perovskite CsSnGeI₃-Based Solar Cells," *Materials*, **15**(9), 3229 (2022). <https://doi.org/10.3390/ma15093229>
- [15] E. Danladi, A.O. Salawu, M.O. Abdulmalik, E.D. Onoja, E.E. Onwoke, and D.S. Adepehin, "Optimization of Absorber and ETM Layer Thickness for Enhanced Tin based Perovskite Solar Cell Performance using SCAPS-1D Software," *PA*, **02**(01), 1–11 (2022). <https://doi.org/10.47514/phyaccess.2022.2.1.001>
- [16] E. Danladi, M. Kashif, A. Ichoja, and B. B. Ayiyya, "Modeling of a Sn-Based HTM-Free Perovskite Solar Cell Using a One-Dimensional Solar Cell Capacitance Simulator Tool," *Trans. Tianjin Univ.* **29**(1), 62–72 (2023). <https://doi.org/10.1007/s12209-022-00343-w>
- [17] W. Shockley, and H.J. Queisser, "Detailed Balance Limit of Efficiency of p-n Junction Solar Cells," *Journal of Applied Physics*, **32**(3), 510–519 (1961). <https://doi.org/10.1063/1.1736034>
- [18] D. Jalalian, A. Ghadimi, and A. Kiani, "Modeling of a high performance bandgap graded Pb-free HTM-free perovskite solar cell," *Eur. Phys. J. Appl. Phys.* **87**(1), 10101 (2019). <https://doi.org/10.1051/epjap/2019190095>
- [19] M.K. Hossain, *et al.*, "An extensive study on multiple ETL and HTL layers to design and simulation of high-performance lead-free CsSnCl₃-based perovskite solar cells," *Sci. Rep.* **13**(1), 2521 (2023). <https://doi.org/10.1038/s41598-023-28506-2>
- [20] M.K. Hossain, *et al.*, "Numerical Analysis in DFT and SCAPS-1D on the Influence of Different Charge Transport Layers of CsPbBr₃ Perovskite Solar Cells," *Energy Fuels*, **37**(8), 6078–6098 (2023). <https://doi.org/10.1021/acs.energyfuels.3c00035>
- [21] J. Chen, and N.-G. Park, "Inorganic Hole Transporting Materials for Stable and High Efficiency Perovskite Solar Cells," *J. Phys. Chem. C*, **122**(25), 14039–14063 (2018). <https://doi.org/10.1021/acs.jpcc.8b01177>
- [22] E. Danladi, *et al.*, "Highly efficient, hole transport layer (HTL)-free perovskite solar cell based on lithium-doped electron transport layer by device simulation," *Emergent Mater.* **6**(6), 1779–1795 (2023). <https://doi.org/10.1007/s42247-023-00558-0>

- [23] M.K.A. Mohammed, "High-performance hole conductor-free perovskite solar cell using a carbon nanotube counter electrode," *RSC Adv.* **10**(59), 35831–35839 (2020). <https://doi.org/10.1039/D0RA05975G>
- [24] N. Fakhri, M.S. Naderi, S.G. Farkoush, S.S. Nahaei, S.-N. Park, and S.-B. Rhee, "Simulation of Perovskite Solar Cells Optimized by the Inverse Planar Method in SILVACO: 3D Electrical and Optical Models," *Energies*, **14**(18), 5944 (2021). <https://doi.org/10.3390/en14185944>
- [25] S. Zandi, P. Saxena, and N.E. Gorji, "Numerical simulation of heat distribution in RGO-contacted perovskite solar cells using COMSOL," *Solar Energy*, **197**, 105–110 (2020). <https://doi.org/10.1016/j.solener.2019.12.050>
- [26] M.K. Hossain, M.H.K. Rubel, G.F.I. Toki, I. Alam, Md.F. Rahman, and H. Bencherif, "Effect of Various Electron and Hole Transport Layers on the Performance of CsPbI₃-Based Perovskite Solar Cells: A Numerical Investigation in DFT, SCAPS-1D, and wxAMPS Frameworks," *ACS Omega*, **7**(47), 43210–43230 (2022). <https://doi.org/10.1021/acsomega.2c05912>
- [27] E. Danladi, *et al.*, "Modeling and simulation of > 19% highly efficient PbS colloidal quantum dot solar cell: A step towards unleashing the prospect of quantum dot absorber," *Optik*, **291**, 171325 (2023). <https://doi.org/10.1016/j.ijleo.2023.171325>
- [28] P.K. Jha, *et al.*, "Study of Eco-Friendly Organic-Inorganic Heterostructure CH₃NH₃SnI₃ Perovskite Solar Cell via SCAPS Simulation," *J. Electron. Mater.* **52**(7), 4321–4329 (2023). <https://doi.org/10.1007/s11664-023-10267-3>
- [29] K. Nishimura, *et al.*, "Lead-free tin-halide perovskite solar cells with 13% efficiency," *Nano Energy*, **74**, 104858 (2020). <https://doi.org/10.1016/j.nanoen.2020.104858>
- [30] H.-J. Du, W.-C. Wang, and J.-Z. Zhu, "Device simulation of lead-free CH₃NH₃SnI₃ perovskite solar cells with high efficiency," *Chinese Phys. B*, **25**(10), 108802 (2016). <https://doi.org/10.1088/1674-1056/25/10/108802>
- [31] Guo, *et al.*, "Effects of Transition Metal Substituents on Interfacial and Electronic Structure of CH₃NH₃PbI₃/TiO₂ Interface: A First-Principles Comparative Study," *Nanomaterials*, **9**(7), 966 (2019). <https://doi.org/10.3390/nano9070966>
- [32] N.J. Valeti, K. Prakash, and M.K. Singha, "Numerical simulation and optimization of lead free CH₃NH₃SnI₃ perovskite solar cell with CuSbS₂ as HTL using SCAPS 1D," *Results in Optics*, **12**, 100440 (2023). <https://doi.org/10.1016/j.rio.2023.100440>
- [33] M. Liu, M.B. Johnston, and H.J. Snaith, "Efficient planar heterojunction perovskite solar cells by vapour deposition," *Nature*, **501**(7467), 395–398 (2013). <https://doi.org/10.1038/nature12509>
- [34] O.A. Muhammed, E. Danladi, P.H. Boduku, J. Tasiu, M.S. Ahmad, and N. Usman, "Modeling and Simulation of Lead-Free Perovskite Solar Cell Using SCAPS-1D," *EEJP*, (2), 146-154 (2021). <https://doi.org/10.26565/2312-4334-2021-2-12>
- [35] N.F. Mott, and E.A. Davis, *Electronic processes in non-crystalline materials*, 2nd ed. in *International series of monographs on physics*, (Clarendon Press, Oxford, 2012).
- [36] I. Qasim, *et al.*, "Numerical optimization of (FTO/ZnO/CdS/CH₃NH₃SnI₃/GaAs/Au) perovskite solar cell using solar capacitance simulator with efficiency above 23% predicted," *Opt. Quant. Electron.* **53**(12), 713 (2021). <https://doi.org/10.1007/s11082-021-03361-5>
- [37] S. Ahmed, F. Jannat, Md.A.K. Khan, and M.A. Alim, "Numerical development of eco-friendly Cs₂TiBr₆ based perovskite solar cell with all-inorganic charge transport materials via SCAPS-1D," *Optik*, **225**, 165765 (2021). <https://doi.org/10.1016/j.ijleo.2020.165765>

SCAPS-1D АНАЛІЗ НЕТОКСИЧНИХ БЕЗСВИНЦЕВИХ СОНЯЧНИХ ЕЛЕМЕНТІВ НА ОСНОВІ ПЕРОВСКІТУ MASnI₃ З ВИКОРИСТАННЯМ НЕОРГАНІЧНИХ ШАРІВ ТРАНСПОРТУ ЗАРЯДУ

Меттью І. Амані^а, Абубакар С. Юсуф^б, Егвубаре Акпогума^с, Стівен О. Егаге^д, Джеймс Енейе^д, Раймонд М. Агаку^е, Ліліан С. Ечебірі^і, Еммануель У. Ечебірі^г, Еммануель О. Аме^ф, Чінсьєре І. Ерірогу^б, Ніколас Н. Тасі, Ентоні С. Озурумба^і, Елі Данладі^а

^аКафедра фізики, Федеральний університет наук про здоров'я, Отукпо, штат Бенуе, Нігерія

^бКафедра фізики, Федеральний технологічний університет, Мінна, штат Нігер, Нігерія

^сЦентр ядерних технологій, Комісія з атомної енергії Нігерії, Абуджа, Нігерія

^дКафедра фізики, Університет Бінгема, штат Насарава, Нігерія

^еКафедра фізики, Університет штату Бенуе, штат Бенуе, Нігерія

^фКафедра фізики, Державний університет Насарава, штат Насарава, Нігерія

^гВідділ електротехніки/електронної інженерії Нільського університету Нігерії

^іФакультет фізики, Університет штату Нігерії Ннсукка, штат Енузу, Нігерія

^іФакультет фізики, Університет штату Нігерії Ннсукка, штат Енузу, Нігерія

^іАфриканський центр передового досвіду в галузі енергетики майбутнього та електротехнічних систем,

Федеральний технологічний університет, Оверрі, штат Імо, Нігерія

Перовскітні сонячні батареї (PSC) привернули велику увагу завдяки своїй високій ефективності та низькій вартості. У цій дослідницькій роботі сонячний елемент на основі йодиду метиламонію олова (CH₃NH₃SnI₃) моделювався за допомогою інструменту моделювання одновимірної ємності сонячного елемента (SCAPS-1D). Інструмент SCAPS-1D заснований на рівняннях Пуассона та напівпровідників. Після ретельного дослідження початковий пристрій має наступні параметри: Ефективність перетворення потужності (PCE) = 15,315%, коефіцієнт заповнення (FF) = 64,580%, щільність струму (Jsc) = 29,152 mA/cm² і напруга холостого ходу (Voc) = 0,813 В. Досліджено вплив товщини абсорбера та ETL систематично. На продуктивність змодельованого пристрою суттєво вплинула товщина абсорбера та ETL. Оптимізована товщина поглиначка становила 0,5 мкм, а товщина ETL становила 0,02 мкм, що призвело до оптимізованого PCE 15,411%, FF 63,525%, Jsc 29,812 mA/cm² і Voc 0,814 В. Крім того, вплив температури на оптимізований пристрій було оцінено та виявлено, що це впливає на продуктивність пристрою. Ця модель показує перспективу CH₃NH₃SnI₃ як перовскітного матеріалу для виробництва нетоксичних екологічно чистих сонячних елементів з високою ефективністю.

Ключові слова: перовскітний сонячний елемент; SCAPS-1D; CH₃NH₃SnI₃; фотоелектричний

PERFORMANCE OPTIMIZATION OF MgHfS₃ CHALCOGENIDE PEROVSKITE SOLAR CELLS USING SCAPS-1D

 Abdulai M. Feika^a,  Muteeu A. Olopade^{a,b},  Adeyinka D. Adewoyin^{b,c,*}

^aDepartment of Physics, Fourah Bay College, University of Sierra Leone, Freetown, Sierra Leone

^bDepartment of Physics, Faculty of Science, University of Lagos, Akoka, Lagos, Nigeria

^cPhysics Unit, Distance Learning Institute, University of Lagos, Nigeria

*Corresponding Author e-mail: dadeyinka@unilag.edu.ng, kingdavidonfire@gmail.com

Received June 24, 2024; revised August 2, 2024; accepted August 20, 2024

In this work, magnesium hafnium sulfide MgHfS₃ perovskite solar cells have been investigated using numerical modelling and simulation. Perovskite solar cells have received increasing recognition owing to their promising light-harvesting properties. The modelling and simulation of MgHfS₃ was successfully carried out using the Solar cell capacitance simulator (SCAPS-1D) software. Consequently, this study developed a base model structure of FTO/TiO₂/MgHfS₃/Cu₂O/Au and subsequently explored the effect of varying device layer properties such as absorber thickness, total and interface defect densities with a view of optimizing these parameters for better device performance. Simulating the base model gave the performance characteristics of 0.99 V, 25.21 mA/cm², 57.59%, and 14.36% which are the open-circuit voltage (V_{oc}), short-circuit current density (J_{sc}), fill factor (FF) and PCE respectively. The optimal absorber thickness was found to be 300 nm and the optimum density of defects for both TiO₂/Absorber interface and Absorber/Cu₂O interface are respectively 10¹⁰ cm⁻³ and 10⁹ cm⁻³. The obtained optimized PV parameters are $V_{oc} = 1.2629$ V, $J_{sc} = 24.44$ mA/cm², FF = 89.46% and PCE = 27.61%. Also, it was established that increasing the device temperature beyond 300K enhanced the short circuit current while other performance characteristics gradually declined. The obtained results suggest that chalcogenide MgHfS₃ is a potential absorber material candidate for the production of cheap and very efficient environment-friendly perovskite solar cells.

Keywords: SCAPS-1D, Perovskites, Optimization, MgHfS₃, Efficiency

PACS: 78.20.Bh; 84.60.Jt; 74.62.Dh; 73.25.+i; 89.30.Cc; 41.20.Cv; 61.43.Bn

1. INTRODUCTION

Perovskite solar cells have emerged as a third-generation solar cell for the replacement of conventional mono and polycrystalline silicon cells as well as second-generation cells, which have issues relating to high cost of production, low efficiency and toxicity. Research issues faced today in chemistry and physics surround maximizing efficiency and reducing energy loss in solar cells to enhance the achieve better performance of solar harvesting materials.

Organic-inorganic lead halide hybrid perovskite solar cells (LHPSC) were introduced as a third-generation device to solve issues of high fabrication cost, low efficiency and toxicity attributed to first-generation silicon solar cells and second-generation thin film solar cells and within a very short time, they achieved an exceptional efficiency of 26.1% [1]. Even though they showed high efficiency compared to their silicon-based counterparts, LHPSC faces intrinsic instability problems caused by moisture, heat and other environmental factors. The toxicity of the lead (Pb) in their material structure also poses a problem and this has restricted their commercialization. Hence, there is a need for the pursuit of substitute materials such as chalcogenide perovskites.

Chalcogenide perovskites (CPs) are good, non-toxic and environmentally friendly photovoltaic (PV) materials which emerged as a result of the shortcomings of hybrid perovskites. They possess both the good electrical properties of halides and the good stability of oxides combined. These properties show they can be good absorbers in solar cells. CPs also follow the regular ABX₃ formula for perovskites, where A and B respectively represent group II cations and group IV transition metals, and X for chalcogen anions, originating from the mineral calcium titanate (CaTiO₃) [2].

A variety of CP materials like Barium Zirconium Sulphide (BaZrS₃) [3], Strontium Zirconium Sulphide (SrZrS₃), Calcium Zirconium Sulphide (CaZrS₃), Strontium Titanium Sulphide (SrTiS₃) and Calcium Strontium Sulphide (CaSnS₃) [4] have been subjected to experimental investigations to ascertain their usefulness for solar cell application. It has also been investigated that Barium zirconium sulphide (BaZrS₃), Strontium zirconium sulphide (SrZrS₃), Barium Hafnium sulphide (BaHfS₃), Strontium Hafnium sulphide (SrHfS₃), Calcium zirconium sulphide (CaZrS₃) and Calcium Hafnium sulphide (CaHfS₃) CPs have a perovskite-type structure with ideal bandgap for application in Photovoltaics [5], [6], [7], [8]. Excitonic properties obtained from theoretical research of CPs reveal that their binding energy (E_B) is greater than that of lead-halide-based perovskites. Also, bandgap and absorption coefficient obtained from Spectroscopic Limited Maximum Efficiency (SLME) show that CPs is a very promising solar cell absorber [9].

Recently, Balogun et al., with the use of density functional theory (DFT), investigated the optoelectronic properties of Chalcogenide Magnesium Hafnium Sulfide (MgHfS₃) to determine its bandgap, absorption spectra and material-dependent non-radiation recombination losses. They obtained the band gap and absorption coefficient as 1.43 eV, 4.9×10⁸ m⁻¹ [10]. This study showed that MgHfS₃, whose bandgap is almost near the optimum bandgap for single-junction devices can serve as an efficient absorber material for photovoltaics for which this further study is based.

Simulation software such as solar cell capacitance simulator (SCAPS-1D) is most times employed in the exploration of potential single- or multijunction devices to find possible new device structures. It is a one-dimensional simulator that is implemented in the design of thin film solar cell architectures using several layers of semiconductors. The SCAPS software which was created for the study of thin films like CIGS and CdTe type solar cells can simulate solar cell electrical parameters like the current-voltage and quantum efficiency curves among others. Recently, it has been applied to other thin films like CZTS, Perovskites, crystalline silicon cells, amorphous silicon and bulk heterostructures. SCAPS-1D has been used by many groups for the construction of the latest device configurations by using recent absorber materials like Antimony Selenide (Sb₂Se₃), and Antimony Sulfide (Sb₂S₃) [11], [12], [13], [14], Cu₂XSnS₄ (where X means Fe, Mg, Mn, Ni, or Sr) [15], Tungsten Diselenide (WSe₂) [16], Tin Sulphide (SnS) [17] and perovskites materials like (FAPbI₃) [18], CsPbI₃ [19], CsPbBr₃ [20], Cs₂SnI₆ [21], Cs₂TiBr₆ [22], CsGeI₃ [23] Cs₂AuBiCl₆ [24], and Cs₄CuSb₂Cl₁₂ [25]. In most of these studies, the results from their simulations are in tandem with experimental results.

In this research, MgHfS₃ is used as solar cell absorber and it is systematically optimized with the aid of SCAPS simulator. Initially, a planar n-i-p CP device structure (FTO/TiO₂/MgHfS₃/Cu₂O/Au) is constructed without considering the impact of parasitic resistances. Thereafter, a methodical study of the device operation is done while varying the CP absorber layer thickness, total (N_t) and interfacial (ETL/Absorber and Absorber/HTL) defect densities. We further explored the influence of parasitic resistances; Series resistance (R_s), Shunt resistance (R_{sh}), and working temperature over the final optimized device to assess the performance of prospective Chalcogenide Perovskite solar devices.

2. DEVICE STRUCTURE AND SIMULATION METHODOLOGY

In this work, a one-dimensional n-i-p planar heterojunction perovskite device architecture (FTO/TiO₂/MgHfS₃/Cu₂O/Au) is simulated using the SCAPS-1D (version 3.3.10) software which is a one-dimensional simulation software developed by the Department of Electronics and Information systems, Ghent, Belgium, that computes energy bands, concentrations, J-V characteristics, ac characteristics and spectral response using the basic semiconductor equations comprising of Poisson's (1) and Continuity equations for holes (2) and electrons (3) as shown below [26].

$$\frac{d}{dx} \left[\varepsilon(x) \frac{d\psi}{dx} \right] = q [p(x) - n(x) + n_D^+(x) - n_A^-(x) + p_t(x) - n_t(x)] \quad (1)$$

$$\frac{1}{J} \frac{dJ_p}{dx} + R_p(x) - G(x) = 0 \quad (2)$$

$$-\frac{1}{J} \frac{dJ_n}{dx} + R_n(x) - G(x) = 0 \quad (3)$$

Where ε is the permittivity, q is the electron charge, ψ is the electrostatic potential, n and p are both electron and hole concentrations, n_t is the trapped electron, p_t is trapped hole, n_D^+ is the ionized donor-like doping and n_A^- is the ionized acceptor-like doping concentration, $R_n(x)$, $R_p(x)$ are electron and hole recombination rates, $G(x)$ is the generation rate, J_n and J_p are the electron and hole current density. The SCAPS software comes in handy since it can sometimes be risky, time and resource-consuming to design and fabricate a solar cell without numerically simulating it first. Simulation therefore minimizes risk and time and also analyses the cell layers for proper optimization.

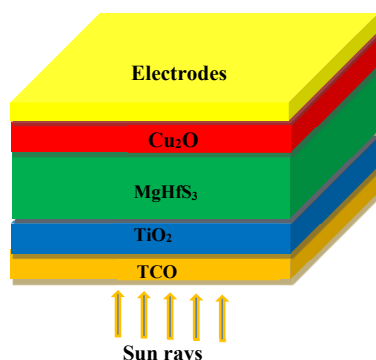


Figure 1. The schematic of n-i-p chalcogenide perovskite solar cell

In this simulation, the absorber layer material used was Magnesium Hafnium Sulfide (MgHfS₃) with a bandgap of 1.43 eV. Titanium Dioxide (TiO₂) and Cuprous Oxide (Cu₂O) were used as the electron transport layer (ETL), and as Hole Transport Layer (HTL) respectively. The proposed architecture is shown in Fig. 1 and each simulation was performed using a solar spectrum of one sun AM 1.5 G and 300K working temperature.

Input parameters for all the layers, such as material bandgap, electron and hole mobilities, electron affinity, ETL/Absorber and Absorber/HTL interface defect densities and other input parameters listed in Table 1 and Table 2 respectively are adopted from results of previously published theoretical and experimental work [6], [7], [10], [18], [27], [28], [29]. The optical absorption coefficients of

the three layers were obtained by using the square root sub-model of the SCAPS traditional optical model. Also, the thermal velocity of the electron and hole values are inputted as 1×10^7 cm s⁻¹, and the front and back contacts (FTO and Au) work functions are respectively taken as 4.4 eV and 5.1 eV. The influence of parasitic resistances; Series resistance (R_s) and Shunt resistance (R_{sh}), and working temperature over the final optimized device was explored further to investigate the behaviour of prospective Chalcogenide Perovskite-based single-junction devices.

Table 1. Basic device model layer input values

PARAMETERS	FTO (TCO) [30]	TiO ₂ (ETL) [27]	MgHfS ₃ (Absorber) [6], [7], [10]	Cu ₂ O (HTL) [28]
Thickness (nm)	500	30	500	100
Bandgap (eV)	3.5	3.2	1.43	2.17
Affinity	4	3.9	4.1	3.2
Permittivity	9	9	9.6	7.11
Effective density of states at conduction band	2.2×10^{18}	2.2×10^{18}	2.2×10^{18}	2.02×10^{17}
Effective density of states at valence band	1.8×10^{19}	1.8×10^{19}	1.8×10^{19}	1.1×10^{19}
Electrons mobility	20	20	0.017	200
Holes mobility	10	10	0.059	80
Density of n-type doping	1.0×10^{18}	1.0×10^{19}	1.0×10^{12}	0
Density of p-type doping	0	1	1.0×10^{12}	1.0×10^{18}
Defect density	1.0×10^{15}	1.0×10^{15}	1.0×10^{15}	1.0×10^{15}

Table 2. ETL/Absorber and Absorber/HTL interfacial defects values used in the simulated model

PARAMETERS	ETL/Absorber	Absorber/HTL
Defect type	neutral	Neutral
Capture cross-section e ⁻ s (cm ²)	1.0×10^{-15}	1.0×10^{-18}
Capture cross-section h ⁺ s (cm ²)	1.0×10^{-15}	1.0×10^{-16}
Energetic distribution	Single	Single
Reference for defect energy level (E _t)	Above the highest E _v	Above the highest E _v
Energy with respect to reference (eV)	0.6	0.05
Total defect (cm ⁻²)	1.0×10^{11}	1.0×10^{12}

3. RESULTS AND DISCUSSION

Generally, the absorption coefficient(α) of PV material can help determine how the device performs. Fig. 2. shows the SCAPS software-generated absorption coefficient of the three layers (ETL, CP absorber, and HTL layers) as a variation of the energy function.

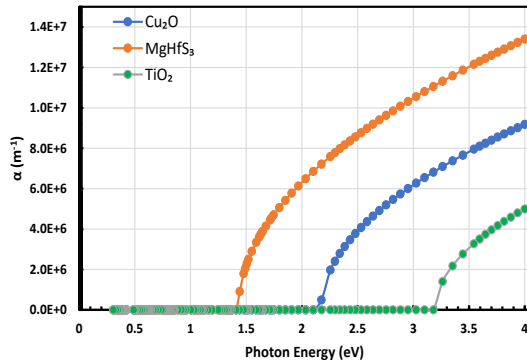


Figure 2. Plot showing the absorption coefficients of Absorber, ETL and HTL layers.

We observed for the absorber, high band-edge values, which confirms the strong light absorption mentioned in previously published theoretical results [10].

The simulation of the basic model device architecture FTO (500 nm)/TiO₂ (30 nm)/MgHfS₃ (500 nm)/Cu₂O (100 nm)/Au shown in Fig. 1 was carried out using the SCAPS simulator. The resulting current-voltage characteristics (J-V) graph is shown in Fig. 3a, wherein the major PV parameters like the open-circuit voltage (V_{oc}), short-circuit current density (J_{sc}), fill factor (FF) and PCE are 0.99 V, 25.21 mA/cm², 57.59%, 14.36% respectively. The plotted quantum efficiency (QE) graph for the device is displayed in Fig. 3b, where it is observed that the QE enlarged rapidly to the apex of 92% at 360 nm and then decreased to zero at 860 nm. Hence, the optical absorption edge is at 860 nm. Consequently, the QE curve completely covers the entire visible spectrum.

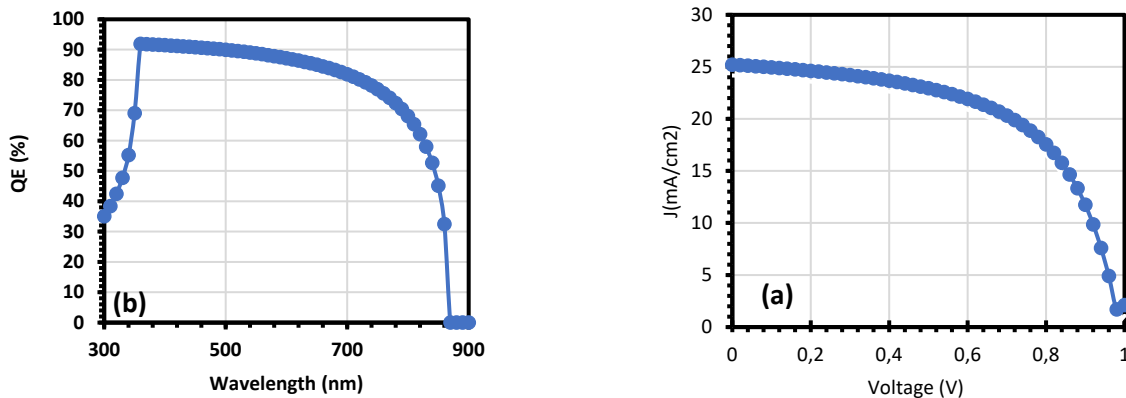


Figure 3. Characteristic J-V curve (a) and QE curve (b) of the Chalcogenide perovskite device.

3.1 Effect of variation of thickness of Absorber layer

The absorber layer thickness is a key simulation parameter since it plays an important part in the device's operation. The absorber layer must be optimized to absorb a maximum number of photons which in turn leads to the required electron-hole pair generation. Reducing the thickness results in a very close depletion layer resulting in an increment in the recombination rate and consequently decreasing the Power Conversion Efficiency (PCE)[31].

Consequently, the absorber thickness was tuned from 100nm to 600nm, keeping all other parameters constant. Its effect on the device efficiency was studied to establish the optimal absorber layer thickness. It was observed that the device's PCE significantly increased from 11.93% to 16.13% while increasing the absorber thickness from 100 nm to 300 nm and then started decreasing as shown in Figure 4. This can be attributed to the absorber layer thickness greater than the optimal limit, and the charge carrier diffusion length, which results in the creation of higher recombination within the layer. The results denote an optimal thickness of 300nm with a corresponding maximum PCE of 16.13% and a fill factor of 68.58%.

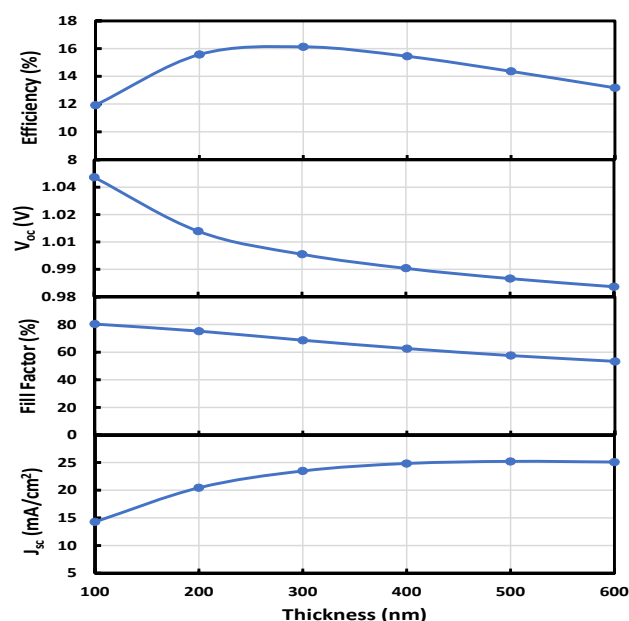


Figure 4. Plot of PV parameters versus absorber layer thickness

recombination occurring. However, the FF and J_{sc} values almost remained the same until N_t values increased above 10^{13} cm^{-3} . As the N_t increases, there is a possible reduction in diffusion lengths of electrons and holes [35]. Hence, lower N_t values give excellent performance in the device as a result of the lower rate of recombination in the absorber layer [36].

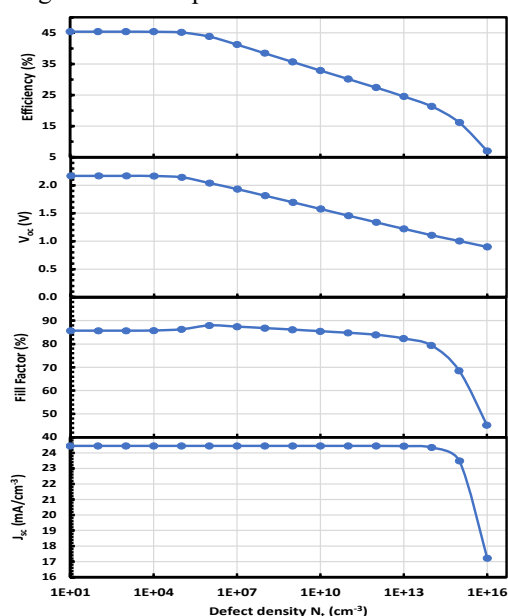


Figure 5. Influence of device PV parameters on absorber defect density.

3.2 Influence of the Absorber Layer Defect Density

In PSC, the defect density of the absorber hugely affects device performance. The overall performance of the PSC can be reduced for higher absorber defects which can result in higher recombination due to the generation of pinholes and a higher rate of degradation of the film [32], [33]. These defects are mostly at the grain surfaces, interfaces and/or boundaries, as a result of badly organized atoms, dangling bonds, film surface dislocation and poor stoichiometry compositions at grain surfaces [34].

Therefore, a systematic investigation on the effect of the influence of the absorber's defect density on the device's parameters by varying its value from 10 cm^{-3} to 10^{16} cm^{-3} as depicted in Fig. 5. It was observed that there is no significant change in the values of both PCE and V_{oc} , while varying the values from 10 cm^{-3} to 10^5 cm^{-3} . After this, there was a gradual decrement observed, which might be because of higher magnitudes of

recombination occurring. However, the FF and J_{sc} values almost remained the same until N_t values increased above 10^{13} cm^{-3} . As the N_t increases, there is a possible reduction in diffusion lengths of electrons and holes [35]. Hence, lower N_t values give excellent performance in the device as a result of the lower rate of recombination in the absorber layer [36].

The optimized defect density value of 10^5 cm^{-3} will be used in the next section to study the influence of the $\text{TiO}_2/\text{Absorber}$ and $\text{Absorber}/\text{Cu}_2\text{O}$ interface defect densities on the PV.

3.3 Effect of $\text{TiO}_2/\text{Absorber}$ and $\text{Absorber}/\text{Cu}_2\text{O}$ interfaces defect densities

The processing technique used in producing third-generation solar cells plays a crucial role in their performance. However, interfacial defects are introduced because of structural mismatch. Imperfections in the perovskite/charge extraction layer heterojunctions cause non-radiative losses, which induce V_{oc} loss [37].

In this section, the device performance is further studied by investigating the effect of interfacial defects, such as the $\text{TiO}_2/\text{Absorber}$ and $\text{Absorber}/\text{Cu}_2\text{O}$ interface defects in the device. The density of the $\text{TiO}_2/\text{Absorber}$ interface defects is varied from 10^5 to 10^{15} cm^{-3} . The 'localized above the valence band edge (E_v)' defect state was chosen for this simulation.

The effect of the $\text{TiO}_2/\text{Absorber}$ interface defect density is shown in Fig. 6(a). It is observed that the FF,

V_{oc} , J_{sc} and PCE reduced significantly as the defect density exceeds 10^{10} cm^{-3} . The reduction in defect density is because of the trap-assisted form of recombination occurring at this interface [38]. No significant contribution was noted beyond 10^{10} cm^{-3} , which signifies that a threshold has been reached to ensure optimal device performance.

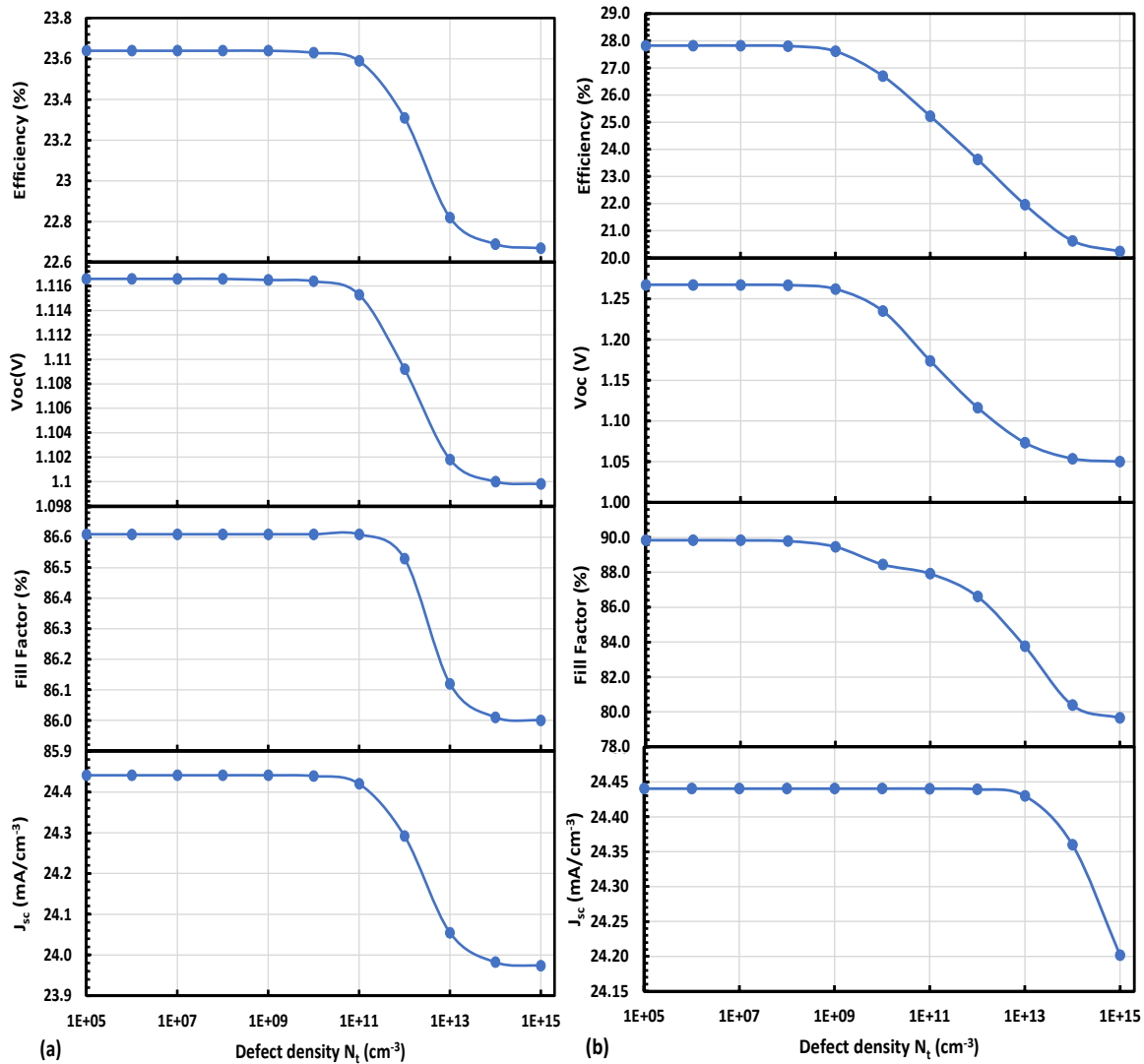


Figure 6. Variation of device PV parameters with defect density at (a) $\text{TiO}_2/\text{Absorber}$ (b) $\text{Absorber}/\text{Cu}_2\text{O}$ interface

The defect density for the $\text{Absorber}/\text{Cu}_2\text{O}$ interface was gradually tuned from 10^5 cm^{-3} to 10^{15} cm^{-3} while keeping the other parameters constant as shown in Fig. 6(b). Consequently, the PCE was drastically altered from 27.61% to 20.24% as the defect density goes beyond 10^9 cm^{-3} whilst the J_{sc} reduced drastically with the defect density exceeding 10^{13} cm^{-3} . It was observed that the $\text{Absorber}/\text{Cu}_2\text{O}$ interface has more impact compared to the $\text{TiO}_2/\text{Absorber}$ interface [39], [40], which may be connected to higher carrier recombination because of the large defect density at the $\text{Absorber}/\text{Cu}_2\text{O}$ interface. Since no crucial changes were observed in the device below the defect density of 10^9 cm^{-3} , the simulated device was considered to be in its optimal performance. It is therefore clear that the increments in the interfacial defect densities particularly influence the V_{oc} and FF instead of the J_{sc} , for both $\text{TiO}_2/\text{Absorber}$ and $\text{Absorber}/\text{Cu}_2\text{O}$ interfaces, which consequently reduces the performance of the device because of more traps and recombination zones. Therefore, the optimum density of defects for both $\text{TiO}_2/\text{Absorber}$ interface and $\text{Absorber}/\text{Cu}_2\text{O}$ interface are respectively 10^{10} cm^{-3} and 10^9 cm^{-3} . Hence, the PCE significantly deteriorates beyond these limits.

The optimized basic device layers input parameters, like the absorber thickness and defect density (N_t), and $\text{TiO}_2/\text{Absorber}$ and $\text{Absorber}/\text{Cu}_2\text{O}$ interfacial defect densities are then incorporated into the device and simulated using these optimum values. Also, the thickness, within the ranges of 30nm to 100nm for the ETL layer and 100nm to 150nm for the HTL layer were tuned respectively to enhance the PV parameters. It was observed that there was no significant contribution of the ETL and HTL layer thicknesses, to the device performance. Therefore, the thicknesses of both ETL and HTL were maintained throughout the simulation. The resulting current-voltage (J-V) characteristics and quantum efficiency of the optimized device is shown in Fig. 7(a) and 7(b) respectively. The obtained optimized PV parameters are $V_{oc} = 1.2629 \text{ V}$, $J_{sc} = 24.44 \text{ mA}/\text{cm}^2$, $\text{FF} = 89.46\%$ and $\text{PCE} = 27.61\%$.

It was however observed that the device performance is enhanced greatly in comparison with the base simulation values. Consequently, the PCE improved from 14.36 % to 27.61 %. The obtained QE graph shown in Fig. 7(b) indicates a major upgrade in the QE compared to the initial simulation values as depicted in Fig. 3(b) and Fig. 7(b). These results of the optimized device depict that the absorber thickness, defect density and Interfacial defect densities play an important part in PV performance enhancement.

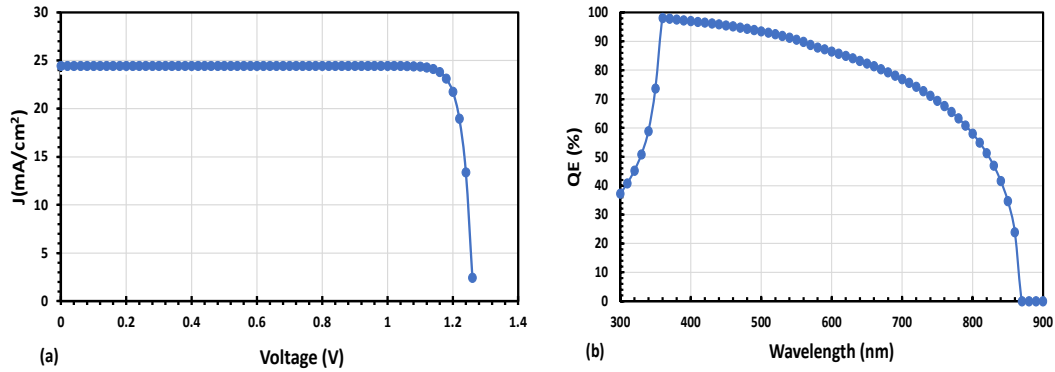


Figure 7. J-V curve (a) and QE curve (b) of optimum CP device.

3.4 Influence of Parasitic Resistances on Device Operation

In actual solar cells, series (R_s) and shunt (R_{sh}) resistances are the main loss mechanisms affecting the performance of the system [18] and they can give a clear impression of how the solar cell operates. Generally, low R_s and higher R_{sh} are associated with high device efficiency. R_s emanates mainly from the reaction of migrated ions from the perovskites layer to the metal contacts thereby restricting charge transfer and resulting in low V_{oc} [41], [42]. R_{sh} is a result of pinholes in the layers or leakage currents caused by manufacturing defects, which in ideal devices cannot be avoided completely but should be kept near the ideal case.

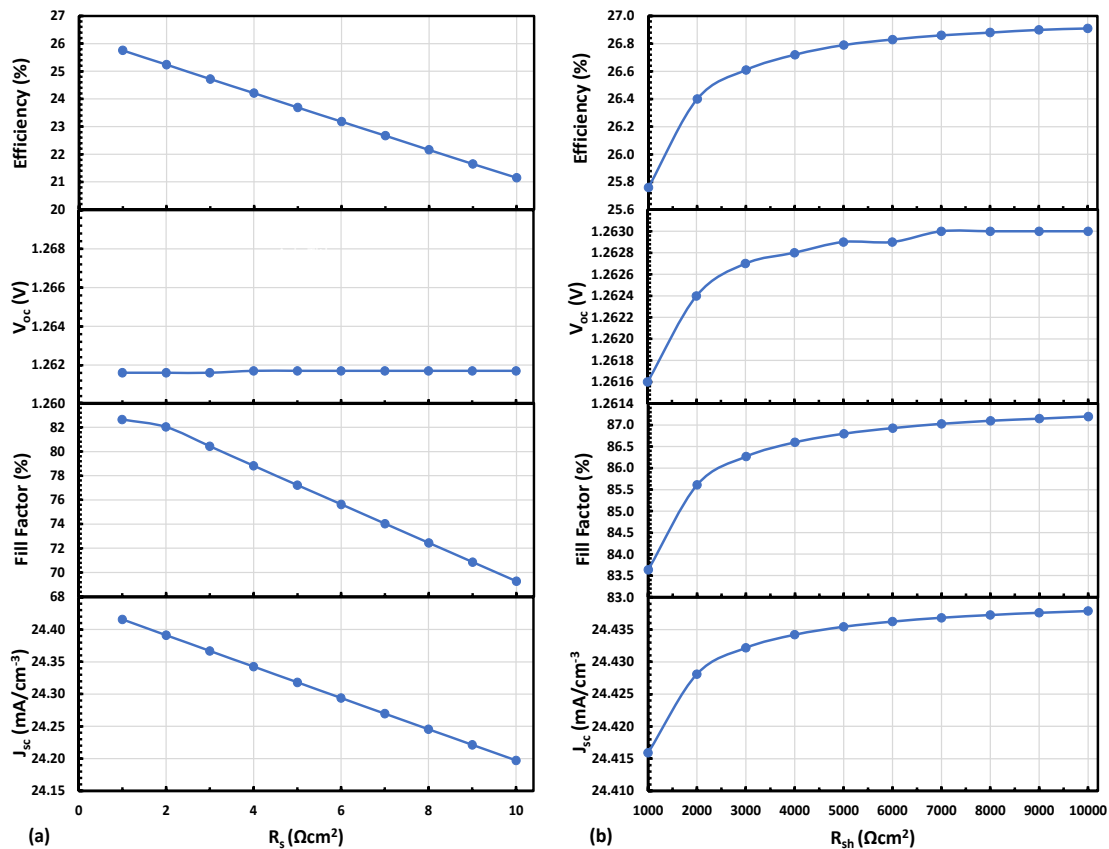


Figure 8. Plots showing the relationship of PV parameters with parasitic resistances, (a) R_s and (b) R_{sh}

In this section, the R_s were varied from 1 Ωcm^2 to 10 Ωcm^2 and R_{sh} from 1000 Ωcm^2 to 10000 Ωcm^2 , to better understand how they influence the operation of the optimized device. The resulting graph illustrating the influence of R_s and R_{sh} on the PV parameters is depicted in Fig. 8(a) and (b) respectively. The results indicated that a slight rise in R_s strongly

reduces both the FF and PCE from 82.64 % to 69.25 % and 25.76 % to 21.15 % respectively, as depicted in Fig. 8(a). Also, as illustrated in Fig. 8(b), the FF, J_{sc} , V_{oc} and PCE rapidly increase with an increment in R_{sh} , with PCE enhancing from 25.76 % to 26.91 %. Therefore, the device performance is improved for higher R_{sh} values. In a real device, solvents and additives are used to enhance morphology behaviour, and passivation substances that perfectly bar shunt pathways are deployed to increase or maintain the R_{sh} value for the effective performance of the device [43], [44], [45], [46].

3.5 Effect of working temperature

Since working temperature has as a significant effect on the operations of the solar cell, temperature values were varied from 300K to 400K under 1 sun constant illumination, while keeping all other simulation input parameters constant. The resulting plot showing the device's PV parameters with different working temperatures is shown in Fig. 9. wherein it was observed that a significant decrease in all PV parameters, except J_{sc} , when the temperature was increased.

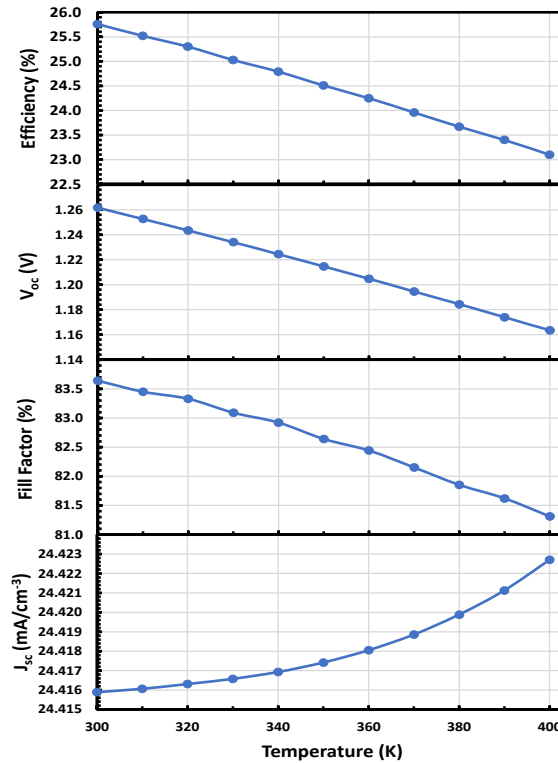


Figure 9. Plot showing the variation of PV parameters with different working temperatures

The V_{oc} behaviour and its temperature dependence can be described by the relation [35], [47].

$$\frac{d}{dT}(V_{oc}) = \frac{V_{oc}}{T} = \frac{E_g/q}{T} \quad (4)$$

Equation (4) shows that an increase in temperature is associated with V_{oc} decrement, which in turn increases the reverse saturation current and a clear decrease in the PCE of the device. The temperature increase may cause some vibrations as a result of thermal excitations, resulting in the recombination of charge carriers [48].

4. CONCLUSION

In this study, we investigated chalcogenide $MgHfS_3$ as an absorber material for solar cells. Consequently, a n-i-p solar cell structure with $MgHfS_3$ perovskite as an absorber layer was systematically modelled and simulated using SCAPS-1D. It was noted that the overall PCE of the PV device baseline model improved from 14.36% to 26.91% through the systematic optimization of the absorber layer thickness, optimum total and interfacial defect densities. The impact on the device performance by parasitic resistances and working temperature was also investigated. There was a reduction in device performance with the introduction of series resistance and increasing working temperature, which provided some ideas on the performance of the device. Our result identifies chalcogenide $MgHfS_3$ as a potential material for the fabrication of cheap but very effective perovskite solar cells. Also, these findings can be helpful for further studies on single-junction chalcogenide perovskite devices.

Acknowledgements

The authors acknowledge Prof. Marc Burgelman and his research group at the University of Ghent for making SCAPS-1D available for our use.

ORCID

- Abdulai M. Feika, <https://orcid.org/0009-0000-5996-2536>; Muteeu A. Olopade, <https://orcid.org/0000-0002-1126-9027>
 Adeyinka D. Adewoyin, <https://orcid.org/0000-0003-2802-1535>

REFERENCES

- [1] NREL, "Photovoltaic Research," Interactive Best Research-Cell Efficiency Chart. Accessed: Mar. 01, 2024. [Online]. Available: <https://www.nrel.gov/pv/interactive-cell-efficiency.html>
- [2] D. Tiwari, O.S. Hutter, and G. Longo, "Chalcogenide perovskites for photovoltaics: current status and prospects," *J. Phys. Energy*, **3**(3), 034010 (2021). <https://doi.org/10.1088/2515-7655/abf41c>
- [3] S. Karthick, S. Velumani, and J. Bouclé, "Chalcogenide BaZrS₃ perovskite solar cells: A numerical simulation and analysis using SCAPS-1D," *Opt. Mater.* **126**, 112250 (2022). <https://doi.org/10.1016/j.optmat.2022.112250>
- [4] H. Shaili, *et al.*, "Synthesis of the Sn-based CaSnS₃ chalcogenide perovskite thin film as a highly stable photoabsorber for optoelectronic applications," *J. Alloys Compd.* **851**, 156790 (2021). <https://doi.org/10.1016/j.jallcom.2020.156790>
- [5] Q.A. Akkerman, and L. Manna, "What Defines a Halide Perovskite?," *ACS Energy Lett.* **5**(2), 604–610 (2020). <https://doi.org/10.1021/acsenergylett.0c00039>
- [6] W. Meng, B. Saparov, F. Hong, J. Wang, D. B. Mitzi, and Y. Yan, "Alloying and Defect Control within Chalcogenide Perovskites for Optimized Photovoltaic Application," *Chem. Mater.* **28**(3), 821–829 (2016). <https://doi.org/10.1021/acs.chemmater.5b04213>
- [7] Y. Nishigaki, *et al.*, "Extraordinary Strong Band-Edge Absorption in Distorted Chalcogenide Perovskites," *Sol. RRL*, **4**(5), 1900555 (2020). <https://doi.org/10.1002/solr.201900555>
- [8] Y.-Y. Sun, M. L. Agiorgousis, P. Zhang, and S. Zhang, "Chalcogenide Perovskites for Photovoltaics," *Nano Lett.* **15**(1), 581–585 (2015). <https://doi.org/10.1021/nl504046x>
- [9] M. Kumar, A. Singh, D. Gill, and S. Bhattacharya, "Optoelectronic Properties of Chalcogenide Perovskites by Many-Body Perturbation Theory," *J. Phys. Chem. Lett.* **12**(22), 5301–5307 (2021). <https://doi.org/10.1021/acs.jpcclett.1c01034>
- [10] R.O. Balogun, M.A. Olopade, O.O. Oyebola, and A.D. Adewoyin, "First-principle calculations to investigate structural, electronic and optical properties of MgHfS₃," *Mater. Sci. Eng. B*, **273**, 115405 (2021). <https://doi.org/10.1016/j.mseb.2021.115405>
- [11] I. Gharibshahian, A.A. Orouji, and S. Sharbati, "Alternative buffer layers in Sb₂Se₃ thin-film solar cells to reduce open-circuit voltage offset," *Sol. Energy*, **202**, 294–303 (2020). <https://doi.org/10.1016/j.solener.2020.03.115>
- [12] V. C. Karade, *et al.*, "Combating open circuit voltage loss in Sb₂Se₃ solar cell with an application of SnS as a back surface field layer," *Sol. Energy*, **233**, 435–445 (2022). <https://doi.org/10.1016/j.solener.2022.01.010>
- [13] Mamta, K. K. Maurya, and V. N. Singh, "Sb₂Se₃ versus Sb₂S₃ solar cell: A numerical simulation," *Sol. Energy*, **228**, 540–549, (2021). <https://doi.org/10.1016/j.solener.2021.09.080>
- [14] Mamta, K.K. Maurya, and V.N. Singh, "Enhancing the Performance of an Sb₂Se₃-Based Solar Cell by Dual Buffer Layer," *Sustainability*, **13**(21), 12320 (2021). <https://doi.org/10.3390/su132112320>
- [15] A. Srivastava, T.R. Lenka, and S. K. Tripathy, "SCAPS-1D Simulations for Comparative Study of Alternative Absorber Materials Cu₂XSnS₄ (X = Fe, Mg, Mn, Ni, Sr) in CZTS-Based Solar Cells," in: *Micro and Nanoelectronics Devices, Circuits and Systems*, **781**, edited by T.R. Lenka, D. Misra, and A. Biswas, (Springer, Singapore, 2022), pp. 329–337. https://doi.org/10.1007/978-981-16-3767-4_31
- [16] Md. D. Haque, Md.H. Ali, and A.Z.Md.T. Islam, "Efficiency enhancement of WSe₂ heterojunction solar cell with CuSCN as a hole transport layer: A numerical simulation approach," *Sol. Energy*, **230**, 528–537 (2021). <https://doi.org/10.1016/j.solener.2021.10.054>
- [17] M. Minbashi, A. Ghobadi, M.H. Ehsani, H.R. Dizaji, and N. Memarian, "Simulation of high efficiency SnS-based solar cells with SCAPS," *Sol. Energy*, **176**, 520–525 (2018). <https://doi.org/10.1016/j.solener.2018.10.058>
- [18] S. Karthick, S. Velumani, and J. Bouclé, "Experimental and SCAPS simulated formamidinium perovskite solar cells: A comparison of device performance," *Sol. Energy*, **205**, 349–357 (2020). <https://doi.org/10.1016/j.solener.2020.05.041>
- [19] D. Jayan K, V. Sebastian, and J. Kurian, "Simulation and optimization studies on CsPbI₃ based inorganic perovskite solar cells," *Sol. Energy*, **221**, 99–108 (2021). <https://doi.org/10.1016/j.solener.2021.04.030>
- [20] M. Mehrabian, E.N. Afshar, and S.A. Yousefzadeh, "Simulating the thickness effect of the graphene oxide layer in CsPbBr₃-based solar cells," *Mater. Res. Express*, **8**(3), 035509 (2021). <https://doi.org/10.1088/2053-1591/abf080>
- [21] A. Chauhan, A. Oudhia, and A.K. Shrivastav, "Analysis of eco-friendly tin-halide Cs₂SnI₆-based perovskite solar cell with all-inorganic charge selective layers," *J. Mater. Sci. Mater. Electron.* **33**(3), 1670–1685 (2022). <https://doi.org/10.1007/s10854-022-07723-x>
- [22] M.R. Jani, *et al.*, "Exploring solar cell performance of inorganic Cs₂TiBr₆ halide double perovskite: A numerical study," *Superlattices Microstruct.* **146**, 106652 (2020). <https://doi.org/10.1016/j.spmi.2020.106652>
- [23] D. Saikia, J. Bera, A. Betal, and S. Sahu, "Performance evaluation of an all inorganic CsGeI₃ based perovskite solar cell by numerical simulation," *Opt. Mater.* **123**, 111839 (2022). <https://doi.org/10.1016/j.optmat.2021.111839>
- [24] A.J. Kale, R. Chaurasiya, and A. Dixit, "Inorganic Lead-Free Cs₂AuBiCl₆ Perovskite Absorber and Cu₂O Hole Transport Material Based Single-Junction Solar Cells with 22.18% Power Conversion Efficiency," *Adv. Theory Simul.* **4**(3), 2000224 (2021). <https://doi.org/10.1002/adts.202000224>
- [25] Y. He, L. Xu, C. Yang, X. Guo, and S. Li, "Design and Numerical Investigation of a Lead-Free Inorganic Layered Double Perovskite Cs₄CuSb₂Cl₁₂ Nanocrystal Solar Cell by SCAPS-1D," *Nanomaterials*, **11**(9), 2321 (2021). <https://doi.org/10.3390/nano11092321>
- [26] M. Burgelman, P. Nollet, and S. Degreve, "Modelling polycrystalline semiconductor solar cells," *Thin Solid Films*, **361–362**, 527–532 (2000). [https://doi.org/10.1016/S0040-6090\(99\)00825-1](https://doi.org/10.1016/S0040-6090(99)00825-1)
- [27] F. Azri, A. Meftah, N. Sengouga, and A. Meftah, "Electron and hole transport layers optimization by numerical simulation of a perovskite solar cell," *Sol. Energy*, **181**, 372–378 (2019). <https://doi.org/10.1016/j.solener.2019.02.017>
- [28] S. Karthick, O.M. Nwakanma, B. Mercyrani, J. Bouclé, and S. Velumani, "Efficient 2T CsKPB(I_{Br})₃ Tin Incorporated Narrow Bandgap Perovskite Tandem Solar Cells: A Numerical Study with Current Matching Conditions," *Adv. Theory Simul.* **4**(11), 2100121 (2021). <https://doi.org/10.1002/adts.202100121>
- [29] V.K. Ravi, *et al.*, "Colloidal BaZrS₃ chalcogenide perovskite nanocrystals for thin film device fabrication," *Nanoscale*, **13**(3), 1616–1623 (2021). <https://doi.org/10.1039/D0NR08078K>

- [30] S. Karthick, J. Bouclé, and S. Velumani, "Effect of bismuth iodide (BiI₃) interfacial layer with different HTL's in FAPI based perovskite solar cell – SCAPS-1D study," *Sol. Energy*, **218**, 157–168 (2021). <https://doi.org/10.1016/j.solener.2021.02.041>
- [31] K. Chakraborty, M.G. Choudhury, and S. Paul, "Numerical study of Cs₂TiX₆ (X = Br-, I-, F- and Cl-) based perovskite solar cell using SCAPS-1D device simulation," *Sol. Energy*, **194**, 886–892 (2019). <https://doi.org/10.1016/j.solener.2019.11.005>
- [32] M.S. Jamal, et al., "Effect of defect density and energy level mismatch on the performance of perovskite solar cells by numerical simulation," *Optik*, **182**, 1204–1210 (2019). <https://doi.org/10.1016/j.ijleo.2018.12.163>
- [33] G. Xing, et al., "Low-temperature solution-processed wavelength-tunable perovskites for lasing," *Nat. Mater.* **13**(5), 5 (2014). <https://doi.org/10.1038/nmat3911>
- [34] F. Wang, S. Bai, W. Tress, A. Hagfeldt, and F. Gao, "Defects engineering for high-performance perovskite solar cells," *Npj Flex. Electron.* **2**(1), 22 (2018). <https://doi.org/10.1038/s41528-018-0035-z>
- [35] L. Et-taya, T. Ouslimane, and A. Benami, "Numerical analysis of earth-abundant Cu₂ZnSn(S_xSe_{1-x})₄ solar cells based on Spectroscopic Ellipsometry results by using SCAPS-1D," *Sol. Energy*, **201**, 827–835 (2020). <https://doi.org/10.1016/j.solener.2020.03.070>
- [36] S. Abdelaziz, A. Zekry, A. Shaker, and M. Abouelatta, "Investigating the performance of formamidinium tin-based perovskite solar cell by SCAPS device simulation," *Opt. Mater.* **101**, 109738 (2020). <https://doi.org/10.1016/j.optmat.2020.109738>
- [37] S. Mahesh, et al., "Revealing the origin of voltage loss in mixed-halide perovskite solar cells," *Energy Environ. Sci.* **13**(1), 258–267 (2020). <https://doi.org/10.1039/C9EE02162K>
- [38] W. Abdelaziz, A. Shaker, M. Abouelatta, and A. Zekry, "Possible efficiency boosting of non-fullerene acceptor solar cell using device simulation," *Opt. Mater.* **91**, 239–245 (2019). <https://doi.org/10.1016/j.optmat.2019.03.023>
- [39] D. Ompong, and J. Singh, "High open-circuit voltage in perovskite solar cells: The role of hole transport layer," *Org. Electron.* **63**, 104–108 (2018). <https://doi.org/10.1016/j.orgel.2018.09.006>
- [40] W. Tress, et al., "Interpretation and evolution of open-circuit voltage, recombination, ideality factor and subgap defect states during reversible light-soaking and irreversible degradation of perovskite solar cells," *Energy Environ. Sci.* **11**(1), 151–165 (2018). <https://doi.org/10.1039/C7EE02415K>
- [41] H. Baig, H. Kanda, A.M. Asiri, M.K. Nazeeruddin, and T. Mallick, "Increasing efficiency of perovskite solar cells using low concentrating photovoltaic systems," *Sustain. Energy Fuels*, **4**(2), 528–537 (2020). <https://doi.org/10.1039/C9SE00550A>
- [42] A. Mahapatra, et al., "Changes in the Electrical Characteristics of Perovskite Solar Cells with Aging Time," *Molecules*, **25**(10), 2299 (2020). <https://doi.org/10.3390/molecules25102299>
- [43] M. Becker, and M. Wark, "Sequentially Deposited Compact and Pinhole-Free Perovskite Layers via Adjusting the Permittivity of the Conversion Solution," *Z. Für Naturforschung A*, **74**(8), 655–663 (2019). <https://doi.org/10.1515/zna-2019-0141>
- [44] Z. Bi, et al., "High Shunt Resistance SnO₂-PbO Electron Transport Layer for Perovskite Solar Cells Used in Low Lighting Applications," *Adv. Sustain. Syst.* **5**(11), 2100120 (2021). <https://doi.org/10.1002/adsu.202100120>
- [45] D. Saranin, et al., "Copper Iodide Interlayer for Improved Charge Extraction and Stability of Inverted Perovskite Solar Cells," *Materials*, **12**(9), 1406 (2019). <https://doi.org/10.3390/ma12091406>
- [46] R. Singh, S. Sandhu, and J.-J. Lee, "Elucidating the effect of shunt losses on the performance of mesoporous perovskite solar cells," *Sol. Energy*, **193**, 956–961 (2019). <https://doi.org/10.1016/j.solener.2019.10.018>
- [47] M.A. Green, "General temperature dependence of solar cell performance and implications for device modelling," *Prog. Photovolt. Res. Appl.* **11**(5), 333–340 (2003). <https://doi.org/10.1002/pip.496>
- [48] Y.H. Khattak, F. Baig, S. Ullah, B. Mari, S. Beg, and H. Ullah, "Enhancement of the conversion efficiency of thin film kesterite solar cell," *J. Renew. Sustain. Energy*, **10**(3), 033501 (2018). <https://doi.org/10.1063/1.5023478>

ОПТИМІЗАЦІЯ СОНЯЧНИХ ЕЛЕМЕНТІВ НА ОСНОВІ ХАЛЬКОГЕНІДУ ПЕРОВСКІТУ MgHfS₃ З ВИКОРИСТАННЯМ SCAPS-1D

Абдулай М. Фейка^a, Мутеу А. Олопаде^{a,b}, Адейнка Д. Адевоїн^{b,c}

^aФакультет фізики, Коледж Фура-Бей, Університет Сьєрра-Леоне, Фрітаун, Сьєрра-Леоне

^bКафедра фізики, Факультет природничих наук, Університет Лагосу, Аюка, Лагос, Нігерія

^cВідділ фізики, Інститут дистанційного навчання, Університет Лагосу, Нігерія

У цій роботі перовскітні сонячні батареї магнію-гафнію сульфіді MgHfS₃ були досліджені за допомогою чисельного моделювання та моделювання. Перовскітні сонячні батареї отримали все більше визнання завдяки їхнім багатообіцяючим властивостям збору світла. Моделювання MgHfS₃ було успішно проведено за допомогою програмного забезпечення моделювання смності сонячних батарей (SCAPS-1D). В дослідження розроблено структуру базової моделі FTO/TiO₂/MgHfS₃/Cu₂O/Au і досліджено вплив змінних властивостей шару пристрою, таких як товщина поглинач, загальна щільність дефектів і щільність дефектів на межі розділу, з метою оптимізації цих параметрів для кращої продуктивності пристрою. Симуляція базової моделі дала робочі характеристики 0,99 В, 25,21 мА/см², 57,59% і 14,36%, які є напругою холостого ходу (V_{oc}), щільністю струму короткого замикання (J_{sc}), коефіцієнтом заповнення (FF) і PCE відповідно. Було встановлено, що оптимальна товщина поглинач становить 300 нм, а оптимальна щільність дефектів як для межі поділу TiO₂/поглинач, так і для межі поглинач/Cu₂O становить відповідно 1010 см⁻³ і 109 см⁻³. Отримані оптимізовані параметри PV становлять V_{oc} = 1,2629 В, J_{sc} = 24,44 мА/см², FF = 89,46% і PCE = 27,61%. Крім того, було встановлено, що підвищення температури пристрою понад 300 К посилює струм короткого замикання, тоді як інші характеристики продуктивності поступово знижуються. Отримані результати свідчать про те, що халькогенід MgHfS₃ є потенційним кандидатом на поглинач для виробництва дешевих і дуже ефективних екологічно чистих перовскітних сонячних елементів.

Ключові слова: SCAPS-1D; перовскіти; оптимізація; MgHfS₃; ефективність

RADIATION OF ELECTROMAGNETIC WAVES BY REGULAR AND BICONICAL DIPOLES WITH VARIABLE DISTRIBUTED SURFACE IMPEDANCE AND ARBITRARY EXCITATION

✉Mikhail V. Nesterenko*, ✉Victor A. Katrich, Yurii V. Arkusha, Vladimir V. Katrich

V.N. Karazin Kharkiv National University, 4, Svobody Sq., Kharkiv, Ukraine, 61022

*Corresponding Author e-mail: mikhail.v.nesterenko@gmail.com

Received June 5, 2024; revised July 16, 2024; accepted August 19, 2024

An approximate analytical solution of a problem concerning the radiation of electromagnetic waves by regular and biconical dipoles with constant and variable complex distributed surface impedance and arbitrary excitation is derived. Solution correctness is confirmed by satisfactory agreement of experimental and numerical results from well-known literary sources. Numerical results are given for the input characteristics and radiation fields of the dipoles in the cases of its symmetric and asymmetric excitation by a point source.

Keywords: Regular dipole; Biconical dipole; Variable distributed surface impedance; Arbitrary excitation; Current distribution; Input characteristics; Radiation fields

PACS: 02.70.Pt; 78.70.Gq; 84.40.-x

Currently, a variety of single-frequency and multi-frequency antenna structures are used in mobile and stationary communication systems [1-3]. These can be antennas protruding beyond the body of an electronic device [4-10], patch antennas directly integrated into communication devices, for example, [11-21] and references therein. To create multi-band (multi-channel) antennas, researchers have repeatedly proposed the use of dipoles with an asymmetric excitation point [7, 9, 22-28]. But in many cases, designers take the path of combining several antenna structures operating at different frequencies into one system. This choice significantly complicates the design of the antenna element and is an undesirable factor on the path to its miniaturization. In order to reduce the weight and size parameters of the antenna structure, it was also proposed to change the radius of the cross section of the dipole along its length according to a certain law, for example, linear (biconical dipole) [29-42]. However, these publications are devoted to calculating the characteristics of ideally conducting dipoles excited at the geometric center by a concentrated electromotive force (EMF) (symmetrical dipoles). In [42], it is proposed, for example, to create a three-frequency structure to use three different-sized symmetrical biconical dipoles, made of pure gold.

In [43], using a generalized method of induced EMF, the authors obtained an approximate analytical solution to the problem of current distribution in an asymmetric biconical dipole with a distributed surface impedance and arbitrary excitation. A characteristic property of such antenna design is the possibility of resonant tuning to selected frequencies depending on the geometric and electrophysical parameters of the dipole. Analysis of the input characteristics of the proposed dipole antenna showed the possibility of practical application of this antenna for multi-band portable radio stations, base stations and other antenna systems, for example, in unmanned aerial vehicles.

In this paper, for the first time a most general approximate analytical solution to the problem of the radiation of electromagnetic waves by regular and biconical dipoles with a variable distributed surface impedance and arbitrary excitation is obtained. Thus, we will combine in one design all the advantages of asymmetric excitation, biconical geometry and the presence of a variable distributed surface impedance. The antenna characteristics will be modelled by using the numerical-analytical method, known as generalized method of induced EMF, proposed by the authors earlier in [25, 26].

PROBLEM FORMULATION AND SOLUTION OF THE INTEGRAL EQUATIONS

Let us limit ourselves by the linear law of the radius change along the dipole (Fig. 1), which, in its turn, is rather good approximation for another dependences $r(s)$, for example, exponential one, at small angles ψ . Let the dipole of the $2L$ length and the variable radius according to the function $r(s)$ is located in free space. It has the variable distributed internal linear impedance $z_i(s) = z_i^s(s) + z_i^a(s)$ and is excited by the electrical field $E_{0s}(s)$ of the given sources (tangential component). The monochromatic fields and currents depend on time t as $e^{i\omega t}$ ($\omega = 2\pi f$ is the circular frequency, f is the linear frequency, measured in Hz). We assume that the dipole stays electrically thin in the operating frequency band, i.e. $kr(s) \ll 1$, $r(s) \ll 2L$, where $k = 2\pi/\lambda$, λ is the wavelength in free space. Then the integral equation relatively to the $J(s)$ current for the impedance boundary condition on the dipole surface [38]:

$$\left(\frac{d^2}{ds^2} + k^2 \right) \int_{-L}^L J(s') \frac{e^{-ik\tilde{R}(s,s')}}{\tilde{R}(s,s')} ds' = -\frac{i\omega}{\cos\psi} [E_{0s}(s) - z_i(s)J(s)], \quad (1)$$

where $\tilde{R}(s, s') = \sqrt{(s - s')^2 + r^2(s)}$, $\psi = (\psi_1 + \psi_2) / 2$, s and s' are the local coordinates related to the dipole axis and surface. Note that at $r(s) = \text{const} = r$, equation (1) transforms into an equation for the current in an dipole of constant radius with a quasi-one-dimensional core $\tilde{R}(s, s') = \bar{R}(s, s') = \sqrt{(s - s')^2 + r^2}$.

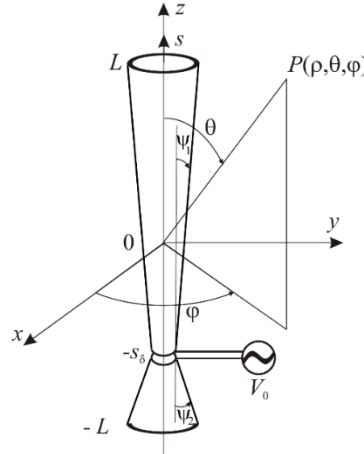


Figure 1. The geometry of the problem and accepted notations

To solve the equation (1) it is expedient to represent it in the form of the system of two coupled integral equations, concerning to the unknown currents $J^s(s)$ and $J^a(s)$, the first one of which is symmetrical, and the other – antisymmetrical relatively to the s variable:

$$\begin{cases} \left(\frac{d^2}{ds^2} + k^2 \right) \int_{-L}^L J^s(s') \frac{e^{-ik\tilde{R}(s,s')}}{\tilde{R}(s,s')} ds' = -\frac{i\omega}{\cos\psi} \{ [E_{0s}^s(s) - [z_i^s(s)J^s(s) + z_i^a(s)J^a(s)]] \}, \\ \left(\frac{d^2}{ds^2} + k^2 \right) \int_{-L}^L J^a(s') \frac{e^{-ik\tilde{R}(s,s')}}{\tilde{R}(s,s')} ds' = -\frac{i\omega}{\cos\psi} \{ E_{0s}^a(s) - [z_i^s(s)J^a(s) + z_i^a(s)J^s(s)] \}. \end{cases} \quad (2)$$

The dipole currents can be presented as product of the unknown complex amplitudes $J_n^{s,a}$ and distribution functions $f_n^{s,a}(s')$ ($n = 0, 1$) as

$$J^{s,a}(s') = J_0^{s,a} f_0^{s,a}(s') + J_1^{s,a} f_1^{s,a}(s'), \quad f_n^{s,a}(\pm L) = 0. \quad (3)$$

The solution of the equations system (2) can be obtained by the generalized method of induced EMF [25, 26]. To do so, let us multiply the left- and right- hand parts of the equations (2) by the functions $f_n^s(s)$ and $f_n^a(s)$, and integrate the resulting expressions over the dipole length. Thus, the following system of linear algebraic equations (SLAE) is obtained

$$\begin{cases} J_0^s Z_{00}^{s\Sigma} + J_1^s Z_{01}^{s\Sigma} + J_0^a \tilde{Z}_{00}^{sa} + J_1^a \tilde{Z}_{01}^{sa} = -(i\omega / 2k \cos\psi) E_0^s, \\ J_0^s Z_{10}^{s\Sigma} + J_1^s Z_{11}^{s\Sigma} + J_0^a \tilde{Z}_{10}^{sa} + J_1^a \tilde{Z}_{11}^{sa} = -(i\omega / 2k \cos\psi) E_1^s, \\ J_0^a Z_{00}^{a\Sigma} + J_1^a Z_{01}^{a\Sigma} + J_0^s \tilde{Z}_{00}^{as} + J_1^s \tilde{Z}_{01}^{as} = -(i\omega / 2k \cos\psi) E_0^a, \\ J_0^a Z_{10}^{a\Sigma} + J_1^a Z_{11}^{a\Sigma} + J_0^s \tilde{Z}_{10}^{as} + J_1^s \tilde{Z}_{11}^{as} = -(i\omega / 2k \cos\psi) E_1^a. \end{cases} \quad (4)$$

Here ($m = 0, 1; n = 0, 1$),

$$Z_{mn}^{s,a} = \frac{1}{2k \cos\psi} \left\{ -\frac{df_m^{s,a}(s)}{ds} A_n^{s,a}(s) \Big|_{-L}^L + \int_{-L}^L \left[\frac{d^2 f_m^{s,a}(s)}{ds^2} + k^2 f_m^{s,a}(s) \right] A_n^{s,a}(s) ds \right\}, \quad (5a)$$

$$A_n^{s,a}(s) = \int_{-L}^L f_n^{s,a}(s') \frac{e^{-ik\tilde{R}(s,s')}}{\tilde{R}(s,s')} ds', \quad E_m^{s,a} = \int_{-L}^L f_m^{s,a}(s) E_{0s}^{s,a}(s) ds, \quad (5b)$$

$$\tilde{Z}_{mn}^{s,a} = -\frac{i\omega}{2k \cos\psi} \int_{-L}^L f_m^{s,a}(s) f_n^{s,a}(s) z_i^s(s) ds, \quad Z_{mn}^{(s,a)\Sigma} = Z_{mn}^{s,a} + \tilde{Z}_{mn}^{s,a}, \quad \tilde{Z}_{mn}^{(sa)} = -\frac{i\omega}{2k \cos\psi} \int_{-L}^L f_m^{(s)}(s) f_n^{(a)}(s) z_i^a(s) ds, \quad (5c)$$

As can be seen, SLAE (4) is higher order than a similar SLAE for the case of a constant distributed surface impedance along the length of the dipole. That's why let us consider some particular solutions of the equations system (4), which we will need further.

1. The dipole with the impedance, constant along its length: $z_i^s(s) = const, z_i^a(s) = 0$. Then

$$J^{s,a}(s) = -\frac{i\omega}{2k \cos \psi} \left[\frac{E_0^{s,a} Z_{11}^{(s,a)\Sigma} - E_1^{s,a} Z_{01}^{(s,a)\Sigma}}{Z_{00}^{(s,a)\Sigma} Z_{11}^{(s,a)\Sigma} - Z_{10}^{(s,a)\Sigma} Z_{01}^{(s,a)\Sigma}} f_0^{s,a}(s) + \frac{E_1^{s,a} Z_{00}^{(s,a)\Sigma} - E_0^{s,a} Z_{10}^{(s,a)\Sigma}}{Z_{00}^{(s,a)\Sigma} Z_{11}^{(s,a)\Sigma} - Z_{10}^{(s,a)\Sigma} Z_{01}^{(s,a)\Sigma}} f_1^{s,a}(s) \right]. \tag{6}$$

2. The field of impressed sources has only the symmetrical component $E_{0s}^s(s)$ ($E_{0s}^a(s) = 0$). It is natural to suppose in this case, that it is sufficient to use only the first addendum – $J^a(s) = J_0^a f_0^a(s)$ in the antisymmetric component of the current in the dipole. Then the symmetrical and the antisymmetrical components of the current will be defined by the following formulas:

$$J^s(s) = -\frac{i\omega}{2k \cos \psi} \left[\frac{E_0^s Z_{11}^{sa\Sigma} - E_1^s Z_{01}^{sa\Sigma}}{Z_{00}^{sa\Sigma} Z_{11}^{sa\Sigma} - Z_{10}^{sa\Sigma} Z_{01}^{sa\Sigma}} f_0^s(s) + \frac{E_1^s Z_{00}^{sa\Sigma} - E_0^s Z_{10}^{sa\Sigma}}{Z_{00}^{sa\Sigma} Z_{11}^{sa\Sigma} - Z_{10}^{sa\Sigma} Z_{01}^{sa\Sigma}} f_1^s(s) \right], \tag{7a}$$

$$J^a(s) = -\frac{i\omega}{2k \cos \psi} \frac{E_0^s Z_{00}^{as\Sigma} + E_1^s Z_{01}^{as\Sigma}}{Z_{00}^{sa\Sigma} Z_{11}^{sa\Sigma} - Z_{10}^{sa\Sigma} Z_{01}^{sa\Sigma}} f_0^a(s), \tag{7b}$$

where

$$\begin{aligned} Z_{00}^{sa\Sigma} &= Z_{00}^{s\Sigma} - \frac{(\tilde{Z}_{00}^{sa})^2}{Z_{00}^{a\Sigma}}, & Z_{01}^{sa\Sigma} &= Z_{01}^{s\Sigma} - \frac{\tilde{Z}_{00}^{sa} \tilde{Z}_{01}^{as}}{Z_{00}^{a\Sigma}}, & Z_{10}^{sa\Sigma} &= Z_{10}^{s\Sigma} - \frac{\tilde{Z}_{00}^{as} \tilde{Z}_{10}^{sa}}{Z_{00}^{a\Sigma}}, \\ Z_{11}^{sa\Sigma} &= Z_{11}^{s\Sigma} - \frac{\tilde{Z}_{10}^{sa} \tilde{Z}_{01}^{as}}{Z_{00}^{a\Sigma}}, & Z_{00}^{as\Sigma} &= \frac{Z_{10}^{s\Sigma} \tilde{Z}_{01}^{as} - Z_{11}^{s\Sigma} \tilde{Z}_{00}^{as}}{Z_{00}^{a\Sigma}}, & Z_{01}^{as\Sigma} &= \frac{Z_{01}^{s\Sigma} \tilde{Z}_{00}^{as} - Z_{00}^{s\Sigma} \tilde{Z}_{01}^{as}}{Z_{00}^{a\Sigma}}. \end{aligned}$$

Let the dipole be excited in the point $s = -s_\delta$ by the voltage δ -generator with amplitude V_0 , as shown in Fig. 1. Then

$$\begin{aligned} E_{0s}(s) &= V_0 \delta(s + s_\delta) = E_{0s}^s(s) + E_{0s}^a(s), \\ E_{0s}^s(s) &= (V_0 / 2) [\delta(s + s_\delta) + \delta(s - s_\delta)], \\ E_{0s}^a(s) &= (V_0 / 2) [\delta(s + s_\delta) - \delta(s - s_\delta)], \end{aligned} \tag{8}$$

where δ is the Dirac delta function. Let us choose the functions $f_{0,1}^{s,a}(s)$ according to [26] in the following form:

$$\begin{aligned} f_0^s(s) &= \cos \tilde{k} s_\delta \sin \tilde{k} L \cos \tilde{k} s - (1/2) \cos \tilde{k} L (\sin \tilde{k} |s - s_\delta| + \sin \tilde{k} |s + s_\delta|), \\ f_0^a(s) &= \sin \tilde{k} s_\delta \cos \tilde{k} L \sin \tilde{k} s + (1/2) \sin \tilde{k} L (\sin \tilde{k} |s - s_\delta| - \sin \tilde{k} |s + s_\delta|), \end{aligned} \tag{9}$$

$$f_1^s(s) = \cos \tilde{k} s - \cos \tilde{k} L, \quad f_1^a(s) = \sin ks - (s/L) \sin kL, \tag{10}$$

where $\tilde{k} = k - \frac{i2\pi z_i^{av}}{Z_0 \Omega} \left[\frac{1}{\cos \psi} \left(\frac{3}{2} - \frac{r_\delta}{2r_L} \right) \right]$, $\Omega = 2 \ln \frac{2L}{r_L}$, $z_i^{av} = \frac{1}{2L} \int_{-L}^L z_i(s) ds$ is the mean value of the internal impedance along the dipole length, r_δ and r_L are the radii of the dipole in point $s = -s_\delta$ and in its end. The coefficients $Z_{mn}^{s,a}$ in the formulas (6), (7) can be obtained from (5) and the expressions $E_0^s = \cos \tilde{k} s_\delta \sin \tilde{k} (L - |s_\delta|)$, $E_1^s = \cos \tilde{k} s_\delta - \cos \tilde{k} L$, $E_0^a = -\sin \tilde{k} |s_\delta| \sin \tilde{k} (L - |s_\delta|)$, $E_1^a = \sin ks_\delta - (s_\delta/L) \sin kL$ for (6), $E_0^s = \sin \tilde{k} L$, $E_1^s = 1 - \cos \tilde{k} L$ for (7).

Note that the approximating functions in (4) adequately represent the real physical process if the electrical lengths of the dipole $(2L/\lambda) \leq 1.4$. Two other approximating functions $f_2^s(s)$ and $f_2^a(s)$ valid in the range $1.4 < (2L/\lambda) \leq 2.5$ can also be substituted in the expressions (3). These functions for the perfectly conducting dipole were obtained in [44] in the form

$$f_2^s(s) = \cos \frac{ks}{2} - \cos \frac{kL}{2}, \quad f_2^a(s) = \sin \frac{ks}{2} - \sin \frac{kL}{2}. \tag{11}$$

The input impedance $Z_{in} = R_{in} + iX_{in}$ and admittance $Y_{in} [\text{millimhos}] = G_{in} + iB_{in} = 10^3 / Z_{in}$ can be presented as

$$Z_{in}[\text{Ohm}] = \frac{60i}{J_0^s f_0^s(s_\delta) + J_1^s f_1^s(s_\delta) + J_0^a f_0^a(s_\delta) + J_1^a f_1^a(s_\delta)}. \quad (12)$$

Then, the reflection coefficient in the antenna feeder with the wave impedance W is equal to

$$S_{11} = \frac{Z_{in} - W}{Z_{in} + W}, \quad (13)$$

and the voltage standing wave ratio is determined by the formula $VSWR = \frac{1 + |S_{11}|}{1 - |S_{11}|}$.

The dipole radiation fields in all observation zones will be determined by the following expressions (in the spherical coordinate system ρ, θ, φ in Fig. 1):

$$\begin{aligned} E_\rho(\rho, \theta) &= \frac{k}{\omega} \int_{-L}^L J(s) \frac{e^{-ikR(s)}}{R^3(s)} \left\{ 2R(s) \left[1 + \frac{1}{ikR(s)} \right] \cos \theta - ik\rho \left[1 + \frac{3}{ikR(s)} - \frac{3}{kR^2(s)} \right] s \sin^2 \theta \right\} ds, \\ E_\theta(\rho, \theta) &= -\frac{k \sin \theta}{\omega} \int_{-L}^L J(s) \frac{e^{-ikR(s)}}{R^3(s)} \left\{ 2R(s) \left[1 + \frac{1}{ikR(s)} \right] - ik\rho \left[1 + \frac{3}{ikR(s)} - \frac{3}{kR^2(s)} \right] (\rho - s \cos \theta) \right\} ds, \\ H_\varphi(\rho, \theta) &= \frac{ik^2 \sin \theta}{\omega} \int_{-L}^L J(s) \frac{e^{-ikR(s)}}{R^2(s)} \left[1 + \frac{1}{ikR(s)} \right] \rho ds, \\ E_\varphi(\rho, \theta) &= H_\rho(\rho, \theta) = H_\theta(\rho, \theta) = 0, \\ R(s) &= \sqrt{\rho^2 - 2\rho s \cos \theta + s^2}. \end{aligned} \quad (14)$$

In the far zone at $k\rho \rightarrow \infty$ and $\rho \gg 2L$, expressions (11) are significantly simplified

$$E_\theta(\rho, \theta) = H_\varphi(\rho, \theta) = \frac{ik^2}{\omega} \sin \theta \frac{e^{-ik\rho}}{\rho} \int_{-L}^L J(s) e^{iks \cos \theta} ds. \quad (15)$$

CONFIRMATION OF THE ADEQUACY OF THE PROPOSED MATHEMATICAL MODEL TO A REAL PHYSICAL PROCESS

1. Perfectly conducting regular dipole with symmetric excitation

The dependences of real G_{in} and imaginary B_{in} parts of the input admittance of the regular $r_\delta = r_L = r$ perfectly conducting dipole, excited in the point $s_\delta = 0$, from its electrical length $2L/\lambda$ have been calculated (Fig. 2).

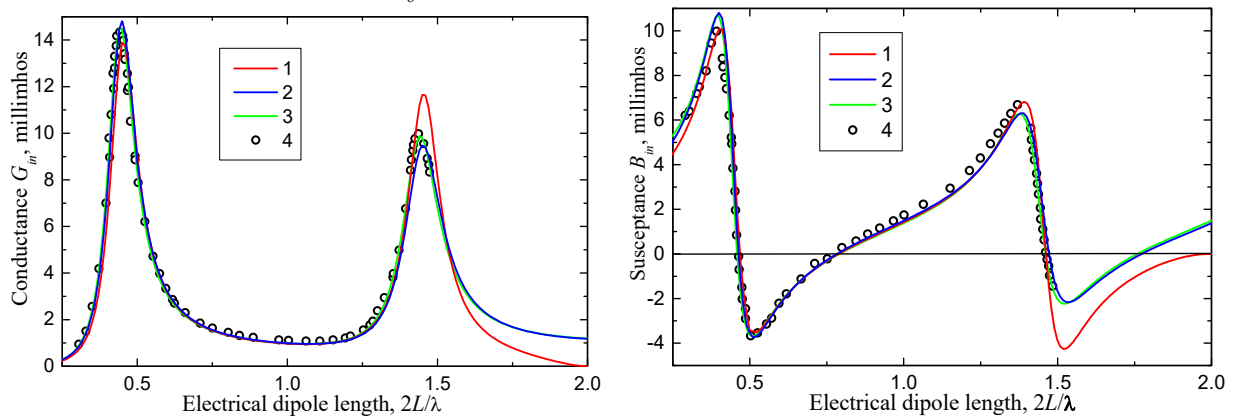


Figure 2. The input admittance versus electrical length of the symmetric regular perfectly conducting dipole at $f = 663$ MHz, $r/\lambda = 0.007022$, $s_\delta = 0$: 1—calculation (the functions (9) and (10)), 2—calculation (the functions (9), (10) and (11)), 3—calculation (the functions (16), 4—the experimental data [45]

Also, the calculated values, obtained by the moment method [22] at the current approximation by means of trigonometric functions of the whole region

$$J(s) = \sum_{n=1}^N J_n \sin \frac{n\pi(L+s)}{2L}, \quad (16)$$

are given here for comparison, what is more, to reach necessary accuracy the functions number in formula (16) are chosen to be equal $N = 24$.

2. Regular dipole with constant surface impedance and symmetric excitation

The dependences of real G_{in} and imaginary B_{in} parts of the input admittance of the regular $r_{\delta} = r_L = r$ dipole with constant distributed surface impedance, excited in the point $s_{\delta} = 0$, from its electrical length L/λ presented in Fig. 3 in comparison with experimental data.

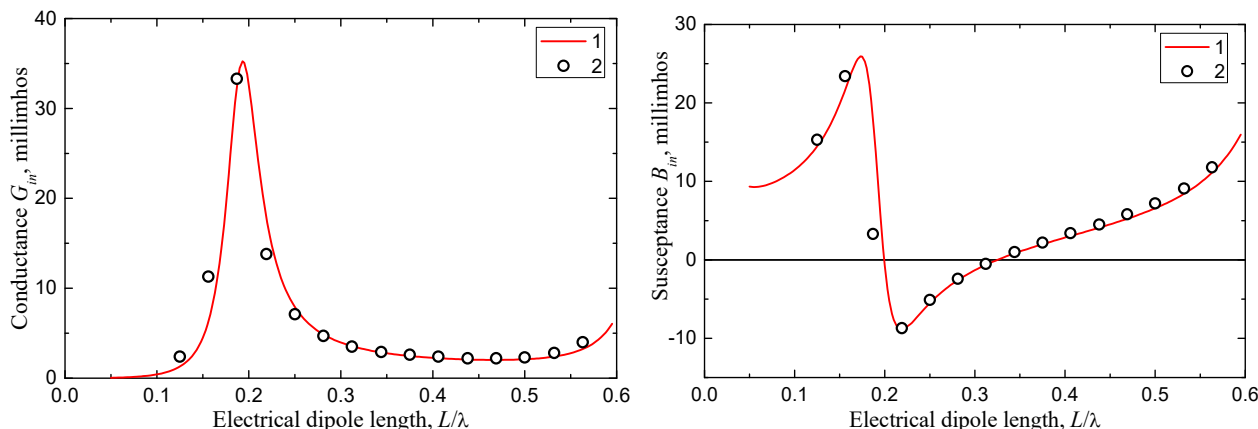


Figure 3. The input admittance versus electrical length of the symmetric regular metallic conductor of the radius $r_i = 0.3175$ cm, covered by the dielectrical ($\epsilon = 9.0$) shell of the radius $r = 0.635$ cm at $f = 600$ MHz: 1–calculation (the functions (9) and (10)), 2–the experimental data [46].

NUMERICAL RESULTS

1. Regular dipole with variable surface impedance and symmetric excitation

Let the dipole be excited in the center ($s_{\delta} = 0$ in Fig. 1) by the hypothetical δ -generator of voltage V_0 : $E_{0s}^s(s) = V_0\delta(s)$, $E_{0s}^a(s) = 0$. Then the current symmetrical component can be approximated by the function

$$f^s(s) = \sin \tilde{k}(L - |s|), \text{ where } \tilde{k} = k - \frac{i\bar{Z}_s^{av}[3/2 - r_{\delta}/(2r_L)]}{2r_L \cos \psi \ln(2L/r_L)}, \bar{Z}_s^{av} = \frac{1}{2L} \int_{-L}^L \bar{Z}_s(s) ds$$

is the mean value of the dipole variable surface impedance, $\bar{Z}_s(s) = \bar{R}_s(s) + i\bar{X}_s(s) = 2\pi r_L z_i(s) / Z_0$ is the complex distributed surface impedance, normalized on the free space wave resistance $Z_0 = 120\pi$ Ohm. We use the following expression for the current antisymmetrical component [25]: $f^a(s) = \sin 2ks - 2 \sin ks \cos kL$, and we represent the $\bar{Z}_s^{s,a}(s)$ functions in the form of $\bar{Z}_s^{s,a}(s) = \bar{Z}_s^{s,a} \phi^{s,a}(s)$.

Let us consider the following simple functions of the impedance distribution (which are realized rather easily in practice) as an example: $\phi^s(s) = 1$ – the distribution, constant along the dipole, $\phi^a(s) = \text{signs} = (|s|/s)$ – the step-function alternating distribution. Substituting $f^{s,a}(s)$ and $\phi^{s,a}(s)$ into the expressions (5) and (7), we obtain the formula for the current in the dipole with these laws of impedance distribution (the lower indices “mn” in (5) are omitted):

$$J(s) = -\frac{i\omega}{2k} V_0 \sin \tilde{k}L \left[\frac{(Z^a + \tilde{Z}^a) \sin \tilde{k}(L - |s|) - \tilde{Z}^{sa} (\sin 2ks - 2 \sin ks \cos kL)}{(Z^s + \tilde{Z}^s)(Z^a + \tilde{Z}^a) - (\tilde{Z}^{sa})^2} \right], \tag{17}$$

where $r(s) = \text{const} = r$,

$$Z^s = \frac{\tilde{k}}{k} [A^s(L) - \cos \tilde{k}L A^s(0)] + \frac{k^2 - \tilde{k}^2}{2k} \int_{-L}^L f^s(s) A^s(s) ds, \quad Z^a = 2 \sin^2 kL A^a(L) - \frac{3}{2} k \int_{-L}^L \sin 2ks A^a(s) ds,$$

$$A^{s,a}(s) = \int_{-L}^L f^{s,a}(s') \frac{e^{-ikR(s,s')}}{R(s,s')} ds',$$

$$\tilde{Z}^s = \frac{\bar{Z}_s^s}{i2\tilde{k}r} (2\tilde{k}L - \sin 2\tilde{k}L), \quad \tilde{Z}^a = \frac{\bar{Z}_s^a}{ikr} \left(3kL - \frac{\sin 4kL}{12} - \frac{7}{3} \sin 2kL + 2kL \cos 2kL \right),$$

$$\tilde{Z}^{sa} = \frac{2\bar{Z}_s^a}{ikr} \left(\frac{2k^2 \sin \tilde{k}L - k\tilde{k} \sin 2kL}{4k^2 - \tilde{k}^2} - 2 \cos kL \frac{k^2 \sin \tilde{k}L - k\tilde{k} \sin kL}{k^2 - \tilde{k}^2} \right).$$

Fig. 4 represents the dependences of the reflection coefficient $|S_{11}|$ from \bar{X}_S^a at $\bar{X}_S^s = const$ in the feeder line with $W=50$ Ohm. As it is seen from graphics, there is a combinations of the values \bar{X}_S^s and \bar{X}_S^a for value $2L=0.25\lambda$ (quarter-wave dipole), at which the reflection coefficient is minimum, that is, the dipole is tuned into resonance. The dependences $|S_{11}|(f)$ in the band of frequencies (Fig. 5) have been calculated in order to ground reliability of the obtained approximate analytical expression (13). Figs. 5, 6 also represent the calculated data, obtained by the method of finite elements, realized in the program “ANSYS HFSS”.

The dipoles represent themselves metallic conductors of the radius r_i , covered by the layer of the magnetodielectric of the thickness $r-r_i$. The materials of the covering for one and the other arms of the dipoles on the frequency $f=3$ GHz have the following electrophysical parameters [47]: 1) dielectric Al_2O_3 , $\epsilon_1=10-i0.015$, $\mu_1=1.0$; 2) ferrite $2\text{CX}1$, $\epsilon_2=10.6-i0.068$, $\mu_2=24.0$. The calculations of the values of the surface impedance components give the following results at these parameters of the magnetodielectrics due to the corresponding formula from [25]:

$$\bar{Z}_S = -i\sqrt{\frac{\mu}{\epsilon}} \frac{I_0(k_1 r)N_0(k_1 r_i) - I_0(k_1 r_i)N_0(k_1 r)}{I_1(k_1 r)N_0(k_1 r_i) - I_0(k_1 r_i)N_1(k_1 r)}. \quad (18)$$

Here $k_1 = 2\pi\sqrt{\epsilon\mu}/\lambda$, $\epsilon = \epsilon' - i\epsilon''$ and $\mu = \mu' - i\mu''$ are the electro-physical parameters of the coating material, r_i is the inner conductor radius, r is the outer radius of coverage, I_n, N_n are the Bessel and Neumann functions of corresponding orders. Then for $2L=0.25\lambda$ and $(r_i/r)=0.5$ $\bar{Z}_S^s = 10^{-6} + i0.09$, $\bar{Z}_S^a = 10^{-6} + i0.08$. As it follows from the plots in Figs. 4, 5, these values are close to the corresponding ratios between \bar{X}_S^s and \bar{X}_S^a for tuning the dipoles into resonance at the frequency $f=3$ GHz.

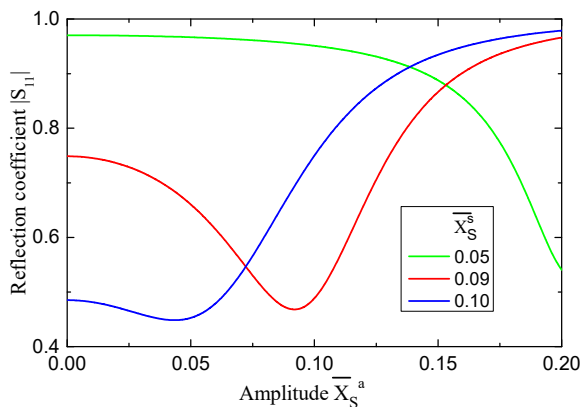


Figure 4. The reflection coefficient versus amplitude of the antisymmetrical surface impedance at $f=3$ GHz, $2L=0.25\lambda$, $(L/r)=75$

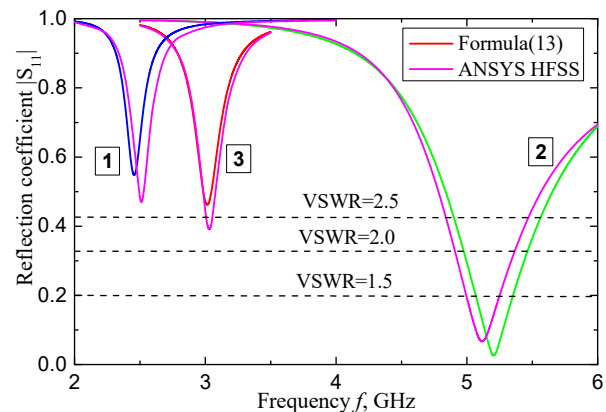


Figure 5. The reflection coefficient versus frequency at $W=50$ Ohm $2L=0.25\lambda$, $(L/r)=75$: 1 - $2\text{CX}1$ (both arms), 2 - Al_2O_3 (both arms), 3 - $2\text{CX}1 + \text{Al}_2\text{O}_3$ (first arm + second arm)

Finally, Fig. 6 shows the current distribution along a dipole with an asymmetric surface impedance in comparison with calculations using the “ANSYS HFSS” program, and Fig. 7 shows the spatial distribution of the radiation field in far zone of such a dipole in comparison with a perfectly conducting half-wave dipole.

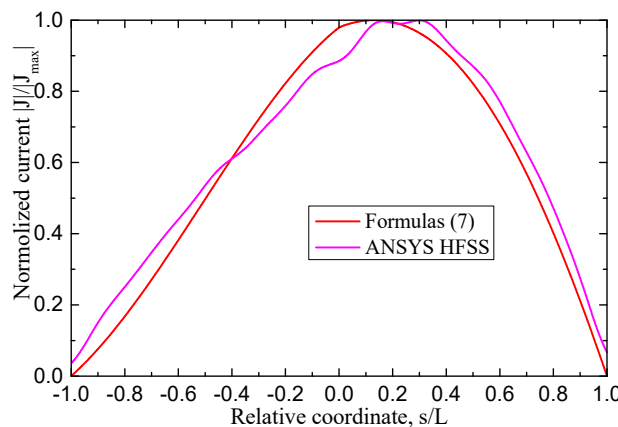


Figure 6. The current distribution along the dipole for the case $2\text{CX}1 + \text{Al}_2\text{O}_3$ (first arm + second arm) at $f=3$ GHz, $2L=0.25\lambda$, $(L/r)=75$

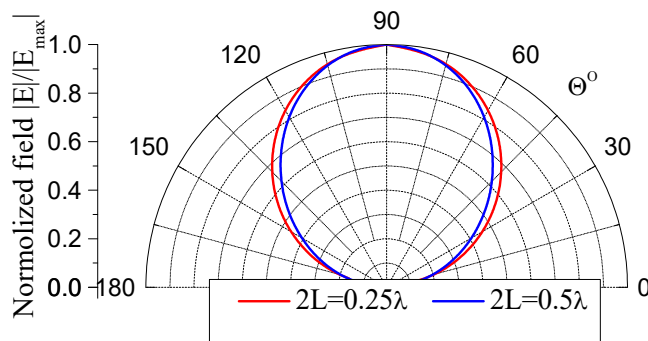


Figure 7. The spatial distribution of the dipole radiation field at $f = 3\text{GHz}$, $(L/r) = 75$ for the cases: 1) $2L = 0.25\lambda$, $2\text{CX} 1 + \text{Al}_2\text{O}_3$ (first arm + second arm); 2) $2L = 0.5\lambda$, $\bar{Z}_s^{s,a} = 0$

2. Perfectly conducting biconical dipole with asymmetric excitation

Let us present the input characteristics (modulus of the reflection coefficient $|S_{11}|$ in the supply feeder line with wave resistance $W = 50 \text{ Ohm}$) of an asymmetric biconical perfectly conducting dipole with dimensions $2L = 138 \text{ mm}$, $r_\delta = 1 \text{ mm}$, $r_L = 3 \text{ mm}$ (Fig. 8). This choice of the dipole length is due to the condition of the first resonance at the frequency $f = 0.9 \text{ GHz}$. Note that for a regular dipole with a radius $r = 2 \text{ mm}$, its length would be equal to $2L = 156 \text{ mm}$. As can be seen from the graphs, an asymmetric biconical dipole (with smaller geometric length than a regular dipole) is also resonant at two or more frequencies. Moreover, this tendency will increase with increasing the angle ψ . Also, if the dipole has a distributed surface impedance of the inductive type, then its resonant length will be even less [26].

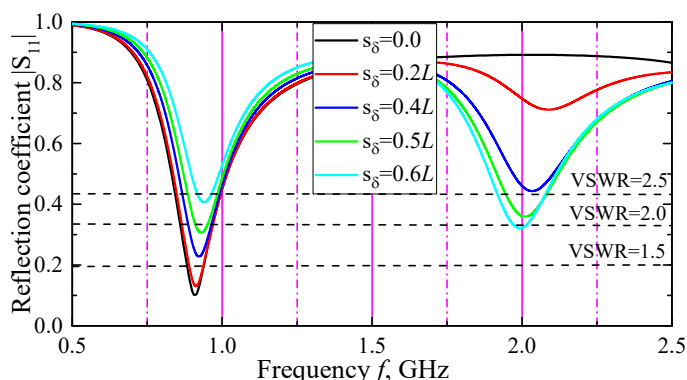


Figure 8. The reflection coefficient in the supply feeder line versus frequency for different positions of the excitation point s_δ at $2L = 138 \text{ mm}$, $r_\delta = 1 \text{ mm}$, $r_L = 3 \text{ mm}$, $\bar{Z}_s^{s,a} = 0$

Fig. 9 shows the spatial distribution of the radiation field of a dipole with an asymmetric excitation in comparison with calculations using the “ANSYS HFSS” program. As can be seen, the spatial distribution of the radiated field in this case has a two-lobe shape, and the level of the lobes can be changed by introducing a complex distributed surface impedance.

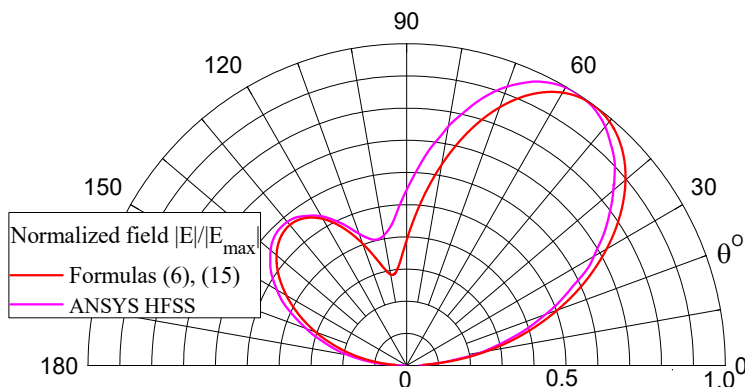


Figure 9. The spatial distribution of the dipole radiation field at $f = 0.9\text{GHz}$, $s_\delta = 0.2L$, $2L = 138 \text{ mm}$, $r_\delta = 1 \text{ mm}$, $r_L = 3 \text{ mm}$, $\bar{Z}_s^{s,a} = 0$

CONCLUSIONS

An approximate analytical solution of a problem concerning a current distribution, input characteristics and radiation fields of the regular and biconical dipoles with constant and variable complex distributed surface impedance and arbitrary excitation derived in the thin-wire approximation. The solution was carried out by the generalized method of induced EMF. Solution correctness is confirmed by satisfactory agreement of experimental results from well-known literary sources, and also of numerical results, performed using the moment method and using a commercial program "ANSYS HFSS". However, the use of commercial programs for dipoles, the electro-physical parameters of which depend on frequency f , raises serious doubts. This could be, for example, material TDK IR-E110 [48], which at the frequency band $f = 7 \div 12$ GHz are $\varepsilon_1 = 8.84 - i0.084$ and $\mu_1 = 2.42 - 0.0825f[\text{GHz}] - i0.994$. The solution presented in the paper is free of such shortcomings, moreover, the calculation time is tens of times (depending on the structure under consideration) less than that of direct numerical methods and commercial programs. The characteristic property of the antenna is the possibility of resonant tuning to the selected frequencies (depending on the geometric and electro-physical parameters of the dipole), which does not decrease the noise-resistant properties as compared with broadband antennas. Numerical results are given for the input characteristics and radiation fields of the dipoles with constant and variable distributed surface impedance in the cases of its symmetric and asymmetric excitation by a point source. Analysis of electrodynamic characteristics of the proposed dipole antennas has proved the possibility of practical applications of these antennas for multi-band portable radio stations, base stations and other antenna structures, for example, for antenna systems of unmanned aerial vehicles due to their small size and low weight compared to perfectly conducting regular dipoles.

ORCID

✉Mikhail V. Nesterenko, <https://orcid.org/0000-0002-1297-9119>; ✉Victor A. Katrich, <https://orcid.org/0000-0001-5429-6124>

REFERENCES

- [1] Z. N. Chen, *Antennas for portable devices*, Chichester, (England: Wiley, 2007).
- [2] K. Fujimoto, and J. R. James, *Mobile antenna systems handbook*, (London, England: Artech House, 2008).
- [3] Z. Zhang, *Antenna design for mobile devices*, (London, England: Wiley, 2017).
- [4] G. Zhou, and B. Yildirim, "A multi-band fixed cellular phone antenna," in: Proc. IEEE AP-S Int. Symp. **1**, 112 (1999). <https://doi.org/10.1109/APS.1999.789095>
- [5] N. Odachi, S. Sekine, H. Shoki, and Y. Suzuki, "A rod antenna with a meander element for hand-held phone," in: Proc. IEEE AP-S Int. Symp. **3**, 1682 (2000). <https://doi.org/10.1109/APS.2000.874565>
- [6] H.-C. Tung, C.-Y. Fang, and K.-L. Wong, "Dual-band inverted-L monopole antenna for GSM/DCS mobile phone," in: Proc. IEEE AP-S Int. Symp. **3**, 30-33 (2002). <https://doi.org/10.1109/APS.2002.1018149>
- [7] C. Song, Y. Huang, J. Zhou, P. Carter, S. Yuan, Q. Xu, and Z. Fei, "Matching network elimination in broadband rectennas for high-efficiency wireless power transfer and energy harvesting," IEEE Trans. Industrial Electronics, **64**, 3950-3961 (2017). <https://doi.org/10.1109/TIE.2016.2645505>
- [8] K. Paramayudha, S. J. Chen, T. Kaufmann, W. Withayachumnankul, and C. Fumeaux, "Triple-band reconfigurable low-profile monopolar antenna with independent tenability," IEEE Open J. Antennas Propag. **1**, 47-56 (2020). <https://doi.org/10.1109/OJAP.2020.2977662>
- [9] W. Hu, T. Feng, S. Gao, L. Wen, Q. Luo, P. Fei, Y. Liu, and X. Yang, "Wideband circularly polarized antenna using single-arm coupled asymmetric dipoles," IEEE Trans. Antennas Propag. **68**, 5104-5113 (2020). <https://doi.org/10.1109/TAP.2020.2975275>
- [10] Y. Luo, and Y. Liu, "Nona-band antenna with small nonground portion for full-view display mobile phones," IEEE Trans. Antennas Propag. **68**, 7624-7629 (2020). <https://doi.org/10.1109/TAP.2020.2989874>
- [11] S. Wang, and Z. Du, "A dual-antenna system for LTE/WWAN/WLAN/WiMAX smartphone applications," IEEE Antennas Wireless Propag. Lett. **14**, 1443-1446 (2015). <https://doi.org/10.1109/LAWP.2015.2411253>
- [12] R. Tang, and Z. Du, "Wideband monopole without lumped elements for octa-band narrow-frame LTE smartphone," IEEE Antennas Wireless Propag. Lett. **16**, 720-723 (2017). <https://doi.org/10.1109/LAWP.2016.2600761>
- [13] Y. Yang, Z. Zhao, W. Yang, Z. Nie, and Q.-H. Liu, "Compact multimode monopole antenna for metal-rimmed mobile phones," IEEE Trans. Antennas Propag. **65**, 2297-2304 (2017). <https://doi.org/10.1109/TAP.2017.2679059>
- [14] Y. Liu, P. Liu, Z. Meng, L. Wang, and Y. Li, "A planar printed nona-band loop-monopole reconfigurable antenna for mobile handsets," IEEE Antennas Wireless Propag. Lett. **17**, 1575-1579 (2018). <https://doi.org/10.1109/LAWP.2018.2856459>
- [15] D. Huang, Z. Du, and Y. Wang, "A quad-antenna system for 4G/5G/GPS metal frame mobile phones," IEEE Antennas Wireless Propag. Lett. **18**, 1586-1590 (2019). <https://doi.org/10.1109/LAWP.2019.2924322>
- [16] Q. Tan, and F.-C. Chen, "Triband circularly polarized antenna using a single patch," IEEE Antennas Wireless Propag. Lett. **19**, 2013-2017 (2020). <https://doi.org/10.1109/LAWP.2020.3014961>
- [17] R.M. Moreno, J. Kurvinen, J. Ala-Laurinaho, A. Khripkov, J. Ilvonen, J. van Wousterghem, and V. Viikari, "Dual-polarized mm-wave endfire chain-slot antenna for mobile devices," IEEE Trans. Antennas Propag. **69**, 25-34 (2021). <https://doi.org/10.1109/TAP.2020.3001434>
- [18] L. Chang, G. Zhang, and H. Wang, "Triple-band microstrip patch antenna and its four-antenna module based on half-mode patch for 5Gx4 MIMO operation," IEEE Trans. Antennas Propag. **70**, 67-74 (2022). <https://doi.org/10.1109/TAP.2021.3090572>
- [19] C. Sahana, D. Nirmala, and M. Jayakumar, "Dual-band circularly polarized annular ring patch antenna for GPS-aided GEO-augmented navigation receivers," IEEE Antennas Wireless Propag. Lett. **21**, 1737-1741 (2022). <https://doi.org/10.1109/LAWP.2022.3178980>
- [20] R. Lakshmanan, S. Mridula, A. Pradeep, and K. Neema, "Ultra compact flexible monopole antennas for tri-band applications," Prog. Electromagn. Res. C, **130**, 43-55 (2023). <http://dx.doi.org/10.2528/PIERC22110906>

- [21] A. Khade, M. Trimukhe, S. Verblkar, and R. K. Gupta, "Miniaturization of printed rectangular monopole antenna by using slots for triple band applications," *Prog. Electromagn. Res. C*, **130**, 155-167 (2023). <http://dx.doi.org/10.2528/PIERC22122401>
- [22] R. W. P. King, and T. T. Wu, "The cylindrical antenna with arbitrary driving point," *IEEE Trans. Antennas Propag.* **13**, 710-718 (1965). <https://doi.org/10.1109/TAP.1965.1138531>
- [23] B. D. Popovic, "On polynomial approximation of current along thin asymmetrical cylindrical dipoles," *IEEE Trans. Antennas Propag.* **19**, 117-120 (1971). <https://doi.org/10.1109/TAP.1971.1139879>
- [24] Y. Wang, S. Xu, and D. H. Werner, "1 bit dual-polarized reconfigurable transmitarray antenna using asymmetric dipole elements with parasitic bypass dipoles," *IEEE Trans. Antennas Propag.* **69**, 1188-1192 (2021). <https://doi.org/10.1109/TAP.2020.3005713>
- [25] M. V. Nesterenko, V. A. Katrich, Y. M. Penkin, V. M. Dakhov, and S. L. Berdnik, *Thin Impedance Vibrators. Theory and Applications*, (Springer Science+Business Media, New York, 2011).
- [26] M. V. Nesterenko, V. A. Katrich, S. L. Berdnik, O. M. Dumin, and Y. O. Antonenko, "Asymmetric impedance vibrator for multi-band communication systems," *Prog. Electromagn. Res. M*, **102**, 81-89 (2021). <http://dx.doi.org/10.2528/PIERM21031207>
- [27] R. Xu, and Z. Shen, "Dual-band circularly polarized RFID reader antenna with combined dipole and monopoles," *IEEE Trans. Antennas Propag.*, **71**, 9593-9600, (2023). <https://doi.org/10.1109/TAP.2023.3326945>
- [28] X. Liu, K. Ning, S. Xue, L. Ge, K. W. Leung, and J.-F. Mao, "Printed filtering dipole antenna with compact size and high selectivity," *IEEE Trans. Antennas Propag.*, **72**, 2355-2367, (2024). <https://doi.org/10.1109/TAP.2024.3356176>
- [29] S. A. Schelkunoff, "Theory of antennas of arbitrary size and shape," *Proc. IRE*, **29**, 493-521 (1941). <https://doi.org/10.1109/JRPROC.1941.231669>
- [30] C. T. Tai, "On the theory of biconical antennas," *Journal Applied Phys.*, **19**, 1155-1160 (1948). <https://doi.org/10.1063/1.1715036>
- [31] S. A. Schelkunoff, *Antennas Theory and Practice*, (Facsimile Publisher, 1952).
- [32] T. T. Wu, and R. W. P. King, "The tapered antenna and its application to the junction problem for thin wires," *IEEE Trans. Antennas Propag.* **24**, 42-45 (1976). <https://doi.org/10.1109/TAP.1976.1141274>
- [33] S. A. Saoudy, and M. Hamid, "Input admittance of a biconical antenna with wide feed gap," *IEEE Trans. Antennas Propag.* **38**, 1784-1790 (1990). <https://doi.org/10.1109/8.102740>
- [34] S. S. Sandler, and R. W. P. King, "Compact conical antennas for wide-band coverage," *IEEE Trans. Antennas Propag.* **42**, 436-439 (1994). <https://doi.org/10.1109/8.280735>
- [35] K.-L. Wong, and S.-L. Chien, "Wide-band cylindrical monopole antenna for mobile phone," *IEEE Trans. Antennas Propag.* **53**, 2756-2758 (2005). <https://doi.org/10.1109/TAP.2005.851784>
- [36] O. Dumin, P. Fomin, V. Plakhtii, and M. Nesterenko, "Ultrawideband combined monopole-slot radiator of Clavin type," in *Proc. XXVth Int. Sem. Direct Inverse Problems of Electromagn. and Acoustic Wave Theory*, 32-36, (2020). <https://doi.org/10.1109/DIPED49797.2020.9273399>
- [37] P. Fomin, O. Dumin, V. Plakhtii, and M. Nesterenko, "UWB antenna arrays with the monopole-slot radiator of Clavin type," in *Proc. IIIth Ukraine Conf. on Electrical and Computer Engineering*, 258-261, (2021). <https://doi.org/10.1109/UKRCON53503.2021.9575282>
- [38] M. V. Nesterenko, A. V. Gomozov, V. A. Katrich, S. L. Berdnik, and V. I. Kijko, "Scattering of electromagnetic waves by impedance biconical vibrators in a free space and in a rectangular waveguide," *Prog. Electromagn. Res. C*, **119**, 275-285 (2022). <http://dx.doi.org/10.2528/PIERC22020304>
- [39] M. S. Fouad, A. E. Farahat, K. F. A. Hussein, A. A. Shaalan, and M. F. Ahmed, "Super-wideband fractal antenna for future generations of wireless communication," *Prog. Electromagn. Res. C*, **136**, 137-149 (2023). <http://dx.doi.org/10.2528/PIERC23042507>
- [40] F. F. Dubrovka, S. Piltyay, M. Movchan, and I. Zakharchuk, "Ultrawideband compact lightweight biconical antenna with capability of various polarizations reception for modern UAV applications," *IEEE Trans. Antennas Propag.*, **71**, 2922-2929 (2023). <https://doi.org/10.1109/TAP.2023.3247145>
- [41] J. M. Platt, L. B. Boskovic, and D. S. Filipovic, "Wideband biconical antenna with embedded band-notch resonator," *IEEE Trans. Antennas Propag.*, **72**, 2921-2925 (2024). <https://doi.org/10.1109/TAP.2024.3349785>
- [42] I. D. Chiele, M. Donelli, J. Iannacci, and K. Guha, "On chip modulated scattering tag operating at millimetric frequency band," *Prog. Electromagn. Res. M*, **124**, 71-77 (2024). <http://dx.doi.org/10.2528/PIERM23102707>
- [43] M. V. Nesterenko, V. A. Katrich, and S. V. Pshenichnaya, "Multiband asymmetric biconical dipole antenna with distributed surface impedance and arbitrary excitation," *East European J. Physics*, **2**, 450-455 (2024). <https://doi.org/10.26565/2312-4334-2024-2-59>
- [44] R. W. P. King, and G. S. Smith, *Antennas in Matter*, (Cambridge, USA: MIT Press, 1981).
- [45] R. W. P. King, and L. D. Scott, "The cylindrical antenna as a probe for studying the electrical properties of media," *IEEE Trans. Antennas and Propagat.*, **19**, 406-416 (1971). <https://doi.org/10.1109/TAP.1971.1139930>
- [46] D. Lamensdorf, "An experimental investigation of dielectric-coated antennas," *IEEE Trans. Antennas and Propagat.* **15**, 767-771 (1967).
- [47] *Tables of Physical Values. Handbook*, Editor I. K. Kikoin. (Moscow: Atomizdat, 1976). (in Russian)
- [48] K. Yoshitomi, "Radiation from a slot in an impedance surface," *IEEE Trans. Antennas Propag.* **49**, 1370-1376 (2001). <https://doi.org/10.1109/8.954925>

ВИПРОМІНЮВАННЯ ЕЛЕКТРОМАГНІТНИХ ХВИЛЬ РЕГУЛЯРНИМИ ТА БІКОНІЧНИМИ ДИПОЛЯМИ ЗІ ЗМІННИМ РОЗПОДІЛЕНИМ ПОВЕРХНЕВИМ ІМПЕДАНСОМ І ДОВІЛЬНИМ ЗБУДЖЕННЯМ

Михайло В. Нестеренко, Віктор А. Катрич, Юрій В. Аркуша, Володимир В. Катрич

Харківський національний університет імені В. Н. Каразіна, майдан Свободи, 4, Харків, Україна, 61022

Отримано наближений аналітичний розв'язок задачі про випромінювання електромагнітних хвиль регулярними та біконічними диполями з постійним та змінним комплексним розподіленим поверхневим імпедансом і довільним збудженням. Правильність рішення підтверджується задовільним узгодженням експериментальних і чисельних результатів із відомих літературних джерел. Наведено чисельні результати для вхідних характеристик і полів випромінювання диполів у випадках їх симетричного та асиметричного збудження точковим джерелом.

Ключові слова: регулярний диполь; біконічний диполь; змінний розподілений поверхневий імпеданс; довільне збудження; розподіл струму; вхідні характеристики; поля випромінювання

INFLUENCE OF PHTHALIC ACID ON THE PROCESS OF DENDRITE DEVELOPMENT IN LOW-DENSITY POLYETHYLENE DURING ELECTRICAL BREAKDOWN

Sh.A. Zeynalov^a, H.N. Vezirov^b, F.Sh. Kerimov^a, S.I. Safarova^a, K.J. Gulmamedov^a,
A.S. Alekperov^{c,d,*}

^a Azerbaijan Technical University, Baku, AZ-1073, Azerbaijan

^b Institute of Physics, Ministry of Science and Education Republic of Azerbaijan, Baku, AZ-1143, Azerbaijan

^c Azerbaijan State Pedagogical University, Baku, AZ-1000, Azerbaijan

^d Western Caspian University, Baku AZ-1001, Azerbaijan

*Corresponding Author e-mail: aydinalekperov@yahoo.com

Received June 28, 2024; revised August 14, 2024; accepted August 17, 2024

The presented work presents the results of a study on the effect of small amounts of phthalic acid additives on dendrite formation in low-density polyethylene (LDPE). Based on the results obtained, it is shown that the dendrite resistance of LDPE, as expected, increases with the introduction of 0.05 wt% phthalic acid. The established increase in dendrite resistance of LDPE with the introduction of phthalic acid can primarily be explained based on a decrease in inhomogeneities in the form of air pores as a result of accelerated structure formation and the emergence of a more homogeneous supramolecular structure. It was revealed that an increase in dendrite resistance correlates with an improvement in the dielectric characteristics of the composition. The influence of mechanical load on the development of dendrites in polymer dielectrics has been studied. As a result of studying the growth of dendrites in LDPE samples and its optimal composition subjected to unilateral stretching, it was found that under the influence of mechanical tensile stresses, the shape of the surface delimiting tree-like shoots changes, this surface is flattened in the direction of stretching. It has been shown that the rate of dendrite growth increases as mechanical tensile forces increase.

Keywords: LDPE; Dendrites; Tension; Supramolecular structure; Phthalic acid

PACS: 36.20.-r; 72.15.Eb

1. INTRODUCTION

Extensive research is being conducted to study functional materials' structure and dielectric, electrical, thermal and optical properties. These studies are very important both from the point of view of fundamental physics and for determining the possibilities of using materials. Therefore, research in this direction has continued in recent years [1-5]. Polymer and polymer-nanocomposite materials occupy a special place among functional materials. It has been established that, depending on the properties of the nanoparticles included in the composition, interesting physical properties can be observed in these materials [6-10]. The most studied material among polymers is polyethylene. Polyethylene is widely used as high-voltage insulation, particularly in cables, which raises interest in studying the processes of electrical ageing leading to its breakdown. These processes are associated with the appearance of irreversible changes, so-called dendrites or trees, which are a system of micron-diameter and millimeter-length cavities [11]. It is established that electrical dendrites in polymers are hollow tubes with a diameter of 1 μm gradually tapering at the end. Depending on the growth conditions, dendrites can take various forms such as tree-like, bush-like, or cavity forms [12]. According to the literature [11-13], dendrite channels cannot be considered as a continuation of the needle. In [14], the nature of the development of dendrites in epoxy resin under the influence of high voltage is analysed.

Based on photographic recording of flashes during partial discharge, the authors conclude that dendrite branches can be both conductive and non-conducting. So in the case of a bush-shaped dendrite, a flash during partial discharges fills several branches of the dendrite and originates from the needle. This is a dendrite with conducting branches. It reflected light photographs given in show that the non-conducting branches appear white and the conductive branches appear black, apparently due to carbonation. In [15], it is noted that in polyethylene, at some stage of dendrite growth, the phenomenon of the transition of its branches from a non-conducting to a conducting state is observed [16]. It should be noted that in recent years, a large number of works have appeared devoted to the study of pre-breakdown phenomena in polymers in strong electric fields; electroluminescence that occurs before the appearance of dendrites has been discovered [17,18], the occurrence of pores and cracks in polymers in the zone of high electric field strengths when exposed to a sample has been established series of pulses.

2. OBJECTIVE

This study aimed to develop new polymer modifications to increase dendrite resistance, which can be achieved by introducing certain organic and inorganic low-molecular-weight additives. Studying dendrite growth is of great practical interest since dendrites are found in the insulation of cables that have been in operation for a long time. The influence of mechanical stress on the process of dendrite development in the polymer was also investigated.

2. RESEARCH METHODOLOGY

Low-density polyethylene grade 15313-003 was chosen as the research object, and organic compounds such as phthalic acid (chemical formula $C_6H_4(CO_2H)_2$) were used as additives. Additives were introduced into the initial LDPE raw material by mechanical mixing in amounts of 0.01-0.1 wt%. Samples for the study were made in films with a thickness of 50-70 μm by pressing on a PG-60 hydraulic press. Before introducing the additives into LDPE, its dispersion was achieved using sieve analysis on a grain size determination device. The particle size was less than 50 μm .

The effect of mechanical loads on the change in τ with the electric field intensity of polymer materials was measured in a test cell (Fig. 1).

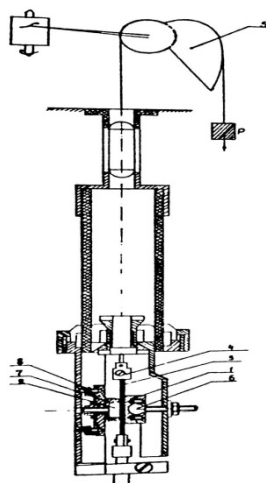


Figure 1. Installation for determining the electrical and mechanical strength of polymer film materials: 1, 2 – electrodes; 3 – sample; 4 – clamps; 5 – lever device; 6 – ball; 7 – security ring; 8 – springs

Dendritic resistance was determined using the method of 2 needles at a frequency of 50 Hz and room temperature on the high-voltage setup AII-70.

Steel needles were used as electrodes; the grounded electrode had a diameter of 80 μm . To obtain standard sizes, the tips of the steel needles for high-voltage electrodes were electrolytically etched in a 2% NaOH solution until the tip diameter was rounded to $4 \pm 0.5 \mu m$. The current magnitude was selected experimentally, depending on the number of needles etched simultaneously. In our case, it ranged from 10-15 A during the simultaneous etching of 70 needles. The diameter of the needle rounding was determined using an MHP microscope equipped with a projection screen (magnification 500 \times).

The samples had the shape of a bar with dimensions of 20 \times 10 \times 4 mm (Fig. 2). To prevent the formation of cracks during the preparation of the sample when inserting the electrodes, the samples and electrodes were heated for 15 minutes in a thermostat close to the melting temperature (at 105K). When inserting the electrodes, the samples were placed in a groove of the device (Fig. 2), and the needles were inserted through the slots.

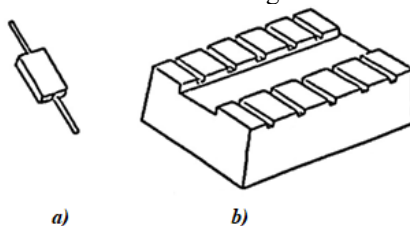


Figure 2. Sample forms (a) and device with a groove (b) for positioning the samples

The distance between the ends of the electrodes was 4 ± 0.1 mm, which was controlled under a microscope.

The electrode device was placed in a desiccator filled with transformer oil to eliminate surface discharges (with an electric strength greater than 25 kV/mm).

Simultaneously, 10 samples were tested. A certain voltage U was applied to the samples for 1 hour. Then, the number of samples in which dendrites grew at the given voltage was determined. For each batch of polymer, several (at least 3) series of samples (10 each) were tested at different voltages.

Based on the experimental data, the dependence of the number of samples with dendrites on the voltage at which they form was plotted. The dependence $n=f(u)$, in the first approximation over a narrow range of variation, can be represented as a straight line. From the graph U_d , the value corresponding to $n=5$, was found and taken as the measure of dendritic resistance. The relative error did not exceed 5%.

3. RESULTS AND DISCUSSIONS

Fig. 3 presents the experimental results obtained using the described method for the film made of LDPE (without additives). As can be seen, the numerical value U_d for the tested samples is 6.8 kV.

However, as shown by the data (Fig. 4), the introduction of phthalic acid (PhAc) into LDPE in an amount of 0.05wt% leads to an increase in U_d to 9.5 kV.

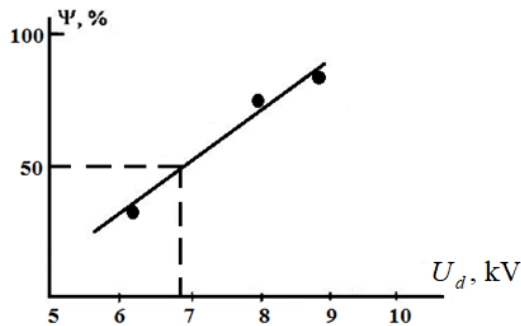


Figure 3. Dependence of LDPE dendritic resistance on electrical voltage

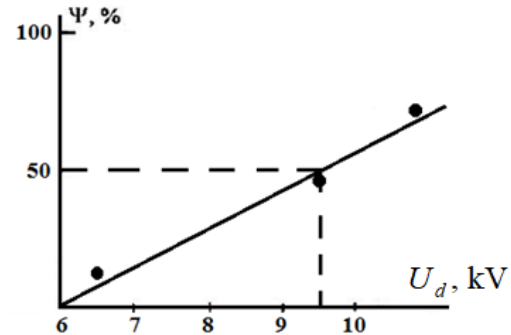


Figure 4. Dependence of dendritic resistance of the LDPE+0.05wt.% PhAc composition on electrical voltage

This means that the organic additive PhAc in a small amount affects the dendritic resistance of LDPE. The observed increase in dendritic resistance of LDPE with the introduction of a small amount of PhAc can primarily be explained by the reduction of inhomogeneities in the form of air pores, resulting from the acceleration of structure formation and the development of a more uniform supramolecular structure.

The development of dendrites in polymers is also influenced by mechanical stresses in the insulation [19,20]. Studies on the growth of dendrites in polyethylene samples subjected to unidirectional tension, with needle electrodes inserted in such a way that the electric field was applied perpendicular to the direction of tension, have shown that under the influence of mechanical tensile stresses, the shape of the surface limiting the tree-like branches changes; this surface flattens in the direction of the tension.

Based on the above, the observed increase in dendritic resistance of LDPE with the introduction of the proposed additive PhAc in the optimal amount (0.05wt.%) should contribute to the improvement of the mechanical strength and dielectric properties of the polymer composition.

We studied the effect of mechanical loads on the change in lifetime τ (the time elapsed from the moment the electrical voltage is applied to the sample until breakdown) of films of the original and modified low-density polyethylene (LDPE).

Fig. 5 shows the dependence of the logarithm of the lifetime lgt of the original and loaded polymer films LDPE and LDPE + 0.05wt% PhAc on the electric field strength E at 293 K.

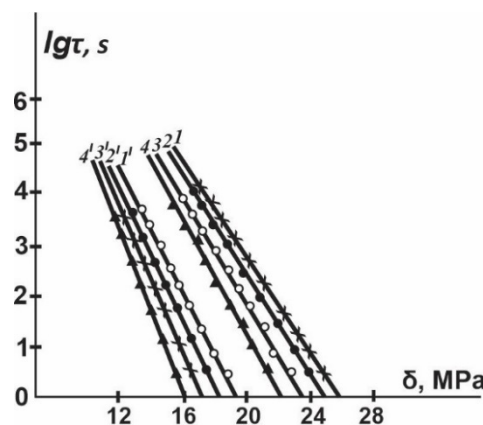


Figure 5. Dependence of the lifetime of polymer films LDPE (1'-4') and LDPE + 0.05wt.%PhAc (1-4) on the electric field strength under the simultaneous influence of different values of mechanical load (σ , MPa):
 1 – 0; 2 – 2.5; 3 – 5; 4 – 7.5; 1' – 0; 2' – 2.5; 3' – 5; 4' – 7.5.

From Fig. 5, it can be seen that at a constant temperature, the presence of a continuously acting mechanical load does not disrupt the linear nature of the dependence of lgt on E . That is, $\tau_E = f(E)$, can be described by the empirical formula:

$$\tau_E = B \exp(-\beta E), \tag{1}$$

where the parameters B and β depend on the nature and temperature of the test.

From Fig. 5, it can be seen that the introduction of phthalic acid into LDPE leads to a significant increase in its electrical strength compared to the original LDPE.

As follows from the obtained results, the process of electrical breakdown of the tested samples is observed even at relatively small values of mechanical stress. However, as the mechanical stress increases, the lifetime of the samples decreases, i.e., the rate of dendrite growth increases with the increase in mechanical load.

The slowdown in the development of the electrical breakdown process with the introduction of the optimal amount of PhAc additive into LDPE (curves 1-4), even in the case of a mechanically stressed state compared to the original LDPE (curves 1' - 4') can be explained by the fact that the accumulation and growth of dendrites in polymer dielectrics under the combined influence of the aforementioned factors, under otherwise identical conditions, also depends on structural features.

It should be noted that the dendritic resistance of crystallizing polymers is significantly influenced by the chemical nature and concentration of the introduced additives, dispersion, surface area and shape of the particles, the presence and nature of functional groups on the surface of the additives, and the physical and electrophysical nature of the additive particles [21,22]. The observed increase in the induction period of dendrite formation in LDPE with the introduction of the proposed phthalic acid (PhAc) additives in the optimal amount (0.05wt%) can be explained by their structuring characteristics, which help to slow down the process of local heating near the tip in a strong electric field and the occurrence of initial defects due to thermal decomposition of the polymer [23-25]. Moreover, the increase in dendritic resistance of LDPE + 0.05 wt% PhAc should contribute to the improvement of the dielectric properties of the polymer composition, the experimental results of which are presented in the table.

Table 1. Influence of additives on the dendritic resistance of LDPE

Composition	U_d kV	Λ - dendrite at 9 kV	$tg\delta$ at ($\nu = 10^6$ Hz)	ϵ at ($\nu = 10^6$ Hz)	ρ_u , Om · m
LDPE	6.8	16.5	$4.5 \cdot 10^{-4}$	2.3	$1 \cdot 10^5$
LDPE+0.05 wt %PhAc	9.5	13	$3 \cdot 10^{-4}$	2.1	$1 \cdot 10^{17}$
LDPE+0.1wt%PhAc	7	16	$4 \cdot 10^{-4}$	2.2	$1 \cdot 10^{11}$

The table shows the influence of organic additives on the dendritic resistance and dielectric properties of low-density polyethylene. Indeed, when modifying the properties of polymers by changing their supramolecular structure (by introducing artificial nucleating agents or other methods), it is important to assess the stability of the supramolecular structure through various mechanical, thermal, ionizing, and other external influences.

Furthermore, the study of the stability of the supramolecular structure showed that after several repeated melting, the size of the structural elements in the LDPE samples containing nucleating agents remains practically unchanged, while in the control samples, they increase.

CONCLUSIONS

The optimal composition of the low-molecular-weight organic additive phthalic acid was determined, and its influence on the process of dendrite formation in low-density polyethylene (LDPE) was investigated. It was found that composites with 0.05% by mass of phthalic acid significantly increase the dendritic resistance of LDPE, as expected. The effect of mechanical stretching on the development of dendrites in polymer dielectrics was studied. It was shown that the rate of dendrite growth increases with increasing mechanical tensile stress.

The observed increase in the induction period of dendrite formation in LDPE with the proposed additive in the optimal amount can be explained by their structuring characteristics. This contributes to slowing down the process of local heating near the tip in a strong electric field and the occurrence of initial defects due to the thermal decomposition of the polymer.

It should be noted that we are conducting comprehensive studies on the structural properties of LDPE and its modifications using electron scanning microscopy, X-ray diffraction, and IR spectroscopy. We are also investigating the effects of gamma radiation doses and UV irradiation on the electrophysical ($\epsilon, tg\delta, \rho_v$) and mechanical properties of LDPE and its modifications. Additionally, we are studying the influence of the small mentioned additive on the rate and mechanism of polyethylene crystallization. The results of these studies will be published in prestigious scientific journals.

ORCID

Sh.A. Zeynalov, <https://orcid.org/0000-0002-0040-6057>

REFERENCES

- [1] Y.I. Aliyev, F.G. Asadov, T.M. Ilyashi, A.O. Dashdemirov, R.E. Huseynov, and S.H. Jabarov, *Ferroelectrics*, **599**, 78 (2022). <https://doi.org/10.1080/00150193.2022.2113641>
- [2] S.H. Jabarov, A.Kh. Nabiyeva, A.V. Trukhanov, S.V. Trukhanov, H.J. Huseynov, and Y.I. Aliyev, *SOCAR Proceedings*, **4**, 171 (2023). <http://dx.doi.org/10.5510/OGP20230400931>
- [3] F.G. Agayev, S.H. Jabarov, G.Sh. Ayyubova, A.V. Trukhanov, S.V. Trukhanov, M.N. Mirzayev, T.G. Naghiyev, and N.T. Dang, *Journal of Superconductivity and Novel Magnetism*, **33**, 2867 (2020). <https://doi.org/10.1007/s10948-020-05544-9>
- [4] T.M. Ilyashi, N.Sh. Mammadova, F.M. Sadigov, R.E. Huseynov, and Y.I. Aliyev, *East European Journal of Physics*, **2**, 297 (2024). <https://doi.org/10.26565/2312-4334-2024-2-33>

- [5] Kh.N. Ahmadova, and S.H. Jabarov, *Arabian Journal for Science and Engineering*, **48**, 8083 (2023). <https://doi.org/10.1007/s13369-022-07449-2>
- [6] R.J. Bashirov, N.E. Ismayilov, R.E. Huseynov, and N.M. Muradov, *Advanced Physical Research*, **6**, 90 (2024). <https://doi.org/10.62476/apr62.90>
- [7] F.V. Hajiyeva, A. Chianese, A.A. Novruzova, and M.A. Ramazanov, *Advanced Physical Research*, **3**(3), 129 (2021). http://jomardpublishing.com/UploadFiles/Files/journals/APR/V3N3/3Hajiyeva_et_al.pdf
- [8] E.M. Gojayevev, Sh.V. Aliyeva, V.V. Salimova, A.Yu. Meshalkin, and S.H. Jabarov, *Surface Engineering and Applied Electrochemistry*, **56**, 740 (2020). <https://doi.org/10.3103/S106837552006006X>
- [9] E.M. Gojayevev, V.V. Salimova, and S.H. Jabarov, *Modern Physics Letters B*, **33**, 1950412 (2019). <https://doi.org/10.1142/S0217984919504128>
- [10] E.M. Gojayevev, Sh.V. Aliyeva, X.S. Khalilova, G.S. Jafarova, and S.H. Jabarov, *International Journal of Modern Physics B*, **33**(26), 1950309 (2019). <https://doi.org/10.1142/S0217979219503090>
- [11] V.A. Volokin, O.S. Geffle, S.M. Lebedev, *Journal of Applied Mechanics and Technical Physics*, **50**(1), 72 (2009). <https://www.sibran.ru/upload/iblock/5e8/5e85ecc2a555187f73f9a583a632f068.pdf>
- [12] O.S. Geffle, S.M. Lebedev, and V.Y. Uschekkov, *Journal of Physics D: Applied Physics*, **37**, 2318 (2004). <http://dx.doi.org/10.1088/0022-3727/37/16/015>
- [13] M.D. Noskov, A.S. Malinovsky, M. Zakk, and A.Y. Shvab, *Journal of Technical Physics*, **72**(2), 121 (2002). <https://journals.ioffe.ru/articles/viewPDF/40073>
- [14] S.M. Lebedov, O.S. Geffle, V.A. Volokin, and P.V. Tarasov, in: *Proc. of the 15th Intern. symp. on high voltage engug*, (Ljubljana, 2007), p. 476.
- [15] M.M. Rezinkina, *Journal of Technical Physics*, **75**(6), 85 (2005). <https://journals.ioffe.ru/articles/viewPDF/8582>
- [16] C. Poliska, Z. Gácsi, P. Barkóczy. *Materials Science Forum*, **508**, 169-174 (2006). <https://doi.org/10.4028/www.scientific.net/MSF.508.169>
- [17] N. Shimizu, and C. Laurent, *IEEE Transactions on Dielectrics and Electrical Insulation*, **5**(5), 113 (1998). <https://doi.org/10.1109/94.729688>
- [18] P.J. Sweeney, L.A. Dissado, and J.M. Cooper, *Journal of Physics D: Applied Physics*, **25**(1), 113 (1992). <https://doi.org/10.1088/0022-3727/25/1/016>
- [19] Sh.A. Zeynalov, B.G. Garadzhaev, S.Kh. Khalilov, F.Sh. Kerimov, and A.M. Alekperov, *Norwegian Journal of Development of the International Science*, **86**, 53 (2022). <https://doi.org/10.5281/zenodo.6606629>
- [20] E.M. Gojaev, A.A. Abdurragimov, F.Sh. Kerimov, and S.İ. Safarova, *AzTU Journal of Scientific Proceedings of Fundamental Science*, **2**, 56 (2018).
- [21] O.S. Geffle, S.M. Lebedov, and Y. P. Pokholkov, in: *IEEE International Conference on Solid Dielectrics*, (Winchester, UK, 2007), pp. 142-145. <http://dx.doi.org/10.1109/ICSD.2007.4290773>
- [22] V.M. Biskov, and V.M.Kosenkov, *Electronic Materials Processing*, Chisinau, **49**(4), 51 (2013). <https://eom.ifa.md/ru/journal/shortview/899>
- [23] M.M. Rezinkina, O.L. Rezinkin, and M.I. Nosenko, *Journal of Technical Physics*, **71**(3), 69 (2001). <https://repository.kpi.kharkov.ua/server/api/core/bitstreams/674b7ccf-5360-41e8-828a-ccf498a3ee38/content>
- [24] L.A. Dissado, J.C. Fothergill, N. Wise, J. Cooper, *J. Phys. D: Appl. Phys.* **33**(19), L109 (2000). <https://doi.org/10.1088/0022-3727/33/19/103>
- [25] A. Tallove, and S. Hagness, *Computational Electrodynamics: The finite difference time domain method*, (Artech House, Boston; London, 2000).

ВПЛИВ ФТАЛЕВОЇ КИСЛОТИ НА ПРОЦЕС РОЗВИТКУ ДЕНДРИТІВ ПОЛІЕТИЛЕНУ НИЗЬКОЇ ГУСТИНИ ПРИ ЕЛЕКТРИЧНОМУ ПРОБОЇ

Ш.А. Зейналлов^а, Х.Н. Везіров^б, Ф.Ш. Керімов^а, С.І. Сафарова^а, К.Й. Гульмамедов^а, А.С. Алекперов^{с,д}

^аАзербайджанський технічний університет, Баку, AZ-1073, Азербайджан

^бІнститут фізики Міністерства науки і освіти Азербайджанської Республіки, Баку, AZ-1143, Азербайджан

^сАзербайджанський державний педагогічний університет, Баку, AZ-1000, Азербайджан

^дЗахідно-Каспійський університет, Баку AZ-1001, Азербайджан

У представленій роботі представлені результати дослідження впливу невеликих кількостей добавок фталевої кислоти на утворення дендритів у поліетилені низької щільності (ПЕНЩ). На підставі отриманих результатів показано, що дендритна стійкість ПЕНЩ, як і очікувалося, зростає при введенні 0,05 мас.% фталевої кислоти. Встановлене підвищення дендритостійкості ПЕНЩ із введенням фталевої кислоти в першу чергу можна пояснити зменшенням неоднорідностей у вигляді повітряних пор внаслідок прискореного структуроутворення та виникнення більш однорідної надмолекулярної структури. Виявлено, що підвищення опору дендритів корелює з поліпшенням діелектричних характеристик композиції. Досліджено вплив механічного навантаження на розвиток дендритів у полімерних діелектриках. У результаті дослідження росту дендритів у зразках ПЕНЩ та його оптимального складу, підданих однобічному розтягуванню, встановлено, що під дією механічних розтягуючих напружень змінюється форма поверхні, що обмежує деревоподібні пагони, ця поверхня сплющується в напрямку розтягування. Було показано, що швидкість росту дендритів збільшується зі збільшенням механічних сил розтягування.

Ключові слова: LDPE; дендрити; напруга; супрамолекулярна структура; фталева кислота

PROTECTIVE EFFECT OF QUERCETIN ON AMYLOID-INDUCED ALTERATIONS IN LIPID BILAYER INTEGRITY

 **Uliana Tarabara**,  **Valeriya Trusova***,  **Galyna Gorbenko**

*Department of Medical Physics and Biomedical Nanotechnologies, V.N. Karazin Kharkiv National University
4 Svobody Sq., Kharkiv, 61022, Ukraine*

**Corresponding Author: valeriya.trusova@karazin.ua*

Received June 15, 2024, revised July 21, 2024; accepted August 14, 2024

The present study employs molecular dynamics simulations to investigate the interactions between quercetin, amyloid fibrils, and POPC lipid bilayers. The results demonstrate that quercetin does not significantly affect the molecular organization of the bilayer, while IAPP fibrils induce substantial structural changes, particularly in the outer monolayer. Quercetin mitigates these effects by reducing the impact on headgroup and glycerol regions and causing a more superficial positioning of IAPP. Additionally, quercetin slightly decreases the order of sn-2 acyl chains, indicating a disordering effect. In a ternary system with POPC, quercetin, and IAPP, the reduction in the deuterium order parameter of sn-2 acyl chains is less pronounced, underscoring quercetin's protective role. Unlike IAPP, ApoAI and insulin fibrils undergo significant structural reorganization in the membrane-bound state. Quercetin attenuative effects are observed only with ApoAI, highlighting its potential as a protective agent against amyloid-induced membrane disruption. These findings provide valuable insights into the interactions between polyphenols, amyloid fibrils, and lipid membranes, contributing to the understanding of membrane-associated amyloid pathologies.

Key words: *Amyloid fibrils; Lipid membranes; Polyphenols; Molecular dynamics*

PACS: 87.14.C++c, 87.16.Dg

The interaction between amyloid fibrils and lipid bilayers is a critical factor in the pathogenesis of several neurodegenerative diseases, including Alzheimer's and Parkinson's diseases. These fibrils, formed by the misfolding and aggregation of proteins, possess a unique structural arrangement characterized by cross- β -sheet conformations, which confer them with significant mechanical stability and resistance to proteolytic degradation [1,2]. The cytotoxicity associated with amyloid fibrils is primarily attributed to their ability to disrupt cellular membranes, thereby compromising cellular integrity and function. This membrane disruption is facilitated by the interaction of amyloid fibrils with lipid bilayers, leading to increased membrane permeability and potential cell death. Quercetin, a naturally occurring flavonoid, has garnered attention for its potential protective effects against oxidative stress and its ability to modulate the interactions of lipid membranes with biomacromolecules [3]. Quercetin is known for its antioxidative properties, which include the inhibition of lipid peroxidation and the scavenging of reactive oxygen species (ROS) [4,5]. These properties are crucial in maintaining the structural integrity of lipid bilayers, which are susceptible to oxidative damage. Moreover, quercetin has been shown to interact with lipid membranes, potentially altering their physical properties and influencing their interactions with amyloid fibrils [6,7]. Recent studies have demonstrated that quercetin can disaggregate amyloid fibrils, such as those formed by A β -peptide, and reduce their cytotoxic effects [8]. This disaggregation ability suggests that quercetin may alter the morphology of amyloid fibrils, leading to the formation of less toxic aggregates that are less capable of disrupting lipid bilayers. Additionally, the binding of quercetin to amyloid fibrils has been shown to decrease the fibril-induced cytotoxicity, further supporting its protective role [9]. The protective effect of quercetin on lipid bilayers against the modulatory action of amyloid fibrils is thus extremely important since understanding the mechanisms by which quercetin exerts its protective effects could lead to the development of novel therapeutic strategies aimed at mitigating the deleterious effects of amyloid fibrils in neurodegenerative diseases. In the present work, using the molecular dynamics simulations, we aimed at elucidating the molecular-level interactions between quercetin, amyloid fibrils, and lipid bilayers to provide insights into the potential of quercetin as a protective agent in the context of amyloid-related cytotoxicity.

METHODS

To perform molecular dynamics (MD) simulations of the model membrane systems the input files were prepared using the web-based graphical interface CHARMM-GUI. The topologies of polyphenols were generated using the CHARMM-GUI Ligand Reader and Modeler. The obtained files were further used to generate the quercetin-lipid systems using the Membrane Builder option. The model lipid bilayer was composed of 72 of 1-palmitoyl-2-oleoyl-sn-glycero-3-phosphatidylcholine (POPC) in each monolayer. The initial distance of quercetin translation from the membrane midplane along the bilayer normal was 10 Å. To obtain a neutral total charge of the system a necessary number of counterions was added. The molecular dynamics simulations of the model membrane systems and analysis of the trajectories were carried out using the GROMACS 2024.2 software with the CHARMM36m force field at a temperature of 310 K in the NPT ensemble with the time step for MD simulations 2 fs. The Particle Mesh Ewald method was utilized for correct treatment of the long-range electrostatic interactions. The bond lengths were constrained using the LINC algorithm. The pressure

and temperature controls were performed using the V-rescale thermostat. The MD simulations were performed with minimization of 50000 steps and equilibration of 12500000 steps. The whole-time interval for MD calculations was 10 ns. The GROMACS command `gmx density` was used to calculate the mass density distribution for various components of the lipid bilayer and density distribution of quercetin across a lipid bilayer. The molecular graphics and visualization of the simulation evolution over time were performed using the Visual Molecular Dynamics (VMD) software.

RESULTS AND DISCUSSION

Molecular dynamics simulations of the systems POPC + quercetin, POPC + IAPP fibril and POPC + quercetin + IAPP fibril revealed that quercetin and IAPP reside at the lipid-water interface and do not leave the lipid bilayer throughout the simulation time. The persistence of both quercetin and IAPP fibrils at the lipid-water interface during the simulation period suggests a stable interaction with the lipid bilayer, which is crucial for understanding their modulatory effects on membrane integrity. Specifically, the localization of quercetin at the lipid-water interface aligns with its amphipathic nature, allowing it to interact favorably with both the hydrophobic core and the polar head groups of the lipid bilayer. Similarly, the retention of IAPP fibrils at the lipid-water interface underscores their propensity to interact with lipid membranes, a characteristic that is implicated in their cytotoxic effects.

The analysis of the density distributions showed that quercetin does not exert significant influence on the molecular organization of headgroup, glycerol and acyl chain regions of POPC bilayer (Fig. 1).

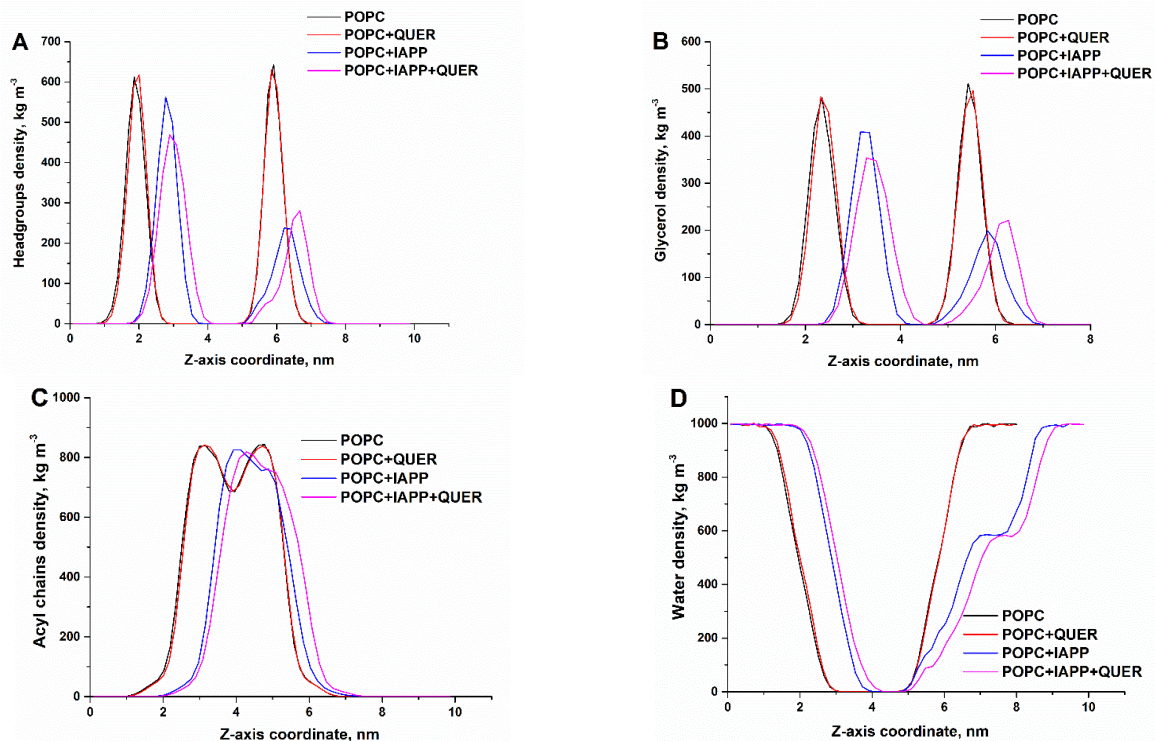


Figure 1. The density distributions of headgroups (A), glycerols (B), acyl chains (C) and water (D) in POPC bilayer in the absence and presence of quercetin, IAPP and quercetin + IAPP

Quercetin may integrate into the bilayer through hydrophobic interactions without disturbing the tightly packed acyl chains, thus maintaining the bilayer's structural integrity. Additionally, its polar nature might allow it to associate with the headgroups without causing significant rearrangement or density changes. In contrast, IAPP fibrils cause a decrease in the density of headgroups and glycerols, with the magnitude of this effect being much greater for the outer monolayer. Likewise, the density distribution of acyl chains and water become asymmetric in the presence of IAPP. These findings suggest that fibrillar IAPP is capable of inducing substantial changes in the lipid bilayer structure. This disruptive influence can be attributed to several factors. IAPP fibrils may insert into the bilayer, displacing or reorganizing lipid molecules, particularly in the outer monolayer where they are more accessible. The fibrillar structure of IAPP can disrupt the orderly arrangement of lipids, leading to decreased density and asymmetry. This disruption is more pronounced in the headgroup and glycerol regions due to their proximity to the aqueous environment where fibrils form. Additionally, IAPP fibrils may interact with both the hydrophobic core and the polar headgroups of the bilayer, causing reorganization that results in the observed density changes.

Remarkably, addition of quercetin leads to some attenuation the fibril impact on the regions of head groups and glycerol in the outer monolayer, accompanied by slight alterations in the acyl chain and water distributions. Additionally, in the presence of quercetin the position of IAPP becomes more shallow (data not shown). The polyphenolic structure of quercetin allows it to integrate into the lipid bilayer, where it can form stabilizing interactions with the polar head groups

and glycerol backbone. This integration may enhance the rigidity and stability of the bilayer, thereby reducing the susceptibility of the membrane to perturbations caused by amyloid fibril formation. By interacting with the lipid head groups, quercetin may also influence the distribution of acyl chains and water molecules, promoting a more ordered and less permeable membrane structure.

As seen in Fig. 2, the deuterium order parameter of sn-1 acyl chains was not influenced by quercetin, but showed a slight decrease in the presence of IAPP fibrils. At the same time, the deuterium order parameter of sn-2 acyl chains attained markedly less values in the presence of quercetin or IAPP relative to the neat POPC, suggesting the disordering effects of this polyphenol and amyloid fibrils on the nonpolar part of POPC bilayer. Notably, in the ternary system POPC + quercetin + IAPP the magnitude of the IAPP-induced decrease of the deuterium order parameter of sn-2 acyl chains appeared to be markedly less compared to the system POPC + IAPP. This finding provides additional arguments in favor of quercetin ability to exert protective effect against the disruption of lipid bilayer structural integrity produced by the IAPP amyloid fibrils

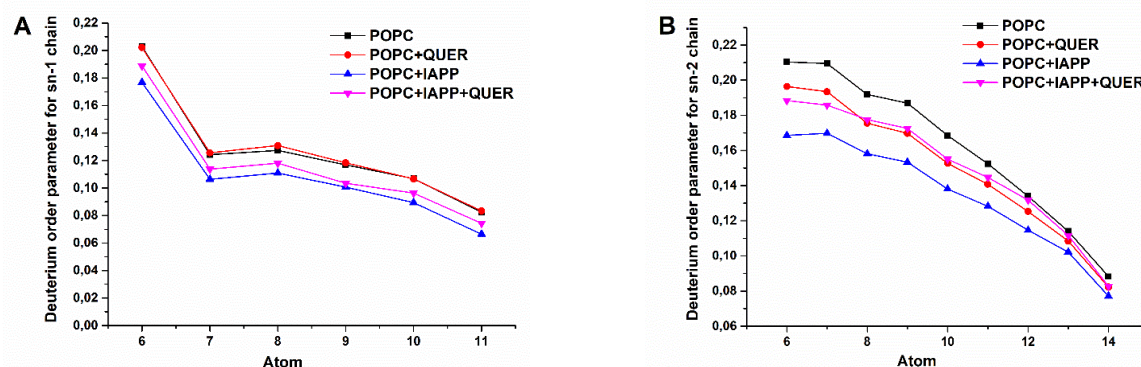


Figure 2. Deuterium order parameter for sn-1 (A) and sn-2 (B) chains calculated for the neat POPC, binary systems POPC + quercetin / IAPP and ternary system POPC + quercetin + IAPP

Contrary to IAPP, amyloid fibrils of apolipoprotein A-I (ApoAI) and insulin (InsF) have undergone significant structural reorganization in the membrane-bound state followed by essential loss of the InsF beta structure and disruption of ApoAI fibril integrity which may be indicative of a destabilization or unfolding of the fibril highly ordered conformation.

These findings highlight the dynamic nature of amyloid fibrils and their potential to alter conformation in response to environmental factors such as membrane binding, which could have implications for understanding the pathophysiology of amyloid-related diseases.

Furthermore, the analysis of the density distributions showed that ApoAI and InsF, similar to IAPP, induce considerable decrease in the density of headgroups, glycerols and acyl chains (Figs. 3, 4).

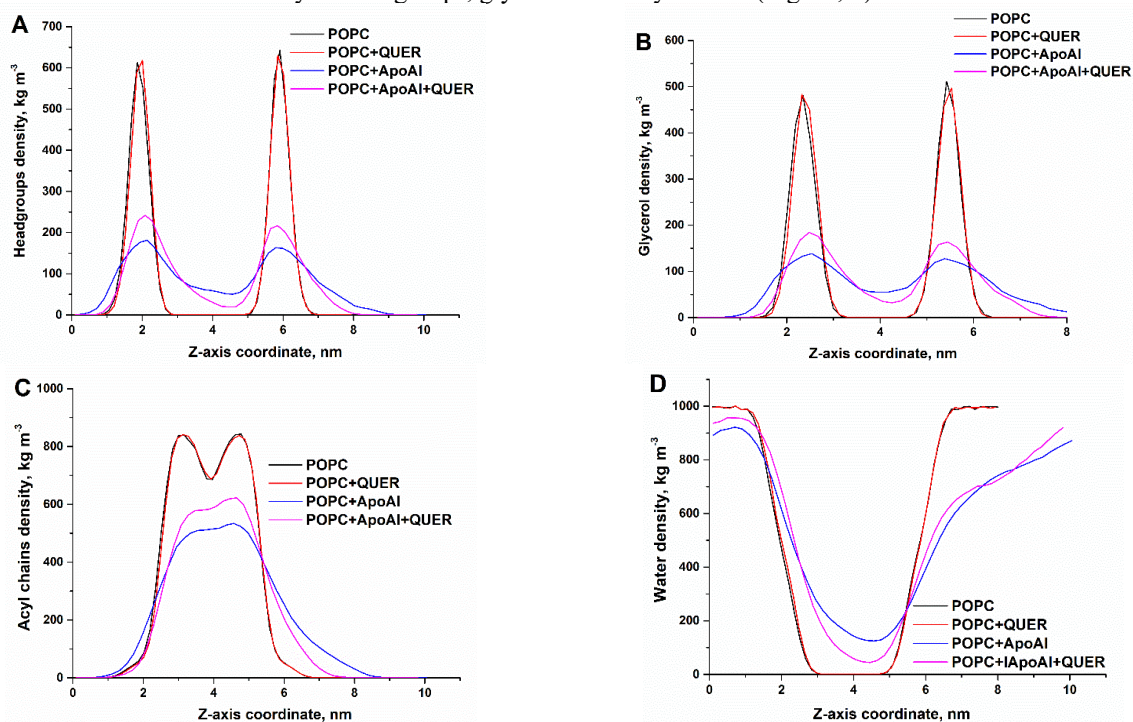


Figure 3. The density distributions of headgroups (A), glycerols (B), acyl chains and water (D) in POPC bilayer in the absence and presence of quercetin, ApoAI and quercetin + ApoAI

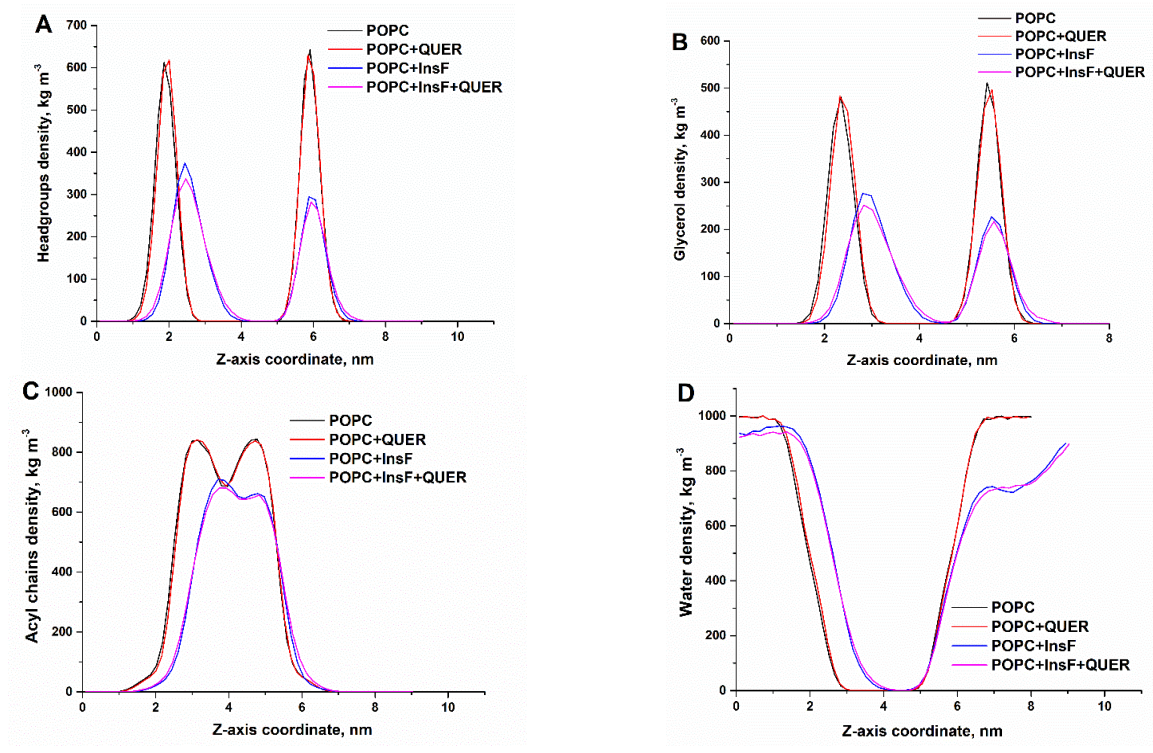


Figure 4. The density distributions of headgroups (A), glycerols (B), acyl chains and water (D) in POPC bilayer in the absence and presence of quercetin, InsF and quercetin + InsF

Remarkably, the attenuative effects of quercetin on the density of lipid molecular groups and the deuterium order parameter of sn-2 acyl chains were observed only for ApoAI (data not shown). These observations may suggest that quercetin interacts with lipid membranes in a manner that alters their structural properties, influencing membrane fluidity and dynamics when ApoAI is present. Likewise, compared to the binary systems POPC + quercetin / ApoAI / InsF, in the ternary systems containing both PF and fibrils, the quercetin tends to reside in a shallower location in the presence of ApoAI and InsF, the ApoAI center of mass shifts to bilayer center, while the position of the InsF center of mass remains unchanged (Fig. 5). This differential positioning may influence the structural and functional dynamics of the lipid bilayer, potentially affecting membrane stability and protein function.

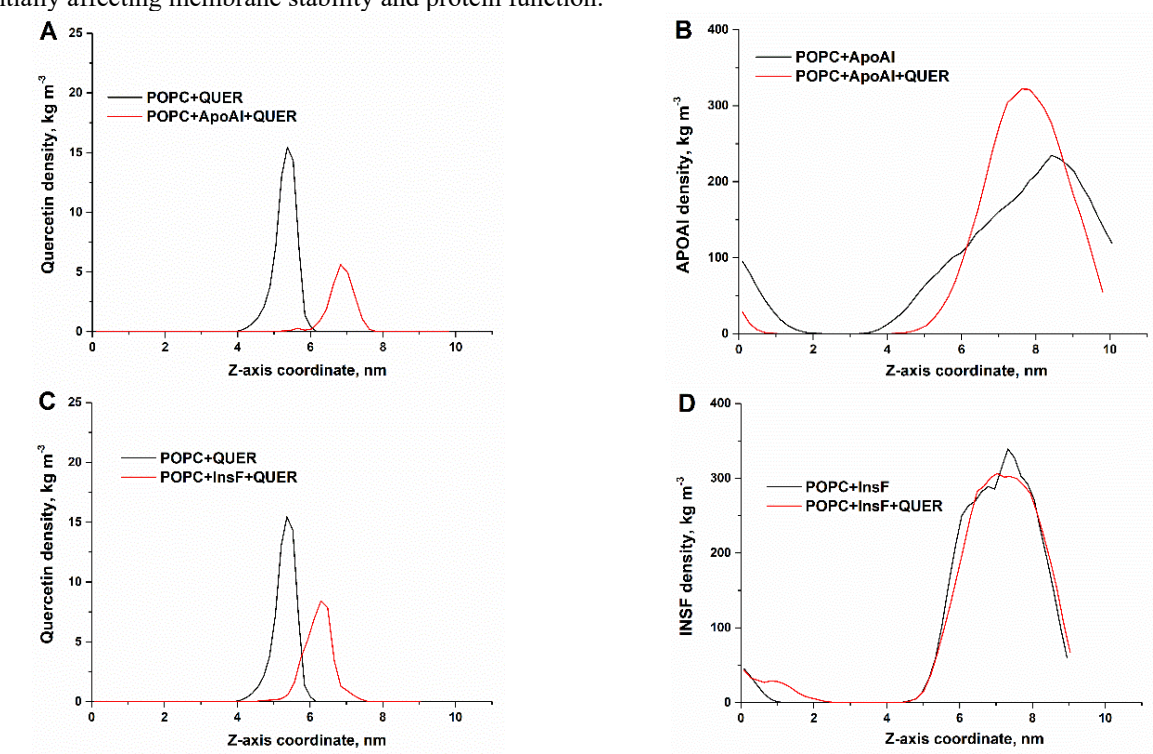


Figure 5. The mass density distributions of quercetin (A, C), ApoAI (B) and InsF (D) in POPC bilayer

Overall, the molecular dynamics simulations conducted on the model systems comprising lipid bilayers and amyloid fibrils reveal the protective mechanisms of polyphenols against amyloid fibril-induced membrane disruption. The inclusion of quercetin demonstrates a protective effect on both the polar and nonpolar regions of the lipid bilayer, mitigating the disruptive influences exerted by amyloid fibrils. Polyphenols, such as quercetin, have been extensively studied for their interactions with lipid membranes, where they exhibit the ability to penetrate and integrate into the lipid bilayer [10]. This integration can lead to alterations in the structural and physicochemical properties of the membrane. The protective role of quercetin in this context is likely attributed to its capacity to interact with both the hydrophilic and hydrophobic regions of the lipid bilayer [11]. This dual interaction is crucial as it allows quercetin to stabilize the membrane structure against perturbations caused by amyloid fibrils, which are known to disrupt membrane integrity by forming pores or altering membrane fluidity. Furthermore, the presence of quercetin in the lipid bilayer may also influence the mechanical properties of the membrane, enhancing its resilience to amyloid-induced stress. By decreasing membrane fluidity, quercetin can potentially prevent the insertion and destabilization caused by amyloid fibrils, thus maintaining membrane integrity. This protective effect is vital in biological systems where membrane disruption can lead to cellular dysfunction and contribute to the pathogenesis of amyloid-related diseases.

CONCLUSIONS

To summarize, the molecular dynamics simulations reveal that quercetin does not significantly alter the molecular organization of the POPC bilayer, while IAPP fibrils induce notable structural disruptions, particularly in the outer monolayer. Quercetin mitigates the impact of IAPP on the headgroup and glycerol regions, aligning with its protective role against polar region changes. The presence of quercetin results in a more superficial positioning of IAPP, and it slightly decreases the order of sn-2 acyl chains, suggesting a disordering effect. In a ternary system with POPC, quercetin, and IAPP, the reduction in the deuterium order parameter of sn-2 acyl chains is less pronounced, further supporting quercetin protective role. Unlike IAPP, ApoAI and insulin fibrils undergo significant structural reorganization when bound to the membrane. Quercetin's attenuative effects are observed only with ApoAI, and in ternary systems, it localizes more shallowly, with ApoAI center of mass shifting toward the bilayer center. These findings highlight quercetin potential as a protective agent against amyloid-induced membrane disruption.

Acknowledgements

This project has received funding through the EURIZON project, which is funded by the European Union under grant agreement No.871072.

ORCID

© Valeriya Trusova, <https://orcid.org/0000-0002-7087-071X>; © Uliana Tarabara, <https://orcid.org/0000-0002-7677-0779>
 © Galyna Gorbenko, <https://orcid.org/0000-0002-0954-5053>

REFERENCES

- [1] D. Li, and C. Liu, *Biochemistry*, **59**, 639 (2020). <https://doi.org/10.1021/acs.biochem.9b01069>
- [2] E. Chatani, K. Yuzu, Y. Ohhashi, and Y. Goto, *Int. J. Mol. Sci.* **22**, 4349 (2021). <https://doi.org/10.3390/ijms22094349>
- [3] I. Shabir, V.K. Pandey, R. Shams, A. Dar, K. Dash, S. Khan, I. Bashir, et al., *Front. Nutr.* **9**, 999752 (2022). <https://doi.org/10.3389/fnut.2022.999752>
- [4] J. Terao, M. Piskula, and Q. Yao, *Arch. Biochem. Biophys.* **308**, 278 (1994). <https://doi.org/10.1006/abbi.1994.1039>
- [5] A. Remigante, S. Spinelli, N. Basile, D. Caruso, G. Falliti, S. Dossena, A. Marino, and R. Morabito, *Int. J. Mol. Sci.* **23**, 7781 (2022). <https://doi.org/10.3390/ijms23147781>
- [6] A. Momchilova, T. Markovska, G. Georgiev, S. Pankov, G. Staneva, D. Petkova, P. Krastev, et al., *Biotechnology & Biotechnological Equipment*, **35**, 943 (2021). <https://doi.org/10.1080/13102818.2021.1939785>
- [7] P. Košinová, K. Berka, M. Wykes, M. Otyepka, and P. Trouillas, *J. Phys. Chem. B.* **116**, 1309 (2012). <https://doi.org/10.1021/jp208731g>
- [8] K. Yu, and C. Lee, *Pharmaceutics*, **12**, 1081 (2020). <https://doi.org/10.3390/pharmaceutics12111081>
- [9] K. Yu, C. Jheng, and C. Lee, *Biomed. Pharmacother.* **151**, 113177 (2022). <https://doi.org/10.1016/j.biopha.2022.113177>
- [10] N. Ulrih, M. Maricic, A. Ota, M. Sentjurc, and V. Abram, *Food Res. Internat.* **71**, 146 (2015). <https://doi.org/10.1016/j.foodres.2015.02.029>
- [11] J. Eid, A. Jraj, H. Greige-Gerges, and L. Monticelli, *Biochim. Biophys. Acta Adv.* **1**, 100018 (2021). <https://doi.org/10.1016/j.bbadv.2021.100018>

ЗАХИСНИЙ ЕФЕКТ КВЕРЦЕТИНУ ПРОТИ АМЛЮЇД-ІНДУКОВАНИХ ЗМІН ЦІЛНОСТІ ЛІПІДНОГО БІШАРУ

Уляна Тарабара, Валерія Трусова, Галіна Горбенко

*Кафедра медичної фізики та біомедичних нанотехнологій, Харківський національний університет імені В.Н. Каразіна
 майдан Свободи 4, Харків, 61022, Україна*

У даному дослідженні було використано метод молекулярної динаміки для вивчення взаємодій між кверцетином, амліоїдними фібрилами та ліпідними бішарами з фосфатидилхоліну. Отримані результати показують, що кверцетин не має значного впливу на молекулярну організацію бішару, тоді як фібрили IAPP викликають суттєві структурні зміни, особливо у зовнішньому моношарі. Кверцетин зменшує ці ефекти, послаблюючи вплив фібрил на зону полярних голівок ліпідів та гліцеролові ділянки, а також спричиняючи більш поверхневе розташування IAPP. Крім того, кверцетин знижує ступінь впорядкованості sn-2 ацильних ланцюгів, що свідчить про його дестабілізуючий ефект. У трьохкомпонентній системі, що складалася з фосфатидилхоліну, кверцетину та IAPP, зниження параметра порядку sn-2 ацильних ланцюгів було менш виражене, що є додатковим аргументом на користь захисної ролі кверцетину. На відміну від IAPP, фібрили ApoAI та інсуліну зазнають значної структурної реорганізації у мембранозв'язаному стані. Ефекти ослаблення у присутності кверцетину спостерігаються лише з ApoAI, що підкреслює його потенціал як захисного агента проти амліоїд-індукованої деструкції ліпідного бішару. Отримані результати мають важливе значення у контексті взаємодії між поліфенолами, амліоїдними фібрилами та ліпідними мембранами, що сприяє розумінню мембрано-асоційованих амліоїдних патологій.

Ключові слова: амліоїдні фібрили, ліпідні мембрани, поліфеноли, молекулярна динаміка

MOLECULAR DOCKING STUDY OF PROTEIN-FUNCTIONALIZED CARBON NANOMATERIALS FOR HEAVY METAL DETECTION AND REMOVAL

Olga Zhytniakivska*, **Uliana Tarabara**, **Kateryna Vus**, **Valeriya Trusova**, **Galyna Gorbenko**

*Department of Medical Physics and Biomedical Nanotechnologies, V.N. Karazin Kharkiv National University
4 Svobody Sq., Kharkiv, 61022, Ukraine*

**Corresponding Author: olga.zhytniakivska@karazin.ua*

Received June 21, 2024; revised July 26, 2024; accepted August 26, 2024

Carbon nanomaterials (CNMs) have emerged as highly effective agents for the removal of heavy metals from contaminated water and environments, owing to their unique structural and chemical properties. However, the hydrophobic nature of CNMs and their tendency to aggregate in most solvents present significant challenges to their practical application. Functionalizing carbon-based nanomaterials with proteins offers a promising solution to these issues, potentially leading to systems with unprecedented performance. Before fabricating protein-CNM systems for heavy metal detection and removal, it is crucial to evaluate the metal-binding affinity and potential interaction modes using computational approaches. In this study, a molecular docking technique was employed to investigate the interactions among heavy metal salts (AsO_4 , $\text{Cd}(\text{NO}_3)_2$, $\text{Fe}(\text{NO}_3)_3$, NiSO_4 , PbSO_4 , PtCl_4), carbon-based nanomaterials (fullerenes C_{24} and C_{60} , and single-walled carbon nanotubes), and β -lactoglobulin. The docking results revealed that: 1) the size, shape, and surface properties of carbon-based materials significantly influence the ability of β -lactoglobulin-CNM complexes to interact with different heavy metals; 2) different heavy metal salts exhibit distinct preferences for the various nanosystems; 3) hydrogen bonding and hydrophobic interactions play a significant role in the complexation of heavy metal salts with β -lactoglobulin-carbon-based materials.

Keywords: Carbon-based nanomaterials; Heavy metals; β -lactoglobulin, Molecular docking

PACS: 87.14.Cc, 87.16.Dg

Detecting and removing heavy metal ions from water is of critical importance due to the severe environmental and health hazards posed by these contaminants [1,2]. Heavy metals such as lead, mercury, cadmium, and arsenic can accumulate in biological systems, causing toxic effects that impact ecosystems and human health. Traditional methods for removing metal ions from water resources, such as solvent extraction [3], ion exchange [4,5], ultrafiltration [6,7], chemical precipitation [8-11], and adsorption [12,13], although beneficial, often have significant limitations. For instance, ion-exchange resins require regeneration with chemical reagents when exhausted, leading to potential secondary pollution [14]. Chemical precipitation is ineffective at low heavy metal concentrations [10,11], while ultrafiltration technology is costly and challenging for large-scale applications [6,7]. Among the various techniques for removing metal ions from aqueous solutions, adsorption is one of the most versatile and widely used methods [12,13]. Numerous low-cost adsorbents, such as activated carbon and carbon nanomaterials, wood char, zeolites, biochar, sawdust, and biopolymers, have proven highly effective in capturing heavy metal ions. Due to their exceptional optical, electrical, chemical, mechanical, and thermal properties, carbon-based nanomaterials are particularly promising for wastewater treatment. Carbon nanomaterials, including carbon nanotubes, fullerenes, graphene, graphene oxide, and activated carbon, have shown a high capacity for adsorbing various heavy metal pollutants [15-25]. For example, carbon nanotubes have demonstrated significant potential for removing heavy metal ions such as lead, cadmium, chromium, copper, and nickel from wastewater, with single-walled carbon nanotubes showing higher absorption capacity compared to multi-walled ones [15-17]. Furthermore, numerous studies indicate that functionalizing or modifying carbon nanotubes enhances their heavy metal adsorption capabilities [18,19]. For instance, Taghavi et al. developed multi-walled carbon nanotubes functionalized with L-cysteine, achieving 89% adsorption efficiency in removing cadmium from water [18]. Similarly, Anitha et al. demonstrated that -COOH functionalized carbon nanotubes exhibit higher adsorption efficiency for Cd^{2+} , Cu^{2+} , Pb^{2+} , and Hg^{2+} than bare single-walled carbon nanotubes [19]. The mechanism by which metal ions are adsorbed onto CNTs is complex and involves several processes, including electrostatic attraction, sorption-precipitation, and chemical interactions between the metal ions and the surface functional groups of the CNTs [15-19].

Graphene is another representative of carbon-based materials, possessing high efficacy for adsorbing heavy metal ions from water. Tabish et al. developed porous graphene as an adsorbent for removing heavy metal ions and other pollutants from water, achieving 80% efficiency in As^{3+} removal, with the material retaining its effectiveness even after regeneration and recycling [20]. Guo et al. created a nanocomposite by partially reducing graphene oxide with Fe_3O_4 via in situ co-precipitation, resulting in an adsorption capacity of 373.14 mg/g for Pb^{2+} ions [21]. Zhang et al. functionalized reduced graphene oxide with 4-sulfophenylazo, achieving maximum adsorption capacities of 689 mg/g for Pb^{2+} , 59 mg/g for Cu^{2+} , 66 mg/g for Ni^{2+} , 267 mg/g for Cd^{2+} , and 191 mg/g for Cr^{3+} [22]. Additionally, Vilela et al. designed a graphene-based self-propelled microbot system capable of removing 80% of Pb^{2+} ions from water [23], while Yang et al. successfully used graphene oxide-sodium alginate beads to remove Mn^{2+} ions with an adsorption capacity of 56.49 mg/g [24]. Developing planar adsorbing materials based on fullerenes, optimized for adsorption, filtration, and

structural properties, also represents a promising direction in adsorption technologies [25-27]. More specifically, incorporating fullerenes into polymer matrices has been shown to enhance the sorption properties of these materials, enabling the effective extraction of heavy metal ions from aqueous electrolyte solutions [25]. In turn, Liang et al. studied the interactions between C60 fullerene and heavy metal ions (Cd, Cu, and Pb) to assess their effects on the uptake, transportation, and accumulation of these coexisting pollutants in four rice cultivars grown in agricultural soil throughout the entire rice life cycle [27]. They found, that the bioaccumulation of Cd²⁺ in the panicles of rice was significantly reduced when exposed to 1000 mg/kg C60 [27].

Despite the efficacy of carbon-based nanomaterials for the adsorption of heavy metals from water they also have several limitations such as i) tendency to aggregate in most solvents and form tangled network structures due to their hydrophobic nature, which can reduce their effective surface area and, consequently, their adsorption efficiency [15,19]; and ii) dependence of the rate of heavy metal adsorption of carbon-based nanomaterials from the medium pH and temperature [15,19]. Functionalizing carbon-based nanomaterials with polymers may help overcome these drawbacks, empowering their broad application. In this respect, the protein biopolymers have emerged as ideal candidates for conjugation with carbon nanomaterials due to their biological compatibility, structural and chemical variabilities. The special properties of protein and carbon nanomaterials can benefit each other giving rise to systems with a diverse chemical, electronic, catalytic, and biological properties. However, to the best of our knowledge, little is known about the intermolecular interaction of heavy metal ions in the presence of protein-carbon nanomaterials.

The present study is aimed to investigate the molecular interactions between the heavy metals and nanostructures based on the carbon nanomaterials (fullerenes C24, C60 and single-walled carbon nanotube) and β -lactoglobulin using the molecular docking technique.

MOLECULAR DOCKING STUDIES

The fullerene and nanotube structures were generated using the Nanotube Modeler software (version 1.8.0). More specifically, the carbon nanomaterial structures were defined by entering specific parameters into the Nanotube Modeler, including the number of carbon atoms, type of nanomaterial, chirality, and symmetry. The fullerenes with 24 and 60 carbon atoms (C24 and C60, respectively) and a single-walled carbon nanotube with a chirality of 10 and tube length 25 Å were composed. To ensure accuracy and reliability, the generated structures were validated using standard techniques, such as energy minimization.

The heavy metal salt structures (AsO₄, Cd(NO₃)₂, Fe(NO₃)₃, NiSO₄, PbSO₄, PtCl₄) were built in MarvinSketch (version 18.10.0) and optimized in Avogadro (version 1.1.0) [28,29]. The three-dimensional X-ray crystal structure of bovine β -lactoglobulin was obtained from the Protein Data Bank (<https://www.rcsb.org/>) using the PDB ID 1QG5. The docking of the carbon nanomaterial+protein+heavy metal complexes was carried out using the web-based HDOCK server. The docking studies were performed in two steps. Initially, the “blind docking” modeling was used to determine the most energetically favorable complexes of fullerenes and carbon nanotube with the protein. Next, the lowest binding energy conformer was selected for each docking simulation and was applied for further docking analysis with the heavy metal salts. The protein-ligand interaction profiler PLIP (<https://plip-tool.biotec.tu-dresden.de/plip-web/plip/index>) was used to further characterize the carbon nanomaterial+protein+heavy metal complexes [30].

RESULTS AND DISCUSSION

Due to their exceptional optical, electrical, chemical, mechanical, and thermal properties, carbon-based nanomaterials have gained significant attention in recent decades and have been utilized across various fields, including electronic devices, healthcare, energy, and environmental protection, among others. However, the high surface area of carbon-based units leads to strong attractive forces between them, causing aggregation and poor solubility, which can hinder their application [15,19]. Covalent functionalization with various polar groups and moieties [15,19] or hybridization with polymers can help mitigate these issues [15, 24,25]. In this context, protein biopolymers have emerged as ideal candidates for conjugation with carbon-based nanomaterials to enhance their dispersibility and material properties [31,32]. Before fabricating such nanomaterials for specific purposes, it is reasonable to assess the potential interaction modes between carbon-based structures, proteins, and targeted ligands using computational tools, particularly molecular docking techniques. This study aims to evaluate the feasibility of creating carbon-based nanomaterials (fullerenes C24 and C60, and single-walled carbon nanotubes) functionalized with β -lactoglobulin for heavy metal detection using molecular docking techniques. The choice of β -lactoglobulin for functionalizing carbon-based materials is based on its recently demonstrated effectiveness in developing nanocomposites for the detection and adsorption of heavy metal ions [33]. More specifically, a hybrid activated carbon membrane containing β -lactoglobulin amyloid fibrils appeared highly effective for the removal of heavy metal ions from wastewater [33].

Initially, to explore the molecular-level interactions between β -lactoglobulin and carbon-based nanomaterials materials, molecular docking calculations were conducted using the HDOCK server, with the main emphasis on determining the positioning of the CNs on the protein surface along with the specific amino acid residues and the types of interactions that contribute to the formation of the most energetically stable complexes. The obtained docking results indicate that the binding of C24 fullerene is stabilized by the hydrophobic interactions with the residues GLN_{35A}, TYR_{42A}, TRP_{61A}, THR_{154A} (Figure 1). The C60-protein complexation was presumably driven by the hydrophobic interactions with

the residues PHE_{151A}, ASN_{152A}, and THR_{154A} of the helical β -lactoglobulin region. In addition, the C60 complexation was additionally stabilized by the π -stacking with the PHE_{151A}. As seen from Figure 1 (panel c), the carbon nanotube formed stable contacts with the outer surface of the protein presumably through the hydrophobic interactions with TRP_{61A}, LEU_{149A}, PHE_{151A}, ASN_{152A}, THR_{154A}, π -stacking with PHE_{151A} and the π -Cation Interactions with ARG_{40A}. The obtained results align well with numerous studies that categorize the binding interactions between carbon-based nanomaterials and proteins into three main subgroups: hydrophobic interactions (nonpolar solvation), π - π stacking (between sp^2 carbon structures and aromatic residues of proteins), and van der Waals forces (occurring between the surfaces of the interacting molecules) [34–37]. More specifically, the predominant role of the hydrophobic interactions in the complexation of carbon nanotubes with β -lactoglobulin [37] and blood proteins [38] was reported previously. In addition, Karchemsky et al. demonstrated the adsorption of carbon nanotubes on the β -lactoglobulin surface is a diameter-selective [37]. The docking scores of the obtained complexes were decreased in the following raw β -lactoglobulin+F24 (-113.16) \rightarrow β -lactoglobulin+F60 (-121.71) \rightarrow β -lactoglobulin+nanotube (-262.14). The observed decrease in docking scores with the increasing size of the carbon-based nanomaterials can be attributed to their larger surface area, which provides more binding sites for interactions.

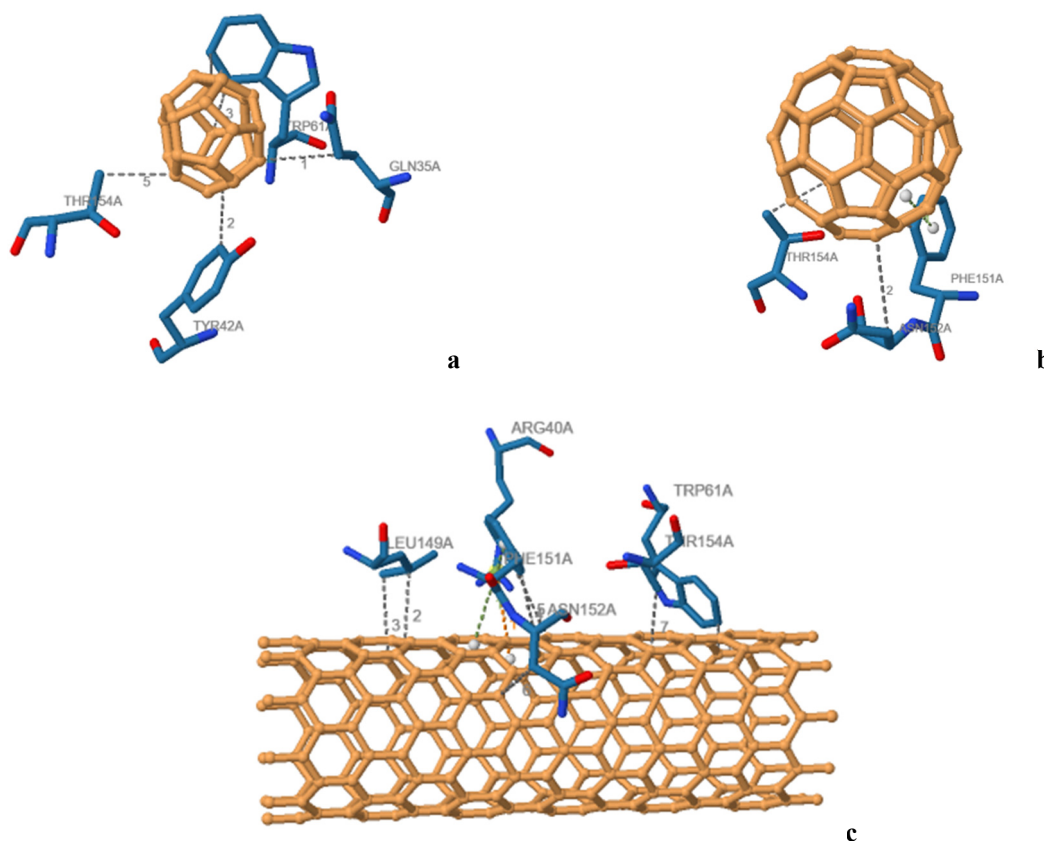


Figure 1. The binding interactions for the complexes between the β -lactoglobulin, fullerenes C24 (a), C60 (b) and carbon nanotube (c)

At the next step, the lowest binding energy conformers from the nanostructure-protein docking were selected and further used for the docking with the set of heavy metal salts. Presented in Figure 2 are the results of the analysis of the most energetically favorable complexes obtained after the docking in HDOCK and their characterization in the protein-ligand interaction profiler PLIP (Table 1). It was observed that in the F24- and F60-containing nanosystems, the protein binding sites for the investigated metal salts are located in close proximity to each other and the fullerenes. More specifically, our docking results indicate that in the F24-lactoglobulin system AsO_4 , $Cd(NO_3)_2$, $Fe(NO_3)_3$, $PbSO_4$ tend to form contacts with both the fullerene and the protein amino acid residues. Meanwhile, the heavy metal salts $NiSO_4$ and $PtCl_4$ penetrate deeper into the protein interior, interacting exclusively with β -lactoglobulin. In turn, for the C60-containing systems all salts form the intermolecular contacts with both the protein and the carbon nanomaterials. The PLIP analysis indicates that the interactions of heavy metal salts in F24 and F60 systems are stabilized presumably by the hydrogen bonds with the SER_{21A}, GLN_{59A}, THR_{154A} and ALA_{67A} residues. An exception was $PtCl_4$, where complexation appeared to be driven primarily by hydrophobic interactions. In addition, the PLIP results indicate that $PbSO_4$ and $NiSO_4$ form a salt bridge with ARG_{40A}. The analysis of the docking results for the carbon nanotube-protein systems revealed that: 1) $Cd(NO_3)_2$ and $Fe(NO_3)_3$ interact with the nanotube and the β -lactoglobulin with the salt-protein complexation driven presumably by the hydrogen bonds with the residues ARG_{40A}, TYR_{42A}, GLN_{59A}, TRP_{61A}, THR_{154A}; 2) $PtCl_4$ binds

to the β -lactoglobulin through the hydrophobic interactions with THR_{154A}; 3) the AsO₄, NiSO₄, PbSO₄ do not interact with the protein and possess preferential binding to the nanotube interior. Overall, as shown in Table 1, the docking score for all carbon-based materials is changed in the same salt raw: PtCl₄ → PbSO₄ → NiSO₄ → AsO₄ → Cd(NO₃)₂ → Fe(NO₃)₃.

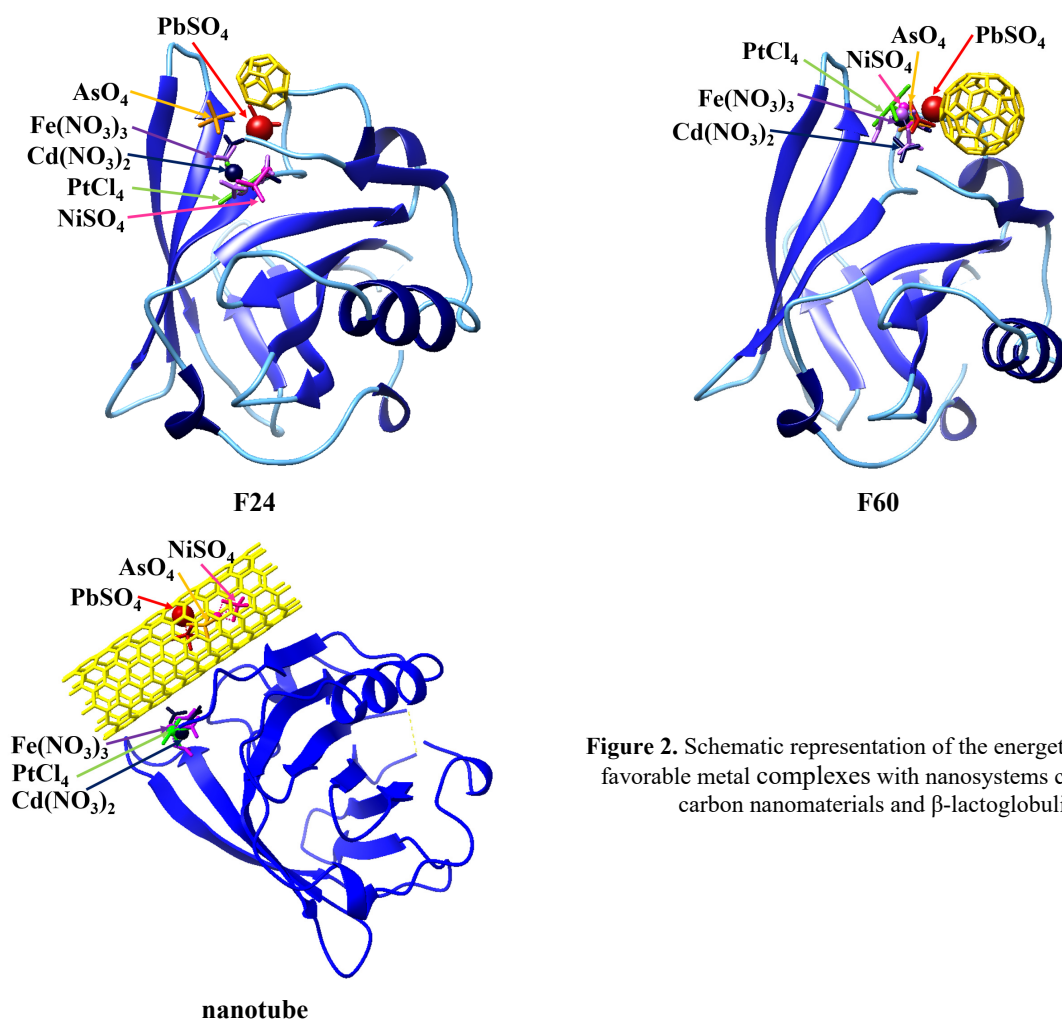


Figure 2. Schematic representation of the energetically most favorable metal complexes with nanosystems containing carbon nanomaterials and β -lactoglobulin

According to the previous studies, the complexation of heavy metal ions with carbon-based materials can be described by at least 5 different mechanisms: 1) physical adsorption assuming the diffusion and deposition of heavy metal ions into pores of an adsorbent without forming chemical bonds with the adsorption capacity dependent on the carbon nanomaterial pore size and surface area [39-41]; 2) ion exchange between the divalent metal cations with protons from the oxygen-containing functional groups of carbon nanomaterial ($-\text{COOH}$, $-\text{OH}$) [39, 42]; 3) surface complexation for the carbon nanomaterials carrying the functional group suitable for the forming multi-atom structures with metal ions [43,44]; 4) electrostatic interaction between the negatively charged groups of carbon nanomaterial and cations [39,40]; 5) precipitation (heavy metal ions can form solid precipitates or coprecipitate with other ions on the adsorbent surface) [39]. Given the unmodified unit (no oxygen-containing, charged groups) used for the creation of carbon-based nanomaterials in our study, the binding of the AsO₄, NiSO₄, and PbSO₄ to the interior of carbon nanotube can be described by the diffusion of heavy metals into the pores.

Notably, the adsorption mechanism of protein-based composites varies depending on the metal (its valence state, ionic radius, and charge-accepting ability) and the protein properties (amino-acid sequence, the accessibility of the potential metal-binding sites) [45-50]. For heavy metal ions, the main mechanisms include [49-50]:

- i) Chemical complexation/chelation occurs due to the abundant $-\text{COOH}$ and $-\text{NH}_2$ groups of the protein-based composites, which coordinate with metal ions to form N-metal and C- $-\text{O}$ -metal complexes.
- ii) the electrostatic interaction is attributed to the free ionizable $-\text{COOH}$ and $-\text{NH}_2$ groups, which could generate positive or negative charges to attract heavy metals;
- iii) the ion exchange of H^+ and OH^- , generated from $-\text{COOH}$ and $-\text{NH}_2$ in the water environment.

Numerous studies indicate the predominant role of heavy metals' inherent chemistry in their interactions with proteins [45-51]. More specifically, the Hard Acid Soft Base theory determines the cations as acids, classifying all metals as hard, soft and borderline [51]. According to the Hard Acid Soft Base theory, hard acids prefer to bind to hard bases and soft acids prefer to bind to soft bases [51]. Proteins containing the amino acid residues possess a higher binding ability

to the “soft” metals (Pt^{2+} and Cd^{2+}) in comparison with “hard” metals (Fe^{3+} , As^{3+}) [51]. The preference mentioned above is linked to differences in their preferred binding mechanisms: metal chelation primarily maintains the structural integrity of protein-soft metal complexes, while electrostatic interactions play a key role in binding “hard” metals [51].

Table 1. Amino acid residues participating in the formation of the most energetically favorable metal-nanosystem complexes

Carbon nanomaterial	Heavy metal salt	Docking score	Amino acid residues forming contact with heavy metals
F24	AsO_4	-63.81	GLN _{59A} , ALA _{67A}
	$\text{Cd}(\text{NO}_3)_2$	-105.40	SER _{21A} , GLN _{59A} , THR _{154A}
	$\text{Fe}(\text{NO}_3)_3$	-135.62	SER _{21A} , GLN _{59A} , THR _{154A}
	NiSO_4	-62.08	SER _{21A} , THR _{154A}
	PbSO_4	-51.66	GLN _{35A} , SER _{36A} , ARG _{40A} , TRP _{61A}
	PtCl_4	-39.41	TYR _{20A} , TYR _{42A} , PHE _{151A}
F60	AsO_4	-70.00	GLN _{35A} , TYR _{42A} , TRP _{61A} , ARG _{40A}
	$\text{Cd}(\text{NO}_3)_2$	-108.99	TRP _{61A} , GLN _{35A} , ARG _{40A} , TYR _{42A} , THR _{154A}
	$\text{Fe}(\text{NO}_3)_3$	-148.40	GLN _{35A} , ARG _{40A} , TYR _{42A} , GLN _{59A} , THR _{154A}
	NiSO_4	-65.54	TYR _{42A} , ARG _{40A}
	PbSO_4	-57.80	GLN _{35A} , TYR _{42A} , ARG _{40A}
	PtCl_4	-42.29	GLN _{35A} , TYR _{42A} , TRP _{61A} , THR _{154A}
NT	AsO_4	-87.49	ND
	$\text{Cd}(\text{NO}_3)_2$	-130.37	TYR _{42A} , GLN _{35A} , TYR _{42A} , THR _{154A}
	$\text{Fe}(\text{NO}_3)_3$	-167.95	ARG _{40A} , TYR _{42A} , GLN _{59A} , TRP _{61A} , THR _{154A}
	NiSO_4	-94.50	ND
	PbSO_4	-73.49	ND
	PtCl_4	-54.67	THR _{154A}

ND means “not determined”

Our docking results indicate that hydrogen bonding and hydrophobic interactions, play a predominant role in the complexation of heavy metal + β -lactoglobulin + carbon-based material systems. The docking simulations were conducted using heavy metal salts, which inherently contain both Lewis acids and Lewis bases. Notably, systems containing soft metals, such as PtCl_4 and $\text{Cd}(\text{NO}_3)_2$, demonstrated a stronger interaction with the protein than with the carbon-based nanomaterials. In contrast, PbSO_4 , which includes the borderline Pb^{2+} ion and the hard SO_4^{2-} base, exhibited a higher binding affinity to the carbon-based materials across all studied systems. Interestingly, AsO_4 was found to interact more efficiently with carbon nanotubes than with fullerenes. In fullerene-containing systems, the binding primarily occurred with β -lactoglobulin. The above finding suggests that the size, shape, and surface properties of carbon-based materials significantly impact the nanocomposite's ability to interact with different heavy metals. This characteristic is highly advantageous for developing selective metal detection platforms. However, further detailed research is necessary to elucidate the precise role of carbon-based materials in the formation of protein-CN nanocomposites for the adsorption and detection of heavy metals.

CONCLUSIONS

To summarize, in the present study the docking technique was used to investigate the interactions of heavy metal salts (AsO_4 , $\text{Cd}(\text{NO}_3)_2$, $\text{Fe}(\text{NO}_3)_3$, NiSO_4 , PbSO_4 , PtCl_4), carbon-based nanomaterials (fullerenes C24 and C60 and single-walled carbon nanotube) and β -lactoglobulin. It was found that: 1) the size, shape, and surface properties of carbon-based materials have a substantial impact on the ability of β -lactoglobulin-CNM complexes to interact with different heavy metals; 2) different heavy metal salts show distinct preferences for the various nanosystems; 3) hydrogen bonding and hydrophobic interactions are crucial in the complexation of heavy metal salts with β -lactoglobulin and carbon-based materials. Overall, these findings provide valuable insights into the design of protein-CNM systems for the detection and removal of heavy metals.

Acknowledgements

This work was supported by the Ministry of Education and Science of Ukraine (the project “Development of novel means of medical diagnostics by biomedical nanotechnologies and modern ultrasonic and fluorescence methods” and the project “Development of economically affordable nanosystems for rapid identification and purification of water from heavy metal ions based on carbon nanoallotropes and amyloids from organic waste”).

ORCID

Olga Zhytniakivska, <https://orcid.org/0000-0002-2068-5823>; Uliana Tarabara, <https://orcid.org/0000-0002-7677-0779>
 Kateryna Vus, <https://orcid.org/0000-0003-4738-4016>; Valeriya Trusova, <https://orcid.org/0000-0002-7087-071X>
 Galyna Gorbenko, <https://orcid.org/0000-0002-0954-5053>

REFERENCES

- [1] P.B. Tchounwou, C.G. Yedjou, A.K. Patlolla, and D.J. Sutton. *Exp. Suppl.* **101**, 133 (2012). https://doi.org/10.1007/978-3-7643-8340-4_6

- [2] M. Balali-Mood, K. Naseri, Z. Tahergorabi, M. Reza Khazdair, and M. Sadeghi, *Front Pharmacol.* **12**, 643972 (2021). <https://doi.org/10.3389/fphar.2021.643972>
- [3] M. Cerna. *Environ Monit Assess.* **34**, 151 (1995). <https://doi.org/10.1007/BF00546029>
- [4] A. Dąbrowski, Z. Hubicki, P. Podkościelny, and E. Robens, *Chemosphere* **56**, 91 (2004). <https://doi.org/10.1016/j.chemosphere.2004.03.006>
- [5] S.A. Cavaco, S. Fernandes, M. Quina, and L.M. Ferreira. *J. Hazard. Mater.* **144**, 634 (2007). <https://doi.org/10.1016/j.jhazmat.2007.01.087>
- [6] N.A.A. Qasem, R.H. Mohammed, and D.U. Lawal, *npj Clean Water*, **4**, 36 (2021). <https://doi.org/10.1038/s41545-021-00127-0J-J>
- [7] J.-J. Kim, Y.-S. Kim, and V. Kumar, *J. Trace Elem. Med. Biol.* **54**, 226 (2019). <https://doi.org/10.1016/j.jtemb.2019.05.003>
- [8] J. Huang, J. *et al.*, *Colloids Surf. A Physicochem. Eng. Asp.* **520**, 361 (2017). <https://doi.org/10.1016/j.colsurfa.2017.02.001>
- [9] N. Kongsricharoern, and C. Polprasert, *Water Sci. Technol.* **31**, 109 (1995). <https://doi.org/10.2166/wst.1995.0350>
- [10] M.T. Alvarez, C. Crespo, and B. Mattiasson, *Chemosphere*, **66**, 1677 (2007). <https://doi.org/10.1016/j.chemosphere.2006.07.065>
- [11] Q. Chen, Z. Luo, C. Hills, G. Xue, and M. Tyrer, *Water Res.* **43**, 2605 (2009). <https://doi.org/10.5539/ep.v1n1p38>
- [12] R. Janani, G. Baskar, K. Sivakumar, V. Sunita, *et al.*, *Environmental Research*, **203**, 111815 (2022). <https://doi.org/10.1016/j.envres.2021.111815>
- [13] Z. Raji, A. Karim, A. Karam, and S. Khalloufi, *Waste*, **1**, 775 (2023). <https://doi.org/10.3390/waste1030046R>
- [14] V.J. Inglezakis, M.A. Stylianou, D. Gkantzou, and M.D. Loizidou, *Desalination*, **210**, 248 (2007). <https://doi.org/10.1016/j.desal.2006.05.04>
- [15] R. Baby, B. Saifullah, and M.Z. Hussein, *Nanoscale Res. Lett.* **14**, 341 (2019). <https://doi.org/10.1186/s11671-019-3167-8>
- [16] C. Lu, H. Chiu, and C. Liu, *Ind. Eng. Chem. Res.* **45**, 2850 (2006). <https://doi.org/10.1021/ie051206h>
- [17] G. Rao, C. Lu, and F. Su, *Sep. Purif. Technol.* **58**, 224 (2008). <https://doi.org/10.1016/j.seppur.2006.12.006>
- [18] M. Taghavi, M.A. Zazouli, Z. Yousefi, *et al.*, *Environ. Monit. Assess.* **187**, 682 (2015). <https://doi.org/10.1007/s10661-015-4911-x>
- [19] K. Anitha, S. Namsani, and J.K. Singh. *J. Phys. Chem. A.* **119**, 8349 (2015). <https://doi.org/10.1021/acs.jpca.5b03352>
- [20] T.A. Tabish, F.A. Memon, D.E. Gomez, *et al.*, *Sci. Rep.* **8**, 1817 (2018). <https://doi.org/10.1038/s41598-018-19978-8>
- [21] T. Guo, C. Bulin, B. Li, *et al.*, *Adsorption Science & Technology*, **36**(3-4), 1031 (2018). <https://doi.org/10.1177/0263617417744402>
- [22] C.Z. Zhang, B. Chen, Y. Bai, and J. Xie, *Separation Science and Technology*, **53**(18), 2896 (2018). <https://doi.org/10.1080/01496395.2018.1497655>
- [23] D. Vilela, J. Parmar, Y. Zeng, Y. Zhao, and S. Sánchez, *Nano Lett.* **16**(4), 2860 (2016). <https://doi.org/10.1021/acs.nanolett.6b00768>
- [24] X. Yang, T. Zhou, B. Ren, A. Hursthouse, and Y. Zhang. *Sci. Rep.* **16**, 10717 (2018). <https://doi.org/10.1038/s41598-018-29133-y>
- [25] O.V. Alekseeva, N.A. Bagrovskaya, and A.V. Noskov, *Prot. Met. Phys. Chem. Surf.* **52**, 443 (2016). <https://doi.org/10.1134/S2070205116030035>
- [26] E. Ciotta, P. Proposito, D. Moscone, N. Collozza, and R. Pizzoferrato, *AIP Conf. Proc.* **2145**, 020008 (2019). <https://doi.org/10.1063/1.5123569>
- [27] L. Chuanzhou, X. Haijun, H. Ziqi, Z. Xu, and H. Jun. *Environmental Pollution*, **235**, 330 (2018). <https://doi.org/10.1016/j.envpol.2017.12.062>
- [28] P. Csizmadia, in: *Proceedings of ECSOC-3, the third international electronic conference on synthetic organic chemistry*, (Budapest, 1999). pp. 367-369, <https://doi.org/10.3390/ECSOC-3-01775>
- [29] M.D. Hanwell, D.E. Curtis, D.C. Lonie, T. Vandermeersch, E. Zurek, and G.R. Hutchison, *J. Cheminform.* **4**, 17 (2012). <https://doi.org/10.1186/1758-2946-4-17>
- [30] M. Adasme, K. Linnemann, S. Bolz, F. Kaiser, *et al.*, *Nucleic Acids Research*, **49**, W530 (2021). <https://doi.org/10.1093/nar/gkab294>
- [31] X. Huang, R. Li, L. Zeng, X. Li, Z. Xi, K. Wang, and Y. Li, *Carbon*, **161**, 350 (2020). <https://doi.org/10.1016/j.carbon.2020.01.069>
- [32] N. Kang, J. Hua, L. Gao, B. Zhang, J. Pang, *Materials*, **14**, 608 (2021). <https://doi.org/10.3390/ma14030608>
- [33] M. Peydayesh, S. Bolisetty, T. Mohammadi, and R. Mezzenga, *Langmuir*. **35**, 4161 (2019). <https://doi.org/10.1021/acs.langmuir.8b04234>
- [34] H. Benyamini, A. Shulman-peleg, H.J. Wolfson, L. Fadeev, M. Gozin. *Bioconjugate Chem*, **17**, 378-386 (2006). <https://doi.org/10.1021/bc050299g>
- [35] S. Marchesan, and M. Prato, *Chem. Commun.* **51**, 4347 (2015). <https://doi.org/10.1039/C4CC09173F>
- [36] F.D. Leo, A. Magistrato, and D. Bonifazi, *Chem. Soc. Rev.* **44**, 6916 (2015). <https://doi.org/10.1039/C5CS00190K>
- [37] F. Karchemsky, E. Drug, E. Mashiach-Farkash, L. Fadeev, H.J. Wolfson, M. Gozin, and O. Regev, *Colloids and Surfaces B: Biointerfaces*, **112**, 16 (2013). <https://doi.org/10.1016/j.colsurfb.2013.07.018>
- [38] C. Ge, J. Du, L. Zhao, and C. Chen, *PNAS*, **108**(41), 16968 (2011). <https://doi.org/10.1073/pnas.110527010>
- [39] C. Duan, T. ma, J. Wang, and Y. Zhou, *JWPE*, **37**, 101339, (2020). <https://doi.org/10.1016/j.jwpe.2020.101339>
- [40] X. Yang, Y. Wan, Y. Zheng, F. He, Z. Yu, J. Huang, H. Wang, *et al.*, *Chem. Eng. J.* **366** 608 (2019). <https://doi.org/10.1016/j.cej.2019.02.119>
- [41] A.H. Fahmi, A.W. Samsuri, H. Jol, and D. Singh, *RSC Adv.* **8**, 38270 (2018). <https://doi.org/10.1039/c8ra06867d>
- [42] K.C. Lai, L.Y. Lee, B.Y.Z. Hiew, S. Thangalazhy-Gopakumar, and S. Gan, *J. Environ. Sci.* **79**, 179 (2019). <https://doi.org/10.1016/j.jes.2018.11.023>
- [43] W. Zhan, L. Gao, X. Fu, S.H. Siyal, G. Sui, and X. Yang, *Appl. Surf. Sci.* **467-468**, 1122 (2019). <https://doi.org/10.1016/j.apsusc.2018.10.248>
- [44] Y. Deng, S. Huang, D.A. Laird, X. Wang, and Z. Meng, **218**, 308 (2019). <https://doi.org/10.1016/j.chemosphere.2018.11.081>
- [45] D. Shalev. *Int. J. Mol. Sci.* **23**, 15957 (2022). <https://doi.org/10.3390/ijms232415957>
- [46] Z. Yang, F. Yang, J.L. Liu, H.T. Wum H. Yang, *et al.*, *Sci Total Environ.* **809**, 151099 (2022). <https://doi.org/10.1016/j.scitotenv.2021.151099>

- [47] K.B. Handing, E. Niedzialkowska, I.G. Shabalin, M.L. Kuhn, H. Zheng, and W. Minor. *Nat Protoc.* **13**, 1062 (2018). <https://doi.org/10.1038/nprot.2018.018>
- [48] J. Zang, C. Li, K. Zhou, H. Dong, B. Chen, F. Wang, and G. Zhao, *Anal. Chem.* **88**, 10275 (2016). <https://doi.org/10.1021/acs.analchem.6b03011>
- [49] Y.F. Lin, C.W. Cheng, C.S. Shin, J.K. Hwang, C.S. Yu, C.H. and Lu, *J. Chem. Inf. Model* **56**, 2287 (2016). <https://doi.org/10.1021/acs.jcim.6b00407>
- [50] M.P. Chantada-Varquez, A. Moreda-Pineiro, M.C. Barciels-Alonso, and P. Bermejo-Barrera, *Appl. Spectr. Rev.* **52**, 145 (2017). <https://doi.org/10.1080/05704928.2016.1213736>.
- [51] R. Pearson, *J. Chem. Educ.* **45**, 981 (1968). <https://doi.org/10.1021/ed045p581>

**ДОСЛІДЖЕННЯ МЕТОДОМ МОЛЕКУЛЯРНОГО ДОКІНГУ ФУНКЦІОНАЛІЗОВАНИХ БІЛКАМИ
ВУГЛЕЦЕВИХ НАНОМАТЕРІАЛІВ ДЛЯ ДЕТЕКТУВАННЯ ТА ВИДАЛЕННЯ ВАЖКИХ МЕТАЛІВ**

Ольга Житняківська, Уляна Тарабара, Катерина Вус, Валерія Трусова, Галина Горбенко

*Кафедра медичної фізики та біомедичних нанотехнологій, Харківський національний університет імені В.Н. Каразіна
майдан Свободи 4, Харків, 61022, Україна*

Вуглецеві наноматеріали (ВН) зарекомендували себе надзвичайно ефективними для видалення важких металів із забрудненої води та навколишнього середовища завдяки своїм унікальним структурним і хімічним властивостям. Однак гідрофобна природа ВН і їхня схильність до агрегації в більшості розчинників створюють значні труднощі для їх практичного застосування. Функціоналізація вуглецевих наноматеріалів за допомогою білків є перспективним вирішенням цих проблем, що може призвести до створення систем з безпрецедентною ефективністю. Перед тим як створювати білково-ВН системи для виявлення та видалення важких металів, важливо оцінити афінність зв'язування металів та можливі взаємодії за допомогою комп'ютерних методів. У цьому дослідженні була використано метод молекулярного докінгу для вивчення взаємодій між солями важких металів (AsO_4 , $\text{Cd}(\text{NO}_3)_2$, $\text{Fe}(\text{NO}_3)_3$, NiSO_4 , PbSO_4 , PtCl_4), вуглецевими наноматеріалами (фулерени C_{24} і C_{60} , а також одностінні вуглецеві нанотрубки) і β -лактоглобуліном. Результати докінгу показали, що: 1) розмір, форма та поверхневі властивості вуглецевих матеріалів суттєво впливають на здатність комплексів β -лактоглобуліну з ВН взаємодіяти з різними важкими металами; 2) афінність солей важких металів до створених наносистем в значній мірі варіюється; 3) водневі зв'язки та гідрофобні взаємодії відіграють суттєву роль у комплексоутворенні солей важких металів з β -лактоглобуліном та вуглецевими матеріалами.

Ключові слова: вуглецеві наноматеріали; важкі метали; β -лактоглобулін, молекулярний докінг

ERRATUM: ELECTRIC FIELD ENHANCEMENT BY GOLD NANO-SPHERE AND ITS CLUSTERS [East European Journal of Physics. 2. 388-393 (2024)]

 P.K. Kushwaha^{a,b,*},  K.Y. Singh^{a,b}, Himmat Singh Mahor^{a,b},  Pramod Kumar Singh^c,  Ravish Sharma^{a,b},
 Kash Dev Sharma^{a,b}

^aDepartment of Physics, B.S.A. (P.G.) College, Mathura (U.P.) India 281004

^bDr. Bhimrao Ambedkar University, Agra (U.P.) India 282004

^cDepartment of Physics, Hindustan College of Science & Technology, Farah, Mathura (U.P.) India 281122

*Corresponding Author e-mail: pankaj08au@gmail.com

The purpose of this Erratum is to correct a misprint presented in the original article.

Keywords: Electric field; Clusters; Nano sphere

In original article, the Figure 3 (left) has scales on X-Axis in micro-meter however it is in nanometer. Similarly, in Figure 3(right) X-Axis and Y- Axis both are in nano-meter instead of micro-meter. The new diagram is shown here:

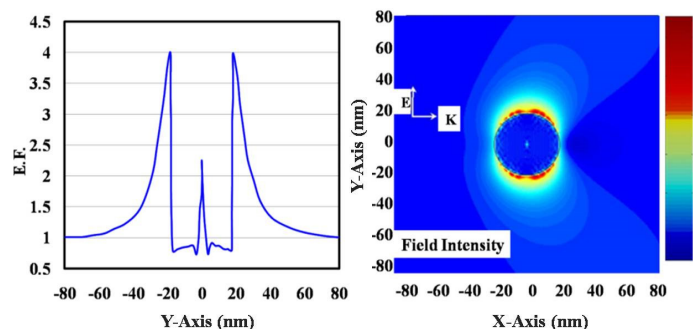


Figure 3. Electric field pattern of a 20 nm radius sphere (K||X, E||Y) on the right, and on the left field enhancement around a nano-sphere along the Y-axis.

Original Article:

P.K. Kushwaha, K.Y. Singh, Himmat Singh Mahor, Pramod Kumar Singh, Ravish Sharma, Kash Dev Sharma, “Electric Field Enhancement by Gold Nano-Sphere and Its Clusters,” East European Journal of Physics, 2, 388-393 (2024). <https://periodicals.karazin.ua/cej/article/view/23288/21526>

ВИПРАВЛЕННЯ: ПІДСИЛЕННЯ ЕЛЕКТРИЧНОГО ПОЛЯ НАНОСФЕРОЮ ЗОЛОТА ТА ЇЇ КЛАСТЕРАМИ, [СХІДНО-ЄВРОПЕЙСЬКИЙ ФІЗИЧНИЙ ЖУРНАЛ. 2. 388-393 (2024)]

П.К. Кушваха^{a,b}, К.Ю. Сінгх^a, Хімнат Сінгх Махор^a, Прамод Кумар Сінгх^c, Равіш Шарма^{a,b}, Каш Дев Шарма^{a,b}

^aКафедра фізики, В.С.А. (Р.Г.) Колеж, Матхура (У.Р.) Індія 281004

^bУніверситет докт. Бхімрао Амбедкар, Агра (У.Р.), Індія 282004

^cФакультет фізики, Індостанський коледж науки та технологій, Фарах, Матхура (У.Р.), Індія 281122

Метою цього Виправлення є виправлення друкарської помилки, представленої в оригінальній статті.

Ключові слова: електричне поле; кластери; наносфера

В оригінальній статті Рисунок 3 (ліворуч) має масштаби на осі X у мікрометрах, але в нанометрах. Подібним чином на малюнку 3 (праворуч) вісь X і вісь Y вказані в нанометрах замість мікрометрів.

Вихідна стаття:

P.K. Kushwaha, K.Y. Singh, H.S. Mahor, P.K. Singh, R. Sharma, K.D. Sharma, “Electric Field Enhancement by Gold Nano-Sphere and its Clusters,” East European Journal of Physics, 2, 388-393 (2024). <https://periodicals.karazin.ua/cej/article/view/23288/21526>

ERRATUM: COSMOLOGICAL DYNAMICS OF ANISOTROPIC KANIADAKIS HOLOGRAPHIC DARK ENERGY MODEL IN BRANS-DICKE GRAVITY [East European Journal of Physics, (2), 10-20 (2024)]

A. Vijaya Prasanthi^{a,b}, G. Suryanarayana^c, Y. Aditya^{d*}, U.Y. Divya Prasanthi^e
^a*AU Trans-Disciplinary Research Hub, Andhra University, Visakhapatnam-530003, India*
^b*Department of Mathematics, Shri Vishnu Engineering College for Women, Bhimavaram-534201, India*
^c*Department of Mathematics, ANITS, Visakhapatnam-533003, India*
^d*Department of Mathematics, GMR Institute of Technology, Rajam-532127, India*
^e*Department of Statistics & Mathematics, College of Horticulture, Dr. Y.S.R. Horticultural University, Parvathipuram-535502, India*
**Corresponding Author e-mail: aditya.y@gmrit.edu.in*

The purpose of this Erratum is to correct a misprint presented in the original article.

Keywords: *Erratum*

In original article, one of the affiliations of A. Vijaya Prasanthi is given as
“Department of Mathematics, Sri Vishnu Engineering College for Women, Bhimavaram-534201, India”,

but it should be

“Department of Mathematics, Shri Vishnu Engineering College for Women, Bhimavaram-534202, India”.

Original Article:

A.V. Prasanthi, G. Suryanarayana, Y. Aditya, U. Divya Prasanthi, “Cosmological Dynamics of Anisotropic Kaniadakis Holographic Dark Energy Model in Brans-Dicke Gravity,” East European Journal of Physics, (2), 10-20 (2024).
<https://periodicals.karazin.ua/eejp/article/view/23101/21480>

ВИПРАВЛЕННЯ: КОСМОЛОГІЧНА ДИНАМІКА АНІЗОТРОПНОЇ ГОЛОГРАФІЧНОЇ МОДЕЛІ ТЕМНОЇ ЕНЕРГІЇ КАНІАДАКІСА В ГРАВІТАЦІЇ БРАНСА-ДІККЕ [East European Journal of Physics, (2), 10-20 (2024)]

А. Віджая Прасанті^{a,b}, Г. Сурьянараяна^c, Ю. Адітья^d, У.Ю. Дів'я Прасанті^e
^a*Центр міждисциплінарних досліджень аАУ, Університет Андхра, Вісакхапатнам-530003, Індія*
^b*Департамент математики, жіночий інженерний коледж Шрі Вішну, Бхімаварам-534201, Індія*
^c*Департамент математики, ANITS, Visakhapatnam-533003, Індія*
^d*Відділ математики, Технологічний інститут GMR, Раджам-532127, Індія*
^e*Кафедра статистики та математики коледжу садівництва, Dr. Y.S.R. садівничий університет, Парватипурам-535502, Індія*

Метою цього Виправлення є виправлення друкарської помилки, представленої в оригінальній статті.

Ключові слова: *виправлення*

Вихідна стаття:

A.V. Prasanthi, G. Suryanarayana, Y. Aditya, U. Divya Prasanthi, “Cosmological Dynamics of Anisotropic Kaniadakis Holographic Dark Energy Model in Brans-Dicke Gravity,” East European Journal of Physics, (2), 10-20 (2024).
<https://periodicals.karazin.ua/eejp/article/view/23101/21480>

*До 75-річчя від дня народження
В.Ф. КЛЕПІКОВА*



13.07.2024 р. виповнилося 75 років від дня народження КЛЕПІКОВА Вячеслава Федоровича – відомого фізика-теоретика, доктора фізико-математичних наук, члена – кореспондента НАН України.

Народився В. Ф. Клепиков у Харкові, закінчив із золотою медаллю фізико-математичну школу № 27, а в 1971 р. – фізико-технічний факультет Харківського державного університету.

У 1972 р. під науковим керівництвом майбутнього академіка НАН України В. Г. Бар'яхтара захистив дисертацію на здобуття наукового ступеня кандидата фізико-математичних наук.

У 1995 р. захистив дисертацію на здобуття наукового ступеня доктора фізико-математичних наук.

У 2003 р. обраний членом-кореспондентом НАН України.

У 1971–1990 рр. працював у Харківському фізико-технічному інституті. У 1990–1992 рр. він ініціював створення при НАН України нової установи – Науково-технічного центру електрофізичної обробки, який згодом було перетворено в Інститут електрофізики і радіаційних технологій (ІЕРТ) НАН України. В. Ф. Клепиков був директором цієї установи від дня створення до 2021 р. На теперішній час працює на посаді радника при дирекції та є Почесним директором інституту.

Основні наукові результати, які здобув В.Ф. Клепиков як особисто, так і в співавторстві:

- передбачені умови гігантського посилення (ВП) ядерного магнітного резонансу (ЯМР) в тонких магнітних плівках, що дає можливість створити на основі таких плівок детектори ядерних спінових хвиль, магнітні аналоги камери Вільсона (детектори електронейтральних частинок), а також ядерні томографи з дуже високою роздільною здатністю;

- розроблені фізичні основи запам'ятовуючих пристроїв з рекордними параметрами, які здатні працювати за умов опромінення;

- розроблені радіаційні методи відновлення властивостей ядерних матеріалів;

- передбачені ефекти радіаційного стимулювання надпластичності;

- створені методи визначення за експериментальними даними таких характеристик частинок, які не можуть бути виміряні безпосередньо (матриці розсіяння, потенціали взаємодії та ін.);

- методи квантової електродинаміки узагальнені на випадок нелокальних полів матерії та застосовані до вирішення проблем фізики електромагнітних взаємодій у ядрах;

- запропоновані методи модифікації та фазових перетворень речовини за допомогою пучків заряджених частинок і створені нові ядерні та радіаційні технології, які широко впроваджені на практиці;

- створені радіаційні технології діагностики, контролю безпеки та подовження ресурсу ядерних реакторів і обладнання АЕС;

- створені нові радіаційні методи для низькотемпературного нанесення зміцнювальних покриттів;

- створені нові радіаційні технології для потреб медицини, агрокомплексу і боротьби з тероризмом (виявлення ядерних, вибухових матеріалів та ін.).

Отримано також низку значних результатів у теорії поля.

Розроблені в ІЕРТ НАН України технології було впроваджено В. Ф. Клепиковим, зокрема, для збереження і знезараження фондів і приміщень при ліквідації наслідків аварій в Національній бібліотеці імені В. І. Вернадського НАН України, у ВАК України та ін.

В. Ф. Клепиков багато років є заступником Академіка-секретаря Відділення ядерної фізики та енергетики НАН України. Він є членом Національної комісії з радіаційного захисту населення України при Верховній Раді України.

В. Ф. Клепиков був керівником низки проектів державних програм і контрактів, результати його досліджень узагальнені в 5 монографіях і більш ніж у 400 наукових працях і винаходах.

В. Ф. Клепиков вправно поєднує наукову, організаційну і педагогічну діяльність, підготував 8 кандидатів і 5 докторів наук.

З 1995 року дотепер В. Ф. Клепиков працює за сумісництвом на посаді професора на фізико-технічному факультеті (зараз – навчально-науковий інститут «Фізико-технічний факультет») Харківського національного університету імені В. Н. Каразіна. Викладає студентам спецкурс «Фазові переходи та критичні явища», задіяний до наукового керівництва в аспірантурі. У 1997 р. йому було присвоєно звання професора по кафедрі теоретичної ядерної фізики. 2008 року ним було створено в університеті кафедру електрофізики і радіаційних технологій подвійного підпорядкування (МОН та НАН України, за рішенням Колегії Міністерства освіти і науки України від 22.11.2006 р. №14/1-13 та Постанови Президії НАН України від 22.11.2006 р. №302 «Про поглиблення інтеграції науки та освіти в сучасних умовах»). Професор В. Ф. Клепиков очолював кафедру до 2012 року, коли при реорганізації фізико-технічного факультету кафедра увійшла до складу новоствореної кафедри матеріалів реакторобудування та фізичних технологій.

В. Ф. Клепиков – заслужений діяч науки і техніки України, лауреат премії ім. М. Островського, премій ім. С. Пекаря та ім. К. Синельникова НАН України, лауреат Державної премії України в галузі науки і техніки.

Наукова спільнота, колеги, учні щиро вітають Вячеслава Федоровича Клепикова зі знаменною датою та бажають міцного здоров'я та довгих років натхненної праці на благо науки.

М.О. Азаренков, А.В. Бабіч, М.І. Базалєєв, О.С. Бакай, Ю.А. Бережної, В.М. Береснев, В.В. Брюховецький, В.А. Білоус, Л.А. Булавін, І.Є. Гаркуша, І.О. Гірка, І.М. Карнаухов, Ю.О. Касаткін, І.В. Кириллін, Г.Д. Коваленко, В.Ю. Корда, О.Ю. Корчин, І.О. Кочешев, П.Е. Кузнецов, І.М. Неклюдов, В.В. Литвиненко, С.В. Литовченко, Р.І. Старовойтов, В.І. Слісенко, Ю.В. Слюсаренко, В.Ю. Сторіжко, В.І. Ткаченко, Г.Д. Толстолицька, І.М. Оніщенко, П.М. Остапчук, Є.М. Прохоренко